Superconductivity at a quantum critical point: A theoretical approach to the understanding of unconventional superconductors in strongly correlated systems.

A DISSERTATION
SUBMITTED TO THE FACULTY OF THE GRADUATE SCHOOL
OF THE UNIVERSITY OF MINNESOTA
BY

Yiming Wu

IN PARTIAL FULFILLMENT OF THE REQUIREMENTS
FOR THE DEGREE OF
DOCTOR OF PHILOSOPHY

Andrey V. Chubukov

August, 2021

© Yiming Wu 2021
ALL RIGHTS RESERVED

Acknowledgements

First of all, I'd like to thank my advisor Andrey Chubukov, for his scientific education and constant help to me. His expertise on correlated electronic systems, mathematical analysis, physical insights and so on, all benefit me during my PhD training. His passion towards physics, hard working spirit and geniality to people around will surely have a lifelong impact on me. He encouraged and supported me participating academic activities such as Gordon Conference in New Hampshire, ICTP workshop in Italy, Florida winter school, KITP grads fellow at UCSB and APS March meetings each year. Without him, I wouldn't accomplish what I have so far. I believe in many years after my graduation, I will still miss this five year training in his group.

I would like to also thank many professors in the physics department at University of Minnesota, for them teaching the courses that I have learned a lot, as part of my scientific education. In particular, I thank my advisor Andrey Chubukov for teaching me advanced quantum mechanics, M. Shifman for teaching me gauge field theory, Alex Kamenev for teaching me solid state physics and quantum field theory in condensed matter physics, Tony Gherghetta for teaching me QED and Jorge Viñals for teaching transport theory. Meanwhile I'm grateful to Boris Shklovskii, Rafael Fernandes for useful discussions on physics problems.

I'm also very grateful to my collaborators, Artem Abanov, Yuxuan Wang, Shangshun Zhang and Avraham Klein, who have contributed significantly to our published papers. Working with them is a wonderful and beneficial experience to me.

In my five Minnesota years, I met lots of good friends, including my peer colleagues Ruiqi Xing, Mengxing Ye, Dmitry Chichinadze, Dan Phan, Saumitran Kasturirangan, Fei Chen, Yang Tang, Qianyi Sheng, Kexin Feng, Hanteng Wang, Zhen Jiang, Huaqing Mao, Daniel Schubring, Yang Yang, Xiuzhong Ye, Xuzhe Yin, Yuting Wang, ect. It's

very helpful to discuss and learn physics from them. In the first two years, Hanteng Wang, Xiuzhong Ye, me and some other people organized a small discussion group on group theory and conformal field theory. Learning from my peer friends is an efficient way to gain knowledge. I'm therefore grateful to all of them.

This work is supported by NSF-DMR-1523036, NSF-DMR-1834856, Allen Goldman Fellowship, Doctoral Dissertation Fellowship and Aneesur Rahman Award from UMN. The author also acknowledges the hospitality of KITP where part of this work was done.

Dedication

To my beloved parents Wu Xuexiao and Wen Yulan.

Abstract

The complexity of strongly correlated electronic system is manifested by the interplay of multiple electronic orders, among which superconductivity is one of the most interesting phases. In experimentally observed phase diagrams for materials such as heavy fermion compounds, cuprates and iron based superconductors, superconductivity is close to other electronic orders such as ferromagnetism, anti-ferromagnetism and nematicity etc. This fact brings about interests of studying the role of a possible underlying quantum critical point(QCP) in determining the unusual properties of these materials. Here we consider an itinerant fermion system which is close to a QCP. Because of the closeness, the collective boson mode due to the order parameter fluctuations will couple to low energy fermions and mediate the fermion-fermion interaction. This effective interaction simultaneously gives rise to two competing fate for the fermions: On one hand it can lead to SC if the there is any pairing instability in at least one pairing channel. On the other hand, the same interaction also diminish fermion coherence and results in non Fermi liquid behavior. These two tendencies compete with each other, in a sense that SC gaps out low energy fermions and reduces the self energy , while non Fermi liquid tends to destroy fermion coherence and is detrimental to SC. In order to capture this story we adopt the approach that Eliashberg first used when he studied the electron-phonon coupling system, i.e. we approximate the fermion self energy by neglecting the vertex corrections, which is controllable when the vertex is parametrically smaller. We further assume the interaction depends only on frequency via a dynamical exponent γ, namely $V(\Omega_m) \propto 1/|\Omega_m|^\gamma$. Based on this model, we unveil many special properties of SC state on both imaginary and real frequency axis, including the 'gap closing' behavior observed in cuprates. As a unique feature of pairing at a QCP, we find there exists an infinite set of solutions to the gap equation, corresponding to different local minima in free energy. This set becomes a continuous one at a special case $\gamma = 2$, which corresponds to phonon-mediated pairing interaction with a vanishingly small phonon frequency. We also studied the odd-frequency pairing state from this model, and find there is no zero bias peak in the quasiparticle density of states which was considered as an evidence of

odd- frequency pairing. At last, in addition to mean field analysis, the superconducting phase fluctuation is also discussed.

Contents

List of Figures

Chapter 1

Starting point: Fermi liquid theory and its breakdown.

1.1 Fermi liquid

Understanding how the electrons in a realistic material behave and affect the macroscopic properties has always been an important yet difficult subject in hard condensed matter physics. Electrons are fermions which are subjected to the law of Fermi statistics. Accordingly, if we consider electrons to be noninteracting, then the ground state ($T = 0$) of this system will be a Fermi sea, and there is a sharp boundary between occupied and unoccupied states. The boundary in energy level is called a Fermi energy, and in momentum space, the manifold of this boundary is called a Fermi surface. In ideal cases, the Fermi surface is S^{d-1} where d is the space dimension of the system. For this ideal 3D Fermi gas, it's straight forward to obtain a relation between the particle density and Fermi momentum,

$$k_F = \left(\frac{3\pi^2 N}{V}\right)^{1/3} \tag{1.1}$$

where N is the electron number and V is the system size so their ratio N/V gives the electron density. The spectral properties of the system can be seen from the spectral function $A(\boldsymbol{k}, \omega)$, which can be measured by ARPES for example. For ideal Fermi gas

we have

$$A(\boldsymbol{k},\omega) = 2\pi\delta(\omega - \xi_{\boldsymbol{k}}) \tag{1.2}$$

which has a δ-function like peak near $\omega = \xi_{\boldsymbol{k}}$ and satisfies the sum rule,

$$\int_{-\infty}^{\infty} \frac{d\omega}{2\pi} A(\boldsymbol{k},\omega) = 1 \tag{1.3}$$

Actually this sum rule is not limited to ideal Fermi gas case, when there is interaction term the rule still holds correct. The momentum distribution function $n_F(\boldsymbol{k})$ is the obtained from integrate out the frequency dependence of $A(\boldsymbol{k},\omega)$ with a weight function $n_F(\omega)$, namely,

$$n_F(\boldsymbol{k}) = \int_{-\infty}^{\infty} \frac{d\omega}{2\pi} A(\boldsymbol{k},\omega) n_F(\omega) \tag{1.4}$$

A ground state this is just a step function: $n_F(\boldsymbol{k}) = 1$ if $|\boldsymbol{k}| \leq k_F$ while $n_F(\boldsymbol{k}) = 0$ if $|\boldsymbol{k}| > k_F$ and the jump happens right at k_F.

Now if we take the electron interactions into consideration, this system can no longer be described directly using the ideal Fermi gas language. By analog with the differece between liquid and gas, a weakly interacting fermion system is then called a Fermi liqud. A quantum field technique is needed in studying such a many-body system, and one can based on this to calculate interested properties perturbatively. However, Landau pointed out that if the interaction is not strong, the system responses to external perturbation just like the ideal Fermi gas does. This is to say, the particle concept inherited from electrons is preserved once the interaction is truned on, i.e. one can still describe the excitations to be non-interacting particles. To make distinction from the original electrons, we now call these quasiparticles. In fact, a quasiparticle has its own effective mass m^*, which is different from the bare electron mass m.

Using the quasiparticle picture, the properties of a Fermi liquid can be drawn and compared to those of an ideal Fermi gas. First of all, the spectral function of a Fermi liquid is

$$A(\boldsymbol{k},\omega) = 2\pi Z\delta(\omega - \xi_{\boldsymbol{k}}) \tag{1.5}$$

which still has a peak at $\omega = \xi_{\boldsymbol{k}_F}$. This peak is there only if the excitation has a very long lifetime and is therefore usually a proof of the applicability of Fermi liquid theory. The factor Z is called a quasiparticle residue and it is a small positive number

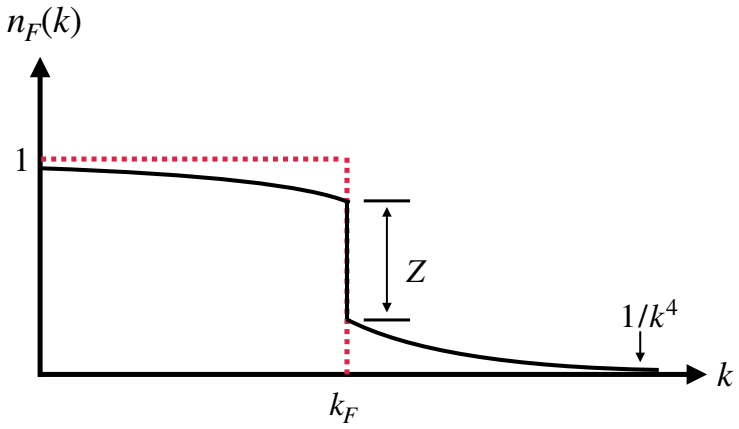

Figure 1.1: Momentum distribution function $n_F(\boldsymbol{k})$ for an ideal Fermi gas (red dashed) and a Fermi liquid (black).

$0 < Z < 1$. Using again (1.4) one easily finds in the Fermi liquid ground state, $n_F(\boldsymbol{k})$ also has a jump at k_F, but here the jump height is Z instead of 1. As can be seen from Figure 1.1. At very large momentum, $n_F(\boldsymbol{k})$ decays as $1/\boldsymbol{k}^4$ which is also called Tan relation[1]. As we mentioned above, the sum rule (1.3) works even when the interaction term in included. However when we apply the sum rule to Fermi liquid spectral function we immediately see (1.5) violates the rule, as the integral gives out Z instead of 1. In fact, by writing down the spectral function as (1.5), we only takes the coherent part in to account. There is still some incoherent part as the background which contributes to the rest in the sum rule, and this incoherent background does not response to the external perturbation like a quasiparticle.

So far we have seen that for a given interacting fermion system, as long as we can find the correct value of m^* and Z we can still treat the quasiparticles as non-interacting. There is also another important question regarding the Fermi momentum: does is changes after the interaction is switched on? We have already given the answer in Figure.1.1 as both black curve and the red dashed curve jump at the same position. So the answer is k_F is the same and it is determined by (1.1). The reason behind this is called Luttinger theorem[2, 3]. It states that the volume enclosed by a Fermi surface is proportional to the particle density of this system. Using mathematical language, (1.1) is immune to the presence of many body interaction.

The calculation of mass renormalization m^* and the quasiparticle residue Z can be done from a microscopic field theory technique. To this end, we notice that a general retarded Green's function with interaction self energy term can be written as (neglecting spin index for a moment, so the Green's function below is the diagonal term in spin space)

$$\begin{aligned} G^R(\boldsymbol{k},\omega) &= \frac{1}{\omega - \xi_{\boldsymbol{k}} - \Sigma(\boldsymbol{k},\omega)} \\ &= \frac{1}{\omega - [\xi_{\boldsymbol{k}} + \operatorname{Re}\Sigma(\boldsymbol{k},\omega)] - i\operatorname{Im}\Sigma(\boldsymbol{k},\omega)} \end{aligned} \tag{1.6}$$

We are interested in the regions close to the Fermi surface, where the term $\xi_{\boldsymbol{k}}+\operatorname{Re}\Sigma(\boldsymbol{k},\omega)$ is vanishingly small. Therefore we can expand it in terms of ω and $\boldsymbol{k}-\boldsymbol{k}_F$. Keeping only the first order, we arrive at the following form for the Green's function

$$G^R(\boldsymbol{k},\omega) \approx \frac{Z}{\omega - \frac{1}{m^*}(k-k_F)k_F + \frac{i}{\tau_{\boldsymbol{k}}(\omega)}} \tag{1.7}$$

Note after using $\approx$ we missed the incoherent background part. By this definition, we have

$$\begin{aligned} Z^{-1} &= 1 - \frac{\partial}{\partial\omega}\operatorname{Re}\Sigma(k_F,\omega)|_{\omega=0}, \\ \frac{m}{m^*} &= Z\left(1 + \frac{m}{k_F}\frac{\partial}{\partial k}\operatorname{Re}\Sigma(k,0)|_{k=k_F}\right), \\ \frac{1}{\tau_{\boldsymbol{k}}} &= -Z\operatorname{Im}\Sigma(\boldsymbol{k},\omega). \end{aligned} \tag{1.8}$$

Here the last line is the definition of quasiparticle lifetime. If the imaginary part of self energy is vanishingly small on Fermi surface, the lifetime of a quasiparticle is very long and this lays the foundation of Fermi liquid theory. For a valid Fermi liquid system, it is shown that $\tau_{\boldsymbol{k}} \sim \xi_{\boldsymbol{k}}^{-2}$. Thus as long as the particles are close enough to the Fermi surface, they are long lived and well defined. We will see in Sec.1.3 that once this condition is not satisfied, the quasiparticle excitation will quickly decay and the system is no loner a Fermi liquid. According to (1.8), in principle we can know all these quantities once we manage to obtain the many body fermion self energy $\Sigma(\boldsymbol{k},\omega)$. However calculating the fermion self energy is not an easy task. One can sum over some particular contributions order by order like we do in random phase approximation(RPA), but sometimes RPA does miss important contributions.

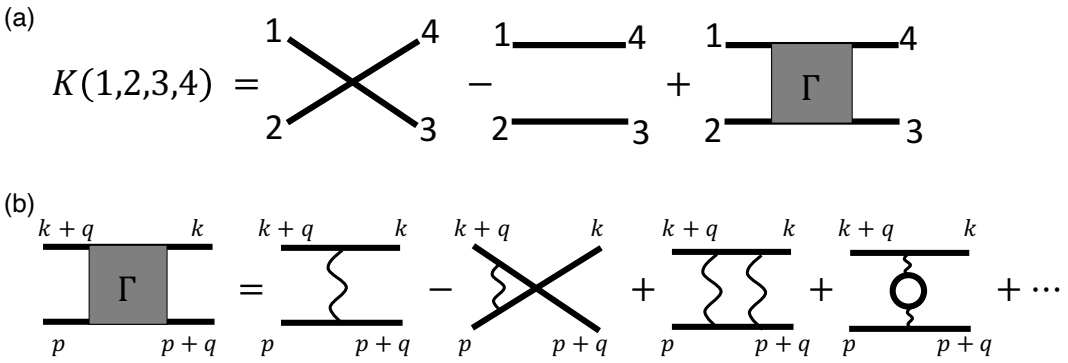

Figure 1.2: (a) Two particle Green's function: definition of the vertex function $\Gamma_{\alpha\beta,\gamma\delta}(p_1, p_2; p_3, p_4)$. (b)The first few term in $\Gamma_{\alpha\beta,\gamma\delta}(p_1, p_2; p_3, p_4)$

Another more organized approach is by introducing a vertex function in the presence of interaction, from which m^* and Z can also be obtained. Moreover, one can also see a possible instability with it when the interaction varies. Unlike the single particle Green's function defined (1.6), the vertex function is connected with a two particle Green's function. This two particle Green's function is necessary be because physical observables such as charge and spin susceptibilities are all in the form of two particle Green's function. Generally it is defined as

$$K_{\alpha\beta,\gamma\delta}(\boldsymbol{p_1}\tau_1, \boldsymbol{p_2}\tau_2; \boldsymbol{p_3}\tau_3, \boldsymbol{p_4}\tau_4) = \langle T_\tau c_{\boldsymbol{p_1}\alpha}(\tau_1) c_{\boldsymbol{p_2}\beta}(\tau_2) c^\dagger_{\boldsymbol{p_3}\gamma}(\tau_3) c^\dagger_{\boldsymbol{p_4}\delta}(\tau_4)\rangle \tag{1.9}$$

Here we use imaginary time for convenience and both c and $c^\dagger$ depend on space time. $\alpha, \beta, \gamma, \delta$ are all spin indices. We can also Fourier transform the imaginary time to get Matsubara frequencies and use $p_j = (i\omega_{j,n}, \boldsymbol{p}_j)$ for short so now the Green's function is $K_{\alpha\beta,\gamma\delta}(p_1, p_2; p_3, p_4)$. For translational invariant system the energy-momentum is conserved, i.e., $p_1 + p_2 = p_3 + p_4$. The evaluation of two particle Green's function leads to our definition of the so called vertex function $\Gamma_{\alpha\beta,\gamma\delta}(p_1, p_2; p_3, p_4)$:

$$\begin{aligned} K_{\alpha\beta,\gamma\delta}(p_1, p_2; p_3, p_4) &= \delta_{\alpha,\gamma}\delta_{\beta,\delta}\delta(p_1 - p_3)\delta(p_2 - p_4)G(p_1)G(p_2) \\ &\quad - \delta_{\alpha,\delta}\delta_{\beta,\gamma}\delta(p_1 - p_3)\delta(p_2 - p_4)G(p_1)G(p_2) \\ &\quad + G(p_1)G(p_2)G(p_3)G(p_4)\Gamma_{\alpha\beta,\gamma\delta}(p_1, p_2; p_3, p_4) \end{aligned} \tag{1.10}$$

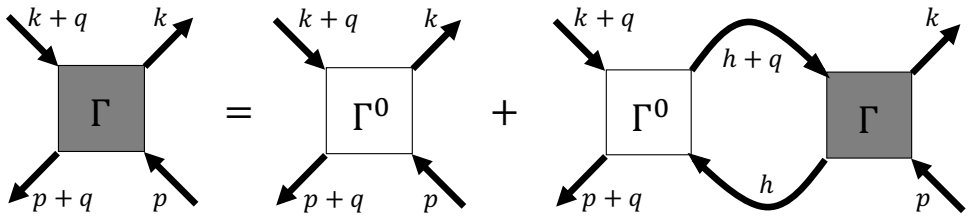

Figure 1.3: Bethe-Salpeter equation for the vertex function

This equation is diagrammatically shown in Figure.1.2(a), where the full single particle Green's function $G(p_j)$ is shown as the thick straight line, while the Grey box is the vertex function Γ. From its definition, we know that the vertex function is antisymmetric on exchanging the momentum p_3 and p_4. Of course one can calculate Γ order by order, and we have shown the first few terms in Figure1.2(b). Note the evaluation of Γ doesn't include the four external fermion legs.

If we continue drawing the all diagrams of Γ to include higher orders, we will find there exist some diagrams which are two-particle reducible. By this we mean one can divide the diagram into two unconnected pieces by cutting two fermion lines. These are the diagrams that contains a particle-hole bubble. As an analog of Dyson equation for the full single particle Green's function, one can follow similar derivation to obtain the following Bethe-Salpeter equation for the vertex function.

$$\Gamma_{\alpha\beta,\gamma\delta}(p,k;q) = \Gamma^0_{\alpha\beta,\gamma\delta}(p,k;q) + \frac{1}{\beta V}\sum_h \Gamma^0_{\alpha\xi,\gamma\eta}(h,k;q)G(h)G(h+q)\Gamma_{\eta\beta,\xi\delta}(p,h;q) \tag{1.11}$$

Where Γ^0 is the two-particle-irreducible part which doesn't contain particle-hole bubble. The p-h bubble has the following properties. At small momentum transfer q the bubble is non-analytic, and its value depends on the double limit $i\Omega_n \to 0$ and $\boldsymbol{q} \to 0$. Consequently, the vertex function at small q, also depends on how the double limit is taken. To see this, consider taking the single particle Green's function in the form of (1.6), then the p-h bubble is

$$\pi(h,q) = G(h)G(h+q) = \frac{m^* Z^2}{k_F}\delta(|\boldsymbol{h}| - k_F)\delta(i\omega_n)\frac{\xi_{\boldsymbol{h}+\boldsymbol{q}} - \xi_{\boldsymbol{h}}}{i\Omega_n - \xi_{\boldsymbol{h}+\boldsymbol{q}} + \xi_{\boldsymbol{h}}} + \pi_{inc} \tag{1.12}$$

The last term is the incoherent part which cannot be described in the quasiparticle

language. Here we use $h = (\omega_n, \boldsymbol{h})$ to denote the internal momentum of the p-h bubble, while $q = (\Omega_n, \boldsymbol{q})$ denotes the external momentum. Now it is clear how this quantity depends on the double limit when $q \to 0$. In the ω limit, when we first take $\boldsymbol{q} = 0$ and then take $\Omega_n \to 0$, the first term in the l.h.s. of (1.12) vanishes, and $\pi^\omega = \pi_{inc}$. While if we first take $\Omega_n = 0$ and then take $\boldsymbol{q} \to 0$, we obtain $\pi^q = -\frac{m^* Z^2}{k_F}\delta(|\boldsymbol{h}|-k_F)\delta(i\omega_n)+\pi_{inc}$.

Because of the non-analyticity of $\pi(h,q)$ at small q, the evaluation of the vertex function Γ at small q also depends on how the double limit is taken. The two-particle irreducible part Γ^0 however, does not depend on this double limit, since it does not contain the p-h bubble. As a result, Γ^0 are the same in both ω and $\boldsymbol{q}$ limit and we don't try to distinguish them in these two limit. It turns out, Γ at small q can be equivalently expressed using both ω and $\boldsymbol{q}$ limit:

$$\begin{aligned}
\Gamma^{\omega}_{\alpha\beta,\gamma\delta}(p,k;q) &= \Gamma^{\omega}_{\alpha\beta,\gamma\delta}(p,k;q) + \frac{1}{\beta V}\sum_h \Gamma^{\omega}_{\alpha\xi,\gamma\eta}(h,k;q)[\pi(h,q)-\pi^{\omega}]\Gamma_{\eta\beta,\xi\delta}(p,h;q) \\
\Gamma^{\boldsymbol{q}}_{\alpha\beta,\gamma\delta}(p,k;q) &= \Gamma^{\boldsymbol{q}}_{\alpha\beta,\gamma\delta}(p,k;q) + \frac{1}{\beta V}\sum_h \Gamma^{\boldsymbol{q}}_{\alpha\xi,\gamma\eta}(h,k;q)[\pi(h,q)-\pi^{\boldsymbol{q}}]\Gamma_{\eta\beta,\xi\delta}(p,h;q)
\end{aligned} \tag{1.13}$$

and from above

$$\begin{aligned}
\pi(h,q)-\pi^{\omega} &= \frac{m^* Z^2}{k_F}\delta(|\boldsymbol{h}|-k_F)\delta(i\omega_n)\frac{\xi_{\boldsymbol{h}+\boldsymbol{q}}-\xi_{\boldsymbol{h}}}{i\Omega_n-\xi_{\boldsymbol{h}+\boldsymbol{q}}+\xi_{\boldsymbol{h}}} \\
\pi(h,q)-\pi^{\boldsymbol{q}} &= \frac{m^* Z^2}{k_F}\delta(|\boldsymbol{h}|-k_F)\delta(i\omega_n)\frac{i\Omega_n}{i\Omega_n-\xi_{\boldsymbol{h}+\boldsymbol{q}}+\xi_{\boldsymbol{h}}}
\end{aligned} \tag{1.14}$$

With the help of the vertex function, the quasiparticle properties mentioned above have alternative expressions. In fact, for Galilean-invariant systems, the mass renormalization, and other thermodynamic properties such as specific heat and magnetic susceptibility, can be determined by Γ^{ω} with all the legs on Fermi surface. The quasiparticle residue is not determined solely on Fermi surface but still can be given by the Γ^{ω}. By utilizing Pitaevskii-Landau relationsone is able to see

$$\begin{aligned}
\frac{1}{Z} &= 1 - \frac{i}{2}\sum_{\alpha\beta}\int \frac{d^{D+1}q}{(2\pi)^{D+1}}\Gamma^{\omega}_{\alpha\beta,\alpha\beta}(p_F,q)\pi_{inc} \\
\frac{1}{m^*} &= \frac{1}{m} - \frac{Z^2 k_F^{D-2}}{2(2\pi)^D}\sum_{\alpha\beta}\int d\Omega_q \Gamma^{\omega}_{\alpha\beta,\alpha\beta}(p_F,q_F)\frac{\boldsymbol{p}_F\cdot\boldsymbol{q}_F}{k_F^2}
\end{aligned} \tag{1.15}$$

1.2 Instabilities in Fermi liquid

The Fermi liquid picture works well when the quasiparticle lifetime is long enough. This is not always true given that the effective fermion interaction could be so strong to destroy the Fermi liquid ground state. It is possible that even at $T = 0$, the system undergoes a phase transition due to the change of external field, pressure etc, or it could be in a totally different ground state when the strength of interaction changes. This is called a quantum phase transition, in distinction with the classical phase transition where it is thermal fluctuations that destroys the order. There are multiple ways to destroy Fermi liquid picture, which corresponds to different instabilities. For example, in Mott transition once the fermion interaction is strong enough, the whole Fermi surface disappears. In some cases, the Fermi surface gets distorted, associated with spontaneous symmetry breaking with $\boldsymbol{Q} = 0$ order parameter. This kind of instability is first studied by Pomeranchuk. The instability can also happen in particle-particle channel, which often gives rise to superconductivity.

1.2.1 Pomeranchuk

This kind of instability is associated with fermion on Fermi surface, and depending on different channel, it can lead to phase separation, ferromagnetism, dynamically generated spin-orbit coupling, or spin and charge nematic order[4, 5, 6, 7, 8, 6, 9, 10, 11, 12].

To probe such instabilities, it is useful to calculate the full susceptibility for a spin or charge sector. A divergence in the full susceptibility often signals such an instability. Including all interaction effects, the exact form of the susceptibility is first given by Leggett[13],

$$\chi_l^{c(s)} = (\Lambda_l^{c(s)} Z)^2 \frac{m^*}{m} \frac{\chi_{l,0}^{c(s)}}{1 + F_l^{c(s)}} + \chi_{l,inc}^{c(s)} \tag{1.16}$$

where $\chi_{l,0}^{c(s)}$ is the bare susceptibility in charge (spin) channel, and in angular momentum l channel. Z is the quasiparticle residue, Λ_l is the triple vertex correction, and m^* is the renormalized mass due to the present of fermion interaction. The last term $\chi_{l,inc}$ is the incoherent part, which cannot be described using Fermi liquid theory. At first glance, if the Landau parameter $F_l^{c(s)}$ is close to -1, the full susceptibility is divergent. Hence $F_l^{c(s)} = -1$ can be viewed as a cretireon of such Pomeranchuck instability. However,

as a result of conservation law of total charge and spin, if the order parameter under investigation happens to coincide with charge and spin current operator, the $l = 1$ sum rule prohibit the full $\chi^{c(s)}_{l=1}$ from diverging. In these two special case, there instability is absent[13, 14, 15].

1.2.2 From Hubbard model to spin-fermion model

Here we use a simple example to demonstrate how the instability can be seen from evaluating the vertex function, and how the interaction gets renormalized when the system is close to such an instability. The example we use here is based on Hubbard constant interaction U. This fermion interaction is constant and does not depend on momentum nor frequency.

The quantity we will compute is the vertex function Γ^{ω} taken in ω limit. This is because, as we mentioned above, some response properties are related to Γ^{ω}. In the first order, it contains two ingredients, as shown in Figure1.4,

$$\Gamma^{\omega,(1)}_{\alpha\beta,\gamma\delta}(k,p) = (-U)[\delta_{\alpha\gamma}\delta_{\beta\delta} - \delta_{\alpha\delta}\delta_{\beta\gamma}] \tag{1.17}$$

The minus sign comes from the antisymmetric property of Γ^{ω}, and is a result of Fermi statistics. Nothing interesting happens in the first order. In the second order, we have listed the related diagrams in Figure1.4. A constant interaction here simplifies our calculation, because one can factor out U in the loop integrals. After doing so, all the integrals are nothing but particle-hole and particle-particle bubbles. Since we are interested in investigating a possible instability in particle-hole channel, we can entirely neglect the particle-particle bubble contribution. Thus we will not consider the first and the last diagrams listed in the second order diagrams in Figure1.4. We are now left with only 3 diagrams in this order. In forth diagram, the factor of 2 comes from symmetry, the fact that we attach the rainbow in the lower or upper position. According to Feynman rule, one must add an additional factor '-1' whenever there is a fermion loop. Mover, when we consider spin summation, we should add a factor of 2 when there is a fermion loop. Therefore the third and the forth second-order-diagrams completely

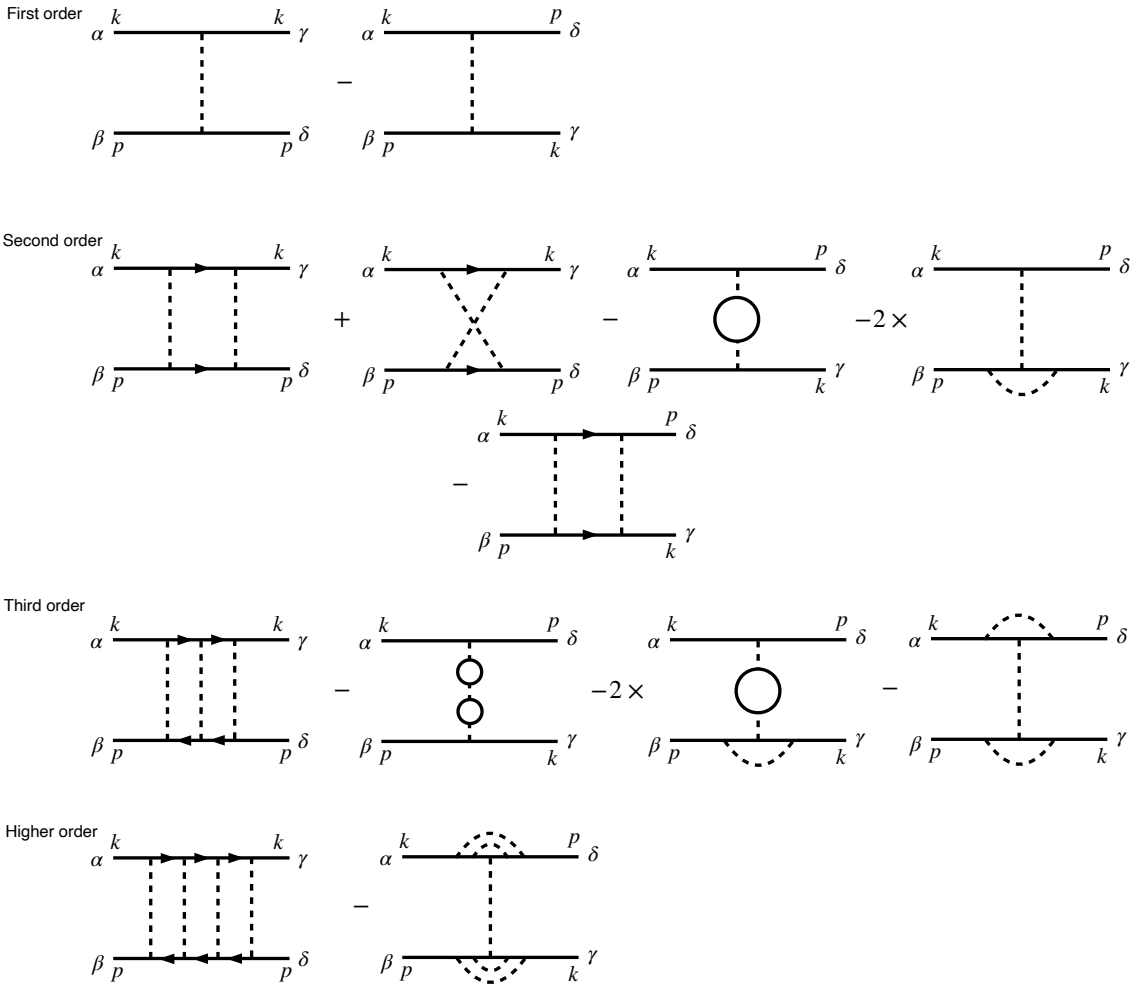

Figure 1.4: The first view orders of the antisymmetric vertex Γ^{ω} with a Hubbard U interaction. The vertex was taken in the ω limit.

cancel out, and we need only to consider the second one, which leads to

$$\Gamma^{\omega,(2)}_{\alpha\beta,\gamma\delta}(k,p) = U^2\Pi_{ph}(k-p)\delta_{\alpha\gamma}\delta_{\beta\delta} \tag{1.18}$$

Here Π_{ph} denotes the bare particle-hole bubble. One may ask why not consider the diagram similar to the forth but with (p,δ) and (k,γ) interchanged. This is because as we said we are in the ω limit, hence the momentum transfer for the p-h bubble is $\boldsymbol{q} = 0$. In this limit, the p-h bubble does not contribute.

Next we consider the third order, and the related diagrams are presented in Figure1.4. By the same logic, in this order, the second and the third diagrams cancel out, while the first and the last remain. They lead to

$$\Gamma^{\omega,(3)}_{\alpha\beta,\gamma\delta}(k,p) = -U^3\Pi^2_{ph}(k-p)[\delta_{\alpha\gamma}\delta_{\beta\delta} - \delta_{\alpha\delta}\delta_{\beta\gamma}] \tag{1.19}$$

Continue doing the same analysis to higher orders, it is not hard to sum up all the related diagrams. For example, from the higher order diagrams shown in Figure1.4, we obtain a contribution $U^4\Pi^3\delta_{\alpha\gamma}\delta_{\beta\delta}$ and $U^5\Pi^4\delta_{\alpha\delta}\delta_{\beta\gamma}$. These two contribution together with the above lower order contributions, form two geometric series. Diagrammatically, we only need to consider those 'ladder' diagrams and 'rainbow' diagrams. This approximation is also called RPA, as we noted earlier. Summing all these diagrams up, we obtain,

$$\Gamma^{\omega}_{\alpha\beta,\gamma\delta}(k,p) = \frac{-U}{1+U\Pi_{ph}(k-p)}\delta_{\alpha\gamma}\delta_{\beta\delta} - \frac{-U}{1-U^2\Pi^2_{ph}(k-p)}\delta_{\alpha\delta}\delta_{\beta\gamma} \tag{1.20}$$

For spin rotation invariant systems, we make use of the completeness of Pauli matrices,

$$2\delta_{\alpha\gamma}\delta_{\beta\delta} = \delta_{\alpha\delta}\delta_{\beta\gamma} + \boldsymbol{\sigma}_{\alpha\delta}\cdot\boldsymbol{\sigma}_{\beta\gamma} \tag{1.21}$$

With this identity, we rewrite the result as a sum of charge and spin channels:

$$\Gamma^{\omega}_{\alpha\beta,\gamma\delta}(k,p) = \frac{1}{2}\frac{-U}{1+U\Pi_{ph}(k-p)}\boldsymbol{\sigma}_{\alpha\delta}\cdot\boldsymbol{\sigma}_{\beta\gamma} - \frac{1}{2}\frac{-U}{1-U\Pi_{ph}(k-p)}\delta_{\alpha\delta}\delta_{\beta\gamma} \tag{1.22}$$

Now interesting things can be seen from the above equation. The effective interactions in charge channel are similar to that in spin channel, with the only difference being the sign of $U\Pi_{ph}$ term in the denominator. Because of this, there is a possibility of

instability in spin channel if $U\Pi_{ph} < 0$. In our notation here, U is a positive quantity when the interaction is repulsive, however Π_{ph} carries a minus sign. For clarity, below is the calculation of Π_{ph} at $i\Omega_m = 0$ and $\boldsymbol{q} \to 0$,

$$\begin{aligned}\Pi_{ph}(i\Omega_m = 0, \boldsymbol{q} \to 0) &= \frac{1}{V}\sum_{\boldsymbol{k}} \frac{n_F(\xi_{\boldsymbol{k}}) - n_F(\xi_{\boldsymbol{k}-\boldsymbol{q}})}{\xi_{\boldsymbol{k}} - \xi_{\boldsymbol{k}-\boldsymbol{q}}} \\ &= \nu \int d\xi \frac{\partial n_F(\xi)}{\partial \xi} = -\nu \int d\xi \delta(\xi) = -\nu\end{aligned} \tag{1.23}$$

where ν is the density of sates near Fermi surface. As a result, $U\Pi_{ph} < 0$ and a possible instability can only happen in spin channel. Indeed, once the interaction U gets strong enough, such that the factor $U\Pi_{ph}$ is close to -1, the vertex in spin channel is enhanced. If $U\Pi_{ph} = -1$, the spin channel vertex diverges. This is a signal that the system is unstable against any magnetic perturbation, and will likely change the ground state to some magnetic ordered state.

Close to such a transition point, which we will call a quantum critical point later, the effective interaction is dominantly in spin channel. Because of this, we can use $-U/(1 + U\Pi_{ph})$ as the staring interaction study other properties of the system. The p-h bubble need not contain zero frequency, and the related fermions are not necessarily strictly on Fermi surface. In fact it can be obtained including finite frequency and this is the Landau damping term. When the magnetic order carries a finite momentum $\boldsymbol{Q}$, we obtain,

$$1 + U\Pi_{ph}(k - p) \propto \xi^{-2} + |\boldsymbol{k} - \boldsymbol{q} - \boldsymbol{Q}|^2 + a|\omega_n - \omega_m| \tag{1.24}$$

If we write the vertex function as $\Gamma^{\omega}_{\alpha\beta,\gamma\delta}(k, p) = V(k - p)\boldsymbol{\sigma}_{\alpha\delta} \cdot \boldsymbol{\sigma}_{\beta\gamma}$, the interaction term is then given by

$$V(k - p) = \frac{g^2}{\xi^{-2} + |\boldsymbol{k} - \boldsymbol{q} - \boldsymbol{Q}|^2 + a|\omega_n - \omega_m|} \tag{1.25}$$

where g is some effective coupling constant. Interaction of this kind, coming from the collective fluctuation mode when close to a magnetic quantum critical point, is often dubbed as spin-fermion model. Later we will use this model as a starting point to study the interplay between superconductivity and non Fermi liquid tendency. We will demonstrate in Sec.2.1.2 how this type of interaction can lead to d-wave superconductivity when $\boldsymbol{Q} = (\pi, \pi)$.

1.2.3 Cooper instability

Starting from a normal Fermi liquid, the system can also experience instability in particle-particle channel. An instability of this kind is also called Cooper instability, which is the onset of superconductivity in charged systems.

To see this, one can step back to the above example where we demonstrate how the instabilities in the direct channel happens. Remember in evaluating the RPA ladder and rainbow diagrams, we automatically neglect the contributions from the particle-particle bubble, and Π_{ph} in (1.22) is a particle-hole bubble. Explicitly, we neglected, e.g. the first and the last diagrams in the second order diagrams of Figure 1.4. Here we do the opposite way. We will sum up all the ladder diagrams which contain a p-p bubble. The series is again a geometric one, and we therefore have

$$\Gamma^{\omega}_{\alpha\beta,\gamma\delta}(k,p) = [\delta_{\alpha\gamma}\delta_{\beta\delta} - \delta_{\alpha\delta}\delta_{\beta\gamma}]\frac{-U}{1+U\Pi_{pp}(q)} \tag{1.26}$$

where $\Pi_{pp}(q)$ denotes the particle-particle bubble with an external momentum q. Explicitly,

$$\begin{aligned}\Pi_{pp}(q) &= \frac{1}{\beta V}\sum_{\boldsymbol{k},\omega_m}\frac{1}{i\omega_m - \xi_{\boldsymbol{k}}}\frac{1}{-i\omega_m + i\Omega_n - \xi_{-\boldsymbol{k}+\boldsymbol{q}}} \\ &= \frac{1}{V}\sum_{\boldsymbol{k}}\frac{n_F(\xi_{\boldsymbol{k}}) + n_F(\xi_{-\boldsymbol{k}+\boldsymbol{q}}) - 1}{i\Omega_n - \xi_{\boldsymbol{k}} - \xi_{-\boldsymbol{k}+\boldsymbol{q}}}\end{aligned} \tag{1.27}$$

To make sense of this integral expression, we only need to consider the simplest case when the external probe is static and uniform. This means we take both $i\Omega_m = 0$ and $\boldsymbol{q} = 0$ in the above expression. In this limit, $\xi_{-\boldsymbol{k}+\boldsymbol{q}} = \xi_{-\boldsymbol{k}} = \xi_{\boldsymbol{k}}$. Using this now the integral reduces to

$$\begin{aligned}\Pi_{pp}(i\Omega_m = 0, \boldsymbol{q}\to 0) &\approx \nu\int_{-\omega_D}^{\omega_D} d\xi\frac{1-2n_F(\xi)}{2\xi} = \nu\int_0^{\omega_D} d\xi\frac{1-2n_F(\xi)}{\xi} \\ &\approx \nu\int_T^{\omega_D}\frac{d\xi}{\xi} = \nu\ln\left(\frac{\omega_D}{T}\right)\end{aligned} \tag{1.28}$$

Here we introduced a new energy scale ω_D, which is actually the upper boundary of the region where our analysis is valid. In the second approximation, we assume $\omega_D \gg T$, so the integral has main contribution from the interval (T, ω_D) where the integrand can be approximated by $1/\xi$.

(1.28) has some appealing features. First, unlike the particle-hole bubble calculated in (1.23), Π_{pp} is a positive quantity. Second, the appearance of logarithm can lead to arbitrary largeness, as long as T is small enough, or ω_D is large enough. With these facts, an instability in (1.27) may happen if $U < 0$. A negative U means attractive interaction. More interestingly, there is no condition on the strength of U for the occurrence of such an instability, because $U\Pi_{pp}$ can be arbitrarily large with the presence of logarithm term. The physical interpretation coming from this behavior is, the Fermi liquid ground state is unstable against any attractive fermion interaction, and even the weakest attraction could change the ground state as long as the temperature is low enough.

The transition temperature T_p for this to happen can be determined by requiring the denominator of (1.27) to be zero. The result is

$$T_p = \omega_D \exp\left(\frac{-1}{\nu|U|}\right) \tag{1.29}$$

This is the transition temperature obtained from the conventional BCS model for superconductivity, and the energy scale ω_D is interpreted as the scale below which fermions become attractive, due to the presence of electron-phonon coupling. In fact ω_D is the typical energy of phonons that mediate the interaction. In some materials we can apply extremely high external pressure to increase ω_D, in order to obtain high temperature superconductors.

Superconductivity of this kind is still a weak coupling theory. For a strong coupling theory, instead of (1.29), T_p often scales with the coupling constant.

1.3 non-Fermi liquid and superconductivity at a quantum critical point

[1] From above we see the validity of Fermi liquid picture is closely related to the smallness of the imaginary part of fermion self energy $\mathrm{Im}\,\Sigma(\boldsymbol{k},\omega)$ at Fermi surface. This is because the quasiparticle life time τ scales as inverse of $\mathrm{Im}\,\Sigma(\boldsymbol{k},\omega)$. If the imaginary part becomes finite even at Fermi surface, the system will enter non Fermi liquid regime, where the

[1] Luttinger liquid is a typical example of non-Fermi liquid. However, since our study is on systems in two or more spacial dimension, we will not discuss this kind of non-Fermi liquid here.

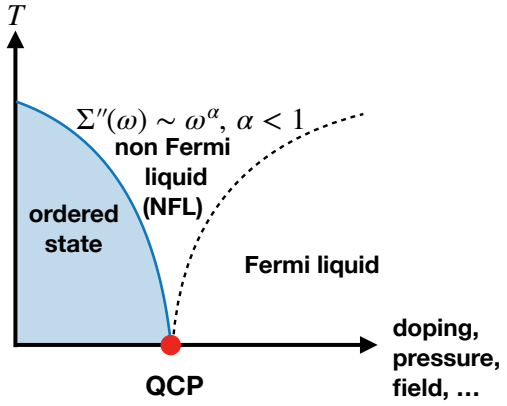

Figure 1.5: Non-Fermi liquid near a quantum critical point.

quasiparticle concept is lost, and the response to external probe becomes incoherent. This non-Fermi liquid, also called strange metal phase, is observed in strongly correlated systems such as heavy fermion compounds, cuprates and so on.

Here we consider a class of non-Fermi liquids which locates above a quantum critical point(QCP)[16, 17, 18, 19, 20, 21, 22, 23, 24, 25, 26, 27, 28, 29, 30, 31, 32, 33, 34, 35, 36, 37, 38, 39, 40, 41, 42, 43, 44]. In Sec.1.2.2 we clearly once the system is close to a QCP, the bare Hubbard interaction U, get strongly renormalized in direct spin channel. Moreover, the form of the interaction changes drastically, i.e. from a constant, static U term to a dynamic interaction (1.25). The new interaction, will destroy the Fermi liquid picture, by strongly renormalizing the fermion self energy.

In Figure 1.5 we show a sketch of non-Fermi liquid arising above a QCP, which marks the onset of some electronic order at $T = 0$ by tunning a parameter such as doping, external pressure or field. Close to the QCP, the fluctuations of that electronic order parameter form a collective boson mode. And in low energy limit this mode is a Goldstone mode and thus massless. This boson mode then couples to fermions on Fermi surface, mediates the fermion fermion interaction. As a result, the fermion self energy is renormalized and scales as $\Sigma(\omega) \sim \omega^{\alpha}$ with $\alpha < 1$. At small frequency $\Sigma(\omega) \gg \omega$ and one can immediately see this is a non-Fermi liquid self energy by e.g. calculating the quasiparticle residue and finding $Z \to 0$.

The same interaction that leads to non-Fermi liquid, can also result in instability in

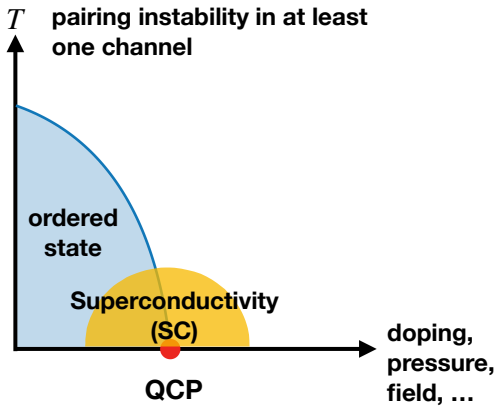

Figure 1.6: Superconductivity above a quantum critical point.

Cooper channel. This is an interesting complexity of quantum critical metals. We show this option in Figure 1.6, where we see a superconducting dome above the SC.

Although coming from the same interaction, these two fates of fermions, Figure 1.5 and 1.6 compete with each other. This is because, on one hand, superconductivity needs fermion coherence to form Cooper pairs and once the pairs condensate it gaps out low energy excitations and restores the original fermions self energy; on the other hand, non-Fermi liquid tendency destroys fermion coherence and hence prohibit quasiparticle pairs forming.

The interplay between superconductivity and non-Fermi liquid will be the central topic of this thesis paper. In the following, we will first introduce the γ-model that we used to tackle this problem, and then we will discuss results from analyzing this model.

Chapter 2

A general model for paring at a quantum critical point

In this chapter, we focus on the paring problem when the system is close to a QCP, where the pairing interaction is mediated by a collective boson mode. Before presenting the general γ model, two concrete examples are discussed. The γ model and associated gap equations are then derived based on these two examples, from a mean field analysis. We will also discuss the extension of this model by introducing a factor N, which differentiates the pairing equation in Cooper channel from that in direct channel. After that, we find the the critical value of N separating a superconducting state from a non Fermi liquid normal state. We also calculate from γ model the mean field level onset temperature for superconductivity, which we denote by T_p, as well as the superconducting gap amplitude Δ_0.

2.1 Two examples

Here we derive the pairing equation for two different systems. The superconducting parameter is chosen as the pairing vertex function $\Phi(\boldsymbol{k}, \omega_m)$. This function, if we neglect the corrections to the fermion self energy $\tilde{\Sigma}(\boldsymbol{k}, \omega_m) = \omega_m + \Sigma(\boldsymbol{k}, \omega)$ from the pairing interaction, coincides with the gap function $\Delta(\boldsymbol{k}, \omega_m)$. But in cases especially when we want to investigate the interplay between superconductivity and non Fermi liquid behavior, we have to consider the interplay between $\Phi(\boldsymbol{k}, \omega_m)$ and $\tilde{\Sigma}(\boldsymbol{k}, \omega_m)$. Like in

many previous studies, the Eliashberg approximation will be used here. We will see from the two examples that although they are totally different systems, the resulting pairing equations, after restricting the momentum on Fermi surface and integrating out the remaining degrees of freedom, are strikingly similar to each other. This lays the foundation of introducing the γ model.

2.1.1 Pairing at a 2D nematic or ferromagnetic QCP

In both cases the charge- and spin-interaction between fermions peaks at small $\boldsymbol{q}$ and can be described by

$$\chi(q) = \frac{g^2}{\boldsymbol{q}^2 + \Gamma\frac{|\Omega_m|}{\boldsymbol{q}}} \tag{2.1}$$

In the case of charge-charge interaction, this term comes from nematic fluctuations, and $\Gamma = g^2 m/(\pi v_F)$ is the Landau damping factor. We approximate the pairing vertex on the Fermi surface so that it depends only on frequency and the explicit position of Fermi surface. The pairing equation then takes the form,

$$\Phi(\omega_n, \theta_k) = T\sum_{\omega_m}\int \frac{pdpd\theta_p}{(2\pi)^2}\frac{\Phi(\omega_m, \theta_p)}{\xi_p^2 + \tilde{\Sigma}^2(\omega_m) + \Phi^2(\omega_m, \theta_m)}\chi(\theta_p - \theta_k, \omega_m - \omega_n) \tag{2.2}$$

Here $\chi(\theta_p - \theta_k, \omega_m - \omega_n)$ is obtained by substituting $\boldsymbol{q} = 2k_F \sin(\frac{\theta_p - \theta_k}{2})$ into Eq.(2.23). To further simplify this equation, we write $\Phi(\omega_n, \theta_k) = \Phi(\omega_n)\cos(n\theta_n)$ and $n = 0, 1, 2, ...$ represents different pairing symmetry channel. If we consider spin singlet pairing, then even-frequency pairing has to be accompanied by s-wave, d-wave etc. pairing symmetry ($n = 0, 2, ...$), while for odd frequency pairing the symmetry is p-wave, f-wave and so on($n = 1, 3, ...$).

Next we show that as long as the Eliashberg treatment works well, the equation for the pairing vertex are the same for different pairing symmetry. To see this, we integrate out the momentum in Eq.(2.2) and introduce $\theta = (\theta_p - \theta_k)/2$, the resulting equation is

$$\Phi(\omega_n)\cos(n\theta_k) = \pi T\sum_{\omega_m}\int\frac{d\theta}{\pi}\frac{\Phi(\omega_m)\cos(2n\theta + n\theta_k)}{\sqrt{\tilde{\Sigma}^2(\omega_m) + \Phi^2(\omega_m)\cos^2(2n\theta + n\theta_k)}}\frac{\lambda_E}{4\sin^2\theta + \lambda_E\frac{|\omega_m - \omega_n|/E_F}{2\sin\theta}} \tag{2.3}$$

where $\lambda_E = g^2/(4\pi E_F)$. Note that this dimensionless parameter λ_E is actually the

same as the Eliashberg small parameter g^2/E_F. We work with the assumption that Eliashberg approximation is valid, and hence we must have $\lambda_E \ll 1$. The smallness of λ_E ensures for the integral of θ in Eq.(2.3) that only small θ contributions are significant. Therefore, it is logical to take $\theta \to 0$ and approximate $\cos(2n\theta + n\theta_k)$ by $\cos(n\theta_k)$ and $\sin\theta$ by θ. Then after the integration of θ and identifying $\Phi\cos(n\theta_k)$ as new Φ one immediately get

$$\Phi(\omega_n) = \pi T \sum_{\omega_m} \frac{\Phi(\omega_m)}{\sqrt{\tilde{\Sigma}^2(\omega_m) + \Phi^2(\omega_m)}} \frac{\bar{g}^{1/3}}{|\omega_n - \omega_m|^{1/3}} \tag{2.4}$$

where $\bar{g} \sim \lambda_E^2 E_F$. Apparently this procedure is immune to the explicit pairing symmetry characterized by n. The only difference is that, for $n \neq 0$ the equation is actually a localized one and the pairing vertex represents its value at some particular position, e.g. θ_k. This is compatible with the patch theory of hot Fermi surface in which different patches of the Fermi surface are decoupled and fermions from different patches don't talk to each other due to the fact that collective bosons are slow compared to fermions[45]. Although we focus on spin-singlet pairing, it's also easy to see for spin-triplet pairing the pairing equation remains the same.

For the case of spin-spin interaction, the argument is completely parallel and we again have exactly the same equation for both even- and odd-frequency pairing. But there are two aspects where the current situation is different from the previous charge-charge interaction: i) the prefactors in the equations of pairing vertex $\Phi(\omega_n)$ are different for singlet and triplet pairing and ii) there is an additional factor of '3' in the equation for self energy $\Sigma(\omega_n)$. In Fig.2.1(a) we show a diagrammatic representation of the linearized pairing equation. The interaction term comes with a spin configuration $\boldsymbol{\sigma}_{\alpha\gamma} \cdot \boldsymbol{\sigma}_{\beta\lambda} = 2\delta_{\alpha\lambda}\delta_{\beta\gamma} - \delta_{\alpha\gamma}\delta_{\beta\lambda}$. When acting this on singlet pairing(the vertex comes with $i\sigma^y$) we have $i\sigma^y_{\alpha\beta}\boldsymbol{\sigma}_{\alpha\gamma} \cdot \boldsymbol{\sigma}_{\beta\lambda} = -3i\sigma^y_{\gamma\lambda}$. While acting on triplet pairing (the vertex comes with σ^x) we have $\sigma^x_{\alpha\beta}\boldsymbol{\sigma}_{\alpha\gamma} \cdot \boldsymbol{\sigma}_{\beta\lambda} = \sigma^x_{\gamma\lambda}$. Then we have '$-3$' and '$+1$' in the singlet and triplet pairing equations respectively. This additional minus sign in singlet pairing vertex means that the isotropic s-wave channel in this case is not prohibited, since the interaction in this channel changes sign and becomes repulsive. As for the self energy illustrated in Fig.2.1(b), it is clear that after the spin summation over the internal spin index, we end up with $\sum_\beta \boldsymbol{\sigma}_{\alpha\beta} \cdot \boldsymbol{\sigma}_{\beta\alpha} = (\boldsymbol{\sigma}^2)_{\alpha\alpha} = 3$, i.e. there is a factor of 3 in

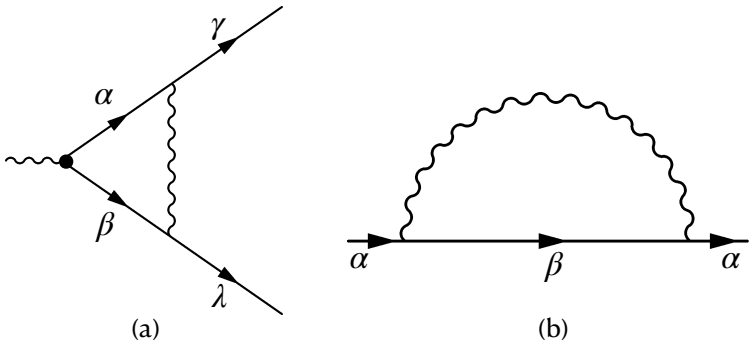

Figure 2.1: Pairing vertex (a) and self energy (b) with spin-spin interaction. $\alpha, \beta, \gamma, \lambda$ are spin indices. The black dot is the spin components of the pairing vertex, which is $i\sigma^y$ for singlet pairing and σ^x for triplet pairing.

the equation for $\Sigma(\omega_n)$. As a comparison, for charge-charge interaction what we have instead is $\delta_{\alpha\beta}\delta_{\beta\alpha} = 1$.

2.1.2 Pairing at a 2D anti-ferromagnetic QCP

In the case when the pairing interaction is mediated by an anti-ferromagnetic order parameter fluctuations, the effective interaction is peaked at some finite momentum $\boldsymbol{Q}$. We consider for simplicity a commensurate case when $\boldsymbol{Q} = (\pi, \pi)$. A typical example which falls into this case is the spin-fermion model which we already discussed in Sec.1.2.2. Here we will see the reason why this model leads to d-wave superconductivity. According to (1.25), the form of interaction is (we use χ instead of V and take $\xi \to \infty$)

$$\chi_{sf}(q) = \frac{g^2}{(\boldsymbol{q} - \boldsymbol{Q})^2 + \Gamma_{sf}|\Omega_m|} \tag{2.5}$$

Consider a generic Fermi surface shown in Figure2.2(a). There are 8 hot spots on the Fermi surface which can be pair-connected by momentum $\boldsymbol{Q}$ either directly or through Umklapp. Since the effective interaction is peaked at $\boldsymbol{Q}$, we can effectively neglect fermions located away from these hot spots. If we take a particular hot spot $\boldsymbol{k}_{h.s.}$, the

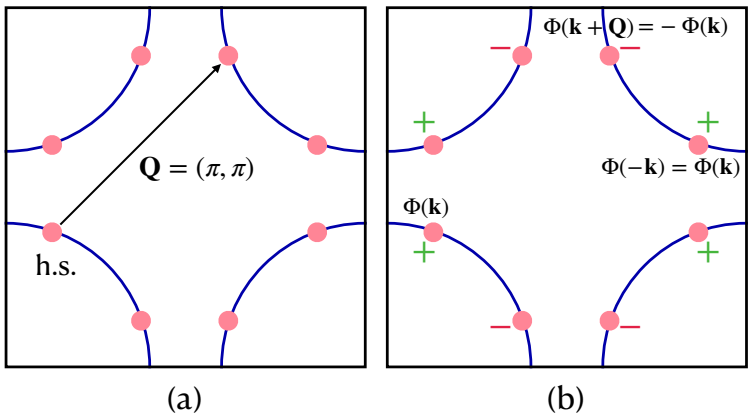

Figure 2.2: (a) Fermi Surface of hot spot model. When the interaction is peaked at $\boldsymbol{Q} = (\pi, \pi)$, there are 8 hot spots on the Fermi surface which can be pair-connected by momentum $\boldsymbol{Q}$ either directly or via Umklapp. (b) For spin-singlet even-frequency paring, we must have $\Phi(\omega_m, -\boldsymbol{k}) = \Phi(\omega_m, \boldsymbol{k})$, thus the pairing symmetry is most likely d-wave.

singlet pairing equation takes similar form to Eq.(2.2) and can be written as,

$$\Phi(\omega_n, \boldsymbol{k}_{h.s.}) = -3T \sum_{\omega_m} \int \frac{d^2\boldsymbol{p}}{(2\pi)^2} \frac{\Phi(\omega_m, \boldsymbol{p})}{\xi_p^2 + \tilde{\Sigma}^2(\omega_m) + \Phi^2(\omega_m, \boldsymbol{p})} \chi_{sf}(\boldsymbol{k} - \boldsymbol{p}, \omega_n - \omega_m) \quad (2.6)$$

Here the factor '-3' is obtained the same way shown in the previous subsection, which is a result of singlet pairing due to spin-spin interaction. This additional minus sign indicates that a s-wave pairing is impossible because $\Phi(\omega_m, \boldsymbol{p})$ has to change sign at some point on Fermi surface in order to have a solution to this equation. Thus we demand $\Phi(\omega_m, \boldsymbol{k}_{h.s.} + \boldsymbol{Q}) = -\Phi(\omega_m, \boldsymbol{k}_{h.s.})$.

For the symmetry related point $\Phi(\omega_m, -\boldsymbol{k}_{h.s.})$, it has to preserves sign because what we are looking for is spin singlet pairing.Therefore we must have $\Phi(\omega_m, -\boldsymbol{k}_{h.s.}) = \Phi(\omega_m, \boldsymbol{k}_{h.s.})$. This combining with the fact that if the hot spots are close to $(0, \pi)$ and symmetry related regions, the gap is unlikely to changes sign, leads to a $d_{x^2-y^2}$ symmetry of the gap. We show this configuration in Figure2.2(b).

After figuring out the pairing symmetry, one can integrate out the momentum in Eq.(2.6). Explicitly, we approximate $\Phi(\omega_m, \boldsymbol{p})$ in the integrand by $-\Phi(\omega_m, \boldsymbol{k}_{h.s.})$ and restrict the integration within a small vicinity around $\boldsymbol{p} = \boldsymbol{k}_{h.s.} + \boldsymbol{Q}$. Then we can

decouple the momentum integration along the directions perpendicular and tangential to the Fermi surface, by virtue of the assumption that bosons are slow mode. After the integration, we end up with the same equation for both even- and odd-frequency pairing,

$$\Phi(\omega_n) = \pi T \sum_{\omega_m} \frac{\Phi(\omega_m)}{\sqrt{\tilde{\Sigma}^2(\omega_m) + \Phi^2(\omega_m)}} \frac{\bar{g}^{1/2}}{|\omega_n - \omega_m|^{1/2}} \tag{2.7}$$

where $\bar{g} \sim g^4/(\Gamma_{sf} v_F^2)$. This equation is almost the same as (2.4), except for a different scaling behavior in the effective interaction term and a different effective coupling constant $\bar{g}$.

2.2 γ model

The fact that both (2.4) and (2.7) share striking similarity is a good indication that there should be a general model behind such that different pairing models can be mapped into this general model. To this end, we consider an itinerant fermion system which is close to a quantum critical point (QCP). The jargon itinerant system is nothing but a Fermi liquid. Close to such a QCP, the effective fermion interaction is mediated by a collective mode fluctuations. We already see this in Sec.1.2.2, where a starting Hubbard model develops into a spin fermion model when the system is close to its magnetic instability, or in our current language, a QCP. This boson-mediated fermion interaction can lead to two fates for fermions. On one hand, it gives rise to superconductivity once there is a pairing instability in at least one pairing channel. On the other hand, it kills the fermion coherence system will eventually become a non Fermi liquid if nothing sets in. These two tendencies actually compete with each other, in a sense that superconductivity is all about physics on Fermi surface so it needs fermion coherence to form a Fermi surface, while non Fermi liquid tendency is weakened if superconductivity gaps our low energy excitations and restores the original fermion self energy. In this section we introduce γ model which contains the interplay between these two fate of fermions. In the γ model we approximate both the fermion self energy $\Sigma(k)$ and pairing vertex $\Phi(k)$ by their vales on Fermi surface, and model the pairing interaction by $V(\Omega_n) \sim 1/|\Omega_n|^\gamma$ with $\gamma > 0$. Different pairing models can be mapped in this γ model with a certain value of γ. Below we will first derive two Eliashberg type equations from a mean field analysis.

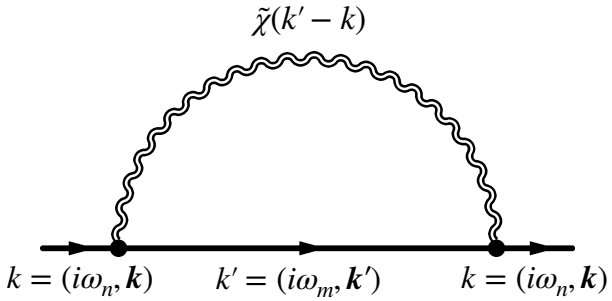

Figure 2.3: Self energy $\Sigma(k)$ in Eliashberg approximation. The wavy line represents effective fermion-fermion interaction. This is a self consistent equation for $\Sigma(k)$ since the fermion Green's function depends on $\Sigma(k)$.

After that, we will discuss possible extensions.

2.2.1 Derivation of mean field equations

A full description of itinerant fermions near a QCP involves an action which contains fermion sector, boson sector and the coupling between them. Therefore, our departing point is to write an action that contains all the ingredients needed. First of all, the simplest piece is the free fermion action,

$$S_0 = \sum_{k,\sigma} \bar{\psi}_\sigma(k)(-i\omega_n + \xi_{\boldsymbol{k}} - \Sigma(k))\psi_\sigma(k) \tag{2.8}$$

Here $(\bar{\psi}, \psi)$ are Grassmannian variables denoting the fermion field. σ is the spin index. And as usual $k = (\boldsymbol{k}, i\omega_n)$ contains both momentum and frequency. Next we consider the corrections to fermion self energy, due to the presence of the pairing interaction. As we mentioned in the very beginning, a full evaluation of fermion self energy is impossible. Therefore, we here adopt the Eliashberg approximation, in which the vertex corrections are neglected. Diagrammatically it is shown in Figure.2.3. According to this approximation, the self energy can only be obtained in a self consistent way, because the evaluation requires input of the Green's function, which in turn also depend on the self energy. This self consistent equation is $\Sigma(k) = \sum_{k'} \chi(k'-k)\mathcal{G}(k')$. In order to obtain

the correct equation, the self energy part action is

$$S_\Sigma = \sum_{k,k'} \bar{\Sigma}(k)\chi^{-1}(k-k')\Sigma(k) \tag{2.9}$$

Here χ^{-1} is the inverse of χ in an operator sense, i.e. $\sum_{k''} \chi^{-1}(k-k'')\chi(k''-k') = \delta_{k,k'}$

The pairing vertex part S_Ξ can be obtained via Hubbard-Stratonovich (HS) transformation, starting from a four-fermion interaction term in Cooper channel,

$$S_I = -\sum_{k,k',q} \bar{\psi}_\uparrow(k+\frac{q}{2})\bar{\psi}_\downarrow(-k+\frac{q}{2})\chi(k-k')\psi_\downarrow(-k'+\frac{q}{2})\bar{\psi}_\uparrow(k'+\frac{q}{2}) \tag{2.10}$$

The HS transformation introduces $\Xi(\bar{\Xi})$ as auxiliary fields to cancel out the four fermion term, leaving the partition function multiplied by a constant and hence unchanged. Explicitly we have

$$\begin{aligned} S_I \to S_\Xi = S_I + \sum_{k,k',k''} &\Big(\bar{\Xi}(q,k)\chi^{-\frac{1}{2}}(k-k'') + \bar{\psi}_\uparrow(k+\frac{q}{2})\bar{\psi}_\downarrow(-k+\frac{q}{2})\chi^{\frac{1}{2}}(k-k'')\Big) \\ &\Big(\chi^{-\frac{1}{2}}(k''-k')\Xi(q,k') + \chi^{\frac{1}{2}}(k''-k')\psi_\downarrow(-k'+\frac{q}{2})\psi_\uparrow(k'+\frac{q}{2})\Big) \end{aligned} \tag{2.11}$$

Next we make use of $\sum_{k''} \chi^{-\frac{1}{2}}(k-k'')\chi^{-\frac{1}{2}}(k''-k') = \chi^{-1}(k-k')$,$\sum_{k''} \chi^{\frac{1}{2}}(k-k'')\chi^{\frac{1}{2}}(k''-k') = \chi(k-k')$ and $\sum_{k''} \chi^{-\frac{1}{2}}(k-k'')\chi^{\frac{1}{2}}(k''-k') = \delta_{k,k'}$, it is then straightforward to obtain

$$\begin{aligned} S_\Xi = &\sum_{k,k',q} \bar{\Xi}(q,k)\chi^{-1}(k-k')\Xi(q,k') \\ &+ \sum_{k,q} \Big(\Xi(q,k)\bar{\psi}_\uparrow(k+\frac{q}{2})\bar{\psi}_\downarrow(-k+\frac{q}{2}) + \bar{\Xi}(q,k)\psi_\downarrow(-k+\frac{q}{2})\psi_\uparrow(k+\frac{q}{2})\Big) \end{aligned} \tag{2.12}$$

Writing this action combined with S_Σ and S_0 in Nambu space we arrive at the following effective total action:

$$\begin{aligned} S = S_0 + S_\Sigma + S_\Xi = &\sum_{k,k'} \bar{\Sigma}(k)\chi^{-1}(k-k')\Sigma(k) \\ &+ \sum_{k,k',q} \bar{\Xi}(q,k)\chi^{-1}(k-k')\Xi(q,k') + \sum_{k,k'} \bar{\Psi}(k)G^{-1}_{k,k'}\Psi(k'). \end{aligned} \tag{2.13}$$

In the last term the matrix $G^{-1}_{k,k'}$ is defined as,

$$G^{-1}_{k,k'} = \begin{pmatrix} (-i\omega_n + \xi_{\boldsymbol{k}} - \Sigma(k))\,\delta_{k,k'} & \Xi(k-k', \frac{k+k'}{2}) \\ \bar{\Xi}(k'-k, \frac{k+k'}{2}) & \left(-i\omega_n - \xi_{\boldsymbol{k}} - \bar{\Sigma}(-k)\right)\delta_{k,k'} \end{pmatrix}. \tag{2.14}$$

The auxiliary field $\Xi(q,k)$ is actually a generalized version of pairing vertex $\Phi(k)$. To see that, we need to understand the roles of the two arguments in Ξ. When comparing this to a classical two-body problem, one immediately realizes that its first argument is the center of mass momentum, which contains bosonic Matsubara frequencies $i\Omega_n$ while the second one is relative momentum which describes the pairing symmetry and dynamical effects due to dynamical interaction. In contrast, in the conventional BCS model where the interaction is constant near Fermi surface, we have $\Xi(q,k) = \Xi(q, k = \boldsymbol{k})$. If the pairing vertex is enhanced at some finite $\boldsymbol{q} \neq 0$, this state is called a pair density wave(PDW). We will not consider this special case here, and will mainly focus on the usual case when $\boldsymbol{q} = 0$, and this fact allows for a definition of $\Phi(k) = \Xi(q = 0, k)$, where $\Phi(k)$ is the usual pairing vertex that we have already introduced in Sec. In the action, a Nambu basis $\Psi(k) = (\psi_\uparrow(k), \bar{\psi}_\downarrow(-k))^T$ is used for compactness. $\bar{\Sigma}$ and $\bar{\Xi}$ are the complex conjugation of their counterparts and both $\Sigma(\bar{\Sigma})$ and $\Xi(\Xi)$ are treated as independent bosonic fields such that the partition function is given by a functional integral over all fields $Z = \int \mathcal{D}[\bar{\Psi}, \Psi]\mathcal{D}[\bar{\Sigma}, \Sigma]\mathcal{D}[\bar{\Xi}, \Xi]e^{-S}$.

In order to see the competition of non-Fermi liquid and superconductivity described by this action, the fermionic degrees of freedom can be integrated out, resulting an action which contains only the two auxiliary fields $\Sigma(\bar{\Sigma})$ and $\Xi(\bar{\Xi})$,

$$\begin{aligned} S_{\Sigma,\Xi} = &\sum_{k,k'} \bar{\Sigma}(k)\chi^{-1}(k-k')\Sigma(k) \\ &+ \sum_{k,k',q} \bar{\Xi}(q,k)\chi^{-1}(k-k')\Xi(q,k') - \mathrm{Tr}\ln G^{-1}_{k,k'}. \end{aligned} \tag{2.15}$$

The interplay between the tendency towards NFL and the tendency towards SC is embedded in the matrix $G^{-1}_{k,k'}$, and will become clear through saddle point equations. Right at the saddle point we notice that the order parameter peaks at $q = 0$, and we

therefore use $\Phi(k)$ in these equations instead of $\Xi(q,k)$. Now applying $\frac{\delta S_{\Sigma,\Phi}}{\delta\bar{\Sigma}(k)} = \frac{\delta S_{\Sigma,\Phi}}{\delta\bar{\Phi}(k)} = 0$ in addition with some further simplifications one obtains a set of two Eliashberg equations. To derive them, we note that right at saddle point the matrix $G^{-1}_{k,k'}$ is diagonal in k space as long as $q = 0$, and the inverse of it can be obtained by just inversing the 2-by-2 matrix in Nambu space. The action near saddle point is then given by

$$S_{\Sigma,\Phi} = \sum_{k,k'} \bar{\Sigma}(k)\chi^{-1}(k-k')\Sigma(k) + \sum_{k,k'} \bar{\Phi}(k)\chi^{-1}(k-k')\Phi(k') - \mathrm{Tr}\ln G^{-1}_k \tag{2.16}$$

where

$$G^{-1}_k = \begin{pmatrix} -i\omega_n + \xi_{\boldsymbol{k}} - \Sigma(k) & \Phi(k) \\ \bar{\Phi}(k) & -i\omega_n - \xi_{\boldsymbol{k}} - \bar{\Sigma}(-k) \end{pmatrix} \tag{2.17}$$

The equation for $\Sigma(k)$ is given by

$$\frac{\delta S_{\Sigma,\Phi}}{\delta\bar{\Sigma}(k)} = 0 \to \sum_{k'} \chi^{-1}(k-k')\Sigma(k') = \mathrm{Tr}\left(G\frac{\delta}{\delta\bar{\Sigma}(k)}G^{-1}\right) \tag{2.18}$$

where G is the inverse of G^{-1} in (2.17). Noting that

$$\frac{\delta G^{-1}(k')}{\delta\bar{\Sigma}(k)} = \begin{pmatrix} 0 & 0 \\ 0 & -1 \end{pmatrix} \delta_{-k',k} \tag{2.19}$$

it is then straight forward to obtain from (2.18)

$$\sum_{k'} \chi^{-1}(k-k')\Sigma(k') = \frac{-i\omega_n + \xi_{\boldsymbol{k}} + \Sigma(-k)}{(i\omega_n + \xi_{\boldsymbol{k}} - \Sigma(-k))(i\omega_n - \xi_{\boldsymbol{k}} - \bar{\Sigma}(k)) - \Phi(k)\bar{\Phi}(k)} \tag{2.20}$$

The inverse interaction function χ^{-1} in the left hand side of the above equation can be eliminated by multiplying χ on both sides, and the resulting equation for $\Sigma(k)$ is

$$\Sigma(k) = \sum_{k'} \chi(k-k')\frac{-i\omega_m + \xi_{\boldsymbol{k'}} + \Sigma(-k')}{(i\omega_m + \xi_{\boldsymbol{k'}} - \Sigma(-k'))(i\omega_m - \xi_{\boldsymbol{k'}} - \bar{\Sigma}(k')) - \Phi(k')\bar{\Phi}(k')} \tag{2.21}$$

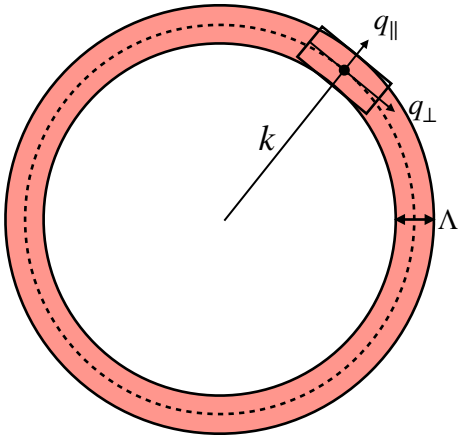

Figure 2.4: Hot Fermi surface (before superconductivity) with fermions coupled to a $\boldsymbol{Q} = 0$ order parameter fluctuation mode. The fermion momentum cutoff Λ is much smaller than k_F. The assumption that bosons are slow mode compared to fermions allows for fermion scattering near FS with relatively larger momentum exchange. For a fermion with momentum $\boldsymbol{k}$, the momentum integration range along $q_\perp$ is much larger than that along $q_\parallel$. As a result, the integration in (2.21) and (2.22) can be decoupled between this two direction.

Derivation of the equation for Φ is completely parallel, for which we have

$$\Phi(k) = \sum_{k'} \chi(k-k') \frac{-\Phi(-k')}{(i\omega_m + \xi_{\boldsymbol{k'}} - \Sigma(-k'))(i\omega_m - \xi_{\boldsymbol{k'}} - \bar{\Sigma}(k')) - \Phi(k')\bar{\Phi}(k')} \tag{2.22}$$

Eq. (2.21) and Eq. (2.22) are the so called Eliashberg equations. Further simplification is allowed if we assume first that bosons are slow compared to fermions, which is true for over damped bosons. This enables us to separate the momentum integration for $\chi(k-k')$ and other fermionic quantities. In fact we have already use this approximation in deriving (2.4) and (2.7) previously. As an example we show this scheme in Figure 2.4 for the case when the whole Fermi surface is hot due to the coupling to a $\boldsymbol{Q} = 0$ fluctuation mode. Generalization the case when the fluctuation mode carries finite momentum ($\boldsymbol{Q} \neq 0$) is straightforward. If bosons are slow compared to fermions, a fermion can be scattered by a boson with relatively large momentum transfer without changing much energy. This means, if we take a fermion with momentum $\boldsymbol{k}$ as is shown in the figure,

the allowed boson momentum range along the tangential direction ($\hat{q}_\perp$) is much larger than that along the radial direction ($\hat{q}_\parallel$). On the other hand, we can approximately take the self energy $\Sigma(k)$ and pairing vertex $\Phi(k)$ as constant within the hot Fermi surface region. By noticing that $\xi_{\boldsymbol{k}}$ changes drastically along $\hat{q}_\parallel$ but remains constant along $\hat{q}_\perp$ while $\chi(i\Omega_m, \boldsymbol{q})$ changes drastically along $\hat{q}_\perp$, one can effectively decouple the momentum integration in (2.21) and (2.22) between these two directions. The one dimensional integration for $\chi(i\Omega_m, \boldsymbol{q})$ often results in the following function form

$$\int dq_\perp \chi(i\Omega_m, \boldsymbol{q}) \propto V(\Omega_m) = \frac{\bar{g}^\gamma}{|\Omega_m|^\gamma} \tag{2.23}$$

Here we introduce an effective coupling constant $\bar{g}$ to make $\chi(\Omega_m)$ dimensionless, and the exponent γ changes for different pairing system, as is mentioned in the main text. Examples of this type include but not limited to: color superconductivity in 3D($\gamma = 0^+$, $V(\Omega_m) \propto \log|\Omega_m|$)[46], pairing at a 2D Ising nematic or ferromagnetic QCP($\gamma = 1/3$)[47, 39, 48, 49, 50], pairing at a 2D spin[16, 17, 51, 36] and charge density wave QCP[52, 53, 54, 55, 56, 57]($\gamma = 1/2$), pairing due to mediation of undamped boson ($\gamma = 1$), pairing in some Fe-based materials($\gamma = 1.2$) and even strong coupling limit of phonon mediated pairing[58, 59, 60, 61, 62, 63, 64, 65] ($\gamma = 2$).

The term with zero frequency transfer $V(0)$ is formally divergent at a QCP but can be eliminated from the equation as we do below. The remaining integral along radial direction $\int dq_\parallel$ is nothing but integral over $\xi_{\boldsymbol{k}}$ and is elementary. The last step to get (2.25) is using the fact that for 2D system where the density of states near Fermi surface can be treated as a constant(which we consider here in the paper for simplicity), the self energy and pairing vertex have the following properties[64],

$$\begin{aligned} &\Sigma(i\omega_n) = i\Sigma(\omega_n), \quad \Sigma(-i\omega_n) = -\Sigma(i\omega_n) \\ &\Phi(i\omega_n) = \Phi(\omega_n), \quad \Phi(-i\omega_n) = \Phi(i\omega_n) \end{aligned} \tag{2.24}$$

with $\Sigma(\omega_n)$ and $\Phi(\omega_n)$ both being real. With all these one can carry out the momentum integration $\int dq_\parallel ... \sim \int d\xi_{\boldsymbol{k}} ...$ in Eq.(2.21) and Eq.(2.22), and the two Eliashberg equations reduced to (2.25).

$$\tilde{\Sigma}(\omega_n) = \omega_n + \pi T \sum_{m\neq n} \frac{\tilde{\Sigma}(\omega_m)}{\sqrt{\tilde{\Sigma}(\omega_m)^2 + \Phi(\omega_m)^2}} \frac{\bar{g}^\gamma}{|\omega_n - \omega_m|^\gamma},$$
$$\Phi(\omega_n) = \pi T \sum_{m\neq n} \frac{\Phi(\omega_m)}{\sqrt{\tilde{\Sigma}(\omega_m)^2 + \Phi(\omega_m)^2}} \frac{\bar{g}^\gamma}{|\omega_n - \omega_m|^\gamma}, \tag{2.25}$$

where we remind that $\tilde{\Sigma}(\omega_n) = \omega_n + \Sigma(\omega_n)$.

In the above equations, the term with $m = n$ in the summation has been excluded, as it contains a divergent term. This divergence is unique which occurs when the system is right at a QCP. Away from a QCP the boson propagator acquires a finite mass, rendering everything regular. We exclude the divergent piece because it does not affect the superconducting properties at all, at least in case when the prefactors in both equations are the same. For clarity, consider combining the two equations into a single one equation for the gap function $\Delta(\omega_n) = \omega_n \Phi(\omega_n)/\tilde{\Sigma}(\omega_n)$,

$$\Delta(\omega_n) = \pi T \sum_{\omega_m} \frac{\Delta(\omega_m) - \Delta(\omega_n)\frac{\omega_m}{\omega_n}}{\sqrt{\omega_m^2 + \Delta^2(\omega_m)}} \frac{\bar{g}^\gamma}{|\omega_m - \omega_n|^\gamma} \tag{2.26}$$

It is then clear that the $m = n$ divergence is indeed eliminated by the vanishing on the numerator. This property is also called Anderson theorem[**?**], who studied the effect from nonmagnetic impurity on s-wave superconductivity. In our case, the divergent piece with zero frequency transfer resembles the role of non magnetic impurities. (2.25) are the basic equations for all our analysis below. And we remind these equations are written on Matsubara axis. In order to obtain the corresponding equations on real frequency axis, one needs to apply spectral decomposition method, as we will discuss in Sec.

2.2.2 Extension to $N \neq 1$

As we mentioned in the beginning of this section, the interplay between superconductivity and non Fermi liquid behavior is embedded in the resulting Eliashberg-type equations, (2.25) or equivalently (2.26). These two fate of fermions are competitive with each other. In order to make a sense of how the relative strength of interaction in direct channel and Cooper channel affect the final fate for fermions, we then extend

the original equations by introducing a factor of $1/N$ in the equation for $\Phi(\omega_n)$. Put it another way, we artificially suppress the pairing interaction in Cooper channel by a factor of $1/N$, while keeping that in the direct channel intact.

This extension brings about at least three benefits. First of all, by tuning the value N, we are able to obtain the condition when superconductivity may occur. It is easy to imagine that, if N is very large such that the pairing interaction in Cooper channel is strongly suppressed, superconductivity will lose and the system behaves like a non Fermi liquid. Therefore, there should exist a critical value N_{cr} at $T = 0$, separating the superconducting state from a non Fermi liquid. We will confirm this and obtain the value of N_{cr} in Sec. Another convenience by this extension is that, we can solve the gap equation analytically in the limit of large N. In this limit, we clearly see simple physics plays an important role in determining the spectral properties of a superconducting state, and this has implication for the realistic system when $N = 1$ and T close to T_p. We will explain this in detail in Sec.3.1 and Sec.3.2.

With this extension, it is also convenient to see the very intriguing features of the gap equation equation (2.25): we find there exist a set of an infinite number of solutions, and each of them has its gap amplitude Δ_n and onset temperature for pairing $T_{p,n}$, where the index $n = 0, 1, 2, ...$ and both of the decays exponentially with increasing n. On Matsubara axis, the solution $\Delta_n(\omega_m)$ changes sign n times between $\omega_n = 0$ and ∞. In most cases except for a special one when $\gamma = 2$, the sign preserving solution with $n = 0$ has the largest condensation energy, which makes it the most energetic favorable pairing state when cooling down. We see below that these multiple solutions actually stems from the eigenvalue problem deduced from the linearized gap equation, with N playing the role of eigenvalue and different solutions playing the role of eigenfunctions.

The extension of (2.25) with the factor of N is,

$$\begin{aligned}
\tilde{\Sigma}(\omega_n) &= \omega_n + \pi T \sum_{m\neq n} \frac{\tilde{\Sigma}(\omega_m)}{\sqrt{\tilde{\Sigma}(\omega_m)^2 + \Phi(\omega_m)^2}} \frac{\bar{g}^\gamma}{|\omega_n - \omega_m|^\gamma}, \\
\Phi(\omega_n) &= \frac{\pi T}{N} \sum_{m\neq n} \frac{\Phi(\omega_m)}{\sqrt{\tilde{\Sigma}(\omega_m)^2 + \Phi(\omega_m)^2}} \frac{\bar{g}^\gamma}{|\omega_n - \omega_m|^\gamma},
\end{aligned} \tag{2.27}$$

We emphasis inclusion of N in these equations must be done only after we eliminate the

$m = n$ term in the summation. Otherwise, the the cancellation of the divergent piece can not be implemented because the numerator now is not vanishing, because of N. Alternatively we can combine the equations for $\Phi(\omega_m)$ and $\tilde{\Sigma}(\omega_m)$ to get an equation for the pairing gap, which is

$$\Delta(\omega_n) = \pi T \sum_{\omega_m} \frac{\frac{1}{N}\Delta(\omega_m) - \Delta(\omega_n)\frac{\omega_m}{\omega_n}}{\sqrt{\omega_m^2 + \Delta^2(\omega_m)}} \frac{\bar{g}^\gamma}{|\omega_m - \omega_n|^\gamma} \tag{2.28}$$

The case $N = 1$ corresponds to the original equation. The existence of multiple solutions becomes transparent in the linearized equations,

$$\begin{aligned} N\Phi(\omega_m) &= \pi T \sum_{n \neq m} \frac{\Phi(\omega_n)}{|\omega_n + \Sigma(\omega_n)|} \frac{\bar{g}^\gamma}{|\omega_n - \omega_m|^\gamma} \\ \Sigma(\omega_m) &= \pi T \sum_{n \neq m} \frac{\bar{g}^\gamma \mathrm{sign}(\omega_n)}{|\omega_n - \omega_m|^\gamma} \end{aligned} \tag{2.29}$$

which are valid when T is close to the pairing onset temperature $T_{p,n}$ and the pairing vertex is vanishingly small. This linearized equation is an eigenvalue problem with N now playing the role of eigenvalue and $\Phi(\omega_m)$ the eigenstate. For clarity of this, the above linearized equation can be transformed into

$$N\Phi(\omega_m) = \sum_n K_{mn}\Phi(\omega_n) \tag{2.30}$$

Where the kernel matrix K_{mn} is readily deduced from (2.29). Thus for a given T, there exists an infinite number of N which satisfies this linearized equation, as the number of discrete Matsubara frequency is formally infinite. In the following section we will see for the case $\gamma < 1$ when the system is right at a QCP and thus the boson propagator is massless, all the $T_{p,n}(N)$ terminates at $N_{cr} > 1$ in zero temperature limit. Then even in the original model where $N = 1$ an infinite number of onset temperature $T_{p,n}$ still exists. This is a unique feature that should be attributed to the specialty of pairing near a QCP. Indeed multiple solutions naturally arise in such an eigenvalue problem in which there is an infinite number of eigenvalues and eigenstates regardless of the form of pairing interaction, but there is no guarantee that all these eigenvalue N truncates at $N_{cr} > 1$ in zero temperature limit. It has been shown that as we move the system

away from a QCP gradually, multiple solutions at $N = 1$ disappear one by one and eventually there will be only one solution as is the BCS model if the bosons acquire a large enough mass. We will come to this topic in Chapter 4.

It is worth mentioning that we apply the extension to γ model only for the case when $\gamma < 1$. This is because, for $\gamma > 1$, the extension to $N \neq 1$ inevitably includes a divergent piece, since both the pairing vertex $\Phi(\omega_m)$ and self energy $\Sigma(\omega_m)$ diverges at $T = 0$ for $\gamma > 1$. This divergence can only be removed in the original case when $N = 1$. Therefore, we will not try to extend the model with a general N for $\gamma > 1$.

2.3 Onset temperature and gap function

In this section, we shown the solution of the linearized gap equation, which determine the onset temperature for pairing T_p. We will also investigate the gap amplitude Δ_0 from the nonlinear gap equation. As we mentioned above, there are multiple solutions to the gap equation. The solution we present here, is the one with the larges onset temperature, $T_p = T_{p,0}$, and the gap function $\Delta(\omega_n)$ is a sign preserving function at $\omega_m \in (0, \infty)$. We begin with the extended model with a general N, then we will focus on the original case when $N = 1$.

2.3.1 With a general N at $\gamma < 1$

We first solve the linearized equation (2.29) with a general N. Because the presence of N, the onset temperature T_p is typically a function of N. Because the role of N is to suppress the superconducting tendency, it is reasonable to expect the larger N, the smaller T_p. In other words, T_p is a decaying function of N. If N takes the largest value, T_p should vanish. Based on this consideration, we first of all study the linearized gap equation at $T = 0$, in order to find the largest possible value for N.

The linearized gap equation in terms on $\Delta(\omega_m)$ is

$$\Delta(x) = \frac{1}{2}\int_{-\infty}^{\infty} dx' \frac{\frac{1}{N}\Delta(x') - \frac{x'}{x}\Delta(x)}{|x'||x' - x|^{\gamma}} \tag{2.31}$$

Here $x = \omega_m/\bar{g}$. Introducing the function $D(\omega_m) = \Delta(\omega_m)/\omega_m$, it is then written as,

after some manipulation,

$$xD(x) = \frac{1}{2N}\int_0^x \frac{dt}{t^\gamma}\left[D(x+t)+D(x-t)-2ND(x)\right]+\frac{1}{2N}\int_x^\infty \frac{dt}{t^\gamma}\left[D(x+t)+D(t-x)\right] \tag{2.32}$$

This equation is exactly solved in Ref. with a rather involved projection method. Here we solve this equation by expanding the function $D(x)$ as

$$D(x) = x^\rho \sum_{n=0}^{\infty} a_n (x^\gamma)^n \tag{2.33}$$

Substitute this into the r.h.s of (2.32) and define $\tilde{\rho} = \rho + \gamma n$ we then have

$$\begin{aligned} xD(x) = \frac{1}{2N}\sum_{n=0}^{\infty} a_n x^{1+\tilde{\rho}-\gamma}\Bigg(&\int_0^1 dt \frac{[(1+t)^{\tilde{\rho}}+(1-t)^{\tilde{\rho}}-2N]}{t^\gamma} \\ &\int_0^\infty dt\frac{t^{\tilde{\rho}}}{(1+t)^\gamma}+\int_0^\infty dt\frac{(1+t)^{\tilde{\rho}}}{t^\gamma}-\int_0^1 dt\frac{(1+t)^{\tilde{\rho}}}{t^\gamma}\Bigg) \end{aligned} \tag{2.34}$$

Note the first and last integral are opposite so they cancel. In these integrals, all IR divergences caused by $\gamma > 1$ completely cancel out. The regular part of these integrals can be expressed via Beta function, defined as

$$B(p,q) = \int_0^1 t^{p-1}(1-t)^{q-1}dt,\ \mathrm{Re}p > 0,\ \mathrm{Re}q > 0 \tag{2.35}$$

or

$$B(p,q) = \int_0^\infty \frac{t^{p-1}}{(1+t)^{p+q}}dt,\ \mathrm{Re}p > 0,\ \mathrm{Re}q > 0 \tag{2.36}$$

Although these conditions may not be satisfied we still use this as an analytic continuation for those integrals. When we also expand the l.h.s of (2.34) we end up with the following

$$\sum_{n=0}^{\infty} a_n x^{\gamma n} = \sum_{n=0}^{\infty} a_n x^{\gamma n-\gamma} F_\gamma(n) \tag{2.37}$$

with $F_\gamma(n)$ given by

$$F_\gamma(n) = \frac{1}{2N}[B(1-\gamma,1+\rho+\gamma n)+B(1+\rho+\gamma n,\gamma-\rho-\gamma n-1)+B(1-\gamma,\gamma-\rho-\gamma n-1)]-\frac{1}{1-\gamma} \tag{2.38}$$

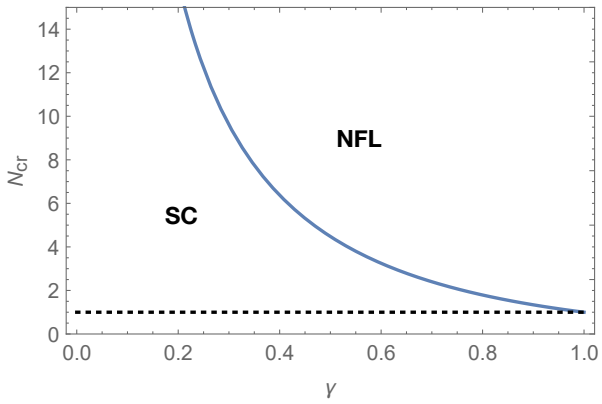

Figure 2.5: Critical values N_{cr} as a function of γ, obtained from (2.44).

In order for (2.38) to be true, we must have $F_\gamma(0) = 0$, and this is the index equation that determines the value of ρ for any given γ. Written explicitly we have

$$B(1-\gamma, 1+\rho) + B(1+\rho, \gamma-\rho-1) + B(1-\gamma, \gamma-\rho-1) = \frac{2N}{1-\gamma} \tag{2.39}$$

The solution is

$$\rho = -1 + \frac{\gamma}{2} \pm i\beta \tag{2.40}$$

At this time $F_\gamma(0) = 0$ is the equation solely for β,

$$B(1-\gamma, \frac{\gamma}{2}+i\beta) + B(\frac{\gamma}{2}+i\beta, \frac{\gamma}{2}-i\beta) + B(1-\gamma, \frac{\gamma}{2}-i\beta) = \frac{2N}{1-\gamma} \tag{2.41}$$

After getting this value of β from this equation, all the coefficients a_n can be obtained via their recursion relation that is

$$a_n = a_{n+1} F_\gamma(n+1) \tag{2.42}$$

If we take $a_0 = 1$, then it is easy to see for $n > 0$

$$a_n = \prod_{m=1}^{n} \frac{1}{F_\gamma(m)} \tag{2.43}$$

In order to have a solution to (5.5), there is a constraint for N. If $N > N_{cr}$, such a

solution does not exist. Therefore, the critical value N_{cr} is set by a vanishing β. Taking $\beta = 0$ in (5.5), one immediately gets

$$N_{cr} = \frac{1-\gamma}{2}\frac{\Gamma^2(\gamma/2)}{\Gamma(\gamma)}\left(\frac{1}{\cos(\pi\gamma/2)}+1\right) \tag{2.44}$$

where $\Gamma(x)$ is the standard Gamma function. We plot the function in Figure 5.2. It is a monotonically decaying function of γ, which diverges at $\gamma \to 0$ and terminate at unity at $\gamma = 1$. This curve separates the SC state and the non Fermi liquid normal state.

We next try to solve the nonlinear gap equation (2.26) with several different N. This will show how the existence of such a critical value N_{cr} affect the actual gap amplitude. The method we apply here and later on is numerical iteration. Since the equation we are about to solve is written on Matsubara axis, which is by definition discretized at any finite T and thus convenient for numerical evaluations. The solution $\Delta(\omega_m)$ is a function of Matsubara frequency. The gap amplitude we show is defined as $\Delta_0 = \Delta(\omega = 0)$, and we approximate it as $\Delta_0 \approx \Delta(\pi T)$. As long as T is small enough, such that πT is close to $\omega = 0$, this approximation is valid. In the limit $T \to 0$, because $\Delta(\omega_m)$ is an analytic function in the upper frequency half plane, it does not matter which direction we approach to ω, i.e. we can approach on real axis as well as on Matsubara frequency axis.

In Figure we show the $\Delta(\pi T)$ for several different N for a particular $\gamma = 0.9$. In this case, we can obtain $N_{cr} = 1.34$ from (2.44). From the figure, we clearly see $\Delta_0(T)$ becomes a non-monotonic function of T as long as $N > 1$. In the original physical case when $N = 1$, it remains a monotonically decaying function of T. We also see there is a clear distinction between $N < N_{cr}$ and $N > N_{cr}$. In the case $N < N_{cr}$, although $\Delta_0(T)$ shows a decreasing trend as T becomes lower and lower, it eventually saturates to some finite value. However for $N > N_{cr}$, $\Delta_0(T)$ tends to vanish in $T \to 0$ limit. Therefore, from this result, we see N_{cr} indeed separate the SC state and a non-Fermi liquid normal state at $T = 0$.

2.3.2 N=1

As was put above, the extension to $N \neq 1$ works well for $\gamma < 1$, but cannot overcome formal divergence for $\gamma > 1$ case. Here in this subsection, we focus back in the original

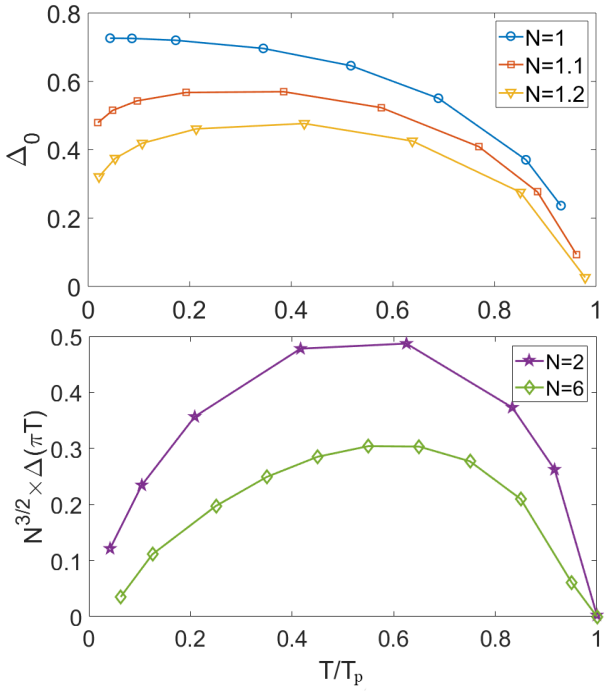

Figure 2.6: The gap amplitude $\Delta_0 = \Delta(\pi T)$ as a function of T for $N < N_{cr}$ (upper panel) and $N > N_{cr}$ (lower panel). This result is obtained for $\gamma = 0.9$, and correspondingly, $N_{cr} = 1.34$. For all $N > 1$, Δ_0 is a non-monotonic function of T. In the limit $T \to 0$, Δ_0 saturates to some nonzero constant for $N < N_{cr}$ but vanishes for $N > N_{cr}$.

model with $N = 1$. We try to understand how the pairing temperature T_p and the gap amplitude Δ_0 behaves for different γ. As there is no longer divergence, we can continue our analysis to all $\gamma > 0$. And like above, we only present results for the solution with largest T_p, and leave discussions about other solutions in Chapter 2.

In Figure 2.7 we plot the pairing temperature T_p, the gap amplitude Δ_0 in $T \to 0$ limit and their ratio $2\Delta_0/T_p$, as a function of γ. We see from the results the pairing temperature diverges as $\gamma \to 0$, and gradually saturates to a constant value $\bar{g}/(2\pi)$. We note that these form of T_p is different from (1.29), where T_p is bounded by the energy scale ω_D. Here we have $T_p \sim \bar{g}$ which is a typical feature when the system enters a quantum critical regime. The gap amplitude Δ_0 also diverges in the small γ limit. More strikingly, it diverges in the same way as T_p does, and as a result, their ratio, $2\Delta_0/T_p$ remains finite. This finite value $2\Delta_0/T_p = 3.53$ is actually the one obtained from a conventional BCS value. To see this, we find by examining the linearized gap equation that

$$T_p = Q_T(1.4458\gamma)^{-1/\gamma} \tag{2.45}$$

where $Q_T = 0.5018$ is a numerical factor. While solving the full nonlinear gap equation at $T \to$) approximately, we obtain

$$\Delta_0 = Q_\Delta(1.4458\gamma)^{-1/\gamma} \tag{2.46}$$

where $Q_\Delta = 0.885$ is another numerical factor. From these two analytical results, we clearly see both T_p and Δ_0 have the exactly same scaling behavior on γ. Taking their ratio gives

$$\left.\frac{2\Delta_0}{T_p}\right|_{\gamma\to 0} = \frac{2Q_T}{Q_\Delta} = 3.53 \tag{2.47}$$

fully consistent with BCS results. The reason behind is, in the limit $\gamma \to 0$, the pairing interaction very weakly depend on frequency, which is almost a constant, as the case in BCS model. Given this, it is no surprise these two results agree with each other. Numerically one has to be cautious because at small γ, the result sensitively depends on the number of Matsubara frequency points used. This is because $\Delta(\omega_m)$ decays slower and slower as $\gamma \to 0$. In practice we run numerical evaluations for different number of frequency points, and extrapolate to the infinite frequency points limit. In

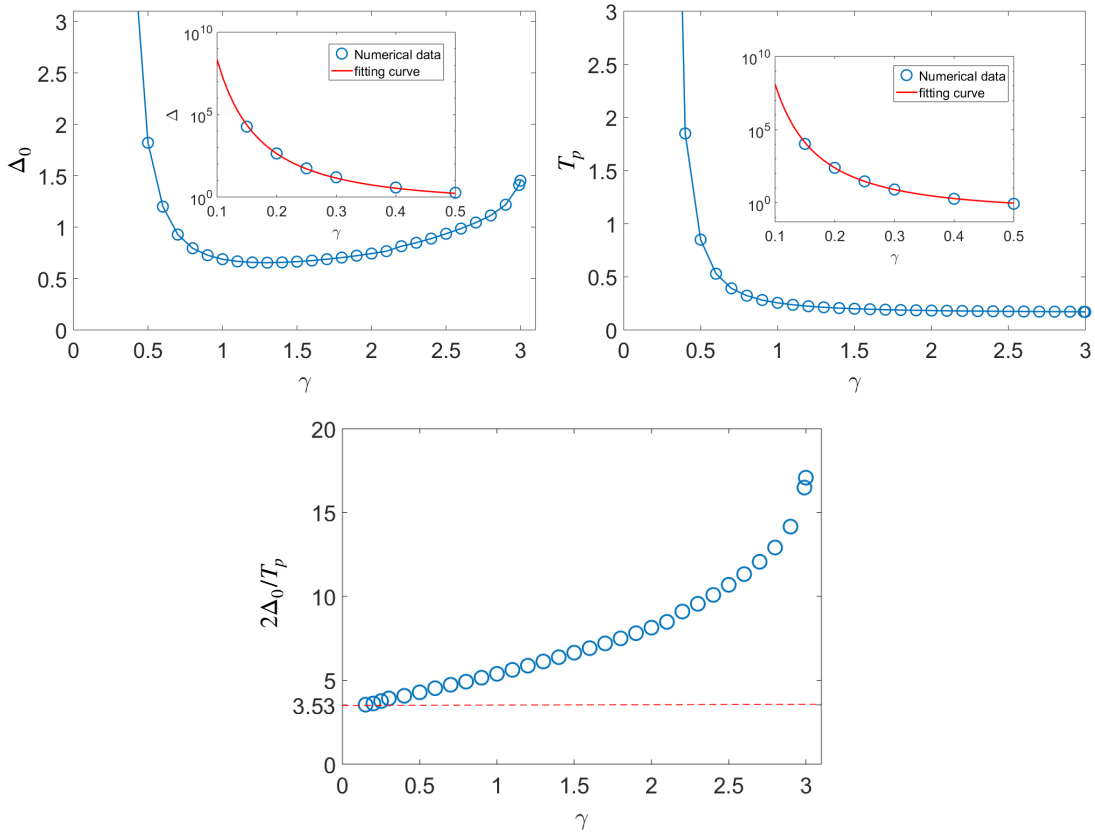

Figure 2.7: Pairing temperature T_p, gap amplitude Δ_0 and their ratio $2\Delta_0/T_p$, as a function of γ. Both T_p and Δ_0 are in units of $\bar{g}$. Both T_p and Δ_0 diverges at $\gamma \to 0$ in exactly the same way, as a result, their ratio remains a finite constant 3.53, which is the same as that obtained from a conventional BCS model. At $\gamma \leq 3$, T_p is finite, Δ_0 diverges as $[1/(3-\gamma)]^{1/3}$.

the inset of the top two plots in Figure 2.7, we compare numerical results with the two functions given in (2.45) and (2.46). Clearly these two ways are consistent.

For large γ, we find T_p always remains finite. Δ_0 however, develops another divergence at $\gamma = 3$. At $\gamma \leq 3$, we find

$$\Delta_0 = \left(\frac{\Gamma\left(\frac{\gamma}{2}\right) \Gamma\left(\frac{3-\gamma}{2}\right)}{\sqrt{\pi}} \right)^{1/\gamma} \tag{2.48}$$

For γ close to $\gamma = 3$, Δ_0 diverges as $[1/(3-\gamma)]^{1/3}$. Because of this divergence, our study on γ model will be mainly on $\gamma \in (0, 3)$.

The ratio $2\Delta_0/T_p$ in γ model is then a monotonic increasing function of γ, starting from the BCS value at $\gamma = 0$ and tends to diverge at $\gamma = 3$. The case $\gamma = 2$ corresponds to the electron-phonon coupling system, in the limit when Debye frequency ω_D is vanishingly small, while the product of ω_D with the e-ph coupling constant remains large. Previous studies using Eliashberg calculations on phonon-mediated s-wave superconductivity found $2\Delta_0/T_p \sim 8 - 13$[66, 67, 68, 69, 64]. Here in γ model we find $2\Delta_0/T_p = 8.3$ which is full consistent with previous results.

Chapter 3

The special role of the first Matsubara frequencies in superconducting gap equations

The superconducting gap equation in γ model and the largest, sign preserving solution have been shown in previous chapter. We also discussed in the extended model (2.27) for $0 < \gamma < 1$ the existence of a critical value N_{cr} separating the superconducting state from a non Fermi liquid normal state. This analysis is at $T = 0$, which means, in the extended model, the pairing temperature $T_p(N)$ as a function of N should terminate at $N = N_{cr}$. However we will see in this chapter that analysis at finite T opposes this conclusion. In Figure 3.1 we present $T_p(N)$ in the N-T plane, for a particular case $\gamma = 0.9$. The plot extends well beyond the corresponding critical value $N_{cr} = 1.34$ when $T \to 0$. The results are obtained by solving the linearized gap equation (2.29) at different temperatures. We clearly see $T_p(N)$ bypasses N_{cr} and tends to infinity in the limit $N \to \infty$. In fact, we will see below that $T_p(N) \propto 1/N^{1/\gamma}$ at large N. The curve $T_p(N)$

The very reason behind it is the special role of $\pm\pi T$ in the gap equations. In the large N limit, dominant contributions in the gap equation are from fermions at these two frequencies. Below we will first discuss what happens to the gap equation on these first Matsubara frequencies. After that, the implication on real frequency properties is

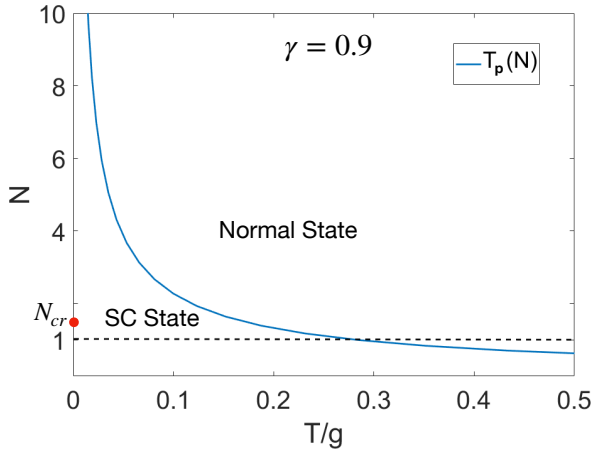

Figure 3.1: The onset temperature of superconductivity, $T_p(N)$, in the QC model, extended to $N > 1$. We set $\gamma = 0.9$.The line $T_p(N)$ by-passes N_{cr} (the red dot). At large N, $T_p(N) \propto 1/N^{1/\gamma}$.

shown, and based on this, we show our numerical results on the crossover of gap closing behavior to gap filling behavior on spectral properties.

3.1 Special role of $\omega_m = \pm\pi T$

The existence of N_{cr} at $T = 0$ would normally imply that this is the termination point of the line $T_p(N)$. However, the numerical solution of (2.29) yields qualitatively different result: T_p is non-zero at any N, and the line $T_p(N)$ by-passes N_{cr} and approaches zero only at $N \to \infty$ (see Fig.3.1). The reason for this behavior has been named in Ref. [70]: the power counting argument that $\Sigma(\omega_m) \propto \omega_m^{1-\gamma}$ does not work for the first two Matsubara frequencies $\omega_m = \pm\pi T$. For these frequencies, Eq. (2.29) yields $\Sigma(\pm\pi T) = 0$ because contributions from positive and negative $\omega_{m'}$ exactly cancel out. To see the consequence of $\Sigma(\pm\pi T) = 0$, consider the equation for $\Phi(\omega_m)$ in the limit $N \gg 1$ and set external $\omega_m = \pi T(2m + 1)$ to πT (i.e., set $m = 0$). For $m' = O(1)$, but $m' \neq -1$, the kernel matrix element $K_{0,m'}$ is independent of T and is of order $1/N$. However, for $m' = -1$ ($\omega_{m'} = -\pi T$), $K_{0,-1} = (1/N)(\bar{g}/(2\pi T))^{\gamma}$ becomes large at small enough T. A simple experimentation shows that[70] in this situation the gap equation

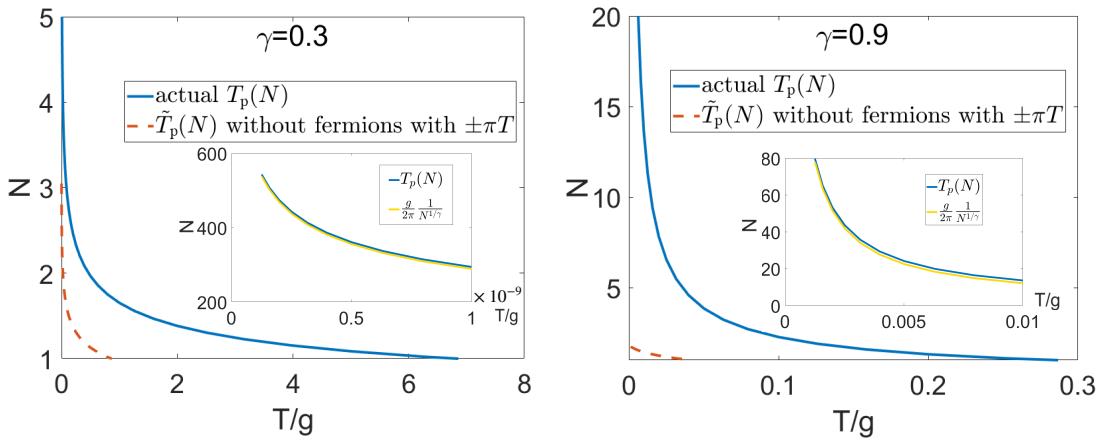

Figure 3.2: The pairing instability temperature $T_p(N)$, obtained by solving the linearized gap equation (2.29) as an eigenvalue/eigengunvction problem for $M = 4000$ Matsubara frequencies, with N playing the role of an eigenvalue. Upper and lower panels are for $\gamma = 0.3$ and $\gamma = 0.9$, respectively. At large N, $T_p(N) \approx (\bar{g}/2\pi)1/N^{1/\gamma}$. For comparison, we also show $\tilde{T}_p(N)$, which we obtained by solving the linearized gap equation without fermions with Matsubara frequencies $\pm\pi T$. The temperature $\tilde{T}_p(N)$ terminates at $T = 0$ at the critical $N = N_{cr}$.

reduces to

$$\Phi(\pi T) \approx \frac{1}{N}\left(\frac{\bar{g}}{2\pi T}\right)^{\gamma}\Phi(-\pi T)$$
$$\Phi(\omega_m) = \frac{1}{N}\left(\frac{\bar{g}}{2\pi T}\right)^{\gamma}\left(\frac{\Phi(\pi T)}{|\frac{1}{2}-\frac{\omega_{m'}}{2\pi T}|^{\gamma}} + \frac{\Phi(-\pi T)}{|\frac{1}{2}+\frac{\omega_{m'}}{2\pi T}|^{\gamma}}\right), \quad m \neq 0, -1 \tag{3.1}$$

We will be searching for even-frequency solutions of the gap equation: $\Phi(\omega_m) = \Phi(-\omega_m)$. Then the first equation in (3.1) sets

$$T_p = \frac{\bar{g}}{2\pi}\frac{1}{N^{1/\gamma}} \tag{3.2}$$

and the second shows that a non-zero $\Phi(\omega_m)$ is induced by $\Phi(\pm\pi T)$ and is suppressed by $N^{1/\gamma}$ for $T \to T_p$.

The functional form $T_p \propto 1/N^{1/\gamma}$ at large N has been verified numerically in Ref. [70] for a particular choice of $\gamma = 0.1$. In Fig.3.2 we show that the same behavior

holds for $\gamma = 0.3$ and 0.9. To see that this behavior is indeed due to the vanishing of $\Sigma(\pm\pi T)$, we exclude $\omega_m = \pi T$ from the set of Matsubara frequencies and then solve again the linearized gap equation. The result is shown in Fig.3.2. We clearly see that $\tilde{T}_p$, obtained this way, tends to zero above some critical value of N, which numerically is close to $N_{cr}(\gamma)$ in Eq. (2.44). This implies that, without the first two Matsubara frequencies, the system would display a conventional behavior, with $\tilde{T}_p(N)$ line terminating at $N = N_{cr}$. That the actual $T_p(N)$ by-passes N_{cr} and vanishes only at $N = \infty$ is then entirely due to the vanishing of the self-energy for fermions with $\omega_m = \pm\pi T$. To check that only fermions with $\omega_m \pm \pi T$ special, we computed $\tilde{T}_p$ by eliminating fermions with $\pm\pi T$ and obtained that $\tilde{T}_p(N)$ behaves similar to $\tilde{T}_p(N)$ and terminates at $N \approx N_{cr}$.

This result indicates that the system behavior may be qualitatively different at low $T < \tilde{T}_p(N)$, when all fermions contribute to the pairing, and at $\tilde{T}_p(N) < T < T_p$, when the pairing is induced by fermions with $\omega_m = \pm\pi T$. At $N > N_{cr}$, $\tilde{T}_p = 0$ and fermions with $\omega_m = \pm\pi T$ determine the system behavior for all $T < T_p$. At small γ, $N_{cr} \approx 4/\gamma \gg 1$, and the lines $T_p(N)$ and $\tilde{T}_p(N)$ remain close down to a very small $T \sim \bar{g}(\gamma)^{1/\gamma} \ll \bar{g}$. However, for $\gamma \leq 1$, the two lines are distinct already at $T \leq \bar{g}$. We emphasize that at these γ, the sizable range $\tilde{T}_p(N) < T < T_p(N)$ exists even for the physical case of $N = 1$. The system properties in in this T range should be, at least qualitatively, the same as that at large N.

The special role of $\pm\pi T$ can also be seen form the non-linear equation for the pairing vertex $\Phi(\omega_m)$ and the equation for the fermionic self-energy $\Sigma(\omega_m)$, which includes the feedback from the pairing. We see from above that at large N, the pairing temperature $T_p(N)$ is obtained by solving the linearized equation for $\Phi(\omega_m)$ for fermions with only two Matsubara frequencies $\omega_m = \pm\pi T$; the pairing vertex $\Phi(\omega_m)$ for other ω_m is then expressed via $\Phi(\pi T) = \Phi(-\pi T)$, see (3.1). We assume and then verify that this holds also for $T < T_p$, i.e., that the non-linear gap equation can be approximated by restricting to $\omega_n = \pm\pi T$ in the r.h.s. of Eq. (2.29). Re-labeling $\Phi(\pi T) = \Phi(-\pi T) = \Phi_0$,

$\tilde{\Sigma}(\pi T) = -\tilde{\Sigma}(-\pi T) = \Sigma_0$, then the original equations become

$$\begin{aligned} \Phi_0 &= \pi T \left(\frac{T_p}{T}\right)^\gamma \frac{\Phi_0}{\sqrt{(\Phi_0^*)^2 + (\tilde{\Sigma}_0)^2}} \\ \tilde{\Sigma}_0 &= \pi T \left[1 + N\left(\frac{T_p}{T}\right)^\gamma \left(1 - \frac{\tilde{\Sigma}_0}{\sqrt{(\Phi_0^*)^2 + (\tilde{\Sigma}_0^*)^2}}\right)\right] \end{aligned} \tag{3.3}$$

The solution of (3.3) to leading order in $1/N$ is

$$\begin{aligned} \Phi_0 &= \pi T \left(\frac{2}{N}\right)^{1/2} \left(\frac{T_p}{T}\right)^\gamma \left(1 - \left(\frac{T}{T_p}\right)^\gamma\right)^{1/2} \\ \tilde{\Sigma}_0 &= \pi T \left(\frac{T_p}{T}\right)^\gamma, \quad or\ \Sigma_0 = \pi T \left(\left(\frac{T_p}{T}\right)^\gamma - 1\right) \end{aligned} \tag{3.4}$$

The superconducting gap $\Delta(\pm\pi T) = \Phi_0 \pi T/\tilde{\Sigma}_0 = \Delta_0$ is

$$\Delta_0 = \pi T \left(\frac{2}{N}\right)^{1/2} \left(1 - \left(\frac{T}{T_p}\right)^\gamma\right)^{1/2} \tag{3.5}$$

The gap Δ_0 vanishes both at $T = 0$ and at $T = T_p$. In between, it is finite, but for any T, $D_0 = \Delta_0/(\pi T)$ is small and at most of order $1/N^{1/2}$. In other words, the gap at $N \gg 1$ remains smaller than the temperature at all $T < T_p$.

Solving next the set of Eliashberg equations for other $\omega_m \neq \pm\pi T$ we obtain at large N

$$\begin{aligned} \Phi(\omega_m) &\approx \Phi_0 \left[\left(\frac{2\pi T}{|\omega_m - \pi T|}\right)^\gamma + \left(\frac{2\pi T}{|\omega_m + \pi T|}\right)^\gamma\right] \\ \Sigma(\omega_m) &\approx 2N\tilde{\Sigma}_0 H\left(\frac{|\omega_m| - \pi T|}{2\pi T}, \gamma\right) \mathrm{sgn}(m + \frac{1}{2}) \end{aligned} \tag{3.6}$$

where $H(a,b) = \sum_1^a n^{-b}$ is a Harmonic number. At large m (but still when $\Sigma(\omega_m) \gg \omega_m$)

$$\Phi(\omega_m) \approx \frac{2\Phi_0}{|m|^\gamma}, \quad \tilde{\Sigma}(\omega_m) \approx 2N \frac{|\tilde{\Sigma}_0|}{1-\gamma} |m|^{1-\gamma} \mathrm{sgn}(m) \tag{3.7}$$

Observe that the self-energy behaves as $\Sigma(\omega_m) \propto T^{1-\gamma}$, at all $\omega_m = O(T)$, including

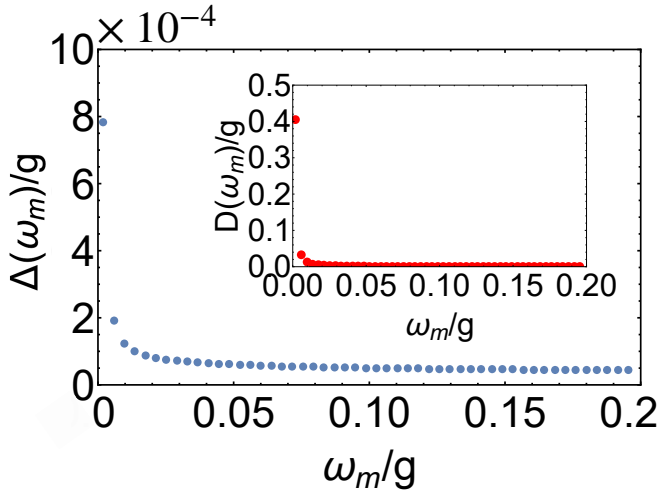

Figure 3.3: The pairing gap $\Delta(\omega_m) = \Phi(\omega_m)\omega_m/\tilde{\Sigma}(\omega_m)$ and $D(\omega_m) = \Delta(\omega_m)/\omega_m$ for $\gamma = 0.9$, $N = 10$ and $T = 0.05T_p$.

$\omega_m = \pm\pi T$. Still, the self-energy at $\pm\pi T$ is smaller in $1/N$ than $\Sigma(\omega_m)$ at other Matsubara frequencies. As the consequence, the pairing gap $\Delta(\omega_m)$ is parametrically larger at $\omega_m = \pm\pi T$ than at other frequencies. From (3.6) we have, at $|\omega_m| \neq \pi T$,

$$\Delta(\omega_m) = \frac{\Phi(\omega_m)}{\tilde{\Sigma}(\omega_m)} = \frac{1}{N}\frac{\Delta_0}{H(m,\gamma)}\left(\frac{1}{m^\gamma} + \frac{1}{(m+1)^\gamma}\right) \propto T\left(\frac{2}{N}\right)^{3/2}\left(1 - \left(\frac{T}{T_p}\right)^\gamma\right)^{1/2}. \tag{3.8}$$

We also see from see (3.8) that at any $T < T_p$, $\Delta(\omega_m)$ at any Matsubara frequency is parametrically smaller than T. Put it differently, $D(\omega_m) = \Delta(\omega_m)/\omega_m$ is small, of order $1/N^{3/2}$, at $m = O(1)$, and even smaller at larger m. We plot $\Delta(\omega_m)$ and $D(\omega_m)$ in Figure 3.3, which clearly shows at large N $\Delta(\omega_m)$ or $D(\omega_m)$ at $\omega_m = \pm\pi T$ dominant over those at other frequencies.

Taking $-iD_0$ as an estimate for small frequency limit of $D(\omega) \equiv \Delta((\omega)/\omega$ in real frequencies, we find that $D(\omega \to 0)$ tends to a finite imaginary value, i.e., at large N we have gapless superconductivity in the sense that $\Delta(\omega) \propto i\omega$. Using then $N(\omega) = N_0\,\mathrm{Re}[1/\sqrt{1 - D^2(\omega)}]$ for the DOS (N_0 is the normal state value), we find that the DOS at zero frequency $N(\omega = 0) = N_0/\sqrt{1 + D_0^2} \approx N_0\left(1 - \frac{1}{2}D_0^2\right)$ is reduced below T_p, compared to the normal state value, but remains finite, as in a gapless superconductor.

To verify this result and to get the full form of $N(\omega)$ we need to obtain $\Delta(\omega)$ as a function of a real frequency ω. This is what we will do in the next section.

3.2 Real frequency properties

To see the consequence of $\pm\pi T$ dominating in the pairing equations and more experiment-related properties coming from the first Matsubara frequency rule, we try to look for solutions of gap equations on real frequency axis. Before that, the gap equation (2.27) has to be properly continued from Matsubara axis to real frequency axis. Below we will first show the analytic continuation procedure, and then solve the real frequency equations in large N limit.

3.2.1 Analytic continuation to real frequency axis

The expressions for $\Phi(\omega_m)$ and $\tilde{\Sigma}(\omega_m)$ in Matsubara frequencies, Eq. (2.27), contain the interaction $V(i\omega_m - i\omega_{m'})$ which is essentially a susceptibility. This susceptibility cannot be converted to real frequency ω by just replacing $z = i\omega_m$ by $z = \omega$ because $V(z - i\omega_{m'}) = (-g^2/(z - i\omega_{m'})^2)^{\gamma/2}$ has branch cuts in a complex plane of z along $z = i\omega_{m'} + z_0$, where z_0 is a real variable (Ref. [62]). Due to this complication, we have to implement the full spectral decomposition procedure. Namely, we depart from Eliashberg equations along Matsubara axis and use Cauchy theorem to express $G(i\omega_m, \boldsymbol{k})$ and $V(i\omega_m - i\omega_{m'})$ in terms of retarded $\mathrm{Im}\, G^R(x, \boldsymbol{k})$ and $V''(x)$ (the imaginary part of $V^R(x)$)along real axis as

$$\begin{aligned} G(i\omega_m, \boldsymbol{k}) &= \int_{-\infty}^{\infty} \frac{dx}{\pi} \frac{\mathrm{Im}\, G^R(x, \boldsymbol{k})}{x - i\omega_m} \\ V(i\omega_m - i\omega_{m'}) &= \int_{-\infty}^{\infty} \frac{dy}{\pi} \frac{V''(y)}{y - i(\omega_m - \omega_{m'})} \end{aligned} \tag{3.9}$$

We then explicitly sum over $\omega_{m'}$ and integrate over $\mathbf{k}$ and obtain the expressions for $\tilde{\Sigma}(i\omega_m)$ and $\Phi(i\omega_m)$, in which the dependence on ω_m is only via $1/(i\omega_m - x - y)$. This form can be straightforwardly continued analytically to real frequency by just replacing $i\omega_m$ by $\omega + i0^+$.

For compactness, we do the calculations in Nambu formalism, in which one operates

with the 2×2 matrix Green's function $\hat{G}(i\omega_m, \boldsymbol{k})$, in which $\Sigma(i\omega_m)$ and $\Phi(i\omega_m)$) as elements of the 2×2 matrix self-energy $\hat{\Sigma}(i\omega_m)$. The Eliashberg equation in Nambu formalism is

$$\hat{\Sigma}(i\omega_n) = -T \sum_m \int \frac{d^2k}{(2\pi)^2} \hat{\tau}_3 \hat{G}(i\omega_m, \boldsymbol{k}) \hat{\tau}_3 V(i\omega_n - i\omega_m), \tag{3.10}$$

where $\hat{\tau}_3$ is a Pauli matrix. $\hat{\Sigma} = \Sigma\hat{\tau}_0 - \Phi\hat{\tau}_1$, and the matrix $\hat{G}(i\omega_m, \boldsymbol{k}) = -(i\omega_m - \xi_{\boldsymbol{k}} - \hat{\Sigma}(i\omega_m))^{-1}$. The diagonal and off-diagonal elements of $\hat{G}(i\omega_m, \boldsymbol{k})$ are normal and anomalous Green's functions in conventional notations.

Substituting the spectral representation (3.9) into (5.11) and performing the summation over ω_m, we obtain

$$\begin{aligned} \hat{\Sigma}(i\omega_n) &= -T \sum_m \int \frac{d^2k}{(2\pi)^2} \int \frac{dxdy}{\pi^2} \hat{\tau}_3 \frac{\operatorname{Im} \hat{G}^R(x, \boldsymbol{k})}{i\omega_m - x} \hat{\tau}_3 \frac{V''(y)}{i\omega_n - i\omega_m - y} \\ &= -\int \frac{d^2k}{(2\pi)^2} \int \frac{dxdy}{\pi^2} \hat{\tau}_3 \operatorname{Im} \hat{G}^R(x, \boldsymbol{k}) \hat{\tau}_3 V''(y) \frac{1}{i\omega_n - x - y} \left(n_F(x) + n_B(-y)\right) \end{aligned} \tag{3.11}$$

Replacing $i\omega_n$ with $\omega + i0^+$ we obtain the self-energy at real frequencies

$$\hat{\Sigma}(\omega) = -\int \frac{d^2k}{(2\pi)^2} \int \frac{dxdy}{\pi^2} \hat{\tau}_3 \operatorname{Im} \hat{G}^R(x, \boldsymbol{k}) \hat{\tau}_3 V''(y) \frac{1}{\omega - x - y + i0^+} \left(n_F(x) + n_B(-y)\right) \tag{3.12}$$

We next express $\operatorname{Im} \hat{G}^R(x, \boldsymbol{k})/(\omega - x - y + i0^+)$ via the full $\hat{G}^R(x, \boldsymbol{k})$ as

$$\begin{aligned} \frac{2 \operatorname{Im} \hat{G}^R(x, \boldsymbol{k})}{\omega - x - y + i0^+} &= \operatorname{Im} \left[\hat{G}^R(x, \boldsymbol{k}) \left(\frac{1}{\omega - x - y + i0^+} + \frac{1}{\omega - x - y - i0^+} \right) \right] \\ &\quad - i \operatorname{Re} \left[\hat{G}^R(x, \boldsymbol{k}) \left(\frac{1}{\omega - x - y + i0^+} - \frac{1}{\omega - x - y - i0^+} \right) \right]. \end{aligned} \tag{3.13}$$

and integrate in (3.12) over x by closing the integration contour over the upper half-plane of complex x. Because $\hat{G}^R(x, \boldsymbol{k})$ is analytic in the upper half plane, the poles come only from $1/(\omega - x - y + i0^+)$ and from $n_F(x)$ (at $x = i(2n+1)\pi T$). Using the

residue theorem, we find

$$
\begin{aligned}
\hat{\Sigma}(\omega) = & -\frac{1}{2}\int \frac{d^2k}{(2\pi)^2}\int \frac{dy}{\pi}V''(y) \\
& \times \left\{ \mathrm{Im}\left[\int \frac{dx}{\pi}\left(n_F(x)+n_B(-y)\right)\hat{\tau}_3\hat{G}^R(x,\boldsymbol{k})\hat{\tau}_3\left(\frac{1}{\omega-x-y+i0^+}+\frac{1}{\omega-x-y-i0^+}\right)\right]\right. \\
& \left. -i\,\mathrm{Re}\left[\int \frac{dx}{\pi}\left(n_F(x)+n_B(-y)\right)\hat{\tau}_3\hat{G}^R(x,\boldsymbol{k})\hat{\tau}_3\left(\frac{1}{\omega-x-y+i0^+}-\frac{1}{\omega-x-y-i0^+}\right)\right]\right\} \\
= & \int \frac{d^2k}{(2\pi)^2}\int \frac{dy}{\pi}V''(y)T\sum_{\omega_n>0}\mathrm{Im}\left[i\hat{\tau}_3\hat{G}^R(i\omega_n,\boldsymbol{k})\hat{\tau}_3\left(\frac{1}{\omega-i\omega_n-y}+\frac{1}{\omega-i\omega_n-y}\right)\right] \\
& + \int \frac{d^2k}{(2\pi)^2}\int \frac{dy}{\pi}V''(y)\left(n_F(\omega-y)+n_B(-y)\right)\times\left[\mathrm{Im}(i\hat{\tau}_3G^R(\omega-y,\boldsymbol{k})\hat{\tau}_3)-i\,\mathrm{Re}(i\hat{\tau}_3G^R(\omega-y,\boldsymbol{k})\hat{\tau}_3)\right] \\
= & 2T\sum_{\omega_n>0}\int \frac{d^2k}{(2\pi)^2}\int \frac{dy}{\pi}V''(y)\,\mathrm{Im}\,\frac{i\hat{\tau}_3\hat{G}^R(i\omega_n,\boldsymbol{k})\hat{\tau}_3}{\omega-i\omega_n-y} \\
& + \int \frac{d^2k}{(2\pi)^2}\int \frac{dy}{\pi}V''\hat{\tau}_3\hat{G}^R(\omega-y,\boldsymbol{k})\hat{\tau}_3\left(n_F(y-\omega)+n_B(y)\right), \qquad (3.14)
\end{aligned}
$$

Using the following definition for $\omega_m > 0$,

$$
\frac{1}{\pi}\int dy\frac{V''(y)}{y-(\omega\pm i\omega_m)} = V(\omega\pm i\omega_m) = \frac{\bar{g}^\gamma}{(\omega_m\mp i\omega)^\gamma} \qquad (3.15)
$$

and also noticing

$$
n_F(y-\omega)+n_B(y) = \frac{1}{2}\left(\tanh\frac{\omega-y}{2T}+\coth\frac{y}{2T}\right) \qquad (3.16)
$$

we finally obtain

$$
\begin{aligned}
\hat{\Sigma}(\omega) = & -2T\sum_{\omega_n>0}\int \frac{d^2k}{(2\pi)^2}\,\mathrm{Im}[i\hat{\tau}_3\hat{G}^R(i\omega_n,\boldsymbol{k})\hat{\tau}_3V(\omega-i\omega_n)] \\
& -\frac{1}{2}\int \frac{d^2k}{(2\pi)^2}\int \frac{dy}{\pi}V''(y)\hat{\tau}_3\hat{G}^R(\omega-y,\boldsymbol{k})\hat{\tau}_3\left(\tanh\frac{\omega-y}{2T}+\coth\frac{y}{2T}\right)
\end{aligned} \qquad (3.17)
$$

Let's now spit this matrix equation into the equations for the pairing vertex $\Phi(\omega)$ and conventional (non-anomalous) self-energy $\Sigma(\omega)$. Expressing $\hat{\Sigma}(\omega)$ as

$$
\hat{\Sigma}(\omega) = \Sigma(\omega)\hat{\tau}_0 - \Phi(\omega)\hat{\tau}_1 \qquad (3.18)
$$

and substituting into the Dyson equation, we obtain

$$\hat{\tau}_3 G(\omega, \boldsymbol{k})\hat{\tau}_3 = \frac{1}{\xi_{\boldsymbol{k}}^2 + \Phi(\omega)^2 - (\omega + \Sigma(\omega) + i0^+)^2}\left(-(\omega + \Sigma(\omega))\hat{\tau}_0 - \xi_{\boldsymbol{k}}\hat{\tau}_3 + \Phi(\omega)\hat{\tau}_1\right) \tag{3.19}$$

where $\xi_{\boldsymbol{k}}$ is the fermionic dispersion. Expressing next $\int d^2k/(2\pi)^2 = N_0 \int d\xi_{\boldsymbol{k}}$, where N_0 is the DOS in the normal state, and integrating over $\xi_{\boldsymbol{k}}$, we further obtain

$$\int \frac{d^2k}{(2\pi)^2}\hat{\tau}_3 G(\omega, \boldsymbol{k})\hat{\tau}_3 = N_0 \int_{-\infty}^{\infty} d\xi_{\boldsymbol{k}}\hat{\tau}_3 G(\omega, \boldsymbol{k})\hat{\tau}_3 = i\pi N_0 \frac{-\tilde{\Sigma}(\omega))\hat{\tau}_0 + \Phi(\omega)\hat{\tau}_1}{\sqrt{\tilde{\Sigma}^2(\omega) - \Phi^2(\omega)}} \tag{3.20}$$

where $\tilde{\Sigma}(\omega) = \omega + \Sigma(\omega)$. Notice here when computing the square root in the denominator, the branch with a positive imaginary part is chosen. This is different from commonly chosen branch which has a positive real part. Substituting this into the r.h.s. of (3.17), absorbing the density of states N_0 into V, and splitting $\hat{\Sigma}(\omega)$ into normal and anomalous components, we obtain

$$\begin{aligned}
\tilde{\Sigma}(\omega) &= \omega + i\pi T \sum_{\omega_m > 0} \frac{\tilde{\Sigma}(\omega_m)}{\sqrt{\Phi^2(\omega_m) + (\tilde{\Sigma}^2(\omega_m))}} \left[V(\omega - i\omega_m) - V(\omega + i\omega_m)\right] \\
&\quad + \frac{i}{2}\int dy V^{''}(y)\left[S_\Sigma(\omega - y)\left(\tanh\frac{\omega - y}{2T} + \coth\frac{y}{2T}\right)\right] \\
\Phi(\omega) &= \pi T \sum_{\omega_m > 0} \frac{\Phi(\omega_m)}{\sqrt{\Phi^2(\omega_m) + \tilde{\Sigma}^2(\omega_m))}} \left[V(\omega - i\omega_m) + V(\omega + i\omega_m)\right] \\
&\quad + \frac{i}{2}\int dy V^{''}(y)\left[S_\Phi(\omega - y)\left(\tanh\frac{\omega - y}{2T} + \coth\frac{y}{2T}\right)\right]
\end{aligned} \tag{3.21}$$

where

$$S_\Phi(\omega) = \frac{\Phi(\omega)}{\sqrt{\tilde{\Sigma}^2(\omega) - \Phi^2(\omega)}}, \quad S_\Sigma(\omega) = \frac{\tilde{\Sigma}(\omega)}{\sqrt{\tilde{\Sigma}^2(\omega) - \Phi^2(\omega)}} \tag{3.22}$$

At a finite T and small y, $\coth(y/(2T)) \approx 2T/y$. Then $V^{''}(y)\coth(y/(2T))$ scales as $T/|y|^{1+\gamma}$, and the integrals over dy in the expressions for $\tilde{\Sigma}(\omega)$ and $\Phi(\omega)$ in (3.21) diverge. This divergent piece corresponds to the divergence in the Matsubara axis equations due to $m = n$ term in the summation. Like what we did in (2.25), the divergence

piece on real frequency axis can also be eliminated by excluding this singular contribution explicitly. By doing so, we arrive at a set of equations free from singularities, and with this the equations can be safely extended to $N \neq 1$. The final equations, with N extension, writes,

$$\begin{aligned}\Phi(\omega) &= A(\omega) + \frac{i}{2N}\int_{-\infty}^{\infty} dy V''(y)\left[S_\Phi(\omega-y)\left(\tanh\frac{\omega-y}{2T} + \coth\frac{y}{2T}\right) - S_\Phi(\omega)\frac{2T}{y}\right] \\ \tilde{\Sigma}(\omega) &= B(\omega) + \frac{i}{2}\int_{-\infty}^{\infty} dy V''(y)\left[S_\Sigma(\omega-y)\left(\tanh\frac{\omega-y}{2T} + \coth\frac{y}{2T}\right) - S_\Sigma(\omega)\frac{2T}{y}\right]\end{aligned} \tag{3.23}$$

where

$$\begin{aligned}A(\omega) &= \frac{\pi T}{N}\sum_{m\geq 0}\frac{\Phi(\omega_m)}{\sqrt{\tilde{\Sigma}^2(\omega_m)+\Phi^2(\omega_m)}}\left[V(\omega-i\omega_m)+V(\omega+i\omega_m)\right] \\ B(\omega) &= \omega + i\pi T\sum_{m\geq 0}\frac{\tilde{\Sigma}(\omega_m)}{\sqrt{\tilde{\Sigma}^2(\omega_m)+\Phi^2(\omega_m)}}\left[V(\omega-i\omega_m)-V(\omega+i\omega_m)\right]\end{aligned} \tag{3.24}$$

Eq.(3.23) can be easily verified by taking $\omega \to i\omega_n = i(2n+1)\pi T$, i.e. by going back to Matsubara axis, and the equations should reduce to those in Eq.(2.25) if the analytic continuation has been done correctly. Indeed, with the replacement $\omega \to i\omega_n$ the thermal factor $(\tanh\frac{i\omega_n - y}{2T} + \coth\frac{y}{2T})$ in Eq.(3.23) vanishes and the integral $\int dy V''(y)/y = \pi V(i\Omega_n = 0)$ accounts for the elimination of zero frequency transfer term in Eq.(2.25) ($\omega_m = \omega_n$ term). Taking into account the contributions from $A(i\omega_n)$ and $B(i\omega_n)$ and using the symmetry property of both $\Phi(\omega_m)$ and $\tilde{\Sigma}(\omega_m)$, Eq.(2.25) is reproduced.

3.2.2 from $\pm\pi T$ to ω/T scaling

To get information of spectral properties on real frequency axis using (3.23), the first step is to solve the gap equation (2.25) on Matsubara frequency axis, and then use them as input to solve the equation with real ω. In this sense, special properties on Matsubara axis have a direct impact on the real frequency properties. The interesting findings we discuss in this subsection is based on this consideration.

We begin with analyzing (3.23) at $\omega = 0$. At this point, the equations become

$$\Phi(0) = \frac{\pi T}{N}\sum_m \frac{\Phi(\omega_m)}{\sqrt{(\Phi(\omega_m))^2 + (\tilde{\Sigma}(\omega_m))^2}} V(\omega_m) + \frac{i}{N}\int dy V''(y)\left(\frac{S_\Phi(-y)}{\sinh y/T} - \frac{S_\Phi(0)}{y/T}\right)$$
$$\tilde{\Sigma}(0) = i\pi T\sum_m \frac{\tilde{\Sigma}(\omega_m)}{\sqrt{(\Phi(\omega_m))^2 + (\tilde{\Sigma}(\omega_m))^2}} V(\omega_m) + i\int dy V''(y)\left(\frac{S_\Sigma(-y)}{\sinh y/T} - \frac{S_\Sigma(0)}{y/T}\right) \tag{3.25}$$

The first term in the formula for $\tilde{\Sigma}(0)$ vanishes by symmetry, after summing up the contributions from positive and negative ω_m.

We first consider large N. We assume and then verify that in this case $\tilde{\Sigma}$ is parametrically larger than Φ not only along the Matsubara axis but also along the real axis. To leading order in $1/N$ we then have for the self-energy, using $\tilde{\Sigma}(\omega)/\sqrt{-i\tilde{\Sigma}(\omega)} = i$,

$$\tilde{\Sigma}(0) = i\int dx V''(x)\left(\frac{1}{\sinh x/T} - \frac{T}{x}\right) = -i\pi T\left(\frac{g}{\pi T}\right)^\gamma S_\gamma, \tag{3.26}$$

where

$$S_\gamma = 2\sin\pi\gamma/2\int_0^\infty \frac{dx}{x^\gamma}\left(\frac{1}{\pi x} - \frac{1}{\sinh \pi x}\right). \tag{3.27}$$

For $\Phi(0)$ we find from Eq. (3.25)

$$\Phi(0) \approx \frac{\pi T}{N}\sum_m \frac{\Phi(\omega_m)}{|\tilde{\Sigma}(\omega_m)|} V(\omega_m). \tag{3.28}$$

Using the fact that at large N the dominant contribution to the Matsubara sum comes from $m = 0, -1$ and substituting the expressions for $\Phi(\pm\pi T)$ and $\Sigma(\pm\pi T)$, we obtain

$$\Phi(0) = \left(\frac{2}{N}\right)^{3/2}\pi T\left(\frac{g}{\pi T}\right)^\gamma\left(1 - \left(\frac{T}{T_p}\right)^\gamma\right)^{1/2}. \tag{3.29}$$

Then $D_0 = \Phi(0)/\tilde{\Sigma}(0)$ is

$$D_0 = i\left(\frac{2}{N}\right)^{3/2}\frac{1}{S_\gamma}\left(1 - \left(\frac{T}{T_p}\right)^\gamma\right)^{1/2}, \tag{3.30}$$

and the DOS at zero frequency is

$$N(0) = N_0 \left(1 - \left(\frac{2}{N} \right)^3 \frac{\left(1 - \left(\frac{T}{T_p} \right)^\gamma \right)}{2S_\gamma^2} \right). \tag{3.31}$$

This agrees, up to a prefactor, with the estimate that we obtained in the analysis on the Matsubara axis, by just assuming that $D(\omega_m = \pi T)$ is comparable to $D(\omega = 0)$.

We emphasize that $N(0)$ differs from the normal state value N_0 at all $T < T_p$, including $T = 0$, where we expect superconductivity to disappear. We will show below that the limit $\omega \to 0$ and $T \to 0$ has to be taken with care, and at any non-zero ω the DOS indeed transforms into N_0 at $T \to 0$. Still, strictly at $\omega = 0$, $N(0) < N_0$. This is somewhat similar to the behavior of $N(\omega)$ in an ideal BCS superconductor, where $N(0) = 0$ for all T up to T_c, while $N(\omega \neq 0)$ approaches N_0 at $T \to T_c$.

We next move to finite ω. In (3.23) for $\Phi(\omega)$, the second term ($(1/N)\int ...$) is of order $\Phi(\omega)/N$ and can be neglected at large N. Evaluating the first term by summing up the contributions from $m = 0, -1$, at which $\Phi(\omega_m)/|\tilde{\Sigma}(\omega_m)|$ is the largest, we obtain

$$\Phi(\omega) = \left(\frac{2}{N} \right)^{3/2} \pi T \left(\frac{g}{\pi T} \right)^\gamma \left(1 - \left(\frac{T}{T_p} \right)^\gamma \right)^{1/2} F_\Phi \left(\frac{\omega}{\pi T} \right), \tag{3.32}$$

where

$$F_\Phi(x) = \frac{1}{2} \left(\frac{1}{(1+ix)^\gamma} + \frac{1}{(1-ix)^\gamma} \right). \tag{3.33}$$

Note that $F_\Phi(x)$ is purely real and even in x, hence $\Phi(\omega)$ is real and even in ω.

Because $\Phi(\omega)$ is small in $1/N^{3/2}$, the self-energy at finite ω remains the same as in the normal state, up to $1/N^3$ corrections:

$$\Sigma(\omega) = \pi T \left(\frac{g}{\pi T} \right)^\gamma F_\Sigma \left(\frac{\omega}{\pi T} \right), \tag{3.34}$$

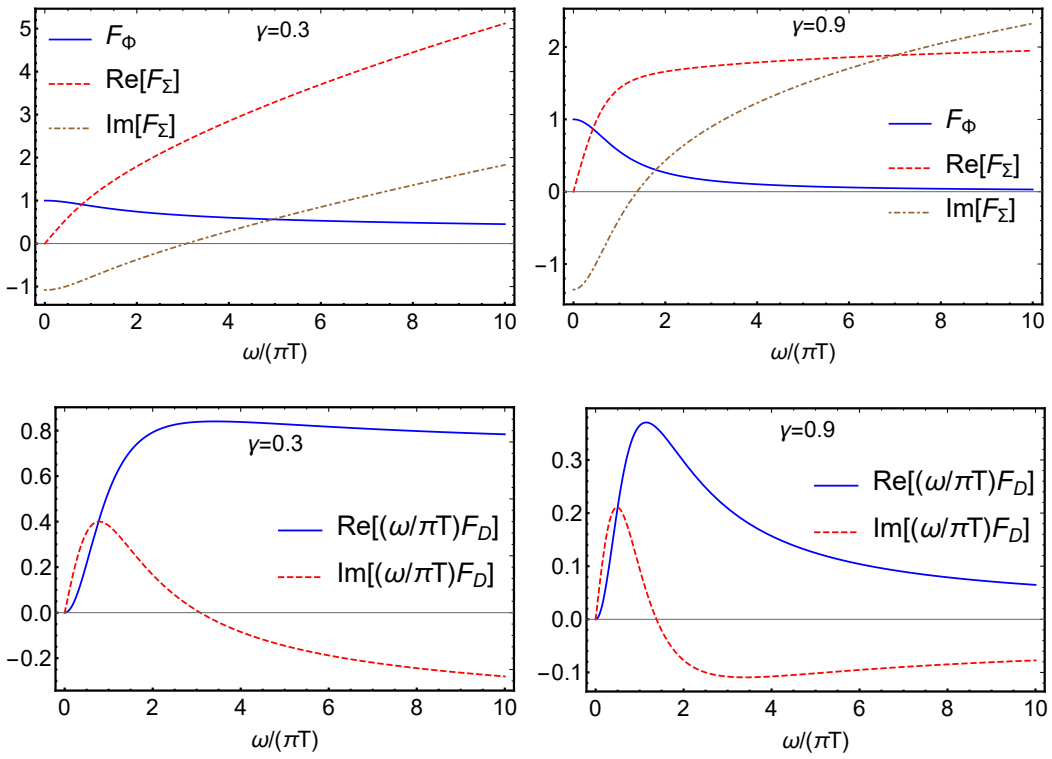

Figure 3.4: The scaling functions $F_\Phi(\frac{\omega}{\pi T})$, $F_\Sigma(\frac{\omega}{\pi T})$ and $\frac{\omega}{\pi T}F_D(\frac{\omega}{\pi T}) = \frac{\omega}{\pi T}F_\Phi(\frac{\omega}{\pi T})/F_\Sigma(\frac{\omega}{\pi T})$ for the pairing vertex, the self-energy and the gap function respectively, see Eqs. (3.33), (3.35), and (3.38). We recall that $F_\Phi(\frac{\omega}{\pi T})$ and $F_\Sigma(\frac{\omega}{\pi T})$ are computed without the thermal contribution. The function $F_\Phi(x)$ is real, $F_\Sigma(x)$ and $F_D(x)$ are complex, i.e., the gap function $\Delta(x)$ is a complex function of frequency. The results are for $\gamma = 0.3$ and $\gamma = 0.9$. Observe that $\mathrm{Im}\, F_\Sigma(x)$ changes sign at some frequency. This sign change is necessary to satisfy KK relation on $\Sigma^*(\pi T) = 0$ (see Fig. 3.5).

where

$$F_\Sigma(x) = i\sum_{m=0}^{\infty}\left(\frac{1}{(2m+1+ix)^\gamma} - \frac{1}{(2m+1-ix)^\gamma}\right)$$
$$-i\sin\frac{\pi\gamma}{2}\int_0^\infty \frac{dy}{y^\gamma}\left(\frac{2}{\pi y} - \coth\frac{\pi y}{2} + \frac{\sinh\pi y}{\cosh\pi y + \cosh\pi x}\right). \tag{3.35}$$

The first term in $F_\Sigma(x)$ is real, the second is imaginary. At large x (i.e., at $\omega \gg \pi T$), $F_\Sigma(x) \approx (x^{1-\gamma}/(1-\gamma))e^{i\pi\gamma/2}$. We plot the scaling functions $F_\Phi(x)$, Re$[F_\Sigma(x)]$, and Im$[F_\Sigma(x)]$ in Figure 3.4.

We see that Im $\left[F_\Sigma\left(\frac{\omega}{\pi T}\right)\right]$ changes sign as a function of frequency (hence, Im $[\Sigma(\omega)]$ also changes sign). This sign change must happen because Im$[\Sigma(\omega)]$ is related by Kramers-Kronig(KK) formula to $\Sigma(\pi T) = 0$:

$$2T\int_0^\infty d\omega \frac{\text{Im}\,\Sigma(\omega)}{\omega^2 + (\pi T)^2} = \Sigma(\pi T) = 0. \tag{3.36}$$

The integral in the r.h.s. of (3.36) vanishes only if Im$[\Sigma(\omega)]$ changes sign at least once . We verified numerically that the KK relation is indeed satisfied, see Figure 3.5. We remind in this regard that Σ is the self-energy without the thermal contribution. The imaginary part of the full self-energy, Im$[\Sigma(\omega)]$, indeed remains positive at all frequencies.

Substituting the results for $\Phi(\omega)$ and $\tilde{\Sigma}(\omega)$ into $\Delta(\omega) = \Phi(\omega)\omega/\tilde{\Sigma}(\omega)$ and $D(\omega) = \Delta(\omega)/\omega$, we obtain

$$\Delta(\omega) = \left(\frac{2}{N}\right)^{3/2}\left(1 - \left(\frac{T}{T_p}\right)^\gamma\right)^{1/2}\omega F_D\left(\frac{\omega}{\pi T}\right),$$
$$D(\omega) = \left(\frac{2}{N}\right)^{3/2}\left(1 - \left(\frac{T}{T_p}\right)^\gamma\right)^{1/2} F_D\left(\frac{\omega}{\pi T}\right). \tag{3.37}$$

At $\omega \leq g$, when $\tilde{\Sigma}(\omega) \approx \Sigma(\omega)$,

$$F_D(x) = \frac{F_\Phi\left(\frac{\omega}{\pi T}\right)}{F_\Sigma\left(\frac{\omega}{\pi T}\right)}. \tag{3.38}$$

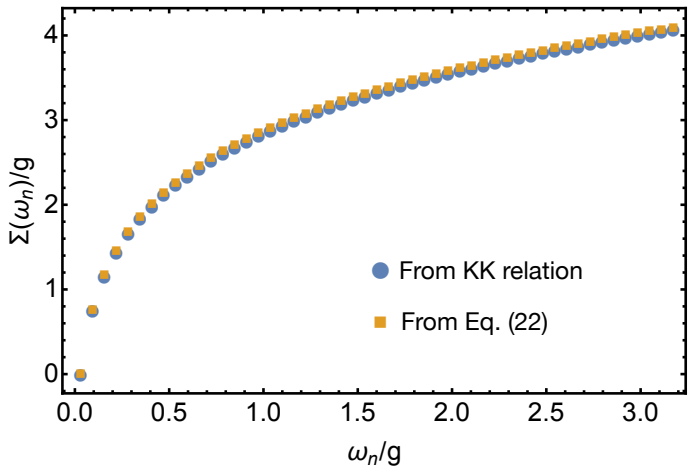

Figure 3.5: The verification of the KK transformation. Yellow squares – the self-energy obtained directly along the Matsubara axis: $\Sigma(i\omega_n) = 2\pi T(\bar{g}/2\pi T)^\gamma H(n,\gamma)$, Eq. (3.6). Blue circles – the self-energy $\Sigma(i\omega_n) = -i\pi T(\bar{g}/\pi T)^\gamma F_\Sigma(\omega_n)$, where $F_\Sigma(i\omega_n) = (2i\omega_n/\pi)\int_0^\infty dx\, \mathrm{Im}\, F_\Sigma(x)/(x^2+\omega_n^2)$ is obtained by KK transformation from $\mathrm{Im}\, F_\Sigma(x)$ along the real axis, see (3.35). The two expressions coincide. To better show this we manually split the two expressions for $\Sigma(i\omega_n)$ by multiplying the yellow curve by 1.01. Observe that $F_\Sigma(i\pi T) = 0$, i.e., the self-energy $\Sigma(i\omega_n)$, extracted from KK transformation, vanishes at the first Matsubara frequency. We set $\gamma = 0.9$ and $T = 0.01\bar{g}$.

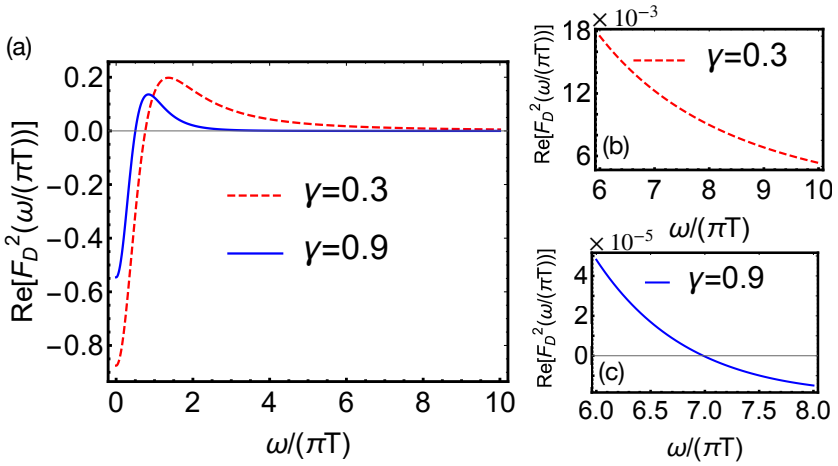

Figure 3.6: (a) The real part of the scaling function $F_D^2(\frac{\omega}{\pi T})$, defined in Eq. (3.38), for $\gamma = 0.3$ and $\gamma = 0.9$. The $\mathrm{Re}[F_D^2(\frac{\omega}{\pi T})]$ determines the frequency dependence of the DOS at large N, Eq. (3.39). In the normal state $F_D = 0$. Observe that $\mathrm{Re}[F_D^2(\frac{\omega}{\pi T})]$ has a peak at $\omega \sim T$. (b) and (c) The magnified plots of $\mathrm{Re}[F_D^2(\frac{\omega}{\pi T})]$ at lager $\omega/(\pi T)$. For $\gamma = 0.3$, $\mathrm{Re}[F_D^2(\frac{\omega}{\pi T})]$ gradually decreases, for $\gamma = 0.9$ it changes sign at $\frac{\omega}{\pi T} \sim 7$.

The DOS is

$$N(\omega) = N_0 \,\mathrm{Re}\left[\frac{1}{(1 - D^2(\omega))^{1/2}}\right] \approx N_0 \left(1 + \frac{1}{2}\,\mathrm{Re}\left[D^2(\omega)\right]\right)$$
$$= N_0 \left(1 + \frac{1}{2}\left(\frac{2}{N}\right)^3 \left(1 - \left(\frac{T}{T_p}\right)^\gamma\right) \mathrm{Re}\left[F_D^2\left(\frac{\omega}{\pi T}\right)\right]\right). \tag{3.39}$$

We see that the magnitude of $N(\omega)/N_0 - 1 \approx \frac{1}{2}\,\mathrm{Re}\, D^2(\omega)$ is determined by the temperature-dependent factor in (3.37) and depends on T/T_p. However, the frequency dependence of $D(\omega)$ and of the DOS is determined by $F_D(\omega/(\pi T))$, which for any given γ is a universal function of ω/T and does not depend on T/T_p. This implies that the characteristic frequency, at which $N(\omega)$ deviates from N_0, is determined by the temperature rather than by the magnitude of the superconducting gap.

Because $F_\Phi(x)$ is real,

$$\mathrm{Re}\, F_D^2(x) = F_\Phi^2(x) \frac{(\mathrm{Re}\, F_\Sigma(x))^2 - (\mathrm{Im}\, F_\Sigma(x))^2}{((\mathrm{Re}\, F_\Sigma(x))^2 + (\mathrm{Im}\, F_\Sigma(x))^2)^2}. \tag{3.40}$$

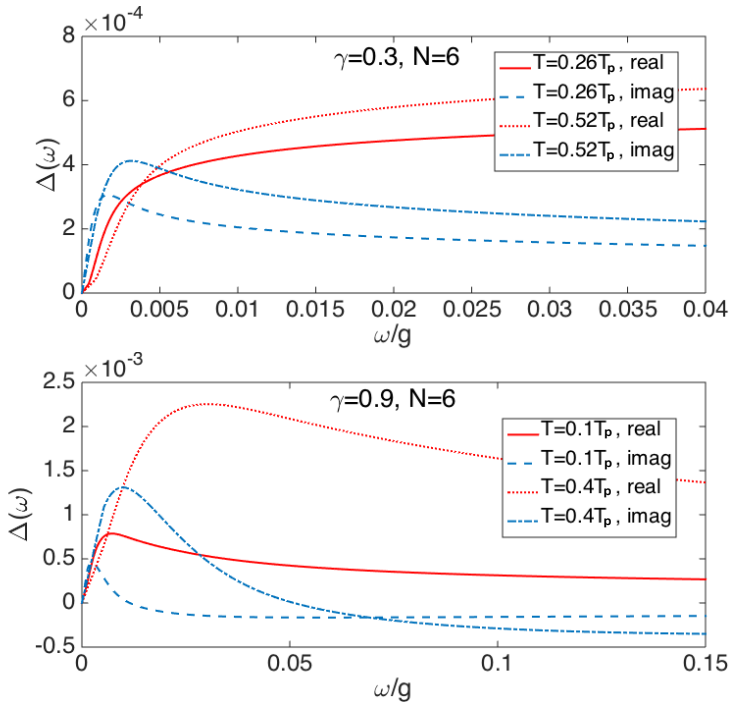

Figure 3.7: $\Delta(\omega)$ for various $T > T_{cross}$. Upper panel: $\gamma = 0.3, N = 6$. Lower panel: $\gamma = 0.9, N = 6$. Red lines are for the real part $\Delta'(\omega)$ and blue lines are for the imaginary part $\Delta''(\omega)$. At small but non zero ω, both the real and imaginary parts are finite, in contrast to the BCS-like behavior where $\Delta''(\omega)$ is zero up to some $\omega_0 \approx \Delta'$ at low temperatures.

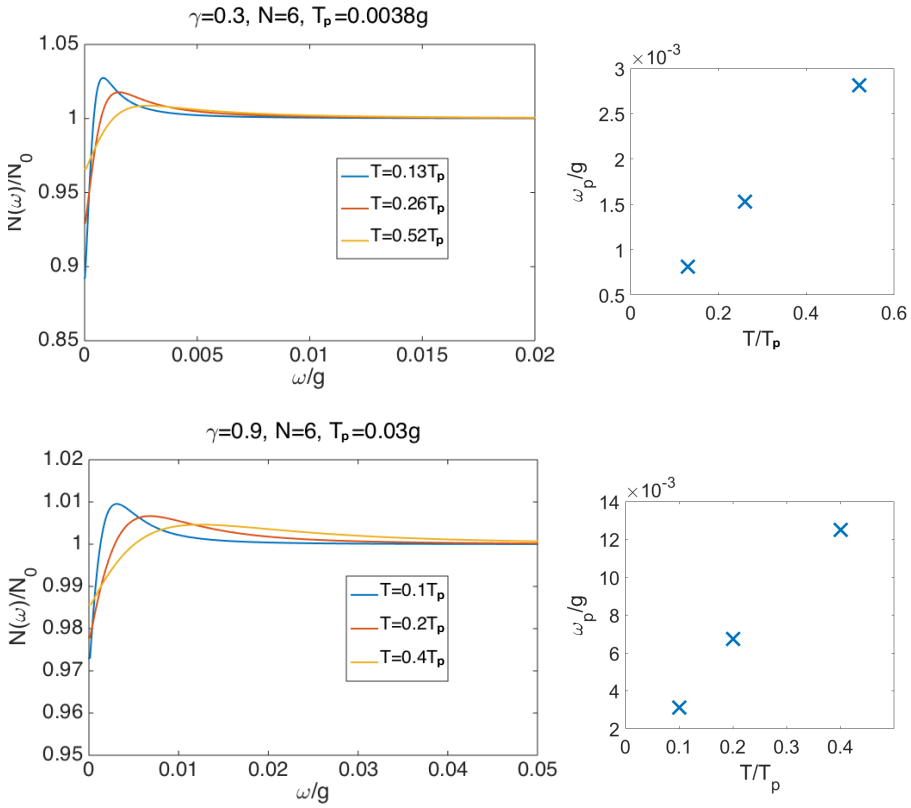

Figure 3.8: The DOS $N(\omega)$ for various $T > T_{cross}$. Upper panel: $\gamma = 0.3, N = 6$. Lower panel: $\gamma = 0.9, N = 6$. Right panels: The temperature dependence of the characteristic frequency ω_p, defined as the peak position of the $N(\omega)$.

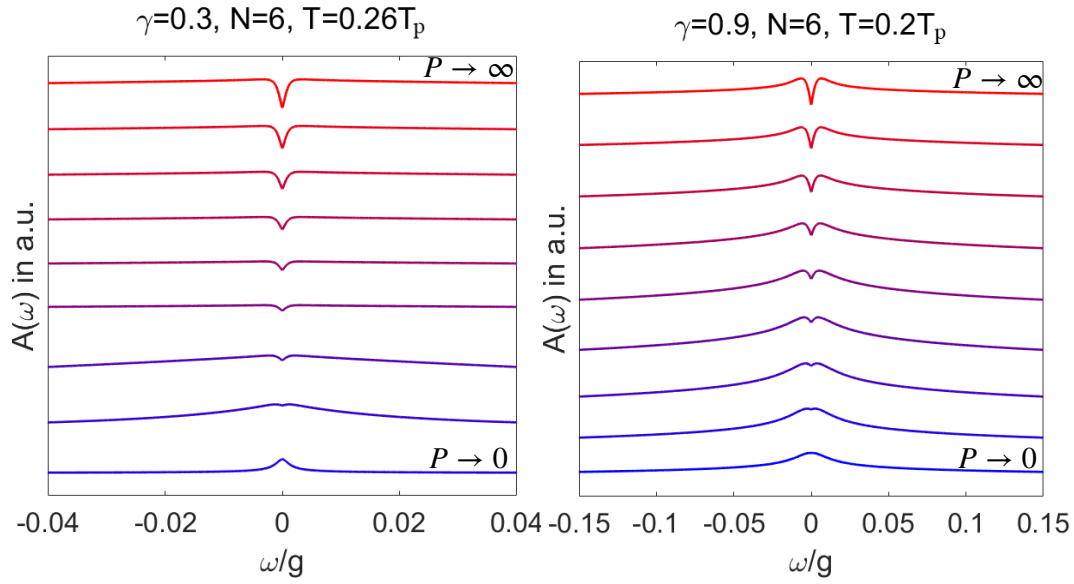

Figure 3.9: The spectral function $A(\omega)$ at a fixed $T > T_{cross}$, plotted as a function of ω for various values of parameter P, which measures the strength of thermal contributions to the self-energy and the pairing vertex. At large P, $A(\omega)$ shows the same behavior as the DOS, with the dip at small ω. At small P, it shows instead the maximum at $\omega = 0$. The plots are for $\gamma = 0.3$ and $\gamma = 0.9$.

At small $x = \omega/\pi T$, $\mathrm{Re}\, F_\Sigma(x) \propto x^2$ and $\mathrm{Im}\, F_\Sigma(x)$ is finite. Then $\mathrm{Re}\, F_D^2(x)$ is negative. At x, where $\mathrm{Im}\, F_\Sigma(x)$ changes sign, $\mathrm{Re}\, F_\Sigma(x)$ is finite, hence for this x $\mathrm{Re}\, F_D^2(x)$ is positive. In between, $\mathrm{Re}\, F_D^2(x)$ necessary changes sign. This in turn implies that $N(\omega) < N_0$ at small x and $N(\omega) > N_0$ at larger x. Then $N(\omega)$ has a dip at $\omega = 0$ and a hump at a characteristic frequency set by temperature, rather than by the gap itself. This frequency *increases with increasing* T. This behavior is qualitatively different from that in a BCS superconductor, where the maximum in the DOS is located at $\omega = \Delta(T)$ and shifts to a lower frequency with increasing T because $\Delta(T)$ gets smaller. We plot $\mathrm{Re}\, F_D^2(x)$ in Fig.3.6 for two different values of the exponent γ. In both cases, the hump at $\omega \sim T$ is clearly visible. The position of the hump shifts to a lower frequency with increasing γ but remains at a finite ω even at $\gamma = 1$.

We see from Fig.3.7 that the imaginary part of $\Delta(\omega)$ is finite even at very small ω, consistent with Eq. (3.37). For the DOS, we clearly see from Fig. 3.8 that there is a dip in $N(\omega)$ at small frequencies and the position of the maximum in $N(\omega)$ is set by the temperature.

A remark is in order here. The integrated DOS $\int d\omega N(\omega)$, with $N(\omega)$ as in Fig.3.8, does have some T dependence. This seems problematic, because the integrated DOS is proportional to the total number of particles, which is the conserved quantity. In fact, there is no contradiction. The reasoning is that the momentum integration in Eliashberg equations is performed assuming particle-hole symmetry, i.e., neglecting contributions from energies of order μ. There are additional contributions to the DOS from energies of order μ, both in the normal and the superconducting state. They are not equal, because μ changes between normal and superconducting states [**?**]. This additional contribution must be included to ensure particle conservation.

We next consider the spectral function $A(\omega) = -(1/\pi)\,\mathrm{Im}[G(k_F, \omega)]$. In terms of original $\Phi(\omega)$ and $\tilde{\Sigma}(\omega)$, we have

$$A(\omega) = -\frac{1}{\pi}\,\mathrm{Im}\left[\frac{\tilde{\Sigma}(\omega)}{\tilde{\Sigma}^2(\omega) - \Phi^2(\omega)}\right]. \tag{3.41}$$

This formula, however, is valid only before we eliminating the thermal divergence in (3.23). Because for spectral function $A(\omega)$, the thermal fluctuation plays an important role. In order to model the thermal strength, we introduce a factor $P = \int dy V''(y) T/y =$

$\pi TV(\Omega_n = 0)$, and re-express $A(\omega)$ as

$$A(\omega) = -\frac{1}{\pi} \mathrm{Im} \left[\frac{\tilde{\Sigma}(\omega)}{(\tilde{\Sigma}(\omega))^2 - (\Phi(\omega))^2} L(\omega) \right], \tag{3.42}$$

where

$$L(\omega) = \frac{\sqrt{\Phi(\omega)^2 - \tilde{\Sigma}(\omega)^2}}{P \,\mathrm{sgn}\,\mathrm{Im}\,\tilde{\Sigma} + \sqrt{\Phi(\omega)^2 - \tilde{\Sigma}(\omega)^2}}. \tag{3.43}$$

To leading order in $1/P$, $A(\omega) \propto \frac{1}{P} \mathrm{Re} \left[\frac{1}{\sqrt{1-\left(\Phi(\omega)/\tilde{\Sigma}(\omega)\right)^2}} \right] \propto N(\omega)/N_0$, i.e., the spectral function has the same dependence on ω as the DOS. Accordingly, at a finite T, $A(\omega)$ is non-zero for any frequency, and the position of the maximum in $A(\omega)$ scales with T and remains at a finite frequency at T_p (see Fig.3.9). If P is finite, either because the system is at some distance from a QCP, or we probe $A(\omega)$ for fermions connected by momenta different from the one at which static χ diverges (e.g., near-nodal fermions in the cuprates, if a pairing boson is an antiferromagnetic spin fluctuation), the behavior of $A(\omega)$ depends on the interplay between P and $\sqrt{\Phi(\omega)^2 - \tilde{\Sigma}(\omega)^2}$ at relevant ω. the other term in $L(\omega)$ in (3.43). If P is smaller, $L(\omega) \approx 1$, and

$$A(\omega) = -\frac{1}{\pi} \mathrm{Im} \left[\frac{\tilde{\Sigma}(\omega)}{(\tilde{\Sigma}(\omega))^2 - (\Phi(\omega))^2} \right]. \tag{3.44}$$

Substituting the expressions for $\Phi(\omega)$ and $\tilde{\Sigma}(\omega)$ we find that in this situation $A(\omega)$ is peaked at zero frequency, as if the system was in the normal state. We show this behavior in Fig.3.9.

The analysis beyond the leading order in $1/N$ proceeds in the same way as for Matsubara frequencies. As N gets smaller, the maximum in the DOS becomes more pronounced, and, at the same time, the DOS at zero frequency, $N(0)$ gets smaller. These modifications get larger as N decreases towards N_{cr} and eventually, at $N < N_{cr}$, the system behavior at the lowest T changes qualitatively. We discuss this in the next Section.

3.3 Gap closing vs. gap filling

We see from above that, in the large N limit, the gap equations on Matsubara frequency axis, have significant contributions from the first two frequencies $\pm\pi T$, and as a result, $\Delta(\pm\pi T)$ is much larger than other $\Delta(\omega_n \neq \pm\pi T)$. The consequence on real frequency axis, is that spectral functions such as quasiparticle density of states $N(\omega)$, has a ω/T scaling, which means characteristic frequencies of $N(\omega)$ scalings with T. In this section, we return to the case with smaller N, and we will see $\pm\pi T$ physics is still important especially when T is close to T_p. Actually we find a temperature scale T_{cross}, and when $T > T_{cross}$, the special role of $\pm\pi T$ is important in the gap equations and $N(\omega)$ displays the ω/T scaling, or equivalently a 'gap filling' behavior. While at smaller $T < T_{cross}$, contributions from all frequencies to the gap equation become comparable, like in the conventional BCS case. As a result, there is no 'gap filling' behavior in the spectral properties. Instead, the temperature evolution of $N(\omega)$ are pretty much the same as what we see from a conventional BCS superconductor, i.e. the 'gap closing behavior'. In this range, the gap in $N(\omega)$ narrows as T increase, and $N(\omega = 0)$ remains vanishingly small. The finding of crossover from 'gap closing' to 'gap filling' at $T \sim T_{cross}$ is the major topic in this section.

We used the same computational procedure as at large N and obtained $\Phi(\omega)$, $\tilde{\Sigma}(\omega)$, and $\Delta(\omega)$ along the real frequency axis. We present the results in Figure 3.10. We clearly see the crossover in the system behavior around $T_{cross}(N)$. At $T < T_{cross}(N)$, the behavior of the gap function is conventional in the sense that Re $\Delta(\omega = 0)$ is finite and Im $\Delta(\omega)$ emerges only above a finite frequency, approximately equal to $\Delta(0)$. The self-energy $\Sigma^*(\omega)$ at $\omega < \Delta_0$ is strongly reduced compared to its value in the normal state. At $T > T_{cross}(N)$, Im $\Delta(\omega) \propto \omega$ at small frequencies, and Re $\Delta(\omega) \propto \omega^2$, i.e., the systems displays the same gapless superconductivity as at $N > N_{cr}$. In the same T range the self-energy $\Sigma^*(\omega)$ almost recovers the normal state value (see Figure 3.10).

In Figure 3.11 we show the behavior of the DOS $N(\omega)$. We see a qualitative change of the behavior between $T > T_{cross}(N)$ and $T < T_{cross}(N)$. At smaller T, $N(\omega)$ is similar to that in a BCS superconductor: it has a sharp peak at $\omega \approx \Delta(0)$ and nearly vanishes below the peak frequency. At T increases, but remains smaller than $T_{cross}(N)$, the position of the maximum in $N(\omega)$ shifts to a smaller frequency because $\Delta(0)$ decreases,

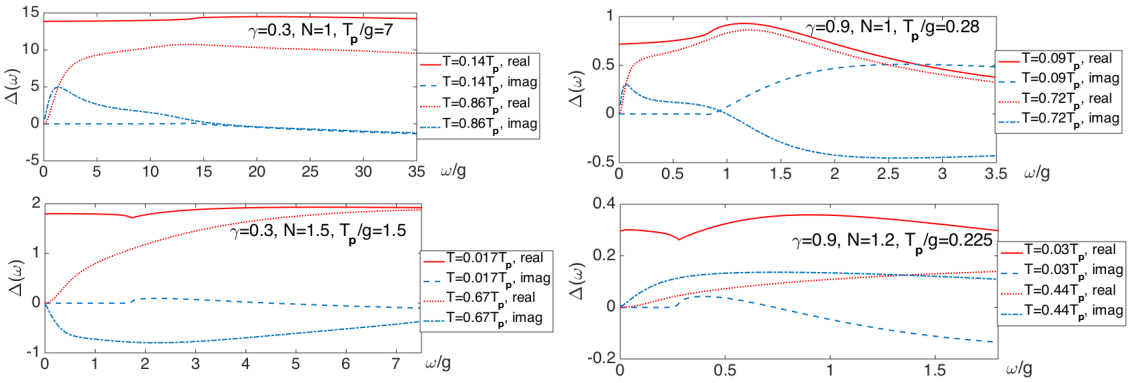

Figure 3.10: Real and imaginary parts of the gap $\Delta(\omega)$ as functions of ω for various T. The results are for $\gamma = 0.3$ and $\gamma = 0.9$, in both cases for $N < N_{cr}$. Red and blue lines are for $\Delta'(\omega)$ and $\Delta''(\omega)$, respectively. The data clearly show a crossover at $T \sim T_{cross}$ from BCS-like behavior at smaller T to the behavior similar to that at $N > N_{cr}$, at larger T.

i.e., the gap in the DOS "closes". However, at higher $T > T_{cross}(N)$, $N(\omega)$ becomes non-zero at all frequencies, and the position of its maximum shifts to a higher frequency as T increases, and remains finite at $T = T_p - 0$, i.e., the gap in the DOS "fills in". We plot the variation of the position of the maximum in $N(\omega)$ with T in the inserts of the plots of the DOS in Figure 3.11.

In Figure 3.12 we present our results for the spectral function $A(\omega)$. It shows a similar crossover around T_{cross}. We recall that the form of the spectral function depends on the strength of the thermal contribution to the self-energy (the P term in Eq. (3.43)). In the limit when the thermal contribution is large, $A(\omega)$ displays the same behavior as $N(\omega)$. In the opposite limit when P is smaller, $L(\omega)$ in Eq. (3.43) is close to one, and $A(\omega)$ at $T < T_{cross}(N)$ has two sharp peaks at frequencies close to $\pm\Delta(0)$, as expected in a BCS superconductor. At $T > T_{cross}(N)$, this behavior changes, and $A(\omega)$ has a single peak at $\omega = 0$. We show the variation of $A(\omega)$ between $T < T_{cross}(N)$ and $T > T_{cross}(N)$ in the right panels of Figure 3.12, for both smaller and larger P. In the left panels, we show the evolution of $A(\omega)$ with increasing P at $T < T_{croos}(N)$ and at $T > T_{cross}(N)$.

The transformation from "gap closing" behavior at small T to "gap filling" behavior

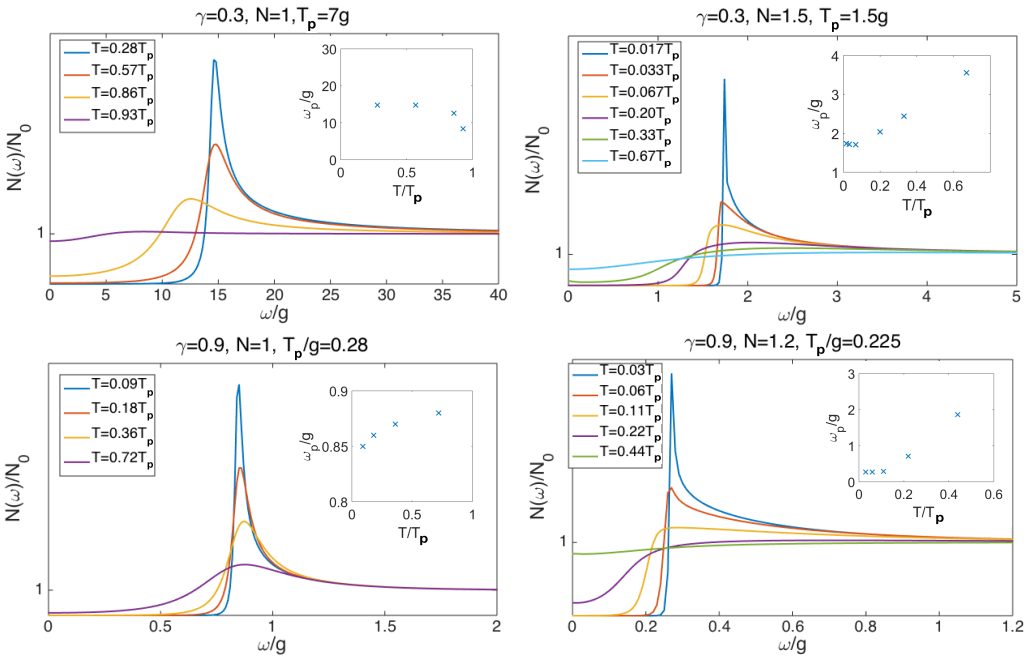

Figure 3.11: DOS $N(\omega)$ as a function of frequency for $\gamma = 0.3$ and $\gamma = 0.9$ and several $N < N_{cr}(\gamma)$. At low $T < T_{cross}$, the DOS has a sharp peak at $\omega = \Delta(T)$ and nearly vanishes below the peak. At higher $T > T_{cross}$ the DOS has qualitatively the same functional form as for large N, and the peak position shifts to a higher frequency with increasing temperature. The insets: the peak position ω_p as function of T/T_p. The crossover at T_{cross} is clearly visible.

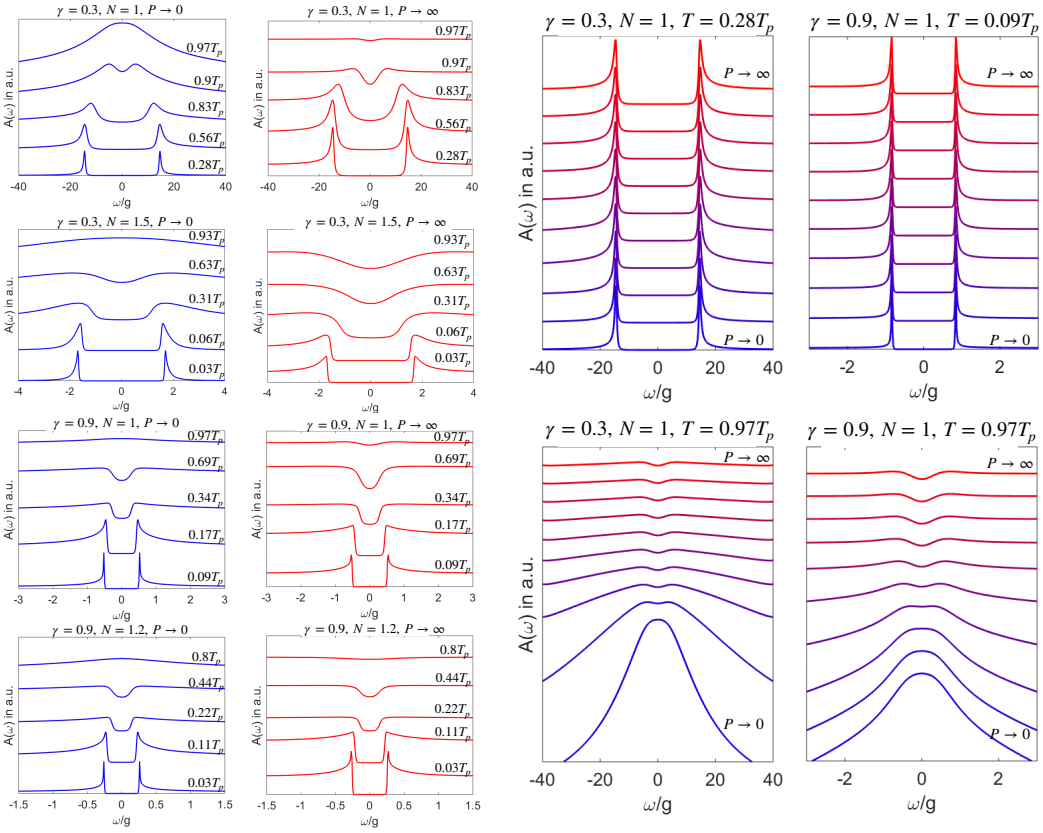

Figure 3.12: The spectral function $A(\omega)$ for $\gamma = 0.3$ and $\gamma = 0.9$ and several $N < N_{cr}$. Left panels: $A(\omega)$ for a set of temperatures at either strong or weak thermal contribution (the limits $P = \infty$ and $P = 0$ in Eq. (3.43)). At small $T < T_{cross}$ the spectral function has sharp peaks at $\omega = \pm\Delta(T)$, like in a BCS superconductor. At $T > T_{cross}$, $A(\omega)$ shows the same behavior as the DOS in Fig. 3.11, when the thermal contribution is strong, and develops a single peak at $\omega = 0$ when the thermal contribution is weak. Right panels – $A(\omega)$ at a fixed T for different strengths of the thermal contribution. Upper panels – $T < T_{cross}$, lower panels – $T > T_{cross}$.

at $T \sim T_p$ has been observed in high-T_c cuprates in ARPES measurements of the spectral function in the antinodal region [71, 72, 73, 74, 75, 76, 77, 78, 79, 80, 81, 82, 83, 84, 85, 86, 87, 88]. Symmetrized data of MDC ARPES measurements along a particular direction of $\mathbf{k}$ in the near-nodal region showed the transformation from two peaks at a finite frequency to a single peak at $\omega = 0$ (this is termed as the appearance of the Fermi arc). These results are consistent with our microscopic analysis for the DOS and also for the spectral function, if we assume that the thermal contribution is stronger in the antinodal region than in the near-nodal region. The strength of thermal contribution scales with the static bosonic susceptibility $V'(0)$. Static $V'(0)$ is larger for antinodal fermions in, e.g., spin-fluctuation models [17, 89, 31], where the interaction is peaked at momentum at or near (π, π).

To quantitatively apply our results to the cuprates, we need to extend our analysis to include the $d-$wave symmetry of the gap function. This is less relevant for the DOS and $A(\omega)$ in the antinodal region, as there the gap can be approximated by the constant, except for $N(\omega)$ at the smallest frequencies at $T < T_{cross}$, as the sharp peak in the DOS gets somewhat broadened after angular integration [90]. However, the $d-$wave angular dependence of the gap must be included into the analysis of the spectral function in the nodal region near Brillouin zone diagonals. To model the $d-$wave case, we added $\cos 2\theta$ factor to $\Phi(\omega)$ and solved the Eliashberg equations at a given T, and γ. We show the results in Figure 3.13, where we plot the spectral function along the Fermi surface. For simplicity, in this calculation we set P to be angle-independent. Making P smaller for nodal fermions and larger for antinodal ones will widen the range of the behavior seen near the nodes.

We see from Figure 3.13 that at $T < T_{cross}$, $A(\omega)$ has two weakly separated peaks in the nodal region and more strongly separated peaks in the antinodal region. This is the expected result for a d-wave superconductor at $T \ll T_c$. At high $T > T_{cross}$, the evolution of the spectral function is similar to the one in Figure 3.9. Namely, near the node $A(\omega)$ has a single maximum at $\omega = 0$, while in the antinodal region $A(\omega)$ has a dip at $\omega = 0$ and a shallow maximum, whose frequency scales with T. In between, the frequency dependence of $A(\omega)$ gradually evolves from a single peak at $\omega = 0$ to two maxima at finite ω and a dip at zero frequency.

This behavior reproduces the key features of ARPES data in Refs. [72, 73, 74, 75,

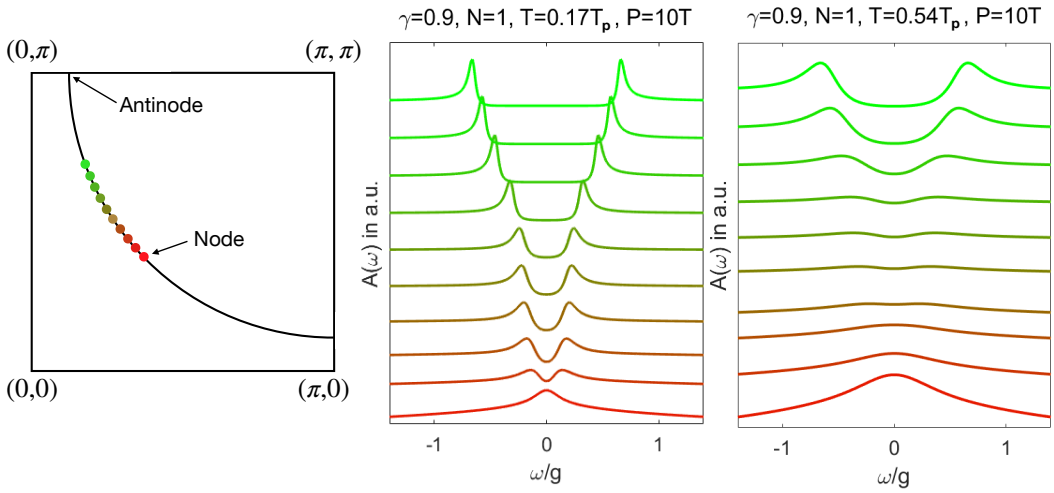

Figure 3.13: The spectral function $A(\omega)$ along the Fermi surface. At $T < T_{cross}$(the middle panel), in the nodal region (Red) $A(\omega)$ has two closely located peaks, which merge at the node. In the antinodal region (Green), the two peaks of $A(\omega)$ are well separated. At $T > T_{cross}$(the right panel) $A(\omega)$ has a maximum in the nodal region, which corresponds the Fermi arc, but in the antinodal region $A(\omega)$ shows two separate maxima. We set $\gamma = 0.9, N = 1$ and $P = 10T$.

78, 76, 77, 82, 83, 84, 85, 86, 87, 88].

Chapter 4

Multiple solutions of superconducting gap equation at a quantum critical point

In this chapter, we discuss in detail the fact that has been mentioned in Sec. 2.2.2: the existence of an infinite set of solutions to the gap equation right at a QCP. Each of these solution has its unique pairing temperature $T_{p,n}$ and gap structures $\Delta_n(\omega_m)$[or alternatively $\Phi_n(\omega_m)$], where $n = 0, 1, 2, ...$ is the solution index. In fact n also means the number of sign changes in $\Delta_n(\omega_m)$ for $\omega_m \in (0, \infty)$. We will show this is a unique feature of pairing at a QCP, and does not exist if the system is moved away from the QCP. We divide our discussion into two parts, i.e. $\gamma < 1$ and $\gamma > 1$, because there is a systematic divergence of $\Phi(\omega_m)$ and $\Sigma(\omega_m)$ at $T = 0$ for $\gamma > 1$ which requires additional care. Moreover, we will see the gap functions at $\gamma > 1$ different from that in $\gamma < 1$ in a fundamental way. As before we begin with the case of $\gamma < 1$, and then continue to $\gamma > 1$.

4.1 $\gamma < 1$

We already shown in Sec.2.3 that for $\gamma < 1$ there is a critical value N_{cr} at $T = 0$ separating non Fermi liquid normal state and superconducting state, and a low frequency

solution to the linearized gap equation has been found using series expansion. In fact, the exact solution of the linearized gap equation at $T = 0$ has been found in Ref. Normally if we think about gap equations at $T = 0$ like the BCS gap equation, we only have a finite Δ solution, i.e. solution to the nonlinear gap equation. The fact that a $\Delta \to 0$ solution to the linearized equation exist is a hint to the existence of multiple solutions to the gap equation. This is because the set of multiple solutions exist already at $T = 0$ and their overall magnitude decays exponentially with the solution number n. Once the overall magnitude of a solution is vanishingly small, there is no difference between a nonlinear equation and a linearized equation.

The existence of multiple solutions can be better seen from finite T analysis. We know from above that finite T analysis gives a pairing temperature T_p [see (3.2)] that bypasses N_{cr} obtained from zero T analysis. For convenience we now call this temperature $T_{p,0}$, where the additional subscript is to make difference from other solutions, and $n = 0$ is actually the one with the largest pairing temperature. If $T_{p,0}$ was the only solution of the linearized gap equation, the phase diagram within the Eliashberg theory would be as in Figure 4.1(a), i.e., there would be an isolated quantum-critical point (QCP) at $T = 0$ and $N = N_{cr}$, with no transition line coming out of it. We show below that this is not the case, and the actual phase diagram is the one in Figure 4.1(b), with infinite number of lines terminating at N_{cr}. For this to hold, the linearized gap equation must have an infinite set of onset temperatures $T_{p,n}$ for any $N < N_{cr}$. This is what we analyze next.

4.1.1 Multiple solutions at a QCP

The linearized gap equation which we will be analyzing is (2.29). It is written in terms of Matsubara frequencies. For convenience of discussion, we here reformulate it in terms of Matsubara number, and absorbing T using a new parameter $K = [\bar{g}/(2\pi T)]^{\gamma}$. We re-write the self-energy as

$$\Sigma(m) = \pi T K A(m) \mathrm{sgn}(2m + 1) \tag{4.1}$$

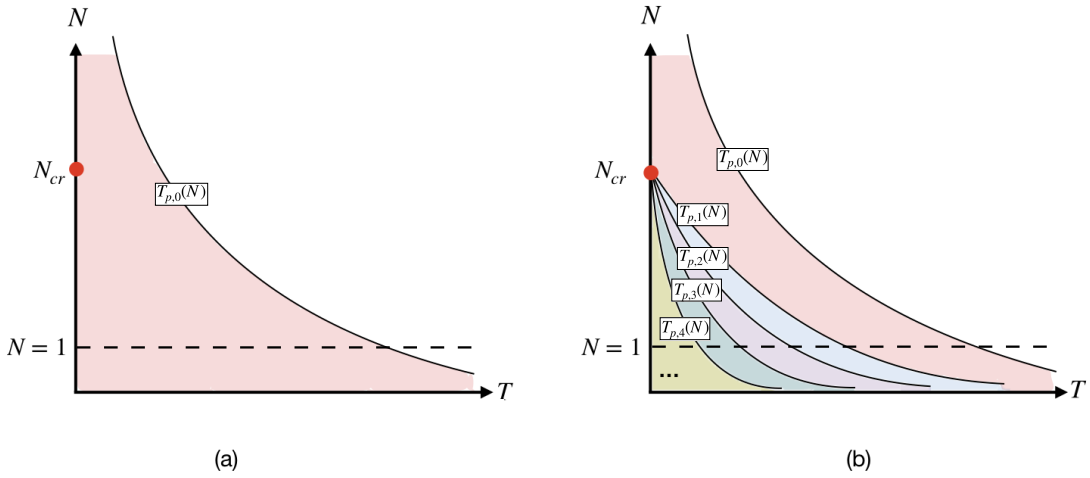

Figure 4.1: Two potential phase diagrams of the γ-model. (a) There exists only one onset temperature $T_{p,0}$ for any given N, like in BCS theory. In this case, N_{cr} is an isolated $T = 0$ QCP, with no transition line attached to it. (b) There exists an infinite set of $T_{p,n}$, which all terminate at $N = N_{cr}$. In this case, a QCP at $N = N_{cr}$ is critical point of an infinite order. We show that the correct phase diagram is the one in the panel (b).

where

$$\begin{aligned} A(m) &= 2\sum_{1}^{m}\frac{1}{n^{\gamma}}, \quad m>0 \\ A(m) &= A(-m-1), \quad m<-1 \\ A(0) &= A(-1)=0 \end{aligned} \tag{4.2}$$

The equations for Φ become,

$$(N-K)\Phi(0)=\sum_{n=1}^{\infty}\frac{\Phi(n)}{A(n)+\frac{2n+1}{K}}\left(\frac{1}{n^{\gamma}}+\frac{1}{(n+1)^{\gamma}}\right) \tag{4.3}$$

and

$$\begin{aligned} N\Phi(m>0)=&\sum_{n=1,n\neq m}^{\infty}\frac{\Phi(n)}{A(n)+\frac{2n+1}{K}}\frac{1}{|n-m|^{\gamma}}+\sum_{n=1}^{\infty}\frac{\Phi(n)}{A(n)+\frac{2n+1}{K}}\frac{1}{(n+m+1)^{\gamma}} \\ &+\frac{K}{N-K}\sum_{n=1}^{\infty}\frac{\Phi(n)}{A(n)+\frac{2n+1}{K}}\left(\frac{1}{n^{\gamma}}+\frac{1}{(n+1)^{\gamma}}\right)\left(\frac{1}{m^{\gamma}}+\frac{1}{(m+1)^{\gamma}}\right) \end{aligned} \tag{4.4}$$

A quick inspection of Eq. (4.4) shows that at low T, when $K \gg 1$, there are two regions of N, in which the solution with $\Phi(m) \neq 0$ may appear: a) $N \approx K$, such that $N-K=$ const, and b) $N=O(1)$, such that $K \gg N$. The first case is how we obtain (3.2) where the first Matsubara rule applies. Here we are interested in the latter case.

Our reasoning to search for additional solutions of the gap equation in the region $N=O(1)$ comes from the $T=0$ analysis in Ref[91]. The key result of that Ref[91] is that for any $N<N_{cr}$ (which is $O(1)$ for a generic $\gamma<1$), there exists an infinite, discrete set of solutions of the non-linear gap equation, $\Delta_n(\omega_m)$. If system properties evolve smoothly between $T=0$ and $T>0$, each gap function evolves with T and has to vanish at some finite $T_{p,n}$. By this logic, there must be an infinite set of $T_{p,n}$ for any given $N<N_{cr}$. Because all $\Delta_n(\omega_m)$ at $T=0$ vanish at $N=N_{cr}$, all $T_{p,n}(N)$ with finite n must approach 0 at $N=N_{cr}$, as in Figure 4.1(b).

We first verify the very assumption that the system behavior evolves smoothly between $T=0$ and $T>0$. This is not a'priori guaranteed, as at $T=0$ the infinite set of solutions for all $N<N_{cr}$ emerges due to a fine balance between the tendencies towards

NFL and pairing. A finite T perturbs this balance, and it is possible in principle that an infinite set of solutions exists only at $T = 0$, while at a finite T only a single solution with a finite Δ survives.

To address this issue, we recall that the origin for the appearance of the set of $\Delta_n(\omega_m)$ at $T = 0$ is the existence of the solution of the linearized gap equation for all $N < N_{cr}$ rather than only for $N = N_{cr}$. In Ref[91] the exact solution of the linearized gap equation is obtained for all $N < N_{cr}$ and $0 < \gamma < 1$. At small $\omega_m \ll \bar{g}$, the exact solution reduces to

$$\Delta(\omega_m) = E|\omega_m|^{\gamma/2} \cos\left(\beta_N \log \frac{|\omega_m|}{\bar{g}} + \phi_N\right) \tag{4.5}$$

where E is an infinitesimally small overall magnitude, $\phi_N = O(1)$ is the phase factor, and β_N is the real solution of $\epsilon_{\beta_N} = N$, where

$$\epsilon_\beta = \frac{1-\gamma}{2} \frac{|\Gamma(\gamma/2(1+2i\beta))|^2}{\Gamma(\gamma)} \left(1 + \frac{\cosh(\pi\gamma\beta)}{\cos(\pi\gamma/2)}\right) \tag{4.6}$$

A solution of this equation with a real $\beta = \pm\beta_N$ exists for $N < N_{cr}$, where we remind N_{cr} is given by (2.44). One can verify that $N_{cr} > 1$ for $0 < \gamma < 1$. At $\gamma \ll 1$, $N_{cr} \approx 4/\gamma$. At $\gamma \to 1$, $N_{cr} \to 1$.

It is instructive to interpret $\epsilon_{\beta_N} = N$ as the dispersion relation and identify β_N with the effective momentum and N with the effective energy. Then one can define the DoE as

$$\nu(N) \propto \left.\frac{d\beta}{d\epsilon_\beta}\right|_{\beta=\beta_N}. \tag{4.7}$$

We plot this function in Figure 5.8. As expected, it is non-zero for all $N < N_{cr}$. It is singular near $N = 0$, where $\nu(N) \propto (1/N)^{(2-\gamma)/(1-\gamma)}$ and near N_{cr}, where $\nu(N) \propto 1/\sqrt{N_{cr} - N}$. This last singularity, however, affects $\nu(N)$ only in the immediate vicinity of $N = N_{cr}$, as one can see from Figure 5.8. The DoE in (4.7) is defined up to an overall factor. In Figure 5.8 we plot $\nu(N)$ without normalizing it.

Now, for a smooth evolution of system properties between $T = 0$ and $T > 0$ the same $\nu(N)$ must emerge if we solve the linearized gap equation by approaching the $T = 0$ limit from a finite T. To verify whether this is the case, we keep $N = O(1)$ and set $K \propto 1/T^\gamma$ to infinity in (4.4).

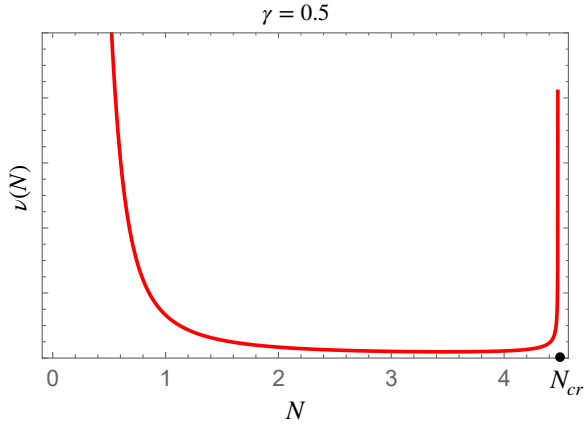

Figure 4.2: The DoE $\nu(N)$ (in arbitrary units) at $T = 0$, for $\gamma = 0.5$. The DoE is non-zero for all $N < N_{cr}$. It has a strong singularity near $N = 0$ and a weaker singularity at $N = N_{cr}$.

At large $n, m \gg 1$, the equation for the pairing vertex can be approximated by an integral equation

$$\Phi_m = \frac{1-\gamma}{2N} \int_0^\infty dn \frac{\Phi_n}{n^{1-\gamma}} \left(\frac{1}{|n-m|^\gamma} + \frac{1}{(n+m)^\gamma} \right) \tag{4.8}$$

This equation has been analyzed in Ref[91] and in earlier works [16, 17, 23, 92, 93]. The solution is

$$\Phi_{m>0} = \frac{E}{m^{\gamma/2}} \cos\left(\beta_N \log m + \phi\right) \tag{4.9}$$

where β_N is the same as in (4.5) and E is an infinitesimally small overall factor. For these m, $\Sigma_m \propto m^{1-\gamma}$, hence

$$\Delta_{m>0} = E m^{\gamma/2} \cos\left(\beta_N \log m + \phi\right) \tag{4.10}$$

The functional form of Δ_m is the same as for the $T = 0$ solution, but at this stage ϕ is a free parameter. To be the solution of the gap equation for all m, this Δ_m (or Φ_m) has to match with the solution at small m, when the discreteness of Matsubara numbers becomes relevant. If this can be achieved by fixing the value of ϕ, then $\nu(N)$ at $T \to 0$ is the same as at $T = 0$.

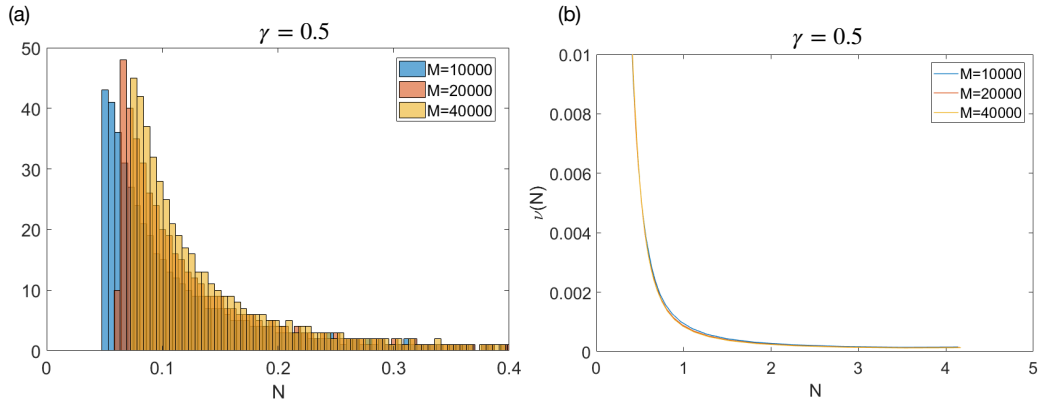

Figure 4.3: Numerical results for the DoE at $T \to 0$. (a) The histogram of the eigenvalues for different number of sampled Matsubara points M. As M increases, more eigenvalues are shifted towards larger N, and the number of eigenvalues in any given interval of N increases. (b) the "smoothened" DoE for different M, normalized such that $\nu(N = 0.5)$ is kept fixed. As M increases, $\nu(N)$ does not change much. The curves are similar to that in Figure 5.8 except for the narrow peak near N_{cr}, as a much larger M is required to get enough eigenvalues near N_{cr}.

This is similar to the $T = 0$ case, where the oscillating $\Delta(\omega_m)$ from (4.5) has to match with the non-oscillating solution $\Delta(\omega_m) \propto 1/|\omega_m|^\gamma$ for $|\omega_m| \gg \bar{g}$. For $T = 0$, the exact solution and the approximate, but highly accurate, analytical solution show that this is the case. Namely, for some particular $\phi = \phi_N$, the exact solution has the form of Eq. (4.5) for $|\omega_m| \ll \bar{g}$ and decays as $1/|\omega_m|^\gamma$ for $|\omega_m| \gg \bar{g}$. For $T \to 0$, we solve the gap equation numerically. We present the results for the DoE in Figure 4.3. While for any finite number M of Matsubara points in numerical calculations the DoE consists of a discrete set of points, we see from the histogram of the eigenvalues in panel (a) that at larger M, more eigenvalues move to larger N and the number of eigenvalues in any fixed interval of N increases. The "smoothened" $\nu(N)$ in panel (b) weakly depends on M and is quite similar to the DoE at $T = 0$ in Figure 5.8. This strongly indicates that Eq. (4.4) has a solution for any $N < N_{cr}$, like at $T = 0$, i.e. the system evolves continuously between $T = 0$ and $T \to 0$.

Next consider the case when T is small, but finite. It is natural to expect that each Δ_n smoothly evolves with T and ends at a finite $T_{p,n}$. We then expect that Eq. (4.4) should have an infinite set of solutions at large but finite K. A qualitative argument

for the existence of the infinite set of $T_{p,n}$ is the following:

- at $m \gg 1$, the difference between summation over Matsubara numbers n and integration is negligible. Hence, the solution of the gap equation, expressed in terms of $\omega_m \approx 2\pi m T$, should be the same as the exact solution at $T = 0$, Eq. (4.5). In terms of m we have

$$\Delta_m = E m^{\gamma/2} \cos\left(\beta_N \log m - \beta_N \log K^{1/\gamma} + \phi_N\right) \tag{4.11}$$

  The phase ϕ_N is fixed by the requirement that $\Delta_m \propto 1/|m|^\gamma$ for $m > K^{1/\gamma}$, but there is another phase factor $-\beta_N \log K^{1/\gamma}$, which depends on K.

- From the analysis at $T \to 0$ we know that the gap equation has solutions for $N < N_{cr}$. The form of a solution is the same as in (4.11), $\Delta_m = E m^{\gamma/2} \cos\left(\beta_N \log m + \tilde{\phi}_N\right)$, with some particular $\tilde{\phi}_N$ which depends on N (for a fixed γ).

- We can match the two forms of Δ_m by relating the phases:

$$\tilde{\phi}_N = \phi_N - \beta_N \log K^{1/\gamma} + \pi n, \tag{4.12}$$

  where n is integer. Solving (4.12), we obtain the set of K_n, for which this identity holds. Note that the additional factor is πn, not $2\pi n$, because we can independently flip the sign of Δ_m at $T \to 0$ keeping Δ_m at $T = 0$ intact.

Solving Eq. (4.12) for the critical temperature, we obtain

$$T_{p,n} \sim \bar{g} e^{-An}, \quad A = \frac{\pi}{\beta_N \gamma} \tag{4.13}$$

This is consistent with the result in Paper I that at $T = 0$, $\Delta_n(\omega_m = 0) \sim \bar{g} e^{-An}$. As N increases towards N_{cr}, $\beta_N \propto (N_{cr} - N)^{1/2}$ gets smaller, and all $T_{p,n}$ with $n > 0$ become exponentially small in $N_{cr} - N$:

$$T_{p,n} \sim \bar{g} e^{-bn/(N_{cr}-N)^{1/2}}, \tag{4.14}$$

where $b = O(1)$. Eq. (4.14) shows that all $T_{p,n}(N)$ terminate simultaneously at $N = N_{cr}$.

A remark is in order here. Eq. (4.13) and the $T = 0$ result for Δ_n are based on the assumption that the solution of the linearized gap equation oscillates up to $\omega_m \sim \bar{g}$ and decays as $1/|\omega_m|^\gamma$ at larger ω_m. This holds for most of $\gamma < 1$, but for very small γ, oscillations extend to larger scale. In this case, Eq. (4.12) has to be modified.

In Figure 4.4 we show the numerical results for $T_{p,n}$ for $n = 1 - 4$, along with the result for $T_{p,0}$ from Eq. (3.2). We set representative γ to be $\gamma = 0.3$ and $\gamma = 0.5$. We verified that $T_{p,0}$ behaves as $1/N^{1/\gamma}$, as expected. At other $T_{p,n}$ lines exponentially approach zero as N tends to N_{cr}, and the slope becomes larger as n increases. To obtain this behavior we used a "hybrid frequency scale" method, which allowed us to numerically cover an exponentially large frequency range and reach very low T, while keeping track of the Matsubara summation at the lowest frequencies. This is achieved by adopting a frequency mesh that overlaps with Matsubara frequencies $\omega_m = \pi T, 3\pi T, \cdots$ at small values and crosses over to a logarithmical spacing beyond a certain scale, above which the discreteness of the Matsubara sum becomes unimportant. It was also used in Ref[94] in addressing the interplay between the first-Matsubara physics and thermal fluctuations.

In Figure 4.5 we plot $T_{p,n}$ with n up to 17 for particular $N = 1$. We clearly see that $T_{p,n}$ scale as e^{-An}, as in Eq. (4.13). We extracted $\beta_{N=1}$ from the fit to the exponential form and obtained $\beta_{N=1} = 1.62$ for $\gamma = 0.3$ $\beta_{N=1} = 1.12$ for $\gamma = 0.5$. These values are quite close to the exact values, extracted from Eq. (4.6): $\beta_{N=1} = 1.71$ for $\gamma = 0.3$ $\beta_{N=1} = 1.27$ for $\gamma = 0.5$. The small difference comes from the numerical error of the hybrid frequency scale, which effectively shifts N up by roughly 0.07 for $\gamma = 0.3$ and 0.13 for $\gamma = 0.5$.

Another result of the $T = 0$ analysis is that the solutions of the non-linear gap equation with different n are topologically distinct — the gap function $\Delta_n(\omega_m)$ changes sign n times as a function of Matsubara frequency. Because we expect that $\Delta_n(m)$, which develops below $T_{p,n}$, becomes $\Delta_n(\omega_m)$ at $T = 0$, it should change sign n times as a function of Matsubara number m. The same should be true for the pairing vertex $\Phi_n(m)$. In Figure 4.6 we show $\Phi_n(m)$ for a few smallest n and for $n = 16, 17$. We see that $\Phi_n(m)$ indeed changes sign n times. At large n, $\Phi_n(m)$ oscillates at large m as a function of $\log m$, with the amplitude proportional to $1/|m|^{\gamma/2}$. This is exactly the same behavior as in Eq. (4.11), given that $\Delta_n(m) \sim \Phi_n(m)|m|^\gamma$. For comparison, in

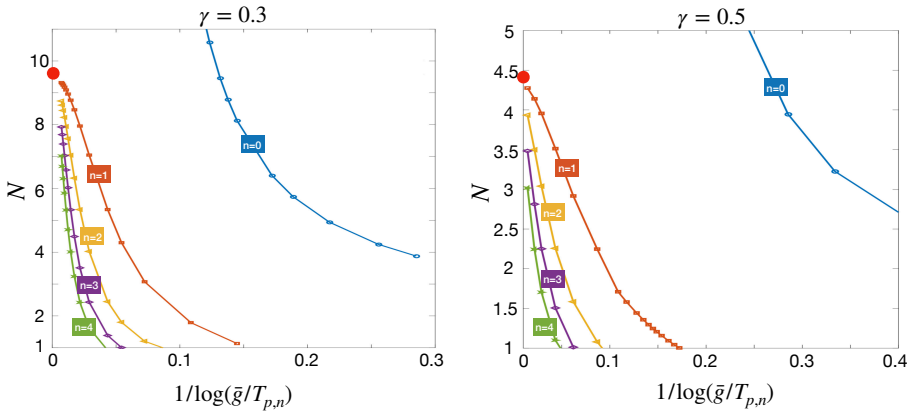

Figure 4.4: The numerical solution of the gap equation for small but finite T for $\gamma = 0.3$ and $\gamma = 0.5$. The temperatures $T_{p,n}$ are the onset temperatures for the pairing in different topological sectors (the corresponding eigenfunctions change sign n times as functions of discrete Matsubara frequency). The highest $T_{p,0} \propto 1/N^{1/\gamma}$ terminates at $N = \infty$. Analytical reasoning shows that all other $T_{p,n}$ vanish at $N = N_{cr}$ (big red dot). Numerical results show that $T_{p,n}$ with finite $n > 0$ indeed approach zero at $N = N_{cr}$.

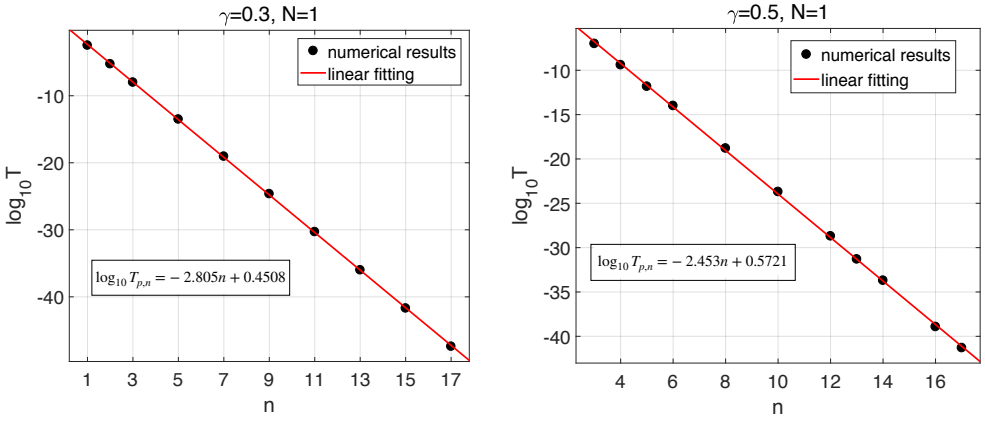

Figure 4.5: $T_{p,n}$ as functions of n for $N = 1$ and $\gamma = 0.3$ and 0.5. The black dots are the data, obtained by varying temperature to find the eigenvalue $N = 1$, and the red lines are linear fitting of $\log T_{p,n}$, with fitting parameters given in the boxes. We clearly see that $T_{p,n}$ scales as e^{-An}, as we obtained analytically.

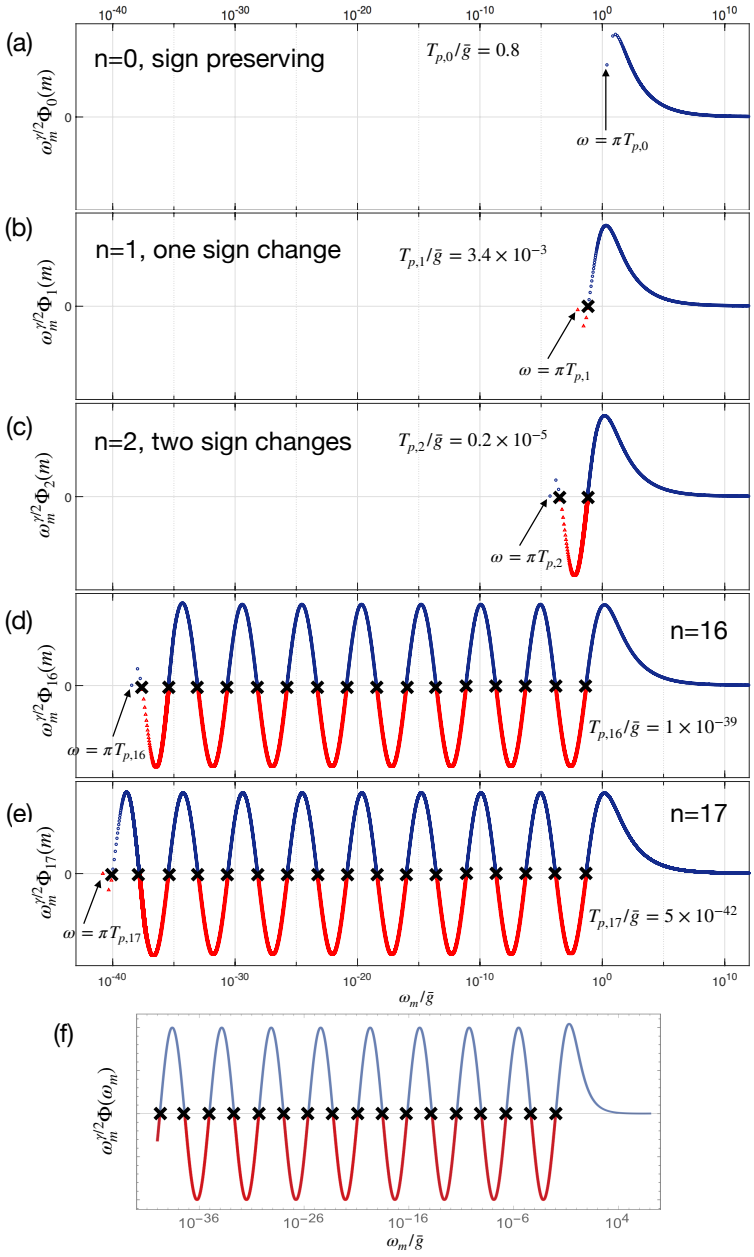

Figure 4.6: Panels (a)-(e) – The pairing vertex, $\Phi_n(m)$ at $T = T_{p,n}$, as a function of the Matsubara frequency $\omega_m = \pi T(2m+1)$ for representative parameters $\gamma = 0.5$ and $N = 1$. We show $\Phi_n(m)$ for $n = 0, 1, 2, 16, 17$. The corresponding $T_{p,n}$ are shown in the figures. For $n = 0$, $\Phi_0(m) \propto (1|m|^\gamma + 1/|m+1|^\gamma)$ does not change sign. Other $\Phi_n(m)$ change sign n times, and $T_{p,n} \propto e^{-An}$. The results for $n = 16, 17$ show that $\Phi_n(m)$ oscillates at $m \gg 1$ as a function of $\log m$, with the amplitude proportional to $1/|m|^{\gamma/2}$. Panel(f) - $\Phi(\omega_m)$ from the exact solution of the linearized equation for the pairing vertex at $T = 0$. The positions of zeros of $\Phi_n(m)$ are marked by crosses. The smallest frequency $\omega_0 = \pi T_{p,n}$ (different for different n) are shown by arrows.

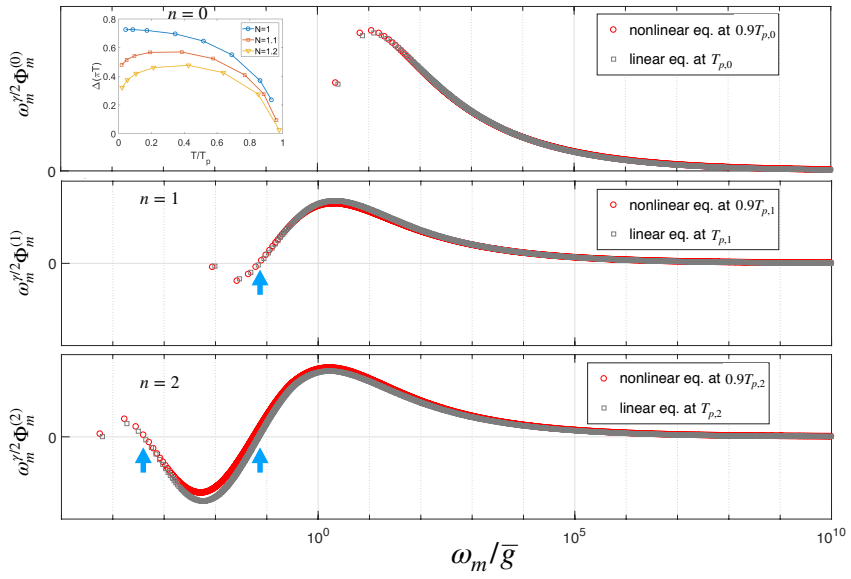

Figure 4.7: The solution of the non-linear equation for the pairing vertex for $T = 0.9T_{p,n}$, along with the solution at $T = T_{p,n} - 0$. The three panels are the solutions for $n = 0, 1, 2$. The number of sign changes remains the same at $T_{p,n}$ and $0.9T_{p,n}$, as indicated by the blue arrows, and the frequencies, at which $\Phi_n(m)$ changes sign, do not shift with T.

the last panel of Figure 4.6 we plot the exact $\Phi(\omega_m)$ at $T = 0$. We see that at $T = T_{p,n}$, the form of $\Phi_n(m)$ for $m \gg 1$ is quite similar to that at $T = 0$.

That $\Phi_n(m)$ has to change the sign at least once follows from the relation between $\Phi(0)$ and $\Phi(m > 0)$, Eq. (4.3). For $K \gg N$:

$$\Phi(0) \approx -\frac{1}{K} \sum_{m=1}^{\infty} \frac{\Phi(m)}{A(m) + \frac{2m+1}{K}} \left(\frac{1}{m^\gamma} + \frac{1}{(m+1)^\gamma} \right) \tag{4.15}$$

This relation shows that even if $\Phi(m)$ has the same sign for all $m > 0$, $\Phi(0)$ would still be of the opposite sign. This is consistent with Figure 4.6, which shows that $\Phi_1(m)$ changes sign at $m = O(1)$ and keeps the same sign at larger m. The same holds for larger n - the first sign change occurs at $m = O(1)$, i.e., at $\omega_m \sim T_{p,n}$. In Figure 4.7 we show the results for $\Phi_n(m)$ for $n = 0, 1, 2$ obtained by solving the non-linear equation for the pairing vertex for $T \leq T_{p,n}$. We expanded to order Φ_m^3 and used the solution at $T = T_{p,n}$ as the source. We see that the number of sign changes remains the same, and the frequencies, at which the sign of $\Phi_n(m)$ changes, remain essentially independent on T. This is consistent with the result in Paper I that at $T = 0$, $\Delta_n(\omega_m)$ changes sign n times at finite ω_m.

4.1.2 Away from a QCP

We now analyze how $T_{p,n}$ and the DoE at $T \to 0$ change away from a QCP, when the pairing boson acquires a finite mass, M_b. We argue that a finite M_b introduces qualitative changes in the system behavior, i.e., there is a qualitative difference between the structure of the DoE at a finite M_b and at $M_b = 0$. Specifically, we argue that a finite M_b (i) makes the number of $T_{p,n}$ for a given N to be finite, and (ii) splits $T_{p,n}$ at the smallest T such that different $T_{p,n}$ terminate at different $N_{cr,n}$, all are smaller than N_{cr}. The temperature $T_{p,0}$ is still non-zero for any N, but at a finite M_b it acquires a conventional form $T_{p,0} \sim M_b e^{-1/\lambda}$, where $\lambda \propto 1/N$ (see Eq. (4.19) below).

We begin with the analytical analysis. We model the bosonic propagator away from a QCP by

$$V(\Omega_m) = \frac{\bar{g}^\gamma}{\left(\Omega_m^2 + M_b^2\right)^{\gamma/2}} \tag{4.16}$$

The linearized gap equation becomes

$$\Delta(\omega_m) = \frac{\bar{g}^\gamma}{N}\pi T \sum_{m' \neq m} \frac{\Delta(\omega'_m) - N\Delta(\omega_m)\frac{\omega'_m}{\omega_m}}{|\omega'_m|} \frac{1}{\left(|\omega_m - \omega'_m|^2 + M_b^2\right)^{\gamma/2}}. \tag{4.17}$$

Consider first the limit $T \to 0$. Replacing the summation over frequency by integration with T as the lower limit, we immediately find that at a finite M_b there is a simple difference between sign-preserving and sign-changing solutions for $\Delta(\omega_m)$. For the sign-preserving solution, $\Delta(0)$ is finite. Taking properly the limit $\omega_m \to 0$, we obtain $T_{p,0}$ from self-consistent equation on $\Delta(0)$:

$$\left(1 + \left(\frac{\bar{g}}{M_b}\right)^\gamma\right) = \frac{1}{N}\left(\frac{\bar{g}}{M_b}\right)^\gamma \log\frac{M_b}{T_{p,0}}. \tag{4.18}$$

The second term in the l.h.s. is the contribution from the self-energy, which away from a QCP has a Fermi liquid form at frequencies below M_b. Solving for $T_{p,0}$, we find

$$T_{p,0} \sim M_b e^{-N(1+\lambda)/\lambda}, \quad \lambda = 1 + \left(\frac{\bar{g}}{M_b}\right)^\gamma \tag{4.19}$$

We see that $T_{p,0}$ is still non-zero for any N, however its dependence on N is exponential. This is similar to the case of a BCS superconductor, where T_c is finite for arbitrary weak coupling, albeit exponentially small. For $N = 1$, Eq. (4.19) has the same structure as McMillan formula $T_c \sim \omega_D e^{-(1+\lambda)/\lambda}$ (Ref. [**?**]). In qualitative distinction to the behavior at a QCP, now the existence of a non-zero $T_{p,0}$ for arbitrary large N is due to ordinary Cooper logarithm in a Fermi liquid rather than to special properties of fermions with $\omega_m = \pm\pi T$ in a NFL regime. As a consequence, $\Delta_0(\omega_m)$, emerging below $T_{p,0}$, does not vanish at $T = 0$, i.e, at any N the ground state is a superconductor. In this respect, there is no critical N_{cr}, separating normal and superconducting states at $T = 0$.

For solutions with $n > 0$, $\Delta_n(\omega_m)$ must vanish at $\omega = 0$ because there is just a single solution with a finite $\Delta(0)$. This sets the condition

$$\Delta(0)\left(1 + \left(\frac{\bar{g}}{M_b}\right)^\gamma\right) = \frac{\bar{g}^\gamma}{N}\int_0^\infty \frac{\Delta_n(\omega'_m)}{\omega'_m} \frac{d\omega'_m}{\left((\omega'_m)^2 + M_b^2\right)^{\gamma/2}} = 0 \tag{4.20}$$

We show below that $\Delta_n(\omega'_m)$ scale as $(\omega'_m)^2$ at small ω'_m, hence the integral in (4.20)

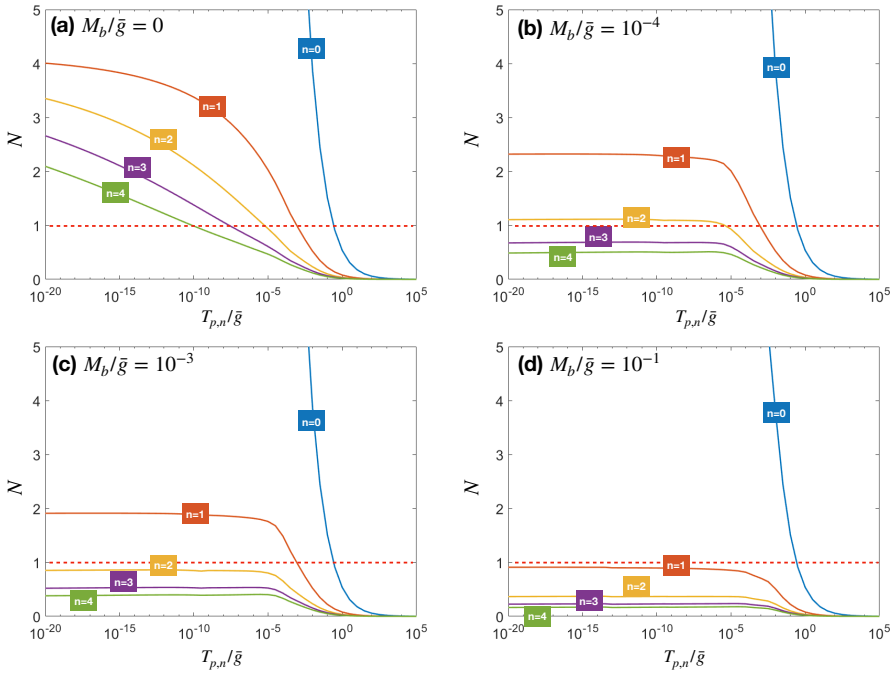

Figure 4.8: The solutions of the linearized gap equation for a finite boson mass M_b. Different panels are for different $M_b/\bar{g}$, shown in the figures. We set $\gamma = 0.5$. The critical temperatures $T_{p,n}$ now terminate at different $N_{cr,n}$. This is qualitatively different from the behavior at a QCP, where all $T_{p,n}$ with $n > 0$ terminate at the same $N = N_{cr}$.

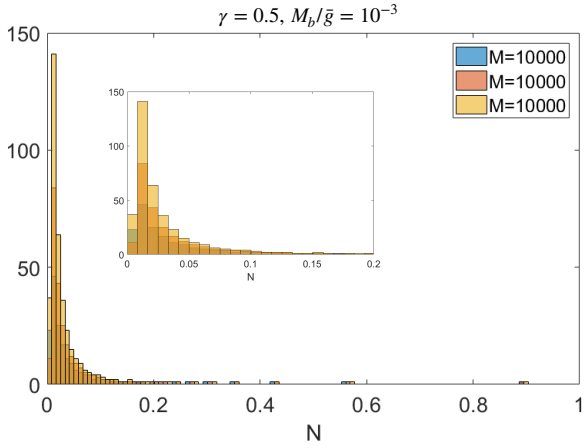

Figure 4.9: The histogram of the DoE for a finite boson mass $M_b/\bar{g} = 10^{-3}$ and $\gamma = 0.5$. We see that the histogram is heavily shifted towards $N = 0$ because now there is a finite number of points in a given interval around a particular N even when the total number of sampling Matsubara points M tends to infinity. This is qualitatively different from the case $M_b = 0$ in Figure 4.3, where the number of points in a given interval around any $N < N_{cr}$ scales with M.

is infra-red convergent. Eq. (4.20) then implies that $\Delta_n(\omega_m)$ must change sign n times at some finite ω'_m. This is qualitatively different from the situation at a QCP. There, all $T_{p,n}$ with finite n terminate at $T = 0$ at $N = N_{cr}$. The gap function at $N = N_{cr}$ vanishes at $\omega_m = 0$, yet it remains sign-preserving (see Paper I for details). This holds at a QCP because $\Delta(\omega'_m) \propto |\omega'_m|^{\gamma/2}$, in which case $\Delta(\omega'_m)/\omega'_m$ is singular at $\omega_m \to 0$, and one cannot just set $\omega_m = 0$ in the gap equation, as it is done in Eq. (4.20). At small M_b, $T_{p,n}$ approaches zero at N only slightly below N_{cr}, and $\Delta_n(\omega'_m)$ must recover the gap function at a QCP at $N = N_{cr}$ at frequencies above some scale, which vanishes when $M_b \to 0$. Because $\Delta(\omega_m)$ at $N = N_{cr}$ is sign-preserving, the n sign changes of $\Delta_n(\omega_m)$ have to occur below this scale.

We now expand in ω_m in the r.h.s. of the gap equation (4.17) for $\Delta_{n>0}(\omega_m)$. Expanding and using (4.20) to cancel out the leading term, we obtain $\Delta_n(\omega_m) = A_n(\omega_n/M_b)^2$, where A_n is given by

$$A_n = \left(\frac{\bar{g}}{M_b}\right)^{\gamma} \frac{\gamma}{N} \int_0^{\infty} dx \frac{\Delta_n(x)}{x} \frac{x^2(1+\gamma) - 1}{(x^2+1)^{2+\gamma/2}} \tag{4.21}$$

where $x = \omega_m/M_b$. The integral in (4.21) converges at $x = O(1)$, hence by order of magnitude $A_n \sim \bar{g}^\gamma/(M_b^{2+\gamma}N)$ with $n-$dependent prefactor. For an estimate, we assume that at large n the integral is determined by $x_n \sim 1/n$, before oscillations begin, and that $\Delta_n(x < x_n) \approx A_n x^2$. Substituting into (4.21), we obtain that the solution is possible only for a given $N \sim 1/n^2$

$$N\gamma = -\frac{x_n^2}{2}\left(\frac{\bar{g}}{M_b}\right)^\gamma \int_0^{x_n} dx x \frac{x^2(1+\gamma)-1}{(x^2+1)^{2+\gamma/2}} \tag{4.22}$$

The outcome of this analysis is that at a non-zero M_b the solutions of the linearized gap equation for different n exist at different N, i.e., each $T_{p,n}$ terminates at its own $N_{cr,n}$.

In Figure 4.8 we show the results of the numerical solution of the gap equation for a finite M_b. We see that $T_{p,n}$ indeed terminate at different N. We verified that $T_{p,0}$ is exponential in N, like in Eq. (4.19). The number of solutions, for which $T_{p,n}$ crosses $N = 1$, is finite for any non-zero M_b. It decreases one by one with increasing M_b and vanishes once M_b exceeds some critical value. At larger M_b, there is only one onset temperature $T_{p,0}$ for the physical case $N = 1$, and the behavior below $T_{p,0}$ is qualitatively the same as in BCS theory.

The same behavior shows up in the analysis of the DoE at $T \to 0$. Because there is only a finite number of termination points of $T_{p,n}$ in any finite interval of N, the normalized DoE $\nu(N)$ vanishes for all $N \neq 0$ in the formal limit $M \to \infty$, where M is the number of Matsubara points, probed in a numerical calculation. Because termination lines cluster around $N = 0$, and the total $\int dN\nu(N) = 1$, the DoE becomes $\nu(N) = \delta(N)$ in this limit. In practice, this implies that the DoE will decrease for any finite N when M increases, and the histogram of $\nu(N)$ will shift with increasing M towards $N = 0$. In Figure 4.9 we show the numerical results for $\nu(N)$. We see precisely this behavior. Note also that the largest $N_{cr,1}$ shifts down from N_{cr} as M_b increases.

4.2 $\gamma > 1$

The infinite set of solutions $\Delta_n(\omega_m)$ also exist for $\gamma > 1$. In this case, we only focus on $N = 1$, i.e. the original model without extension, where the gap equation is regular at $T = 0$. In this case, one can follow similar procedure to obtain an exact solution to the

linearized gap equation at $T = 0$, which oscillates in logarithmic scale up to $\omega_m \sim O(\bar{g})$ and then starts decaying as $1/|\omega_m|^\gamma$. The solutions $\Delta_n(\omega_m)$ also changes sign n times for $\omega_m \in (0, \infty)$, and $n = \infty$ corresponds to the solution at $T = 0$. In this section we will see, the gap function for $\gamma > 1$ are different from the ones for $\gamma < 1$ in the sense that there are additional dynamical vortices on the complex frequency plane. The function $\Delta_n(\omega_m)$ naturally has n vortices on Matsubara axis, in addition to these, there are also vertices on the complex frequency plane for $\gamma > 1$. The number of these additional vertices increases as γ increases, and becomes infinite once $\gamma \to 2$. Interestingly, we find the number of these additional vortices, depends only on γ. Namely, for each given γ, different solutions labeled by n, have the same number of additional vortices. As a consequence of these dynamical vortices, along the real frequency axis, the phase of the gap function, winds up multiples times of 2π. The case $\gamma = 2$ is very special, not only because the number of vortices becomes infinite, but also due to the fact that all the gap structures $\Delta_n(\omega_m)$ becomes identical. Therefore, the condensation energy for all the solutions becomes the same, which opens a phase fluctuation channel to kill the superconducting long range coherence. Below we discuss these interesting features in detail. And as we explained, we will only discuss $N = 1$ case.

4.2.1 Solutions on Matsubara frequency axis

The solutions on Matsubara axis can be easily obtained, but before discussing the solutions, we remind that a solution $\Delta_n(\omega_m)$ changes sign n times for $\omega_m > 0$. If we view ω_m as a continuous variable, then there are n nodal points along Matsubara frequency axis, where $\Delta_n(\omega_m)$ vanishes. These points are also vortices if we look at the complex phase of Δ_n on the complex frequency plane.

For definiteness, let's compare the behavior of sign-preserving $\Delta_0(\omega_m)$ and of $\Delta_1(\omega_m)$, and $\Delta_2(\omega_m)$, which change sign once and twice between $\omega_m = 0$ and $\omega_m = \infty$, respectively. We show these functions in the left panel of Figure 4.10. Suppose that $\Delta_1(\omega_m)$ changes sign at $\omega_m = \omega_1$. Near this frequency, $\Delta_1(\omega_m) = -c(\omega_m - \omega_1)$, where $c > 0$ for consistency with the figure. Let us analytically continue $\Delta_1(\omega_m)$ to a near vicinity of the Matsubara axis, to $z = \omega' + i\omega''$ (on the Matsubara axis, $z = i\omega_m$). Because $\Delta_1(\omega_m)$ is non-singular, $\Delta_1(z) = \Delta_1(i\omega_m \to \omega' + i\omega'')$. For any non-zero ω', $\Delta_1(z)$ is a complex function: $\Delta_1(z) = \Delta_1'(z) + i\Delta_1''(z)$, and we can introduce the phase of $\Delta_1(z)$

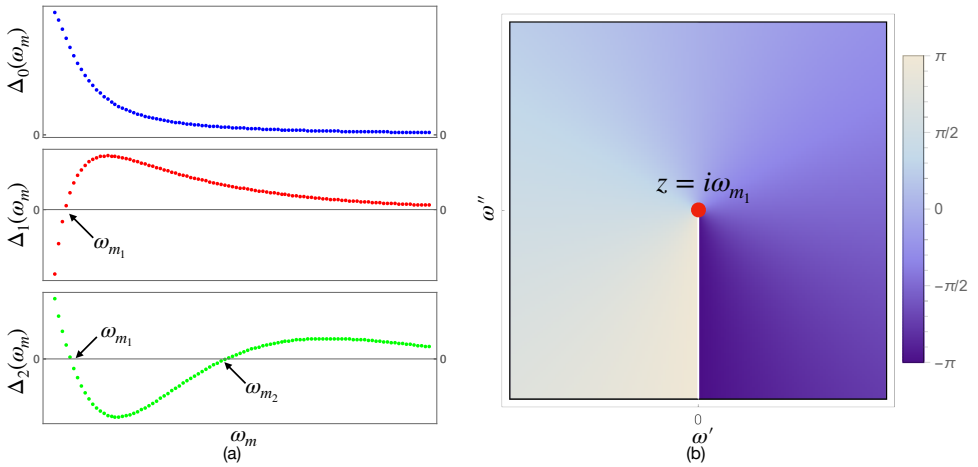

Figure 4.10: Left panel: The schematic forms of the first 3 solutions of the gap equation $\Delta_0(\omega_m)$, $\Delta_1(\omega_m)$ and $\Delta_2(\omega_m)$. A gap function $\Delta_n(\omega_m)$ changes sign n times at $\omega_m > 0$. Right panel: Variation of the phase of $\Delta_1(z)$ around the nodal point at $\omega_m = \omega_1$ ($z = \omega' + i\omega''$). Anticlockwise circulation of the phase around $z = i\omega_1$ is 2π. The same holds for any other nodal point.

as

$$\eta_1(z) = \mathrm{Im} \log \Delta_1(z). \tag{4.23}$$

We plot the variation of $\eta_1(z)$ around $z = i\omega_1$ in the right panel of Figure 4.10. We see that the phase varies by 2π upon anticlockwise circulation around ω_1. This implies that the nodal point at ω_1 is in fact the center of a dynamical vortex. One can easily verify that $\Delta_n(\omega_m)$ with a generic n contains n vortices, each with anticlockwise circulation 2π.

One can straightforwardly verify that n vortices on the Matsubara axis give rise to $2\pi n$ phase variation on the real axis, between $-\infty$ and ∞. To see this, one should compute $\int_{-\infty}^{\infty} d\omega \partial\eta_1(\omega)/\partial\omega$ by closing the integration contour over the upper half-plane. The function $\partial\eta_1(\omega)/\partial\omega$ is analytic in the upper half-plane except for the nodal points where it has simple poles. Modifying the contour to circle out each nodal point, one obtains $2\pi n$ phase variation from the vortices. In addition, there is also the $\pi\gamma$ from the integral over the upper half-circle, due to the fact that at the largest frequencies, $\Delta_n(z) \propto 1/(-z^2)^{\gamma/2}$. This form is consistent with $\Delta_n(\omega_m) \propto 1/|\omega_m|^{\gamma}$, as one can easily

verify by Cauchy relation.

The $n = 0$ solution at $T = 0$ for all γ has been obtained in Figure 2.7. Here we note that at large ω_m, the solution can be approximated by

$$\Delta_0(\omega_m) \approx Q_\gamma \left(\frac{\bar{g}}{|\omega_m|} \right)^\gamma \tag{4.24}$$

where Q_γ is given by

$$Q_\gamma = \int_0^\infty \frac{d\omega'_m \Delta_0(\omega'_m)}{\sqrt{\Delta_0^2(\omega'_m) + (\omega'_m)^2}} \tag{4.25}$$

The $n = \infty$ solution at $T = 0$ is obtained exactly in Ref[95]. Here we omit the lengthy derivation and only discuss the its important properties. Introducing $y = (|\omega_m|/\bar{g})^\gamma$, the limiting forms of $\Delta_\infty(y)$ can be found analytically. For $y \ll 1$ we have

$$\Delta_\infty(y) \sim y^{1/2} \cos(\beta \log y + \phi) \tag{4.26}$$

where ϕ is some γ-dependent number. At $y \gg 1$,

$$\Delta_\infty(y) \sim \frac{1}{y} \tag{4.27}$$

which agrees with (4.24), since the large ω_m behavior are the same for any n. The corrections to (4.26) hold in powers of y and form two series, local and nonlocal, depending on whether they come from fermions with running frequencies of order ω_m or much larger frequencies, of order $\bar{g}$. The full $\Delta_\infty(y)$ for $y < 1$ is

$$\Delta_\infty(y) = \mathrm{Re} \sum_{n=0}^\infty e^{i(\beta \log y + \phi)} C_n^< y^{n+1/2} + \sum_{n,m=0}^\infty D_{n,m}^\infty y^{n+\beta_m+1/2} \tag{4.28}$$

where the first term describes the sum of the leading term and the local corrections, and the second term describes the nonlocal corrections. In the latter, β_m are the solutions of $\epsilon_{i\beta_m} = 1$ for imaginary argument. There is an infinite set of such β_m, specified by $m = 0, 1, 2, ...$ For $\gamma > 1$, the corrections to (4.27) hold in powers of $1/y$ and also form two series:

$$\Delta_\infty(y) = \sum_{n=0}^\infty C_n^> \frac{1}{y^{n+1}} + \sum_{n,m=0}^\infty D_{n,m}^> \frac{1}{y^{n+1+(2m+1)/\gamma}} \tag{4.29}$$

Equation (4.27) is the $C_0^>$ term in this series.

The difference between $\gamma > 1$ and $\gamma < 1$ resides in the convergence of (4.29). For $\gamma < 1$ the series are convergent, while for $\gamma > 1$, the series converges up to some $n_{max} \sim y^{1/(\gamma-1)}$. In addition to this series, there is a universal contribution for $y \gg 1$.

$$\Delta_\infty^u(y) \sim y^{\frac{1}{2(\gamma-1)}} e^{-\frac{\pi}{A_\gamma} y^{1/(\gamma-1)}} \cos\left[y^{1/(\gamma-1)} \frac{\gamma-1}{A_\gamma}\left(1 - \frac{\pi^2}{2(\gamma-1)^2}\right) - \frac{\pi}{4}\right] \tag{4.30}$$

where

$$A_\gamma = \gamma\left[\frac{\pi}{2\Gamma(\gamma)\cos[\pi(2-\gamma)/2]}\right]^{1/(\gamma-1)} \tag{4.31}$$

This university piece is exponentially small on Matsubara axis, but will become significant once analytically continued on to real axis.

To analyze the behavior of $\Delta_n(\omega_m)$ at a finite n, one has to solve the nonlinear gap equation at $T = 0$ for a class of functions which change sign n times. At $\omega_m > \bar{g}$, $\Delta_n(\omega_m)$ decreases as $1/|\omega_m|^\gamma$ and has an exponentially small oscillating piece, the same as in (4.30). At $\omega_m < \bar{g}$, $\Delta_n(\omega_m)$ oscillates n times and saturates at the smallest ω_m at $\Delta_n(0)$, which decreases with increasing n. To estimate the magnitude of $\Delta_n(0)$ and, more generally, understand why there is a discrete set of solutions, we use the solution of the linearized gap equation, Eq. (4.26), as an input, and treat the nonlinear terms by expanding in powers of $\Delta_n(\omega_m)/\omega_m$. The gap function, obtained this way, is represented by the series

$$\Delta_n(y) = \bar{g} y^{1/2} \sum_{m=0}^{\infty} C_n^{2m+1} f_m(y) \tag{4.32}$$

where $f_0(y) = \cos(\beta \log y + \phi)$, $f_{m\geq 1}(y)$ are obtained in the order-by-order expansion in $\Delta_n(\omega_m)/\omega_m$, and C_n is yet unknown factor. Evaluating the few first $f_m(y)$, we obtain that they are also oscillating functions of $\log y$ with $y-$dependent prefactors of order $(1/y^{2m})^{1/\gamma-1/2}$. The perturbative expansion holds as long as $C_n < y^{(1/\gamma-1/2)}$. In this range, one can approximate the rhs of (4.32) by the $m = 0$ term for order-by-magnitude estimates. The function $f_0(y)$ changes sign n times between $y = O(1)$ and $y_{min} \sim e^{-n\pi/\beta}$. It is natural to associate y_{min} with the lower boundary of the perturbative expansion. Doing this, we obtain a discrete set of C_n:

$$C_n \sim e^{\frac{-n\pi}{\beta}(1/\gamma-1/2)} \tag{4.33}$$

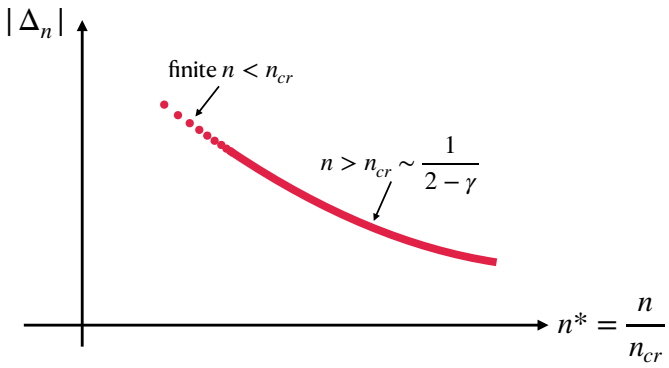

Figure 4.11: A schematic dependence of Δ_n on n at $\gamma \to 2$, at some fixed ω_m. All Δ_n with finite n tend to the same value, while the magnitude of $\Delta_{n\to\infty}$ depends on the ratio $n^* = n/n_{cr}$, where $n_{cr} \sim 1/(2-\gamma)$.

For large n, $\Delta_n(y) \approx \bar{g} y^{1/2} C_n \cos(\beta \log y + \phi)$. For $n = O(1)$, $C_n = O(1)$, and one needs to keep the full series in (4.32). This reasoning also yields $\Delta_n(0) \sim y_{min}^{1/2} C_n \sim (y_{min})^{1/\gamma} \sim \bar{g} e^{-n\pi/(\beta\gamma)}$.

Eq. (4.33) shows that for a generic γ, $C_n = O(1)$ for $n = O(1)$, and decays exponentially at larger n. However, for γ close to 2, the dependence on n in (4.33) is actually via the product $n^* = n(2-\gamma) \sim n/n_{cr}$. In the limit $\gamma \to 2$, $n^* \to 0$ for any finite n. The corresponding C_n then become independent on n and coincide with C_0 up to corrections, which become relevant only at the smallest y. At the same time, at $n \to \infty$, n^* becomes a continuous variable, whose value depends on how the double limit $n \to \infty$ and $\gamma \to 2$ is taken. Then $C_{n\to\infty}$ and $\Delta_{n\to\infty}$ become continuous functions of n^*. [1] We illustrate this in schematically in Figure 4.11. Now, each gap function $\Delta_n(\omega_m)$ generates a certain condensation energy $E_{c,n}$. For a generic $\gamma < 2$, the spectrum of $E_{c,n}$ is discrete, and $E_{c,0}$ is the largest by magnitude. Then, at low $T \ll T_{p,0}$, only the $n = 0$ solution matters, while the existence of other $E_{c,n}$ affects the system behavior only at $T \leq T_{p,0}$. As γ increases towards two, the spectrum of $E_{c,n}$ becomes denser, and $(E_{c,0} - E_{c,n})/E_{c,0}$ progressively gets smaller for any finite n. At $\gamma \to 2$, the spectrum of $E_{c,n}$ can be viewed as almost continuous spectrum with a small gap, i.e.,

[1] This is similar to the behavior of Δ_n for $\gamma \approx 1$ in the extended γ model, when the extension parameter $N \neq 1$.

there emerges a branch of low-energy "longitudinal" gap fluctuations. These fluctuations affect the system behavior beginning at a progressively smaller T, as γ approaches two. At $\gamma = 2 - 0$, the spectrum of condensation energies becomes a gapless continuous function $E_c(n^*)$ with $E_c(0) = E_{c,0}$ and $E_c(\infty) = E_{c,\infty}$.

4.2.2 Solutions on real frequency axis

The gap equations along real frequency axis has been given in (3.23). For convenience, rewrite the two equations in a single one with introducing $D(\omega) = \Delta(\omega)/\omega = \Phi(\omega)/\tilde{\Sigma}(\omega)$,

$$D(\omega)B(\omega) = A(\omega) + C(\omega) \tag{4.34}$$

where $A(\omega)$ and $B(\omega)$ have been given in (3.24), while $C(\omega)$ is

$$C(\omega) = \frac{i}{2}\int_{-\infty}^{\infty} d\Omega V''(\Omega)\frac{D(\omega-\Omega) - D(\omega)}{\sqrt{1 - D^2(\omega-\Omega)}}\left(\tanh\frac{\omega-\Omega}{2T} + \coth\frac{\Omega}{2T}\right) \tag{4.35}$$

The case $n = \infty$

For $n = \infty$, the result for small ω can be equivalently obtained by converting (4.26) to real frequency axis. In explicit form, we have in this regime

$$\Delta_\infty(\omega) = C_\infty\left(\frac{|\omega|}{\bar{g}}\right)^{\gamma/2} e^{-\frac{i\pi\gamma}{4}\mathrm{sgn}\omega}\cos\left(\beta\gamma\left(\log\frac{|\omega|}{\bar{g}} - i\frac{\pi}{2}\mathrm{sgn}\omega\right) + \phi\right) \tag{4.36}$$

where C_∞ is infinitesimally small. At largest ω the solution can be equivalently obtained by rotating (4.27) onto real axis,

$$\Delta_\infty(\omega) \propto \left(\frac{\bar{g}}{|\omega|}\right)^{\gamma} e^{(i\pi\gamma/2)\mathrm{sign}\omega} Q_{\infty,\gamma} \tag{4.37}$$

where $Q_{\infty,\gamma}$ is similar to (4.25) but with Δ_0 replaced with Δ_∞. For $\gamma \geq 1$ there is a single crossover between the two limiting forms of $\Delta_\infty(\omega)$, Eqs. (4.36) and (4.37). However, for $\gamma \leq 2$, the new intermediate regime emerges at $\omega > \bar{g}$, as we now demonstrate. In this regime, $\Delta'_\infty(\omega)$ and $\Delta''_\infty(\omega)$ again oscillate, but with the period set by a power of ω rather than by $\log|\omega|$. To see this, we analytically continue the universal piece (4.30)

and obtain,

$$\Delta_\infty(\omega) \propto |\omega|^{\frac{1}{2}\frac{\gamma}{\gamma-1}} \exp\left(-\frac{2-\gamma}{A_\gamma}\left(\frac{|\omega|}{\bar{g}}\right)^{\frac{\gamma}{\gamma-1}}\left[\frac{\pi}{2} - i\frac{\gamma-1}{2-\gamma}\left(1-\frac{\pi^2}{2(\gamma-1)^2}\right)\right]\right) \quad (4.38)$$

For $\gamma \leq 2$, the exponential part of the prefactor is small in $2-\gamma$, and the power-law part increases with ω. As the result, this oscillating contribution exceeds the one from Eq. (4.37) for frequencies between $O(\bar{g})$ and ω_{cr}, where

$$\omega_{cr} \sim \bar{g}\left(\frac{|\log(2-\gamma)|}{2-\gamma}\right)^{1/2} \gg \bar{g}. \quad (4.39)$$

As a result, at $\bar{g} < \omega < \omega_{cr}$, $\Delta^{'}(\omega)$ and $\Delta^{''}(\omega)$ oscillate as functions of $(|\omega|/\bar{g})^{\gamma/(\gamma-1)}$ with weakly, yet exponentially decaying prefactor. To the leading order in $2-\gamma$, Eq. (4.38) gives

$$\Delta_\infty(\omega) \propto |\omega| e^{-(1-\gamma/2)(|\omega|/\bar{g})^2} e^{i(|\omega|/\bar{g})^2/\pi} \quad (4.40)$$

We used $A_2 = \pi$. For completeness, we computed the subleading term under $e^{i\cdots}$. It changes Eq. (4.40) into

$$\Delta_\infty(\omega) \propto |\omega| e^{-(1-\gamma/2)(|\omega|/\bar{g})^2} e^{i\left((|\omega|/\bar{g})^2 + \log((|\omega|/\bar{g})^2)\right)/\pi} \quad (4.41)$$

In Fig. 4.12 (a), we compare the exact $\Delta_\infty(\omega)$ with Eq. (4.41) for $\gamma = 1.91$. We see that the agreement is quite good, and the range of ω^2 oscillations is quite wide for this γ. In Fig. 4.12 (b), we show the variation of the phase $\eta(\omega)$ between $\omega \sim \bar{g}$ and $\omega = \infty$. We see that the phase changes by $2\pi m$, where m is an integer, and the total phase variation is $2\pi m + \pi\gamma/2$. The last piece just follows from (4.37), and the first one is due to oscillations given by (4.40). The integer m increases one-by-one as γ increases towards 2.

The case $n = 0$

At $\gamma \leq 2$, the integral in $C(\omega)$ [see (4.35)] is determined by small Ω. Therefore we expand the difference term in terms of the derivative of $D_0(\omega)$ and obtain the following

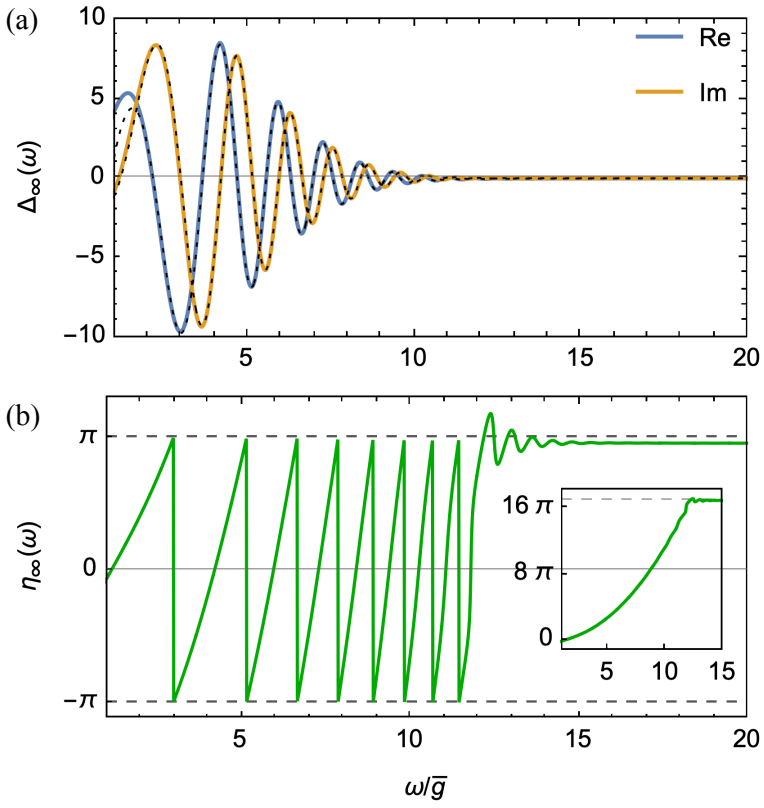

Figure 4.12: (a) Comparison between the exact $\Delta_\infty(\omega)$ along the real frequency axis (blue and orange thick lines) and the universal contribution to $\Delta_\infty(\omega)$ from Eq. (4.41) (black dotted lines) for $\gamma = 1.91$. The agreement is nearly perfect. (b) Variation of the phase of the gap function, $\eta_\infty(\omega)$, between $\omega \sim \bar{g}$ and $\omega = \infty$. For convenience of presentation we confined $\eta_\infty(\omega)$ to $(-\pi, \pi)$, up to small variations. In the inset we plot the continuous $\eta_\infty(\omega)$. We see that the total phase variation between $\omega \sim \bar{g}$ and $\omega = \infty$ is $16\pi + \pi\gamma/2$.

equation,

$$-i\frac{\pi}{2}\bar{g}^{\gamma}\frac{\omega^{2-\gamma}}{\sqrt{1-D_0^2(\omega)}}\left[\dot{D}_0(\omega)-(2-\gamma)\omega\left(\frac{1}{2}\ddot{D}_0(\omega)+\frac{D_0(\omega)(\dot{D}_0(\omega))^2}{1-D_0^2(\omega)}\right)\right]=D_0(\omega)\omega-Q_{\gamma}\left(\frac{\bar{g}}{\omega}\right)^{\gamma}e^{i\pi\gamma/2} \tag{4.42}$$

We follow Refs. [65, 58] and introduce $D_0(\omega)=1/\sin(\phi(\omega))$. Both $D_0(\omega)$ and $\phi(\omega)$ are complex functions of ω. Substituting into (4.42) we obtain

$$\dot{\phi}-\frac{(2-\gamma)}{2}\omega\left(\ddot{\phi}+(\dot{\phi})^2\tan\phi\right)=\frac{2}{\pi\bar{g}^{\gamma}}\left(\omega^{\gamma-1}-Q_{\gamma}\frac{\bar{g}^{\gamma}}{\omega^2}e^{i\pi\gamma/2}\sin\phi\right) \tag{4.43}$$

This equation is similar to the one for $\gamma=2$ and a finite T, analyzed by Combescot in Ref. [58].

At the highest frequencies, the gap function must obey Eq. (4.37). This gap function is reproduced if we choose

$$\phi'(\omega)=2\pi m+\frac{\pi}{2}(\gamma+1) \tag{4.44}$$

$$\phi''(\omega)=\log\frac{2\bar{g}}{Q_{\gamma}}+(\gamma+1)\log\frac{\omega}{\bar{g}} \tag{4.45}$$

where m is integer. We see that at large enough ω, $\phi''(\omega)\gg\phi'(\omega)$. On the other hand, at $\omega\geq\bar{g}$, $\phi'(\omega)\approx(2/\pi\gamma)(\omega/\bar{g})^{\gamma}$, and ϕ'' is small, of order $2-\gamma$. We use this to set the boundary condition at $\omega=\bar{g}$ as

$$\phi'=\frac{2}{\pi\gamma},\quad \phi''=a(2-\gamma), \tag{4.46}$$

where $a=O(1)$. We will argue that the solution of (4.43) is largely independent on a, as long as $a(2-\gamma)\ll 1$. To simplify the calculation, below we neglect $\ddot{\phi}$ term in Eq. (4.43) and use the boundary condition (4.46) as the initial condition for the first order differential equation. We show that the solution of (4.43) without $\ddot{\phi}$ by itself satisfies the boundary condition (4.44 and 4.45). We discuss the role of $\ddot{\phi}$ and the validity of dropping it at the end of this section.

A simple analysis of the Eq. (4.43) without $\ddot{\phi}$ term shows that $\phi''(\omega)$ rapidly increases shortly before $\phi'(\omega)$ reaches $\pi/2$. To see this, we neglect momentarily the Q_{γ} term in (4.43), which gives rise to a small initial ϕ'' and solve the remaining equation as a

quadratic equation on $\dot{\phi}$. We obtain

$$\dot{\phi} = \frac{1 - \sqrt{1 - \frac{4}{\pi}(2-\gamma)\left(\frac{\omega}{\bar{g}}\right)^{\gamma}\tan\phi(\omega)}}{(2-\gamma)\omega\tan\phi(\omega)}. \tag{4.47}$$

(the sign is chosen to satisfy the initial condition). An elementary analysis shows that $\phi''(\omega)$ emerges at $\omega = \omega_a$, where when

$$\left(\frac{\omega_a}{\bar{g}}\right)^{\gamma}\tan(\phi'(\omega_a)) = \frac{\pi}{4}\frac{1}{2-\gamma}, \tag{4.48}$$

This ω_a is smaller than the one at which $\phi'(\omega)$ reaches $\pi/2$. This is essential as in the absence of ϕ'', the behavior near $\phi'(\omega) = \pi/2$ would be singular. Once ϕ'' is nonzero, the singularity is cut. Keeping the Q_γ term, we find that ϕ'' is nonzero at all frequencies, where Eq.(4.43) is valid, but still rapidly increases around ω_a, specified by (4.48).

At larger ω, $\phi''(\omega)$ increases, and eventually $e^{\phi''}$ becomes larger than one. At such frequencies, $\tan\phi \approx i$, and (4.43) simplifies to

$$\begin{aligned}\dot{\phi}'(\omega) &\approx \frac{2}{\pi}\frac{\omega^{\gamma-1}}{\bar{g}^{\gamma}} \\ \dot{\phi}''(\omega) &\approx \frac{2(2-\gamma)}{\pi^2}\frac{\omega^{2\gamma-1}}{\bar{g}^{2\gamma}}\end{aligned} \tag{4.49}$$

Solving, we find $\phi'(\omega) \approx (2/\pi\gamma)(\omega/\bar{g})^{\gamma}$, $\phi''(\omega) \approx (2-\gamma)/(\pi^2\gamma)(\omega/\bar{g})^{2\gamma}$. Note that these forms are universal and do not depend on the boundary condition (i.e., on the factor a in Eq. (4.46)). For $\gamma \approx 2$, $\phi'(\omega) \approx (\omega/\bar{g})^2/\pi$. To compare with $n = \infty$ case, we computed the subleading term. It comes from the second term in $B(\omega)$ and changes $\phi'(\omega)$ to

$$\phi'(\omega) = \frac{1}{\pi}\left(\left(\frac{\omega}{\bar{g}}\right)^2 + \log\left(\frac{\omega}{\bar{g}}\right)^2\right). \tag{4.50}$$

Observe that the rhs of (4.50) is the same function as we found for $n = \infty$, Eq. (4.41). Eq. (4.49) holds up to ω at which $e^{\phi''} \sim (\omega/\bar{g})^3$. At larger frequencies, the second term in the rhs of (4.43) cannot be neglected, and the functional form of $\phi(\omega)$ changes. In Figure 4.13 (a) we show the result of numerical solution of (4.43) We see that there is a single crossover, at $\omega = \omega_{cr} \sim \bar{g}(|\log(2-\gamma)|/(2-\gamma))^{1/(2\gamma)}$, from $\phi(\omega)$ given by (4.49)

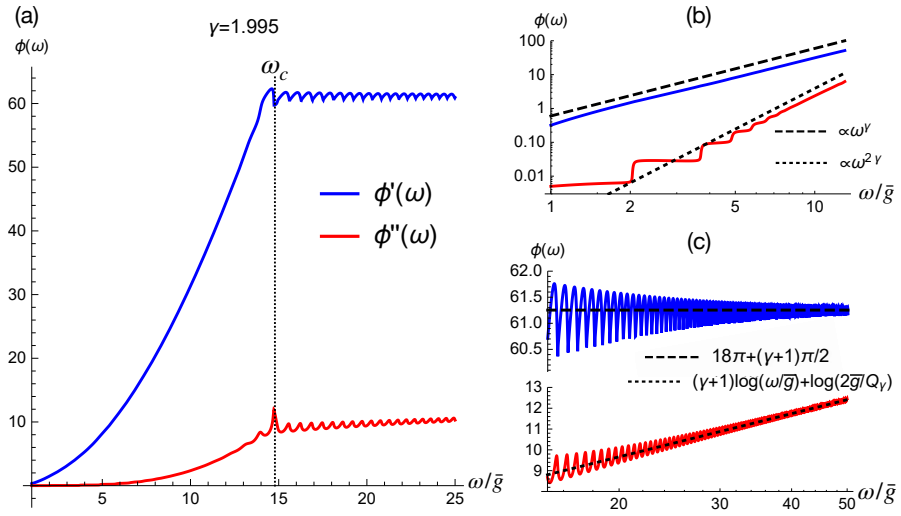

Figure 4.13: (a) The numerical solution of Eq. (4.43) for $\gamma = 1.995$. Frequency is in units of $\bar{g}$. The crossover at $\omega_{cr} \approx 15\bar{g}$ is clearly visible. (b,c) Zoom into regions $\omega < \omega_{cr}$ and $\omega > \omega_{cr}$. At $\omega < \omega_{cr}$, ϕ' grows as ω^γ, while ϕ'' first increases steplike, and then behaves as $\omega^{2\gamma}$. At $\omega > \omega_{cr}$, ϕ' saturates at $2\pi m + (\gamma+1)\pi/2$, where $m = 9$ for $\gamma = 1.995$, while ϕ'' increases as $(\gamma+1)\log\omega/\bar{g}$.

to $\phi(\omega)$ given by (4.44,4.45). In Figure 4.13 (b) and (c) we show separately the behavior of $\phi'(\omega)$ and $\phi''(\omega)$ at $\omega < \omega_{cr}$ and $\omega > \omega_{cr}$. The fits to Eq. (4.49) Eqs. (4.44,4.45), respectively, are almost perfect. Deviations from the high-frequency forms decrease as $1/\omega^\gamma$ and oscillate as trigonometric functions of $(2/\pi\gamma)(\omega/\bar{g})^\gamma$. In Figure 4.14((a) and (b)) we show that the value of ϕ' for $\omega > \omega_{cr}$ is independent on the parameter a in the boundary condition (4.46), as long as $a = O(1)$. At the same time, the value of an integer m in (4.44) changes if we change γ, as is shown in Fig.4.14(c). Specifically, m jumps to the nearest integer at a discrete set of $\gamma_i \leq 2$ (the smaller is $2-\gamma$, the larger is m). We demonstrate this in Figure 4.14(d).

In Figure 4.15(a) we show real and imaginary parts of the gap function

$$\Delta_0(\omega) = \frac{\omega}{\sin\phi(\omega)} = 2\omega\frac{\sin\phi'\cosh\phi'' - i\cos\phi'\sinh\phi''}{\cosh 2\phi'' - \cos 2\phi'} \tag{4.51}$$

We see that both $\Delta_0'(\omega)$ and $\Delta_0''(\omega)$ oscillate between $\omega = O(\bar{g})$ and ω_{cr} and display sign-preserving $1/\omega^\gamma$ behavior at $\omega > \omega_{cr}$. At $\omega \geq \bar{g}$, $\Delta'(\omega)$ varies roughly as

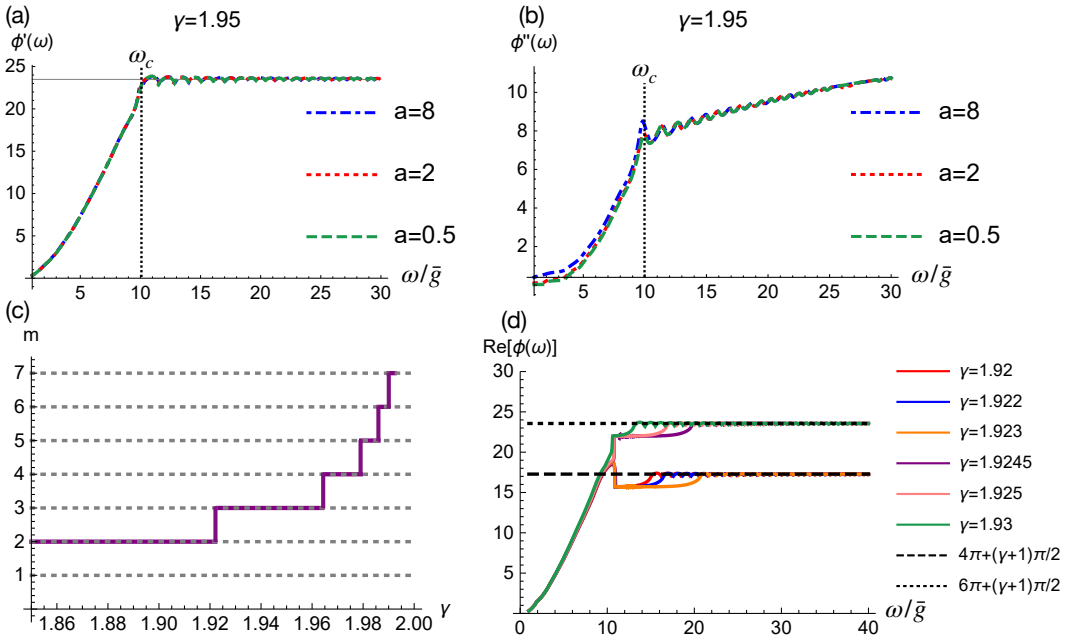

Figure 4.14: (a,b) The functions $\phi'(\omega)$ and $\phi''(\omega)$ for different boundary conditions, set by a parameter a in Eq.(4.46). The figure shows that the value $2\pi m + (\gamma+1)\pi/2$, at which $\phi'(\omega)$ saturates is independent on a. The behavior of $\phi'(\omega)$ in the universal regime, where both ϕ' and ϕ'' are continuous functions of ω, also does not depend on a. (c) Variation of the integer m with γ. There is a discrete set of γ_i, at which m changes by 1. The set becomes progressively more dense at $\gamma \to 2$. (d) The behavior of $\phi'(\omega)$ near one of these $\gamma_i \approx 1.924$. The value of ϕ' at large ω jumps by 2π as γ passes through γ_i and a new vortex moves into the upper half plane of frequency.

$\omega/\sin\left((2/(\pi\gamma))(\omega/\bar{g})^{\gamma}\right)$ and $\Delta^{''}(\omega)$ has almost δ-functional spikes in where $\sin(2/(\pi\gamma))(\omega/\bar{g})^{\gamma})$ is small. At larger $\omega \leq \omega_{cr}$, both Δ' and $\Delta^{''}$ oscillate with progressively decreasing magnitude.

In Figure 4.15(b) we show the variation of the phase of the gap function $\eta(\omega)$. The total variation of η between $\omega = 0$ and $\omega = \infty$ is $2\pi m + \pi\gamma/2$. We emphasize that this is the result for $\Delta_0(\omega)$, which is sign-preserving on the Matsubara axis. We clearly see that there is a huge difference between the forms of the gap function on the real and the Matsubara axis in between $\bar{g}$ and ω_{cr}.

We now use more precise analysis to determine ω_{cr}. In Eq. (4.43) we included only the first two terms in the expansion of $C(\omega)$ in powers of $\dot{\phi}$. Meanwhile, the expansion in derivatives holds in powers of $\dot{\phi}\omega/\bar{g}$ without additional $(2-\gamma)$ in the prefactor. This implies that higher-order terms are not negligible at $\omega > \bar{g}$. We now use the fact that before $\phi(\omega)$ crosses over to (4.49), it shows the universal behavior in the range where $1 < e^{\phi^{''}} < (\omega/\bar{g})^3$. In this regime, (1) $\dot{\phi} \approx \dot{\phi}' \approx (2\pi)\omega^{\gamma-1}/\bar{g}^{\gamma} \gg \bar{g}$, while higher-order derivatives are smaller, and (2) $D(\omega)$ is small, such that $\sqrt{1-D^2} \approx 1$. In this situation, one can sum up the full Taylor series for $(2-\gamma)$ term in $C(\omega)$. We use that $\tan\phi \approx i$ and the n-th detivative $D^n(\omega) \approx i^n(\dot{\phi})^n D$. Integrating each term in Talor series over Ω, we obtain the modified lhs of (4.43) in the form

$$\dot{\phi} - i(2-\gamma)\dot{\phi}F\left(\frac{\omega}{\bar{g}}\dot{\phi}\right) \tag{4.52}$$

where

$$F(x) = \int_0^x \frac{1-\cos y}{y^2} = \mathrm{SI}(x) - \frac{1-\cos x}{x} \tag{4.53}$$

and $\mathrm{SI}(x)$ is SinIntegral. Equation (4.43) is reproduced if we approximate $1-\cos y$ by $y^2/2$. Then $F(x) \approx x/2$. If we use the full expression, we find that at large x, which we are interested in, $F(x) \approx \pi/2$. The equation for ϕ then reduces to

$$\dot{\phi} = \frac{2}{\pi\bar{g}^{\gamma}} \frac{\omega^{\gamma-1} - \frac{Q_{\gamma}\bar{g}^{\gamma}}{\omega^2} e^{i\pi\gamma/2}\sin\phi}{1 - i(2-\gamma)\pi/2} \tag{4.54}$$

We show the solution in Figure 4.16 and present the plots of the gap function $\Delta_0(\omega)$, the phase $\eta_0(\omega)$, and the variation of m with γ in Figure 4.17.

The behavior of $\phi(\omega)$ is qualitatively similar to the one in Figure 4.13, i.e., there is

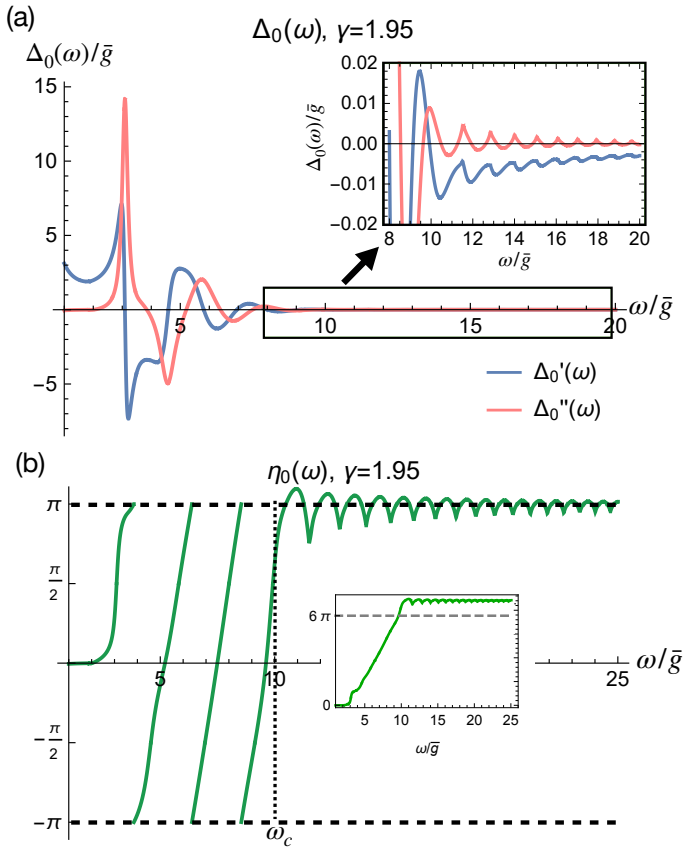

Figure 4.15: Upper panel: frequency dependence of the gap function $\Delta_0(\omega) = \Delta_0'(\omega) + i\Delta_0''(\omega)$, from Eq. (2.26). We set $\gamma = 1.95$. For $\bar{g} < \omega < \omega_{cr}$, both $\Delta_0'(\omega)$ and $\Delta_0''(\omega)$ display oscillations with a decreasing magnitude. For $\omega \geq \omega_{cr}$, $\Delta_0'(\omega)$ becomes negative and does not oscillate. Lower panel: Variation of the phase of the gap $\eta_0(\omega)$ as a function of ω. As before, we confined phase variation to $(-\pi, \pi)$, up to small variations. The phase changes by 2π three times between $\omega = O(\bar{g})$ and ω_{cr}. There are no more 2π phase variations, despite that the phase shows wiggling at large frequencies. In the inset we plot the continuous $\eta_0(\omega)$. We see that the total phase variation between $\omega_m = \bar{g}$ and $\omega_m = \infty$ is $6\pi + \pi\gamma/2$.

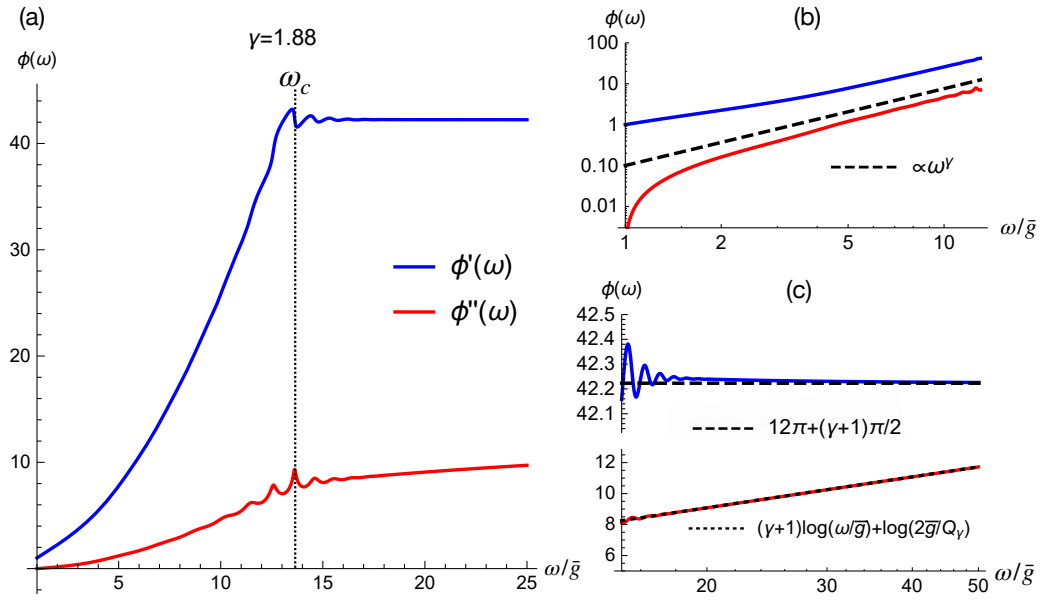

Figure 4.16: (a) The solution of Eq. (4.54) for $\gamma = 1.88$. =(b,c) Zooms into the regions below and above the crossover frequency. The behavior of $\phi'(\omega)$ and $\phi''(\omega)$ is qualitatively similar to that in Fig. 4.14, but differs in detail. In particular, both $\phi'(\omega)$ and $\phi''(\omega)$ approach asymptotic forms $12\pi + (\gamma+1)\pi/2$ and $(\gamma+1)\log\omega$, respectively, without oscillations.

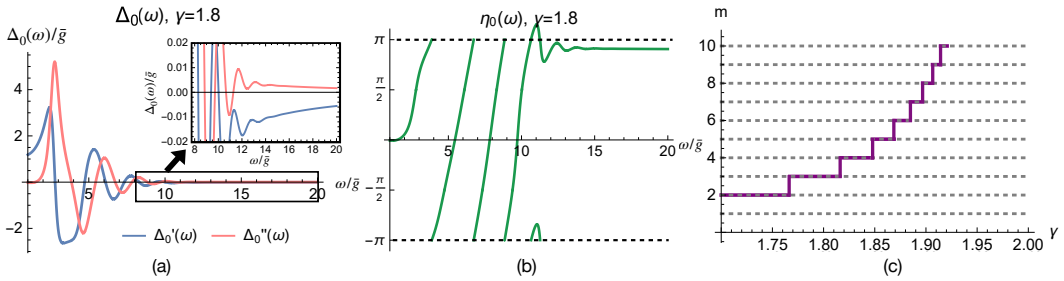

Figure 4.17: (a,b) The same as in Fig. 4.15, but for ϕ' and ϕ'' from Eq.(4.54). At large frequencies, $\Delta(\omega) \propto e^{i\pi\gamma/2}/\omega^{\gamma}$. The total variation of the phase of Δ is $\delta\eta = 2\pi m + \pi\gamma/2$. (c) Variation of m with γ. As before, there is a discrete set of γ_i, where m jumps by 1. The set becomes progressively more dense at $\gamma \to 2$.

a single crossover frequency, and the total variation of $\eta(\omega)$ between $\omega = 0$ and $\omega = \infty$ is $2\pi m + \pi\gamma/2$. However the crossover scale ω_{cr} has different dependence on $2 - \gamma$ compared to Eq. (4.43), and also the dependence of m on γ is different from that in Figure 4.14(b) [and there are no wiggles in $\phi(\omega)$ at $\omega > \omega_{cr}$]. To obtain the modified crossover frequency, ω_{cr}, we note that in the universal regime $1 < e^{\phi''} < (\omega/\bar{g})^3$, $\dot{\phi}'(\omega)$ is still given by (4.49), while

$$\dot{\phi}''(\omega) \approx (2-\gamma)\frac{\omega^{\gamma-1}}{\bar{g}^{\gamma}} \tag{4.55}$$

Accordingly, $\phi'(\omega) \approx (2\pi\gamma)(\omega/\bar{g})^{\gamma}$, $\phi''(\omega) = (2-\gamma)/\gamma(\omega/\bar{g})^{\gamma}$. The crossover frequency is then determined by $e^{\phi''} \sim (\omega/\bar{g})^3$. Solving for ω, we obtain, for $\gamma \leq 2$,

$$\omega_{cr} \sim \bar{g}\left(\frac{|\log(2-\gamma)|}{2-\gamma}\right)^{1/2} \tag{4.56}$$

This is the same scale as ω_{cr} that we obtained for $n = \infty$, Eq. (4.39).

We see therefore that for $n = \infty$ and $n = 0$ the new behavior of the gap function emerges in the same frequency range $\bar{g} < \omega < \omega_{cr}$. Moreover, the period of oscillations in this range is the same function of frequency, Eqs. (4.41) and (4.50).

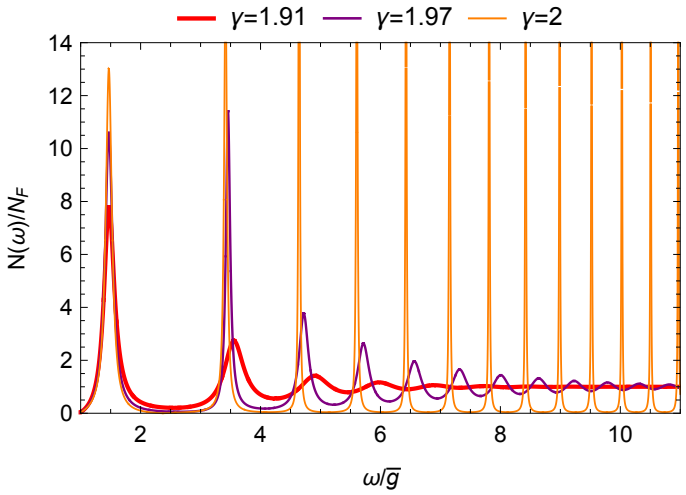

Figure 4.18: The DoS $N(\omega)$ for the $n = 0$ solution, for several γ. Peaks in $N(\omega)$ sharpen as $\gamma \to 2$, while the weight between the peaks is reduced.

In Figure 4.18 we plot the DoS

$$N_0(\omega) = N_F \mathrm{Re} \sqrt{\frac{\omega^2}{\omega^2 - \Delta_\infty^2(\omega)}} \tag{4.57}$$

for several γ. We see that $N_0(\omega)$ vanishes below a certain threshold frequency, and at $\bar{g} < \omega < \omega_{max}$ has a set of maxima and minima. The peaks in $N_0(\omega)$ get progressively sharper as γ approaches 2, while in between the peaks $N_0(\omega)$ gets smaller. The positions of the peaks almost coincide with the maxima of $N_\infty(\omega)$.

4.2.3 Solutions on complex frequency plane

We now use the Cauchy relation

$$\Delta(z) = \frac{2}{\pi} \int_0^\infty dx \frac{\Delta''(x)x}{x^2 - z^2} \tag{4.58}$$

and extend the gap functions $\Delta_n(\omega)$ into the upper frequency half plane, to $z = \omega' + i\omega''$ ($\omega'' > 0$). Earlier, we demonstrated that $\Delta_n(z)$ has n vortices on the Matsubara axis. Here, we analyze the behavior of $\Delta_n(z)$ between the Matsubara and the real axis. We

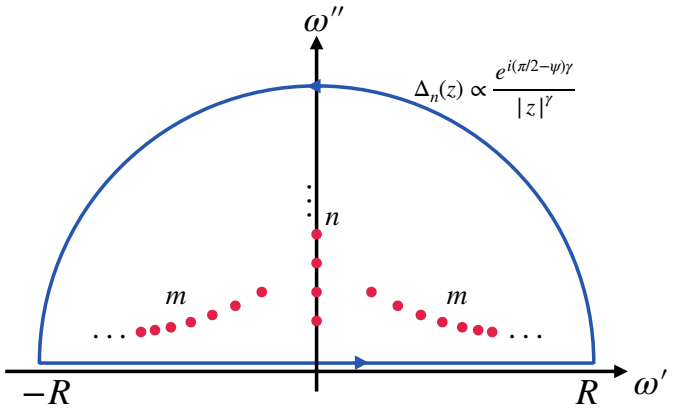

Figure 4.19: The contour Γ used in Eq.(4.59). The contour consists of a real axis and a semicircle(arc) at $z = |z|e^{i\psi}$, $|z| \to \infty$ and $0 < \psi < \pi$. Along the arc, $\Delta_n(z) \propto e^{i(\pi/2-\psi)\gamma}/|z|^\gamma$, so the corresponding contribution to $\delta\eta_L$ is $-\pi\gamma$. Along the real axis, $\delta\eta_\Gamma = 2\pi(n+2m) + \pi\gamma$. The total $\delta\eta_\Gamma$ along Γ is then $2\pi(n+2m)$. The same $\delta\eta_\Gamma$ must be obtained by counting contributions from the poles inside Γ. Each vortex is a pole with residue 2π, hence there should be $n+2m$ vortices. This is consistent with our analysis of $\Delta(z)$: there are n vortices on the Matsubara axis, and $2m$ vortices in the upper half plane near the real axis.

show that as γ increases from one to two, new vortices appear one-by-one in the upper frequency half plane, near the real axis. These vortices are located at $|z| > \bar{g}$, and their number, m, is determined by γ and is the same for all n. When $\gamma \to 2$, m tends to infinity. The emergence of vortices obviously correlates with the oscillations of $\Delta_n(\omega)$ on the real axis, and as such is another consequence of the change of sign of the real part of the interaction on the real axis, $V'(\Omega)$, which becomes repulsive at $\gamma = 1$. The increase of the number of vortices as γ approaches 2 in turn correlates with the decrease of $V''(\Omega)$.

That such vortices must be present can be understood by comparing the behavior of $\Delta_n(z)$ for $|z| > \bar{g}$ near the Matsubara axis and the real axis. Along the Matsubara axis, $\Delta_n(\omega_m)$ is real and does not change sign at $|\omega_m| > \bar{g}$. By continuity, $\Delta'(z)$ near the Matsubra axis should remain sign-preserving, hence $\eta(z)$ does not wind. On the other hand, on the real axis, the phase winds by $2\pi m$, as we found in the previous section. This number is topologically protected against perturbations and can disappear only

upon rotation from real to imaginary z if there are vortices at some complex z. Indeed, let us compute

$$\delta\eta_\Gamma = \mathrm{Im}\int_\Gamma dz\,[\partial \log\Delta(z)/\partial z] \tag{4.59}$$

along the path Γ, which starts at the large negative real $z=-R$, goes along the real axis up to $+R$, and then closes along the large arc in the upper half plane (see Figure 4.19) The arc is chosen such that along it $\Delta_n(z) \propto e^{i(\pi/2-\psi)}/|z|^\gamma$. The total phase variation along the arc is $-\pi\gamma$, and the phase variation along the real axis is $2\pi(n+2m)+\pi\gamma$. The contour integral then gives

$$\delta\eta_\Gamma = 2\pi(n+2m) \tag{4.60}$$

This $\delta\eta_\Gamma$ should be equal to the contribution from inside the contour. Because $\partial\log\Delta(z)/\partial z$ has a simple pole at each point where $\Delta(z)$ vanishes, there must be $n+2m$ vortices inside the contour (we recall that $\Delta(z)$ by itself has no poles in the upper half plane). There are n vortices on the Matsubara axis, the other $2m$ should be located in between the Matsubara and the real axis. By symmetry, there must then be m vortices in the first quadrant, and another m is in the second one.

As an example of dynamical vortex, in Figure 4.20 we show the amplitude of the gap $|\Delta_0(z)|$ and the phase $\eta_0(z)$ in the first quadrant of complex $z=\omega'+i\omega''$ for $|z|>\bar{g}$ for $\gamma=1.75$. We see that there are two vortices at complex z. We verified that this is consistent with $m=2$ in Eq. (4.44) for this γ.

In Figure we show the plot for vortices for both $n=0$ and $n=\infty$ solutions. Comparing the results for $n=0$ and $n=\infty$ we see that in both cases a line of vortices emerges at complex z in the first quadrant, and equal number of vortices forms in the second quadrant. The vortices develop for $\gamma>1$. The number of vortices increases with γ and tends to infinity at $\gamma\to 2$. In this limit, the line of vortices extends to $z=\infty$. We see that the phase winding along the real axis and the number of vortices in the upper frequency half plane for any given γ are very likely the same for $n=0$ and $n=\infty$ A small difference in the values of γ_i, where the new vortices appear in the two cases, is most probably related to the fact that the $n=0$ solution is an approximate one.

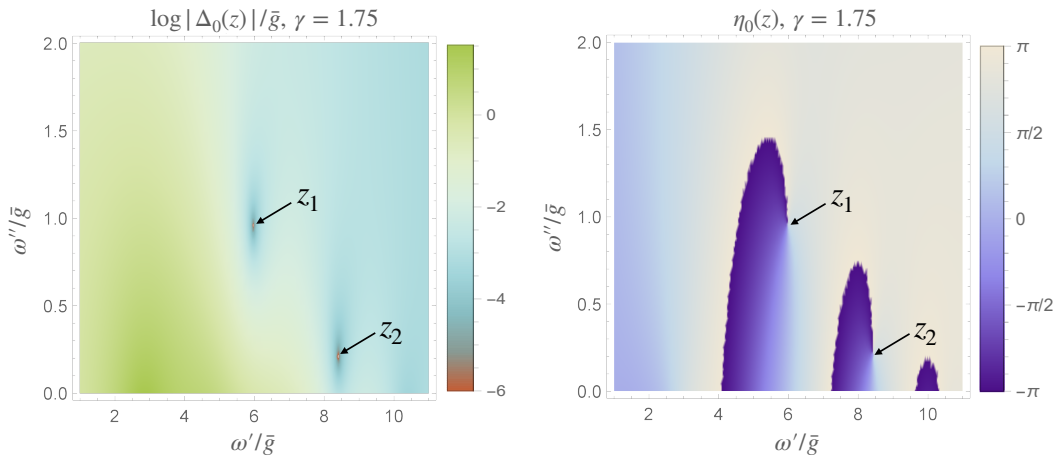

Figure 4.20: The case $n = 0$. Left panel: Plot of $\log|\Delta_0(z)|$ in the upper half plane, for $\gamma = 1.75$. The gap $\Delta_0(z)$ for a generic z in the upper half plane is obtained by analytic continuation from $\Delta''(\omega)$ on the real axis, Eq.(4.54). The two bright points z_1 and z_2 are the locations of the vortices (points where $|\Delta_0(z)| = 0$). Right panel: Plot of $\eta_0(z)$ in the same region.

4.2.4 $\gamma = 2$

The case $\gamma = 2$ corresponds a system with phonon-mediated pairing interaction, taken in the limit that the Debye frequency ω_D vanishes while the product of ω_D and the electron phonon coupling constant remains finite. Pairing in this system has been studied in previous works[65, 58]. Here we explicitly show the set of solutions in this case becomes continuous. Below we first analyze $n = \infty$ solution, and then use it as a building block to find a continuous set of solutions to the nonlinear gap equation.

For $n = \infty$, the solution at $\omega_m \ll \bar{g}$ and $\omega_m \gg \bar{g}$ are still given in (4.26) and (4.27), with now a new definition of $y = \bar{g}^2/|\omega_m|^2$. Written in terms of ω_m, (4.26) is

$$D_\infty(\omega_m) = 2\epsilon \cos\left[\beta \ln \frac{\omega_m^2}{\bar{g}^2} + \phi\right] \operatorname{sgn}\omega \tag{4.61}$$

Here we use $D_\infty = \Delta_\infty/\omega_m$ instead of Δ_∞ for convenience of discussion. In the limit $\gamma \to 2$, we find $\beta = 0.38187$ satisfying $\pi\beta \tanh(\pi\beta) = 1$. The universal piece at $\omega_m \gg \bar{g}$

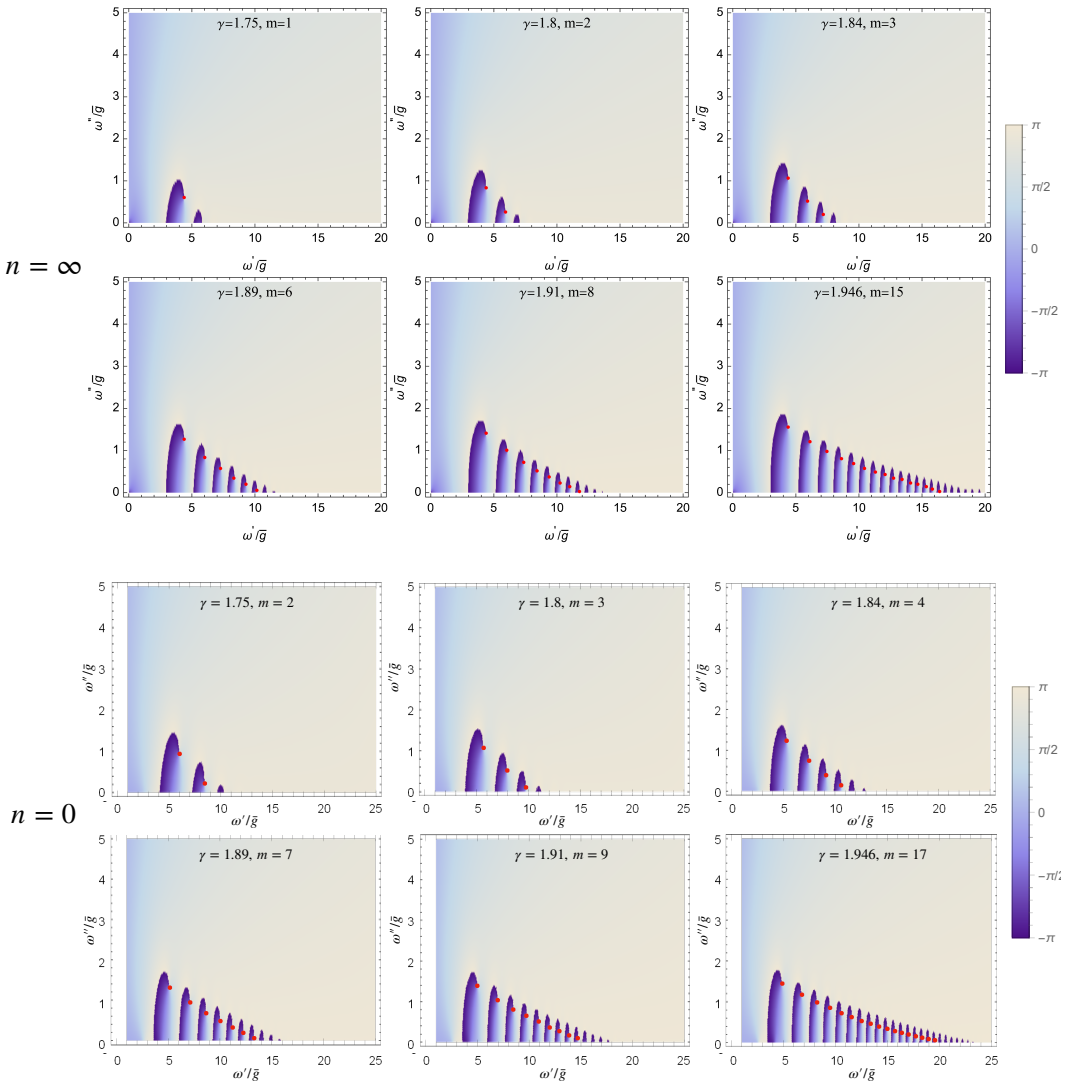

Figure 4.21: Upper panel:The case $n = \infty$. We plot the phase of the gap function $\eta_\infty(z)$ in the upper half plane ($z = \omega' + i\omega''$) for different γ near $\gamma = 2$. The locations of the vortices are marked by red dots. At the vortex core, $\Delta_\infty(z) = 0$ and η_∞ is undefined. This number of vortices m rapidly increases as $\gamma \to 2$. Lower panel: The case $n = 0$. The phase of the gap function $\eta_0(z)$ in the upper half plane ($z = \omega' + i\omega''$) for different γ near $\gamma = 2$. The locations of the vortices are marked by red dots. At the vortex core $\Delta_0(z) = 0$ and η_0 is undefined. The number of vortices is set by m in (4.44). This number rapidly increases as $\gamma \to 2$.

is still there, given by (4.30). Written in terms of ω_m, it is

$$D_{\infty,u}(\omega_m) \propto 2\sqrt{2}e^{-\omega_m^2/\bar{g}^2}\cos\left[\frac{\pi^2-2}{2\pi}\frac{\omega_m^2}{\bar{g}^2}+\frac{\pi}{4}\right] \tag{4.62}$$

To demonstrate the continuous set of solutions, we make use of (4.61) as a building block, and expand the solution as

$$D(\omega_m) = \sum_{j=0}^{\infty} D^{(2j+1)}(\omega_m) \tag{4.63}$$

where

$$D^{(1)}(\omega_m) = D_\infty(\omega_m) = 2\epsilon\cos f(\omega_m)\operatorname{sgn}\omega_m \tag{4.64}$$

with

$$f(\omega_m) = \beta\log\left(\frac{|\omega_m|}{\bar{g}}\right)^2 + \phi \tag{4.65}$$

We will see that $D^{(2j+1)} \sim \epsilon^{2j+1}$.

Substituting $D(\omega_m)$ from (4.63) into (2.26) and expanding in $D^2(\omega'_m)$ in the r.h.s. of (2.26), we obtain the set of equations, which express $D^{(2j+1)}$ for a given j in terms of $D^{(2j+1)}$ with smaller j. For $j=1$, we have

$$D^{(3)}(\omega_m)\omega_m - \frac{\bar{g}^2}{2}\int d\omega'_m\left(D^{(3)}(\omega'_m) - D^{(3)}(\omega_m)\right)\frac{\operatorname{sgn}\omega'_m}{(\omega_m-\omega'_m)^2} = K_3(\omega_m) \tag{4.66}$$

where the source term is

$$K_3(\omega_m) = -\frac{\bar{g}^2}{4}\int d\omega'_m\left(D^{(1)}(\omega'_m) - D^{(1)}(\omega_m)\right)[D^{(1)}(\omega'_m)]^2\frac{\operatorname{sgn}\omega'_m}{(\omega_m-\omega'_m)^2} \tag{4.67}$$

The source term is of order ϵ^3, hence $D^{(3)} \propto \epsilon^3$ ($D^{(5)} \propto \epsilon^5$ and so on). Substituting $D^{(1)}(\omega_m)$ from Eq. (4.64) and evaluating the integrals, we find the source term for $D^{(3)}$ as the sum of the two terms, $K_3 = K_{3a} + K_{3b}$, where

$$K_{3a}(\omega_m) = -\epsilon^3\frac{\bar{g}}{\omega_m}\cos\left(3f(\omega)\right)\left(2\pi\beta\coth(2\pi\beta) - 3\pi\beta\tanh(3\pi\beta)\right)\operatorname{sgn}\omega_m \tag{4.68}$$

and

$$K_{3b}(\omega_m) = -\epsilon^3 \frac{\bar{g}}{\omega_m} \cos\left(f(\omega)\right) \frac{1+\sinh^2(\pi\beta)}{\sinh^2(\pi\beta)} \operatorname{sgn}\omega_m \tag{4.69}$$

Solving for $D^{(3)}$ we find that the first term gives rise to $\epsilon^3 \cos\left(3f(\omega)\right)$, while the second term accounts for the renormalization of the prefactor for $\log(\omega_m^2)$ in $f(\omega_m)$ in (4.65) To order ϵ^2, the dressed $f(\omega_m)$, which we label $f_\epsilon(\omega_m)$, becomes

$$f_\epsilon(\omega_m) = \beta_\epsilon \log\left(\frac{|\omega_m|}{\bar{g}}\right)^2 + \phi_\epsilon \tag{4.70}$$

where

$$\beta_\epsilon = \beta\left(1-\epsilon^2/2\right) \approx \beta(1-\epsilon^2)^{1/2} \tag{4.71}$$

The full $D(\omega_m)$ to order ϵ^3 is

$$D(\omega_m) = 2\left(\epsilon \cos f_\epsilon(\omega_m) + Q_3\epsilon^3 \cos 3f(\omega_m)\right) \operatorname{sgn}\omega_m \tag{4.72}$$

where

$$Q_3 = \frac{2\pi\beta\coth\left(2\pi\beta\right) - 3\pi\beta\tanh\left(3\pi\beta\right)}{2(1-3\pi\beta\tanh\left(3\pi\beta\right))} = \frac{5-(\pi\beta)^2}{16} \approx 0.222 \tag{4.73}$$

Expanding to next order, we find (i) $\epsilon^5 \cos 5f(\omega_m)$ term with the prefactor $Q_5 = 0.043$, (ii) $O(\epsilon^4)$ corrections to β_ϵ in (4.71) ($\beta_\epsilon = 1-0.5\epsilon^2+0.806\epsilon^4$)), and (iii) $O(\epsilon^2)$ corrections to Q_3 ($Q_3 \to Q_{3,\epsilon}$) and to the argument of $\cos 3f(\omega_m)$ in (4.72). We verified that the last correction changes $\cos 3f(\omega_m)$ to $\cos 3f_\epsilon(\omega_m)$ with the same f_ϵ as in (4.70). This is the strong indication that the series contain the same fully renormalized $f_\epsilon(\omega_m)$ in each term. Combining the results, we obtain, for $\omega_m \ll \bar{g}$, $D(\omega_m) = D_\epsilon(\omega_m)$, where

$$D_\epsilon(\omega_m) = 2\epsilon\left(\cos f_\epsilon(\omega_m) + Q_{3,\epsilon}\epsilon^3 \cos 3f_\epsilon(\omega_m) + Q_{5,\epsilon}\epsilon^5 \cos 5f_\epsilon(\omega_m) + ...\right) \operatorname{sgn}\omega_m \tag{4.74}$$

We emphasize that a continuous set of solutions exists only for $\gamma = 2$.

Because $f_\epsilon(\omega_m)$ contains $\log\omega_m^2$, each $D_\epsilon(\omega_m)$ from (4.74) changes sign an infinite number of times down to $\omega_m = 0$, i.e., in our original classification the gap functions from the set are different realizations of $n = \infty$. At $\omega_m = 0$, each $D_\epsilon(\omega_m)$ has an essential singularity as neither $\lim_{\omega_m\to 0} D_\epsilon(\omega_m)$ nor $\lim_{\omega_m\to 0} 1/D_\epsilon(\omega_m)$ exist.

For a generic ϵ, Eq. (4.74) is valid for $\omega_m < \bar{g}$. At larger ω_m, $D_\epsilon(\omega_m) = D_\epsilon/|\omega_m|^2$.

We expect that for every ϵ, the crossover to proper high-frequency behavior can be achieved by fixing the phase factor ϕ_ϵ in (4.70) (see Ref[91] for a similar analysis for the linearized gap equation for $\gamma < 1$).

Next, we see from Eq. (4.71) that β_ϵ^2 decreases with increasing ϵ. It is natural to expect that it vanishes at some $\epsilon_{cr} = O(1)$. The expansion in (4.74) holds only as long as β_ϵ is real, as there is no solution of the nonlinear gap equation for imaginary β_ϵ. For $\epsilon \leq \epsilon_{cr}$, β_ϵ is small, and the range, where $D(\omega_m)$ oscillates, is confined to small $\omega_m \leq \bar{g}e^{-\pi/\beta_\epsilon}$. By properly taking the double limit $\epsilon \to \epsilon_{cr}$ and $\omega_m \to 0$, one can obtain an infinite set of gap functions, which change sign a given number of times in the immediate vicinity of $\omega_m = 0$. At $\epsilon = \epsilon_{cr}$ all these gap functions coincide with $\Delta_0(\omega_m)$ at any $\omega_m > 0$. This agrees with the observation in Ref[95] that as γ increases towards 2, the region, where $\Delta_n(\omega_m)$ with finite n change sign, gets confined to progressively smaller ω_m, while at larger ω_m, all $\Delta_n(\omega_m)$ with $n = 0, 1, 2...$ nearly coincide. We illustrate this in Figure 4.22. For consistency with the notations in previous sections, it is convenient to introduce $\xi = (\epsilon_{cr} - \epsilon)/\epsilon$ and label the continuum set of the gap functions by $\Delta_\xi(\omega_m)$. Then the end point solutions $\epsilon \to 0$ and $\epsilon = \epsilon_{cr}$ are $\Delta_\infty(\omega_m)$ and $\Delta_0(\omega_m)$.

We next analyze the condensation energy E_c. We define E_c as the difference between the actual ground state energy E_Δ at a finite $\Delta(\omega_m)$ and the would be ground state energy of the normal state, $E_{\Delta=0}$. The expression for E_c for $\gamma = 2$ has been obtained before: [96, 97, 98] and we just copy it here:

$$E_c = -N_0 \int_0^\infty d\omega_m \omega_m \frac{(\sqrt{1+D^2(\omega_m)} - 1)^2}{\sqrt{1+D^2(\omega_m)}}$$
$$-N_0 \bar{g}^2 \int_0^\infty d\omega_m d\omega'_m \frac{\left(\sqrt{1+D^2(\omega_m)} - \sqrt{1+D^2(\omega'_m)}\right)^2}{\sqrt{1+D^2(\omega_m)}\sqrt{1+D^2(\omega'_m)}} \frac{\omega_m \omega'_m}{(\omega_m^2 - (\omega'_m)^2)^2} \quad (4.75)$$

This formula has been derived with the use of (**??**) and is therefore valid only for the solutions of the gap equation. Both terms in (4.75) are negative, i.e. any solution of the gap equation lowers the ground state energy compared to the normal state.

Substituting (4.74) into (4.75), we find that $E_c = E_{c,\xi}$ is a continuous function of ξ.

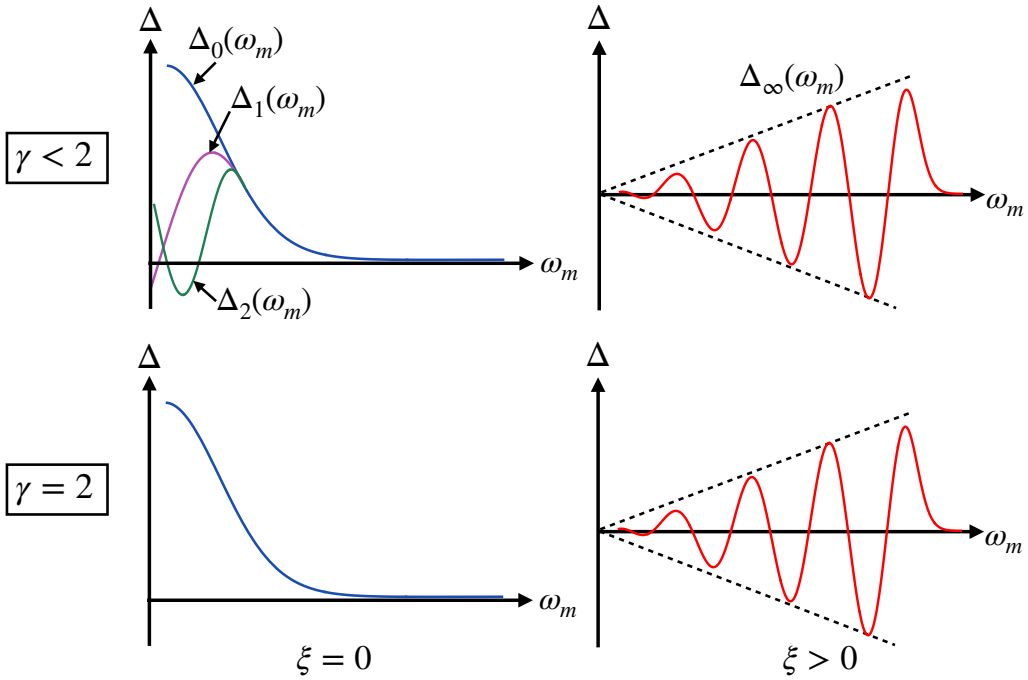

Figure 4.22: The gap function $\Delta_n(\omega_m)$ for $\gamma < 2$ and $\gamma = 2$. For $\gamma < 2$, $\Delta_n(\omega_m)$ changes sign n times. As γ gets close to 2, the frequency region where these n sign changes happen, shrinks to progressively smaller $\omega_m = 0$, and at $\gamma = 2 - 0$, $\Delta_n(\omega_m)$ with finite n collapse into $\Delta_0(\omega_m)$ at all $\omega_m > 0$. The continuum set of $\Delta_\xi(\omega_m)$ at $\gamma = 2 - 0$ emerges from $\Delta_n(\omega_m)$ with $n \to \infty$, and the continuous parameter ξ is determined by how the double limit $n \to \infty$ and $\gamma \to 2$ is taken. As the consequence, all $\Delta_\xi(\omega_m)$ with $\xi > 0$ change sign infinite number of times between $\omega_m = 0$ and $\omega_m \sim \bar{g}$. The solution of the linearized gap equation is the $\xi \to \infty$ limit of this set.

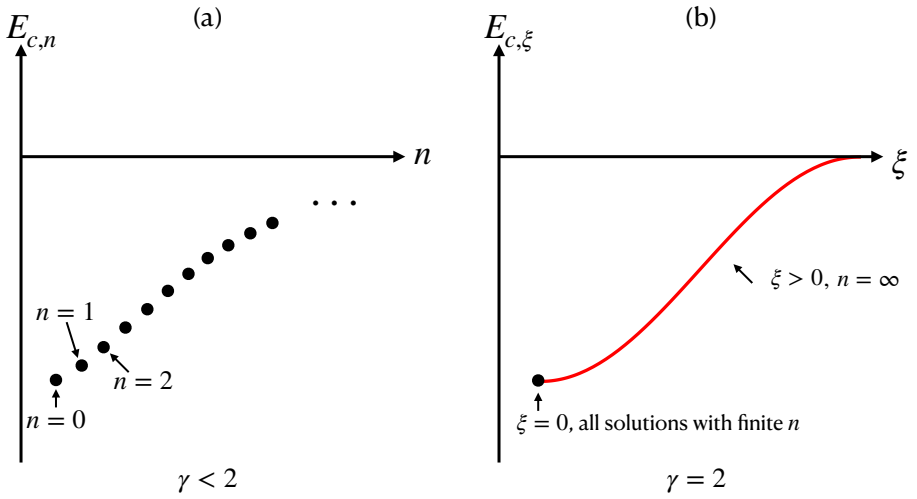

Figure 4.23: (a) The condensation energy E_c the solutions of the Eliashberg gap equation for $\gamma < 2$. $E_c = E_{c,n}$ is a discrete function of a number of a solution, n. The largest condensation energy is for $n = 0$. (b) The condensation energy $E_{c,\xi}$ for $\gamma = 2$. $E_{c,\xi}$ is a continuous function of the parameter ξ. The condensation energy at $\xi = 0$ is the accumulation point of all $E_{c,n}$ from $\gamma < 2$ with finite $n = 0, 1...$ Every other point on the curve $E_{c,\xi}$ comes from the limit $n \to \infty$, and different ξ correspond to different ways how the double limit $n \to \infty$ and $\gamma \to 2$ is taken. In the limit $\xi \to \infty$, E_c is the condensation energy for infinitesimally small gap function $\Delta_\infty(\omega_m)$.

At $\xi \gg 1$,

$$E_{c,\xi} = -aN_0 \frac{\bar{g}^2}{\xi^4} \tag{4.76}$$

where $a = O(1)$. It is natural to expect that $|E_{c,\xi}|$ increases with decreasing ξ and reaches a maximum at $\xi = 0$, see Figure 4.23. [2]

For real frequency solutions, we note that the universal contribution (4.62) once rotated onto real axis, becomes

$$D_{\infty;u}(\omega) \sim \sqrt{2}\epsilon e^{\frac{i}{\pi}\left[\left(\frac{\omega}{\bar{g}}\right)^2 + \log\left(\frac{\omega}{\bar{g}}\right)^2\right]}. \tag{4.77}$$

[2] The second term in (4.75) diverges logarithmically at $\xi = 0$ if we use $D_0(\omega) \approx \Delta(0)/\omega$ at small frequencies. This divergence comes from the putative normal state energy $E_{\Delta=0}$ while the ground state energy E_Δ remains finite. For $\xi > 0$, both $E_{\Delta=0}$ and E_Δ have logarithmic singularities, which cancel out in $E_c = E_\Delta - E_{\Delta=0}$.

which is no longer exponentially small and is oscillating for $\omega > \bar{g}$. The oscillating period is set by $\omega^2/\bar{g}^2$ rather than by $\ln(\omega^2/\bar{g}^2)$ for $\omega < \bar{g}$.

The $n = 0$ solution on real frequency axis is governed by an approximated equation similar to (4.43), and the result is

$$D_0(\omega) = \frac{1}{\sin \phi_0(\omega + i0)} \tag{4.78}$$

where

$$\phi_0(\omega) \approx \frac{1}{\pi}\left(\log\left(\frac{\omega}{\bar{g}}\right)^2 + \left(\frac{\omega}{\bar{g}}\right)^2 + C\right) \tag{4.79}$$

This is a sign-changing function of ω, whose real part almost diverges at a set of frequencies where $\phi_0(\omega) = p\pi$, and $p = 1, 2..$ is an integer. The imaginary component $D_0''(\omega)$ is a set of $\delta-$functions at these frequencies.

The continuous set of solutions also exist on real frequency axis, and can be seen by similar expansion that we used in obtaining (4.74). For derivation details please see Ref[**?**]. Here we only present the solutions. The continuous set can also be described using a parameter ξ, and the solution is expressed as

$$D_\xi(\omega) = \frac{-2ie^{i\phi_0(\omega)}}{1 + \xi - e^{2i\phi_0(\omega)}/(1+\xi)} = \frac{1}{\sin[\phi_0(\omega) + i\log(1+\xi)]} \tag{4.80}$$

where ϕ_0 is given by (4.79). The parameter ξ runs between 0 and ∞. For $\xi = 0$, Eq. (4.80) yields $D_0(\omega) = 1/\sin\phi_0(\omega)$, which agrees with (4.78) (one should add $i0$ to ω in this case). At $\xi \to \infty$ we recover, by construction, the solution of the linearized gap equation. For any ξ, including $\xi = 0$, $D_\xi(\omega)$ oscillates up to an infinite frequency, and its phase $\eta_\xi(\omega)$ winds up by an infinite number of 2π between $\omega \sim \bar{g}$ and $\omega = \infty$.

We see therefore that in both limits $\omega \ll \bar{g}$ and $\omega \gg \bar{g}$, the solutions of the non-linear gap equation form a continuous one-parameter set, Eq. (4.80). We conjecture that for any value of ξ, one can merge small-ω and large-ω expressions into a single $D_\xi(\omega)$.

With $D(\omega)$ we can calculate the fermionic density of states, defined in (4.57). In our case, the form of $N(\omega) = N_\xi(\omega)$ strongly depends on ξ. At small $\omega < \bar{g}$, $N_\xi(\omega)$ remains finite down to $\omega = 0$ for all $\xi > 0$. In this respect, all such solutions describe gapless superconductivity. The gap function $\Delta_0(\omega)$ tends to a finite $\Delta_0(0)$ at small ω,

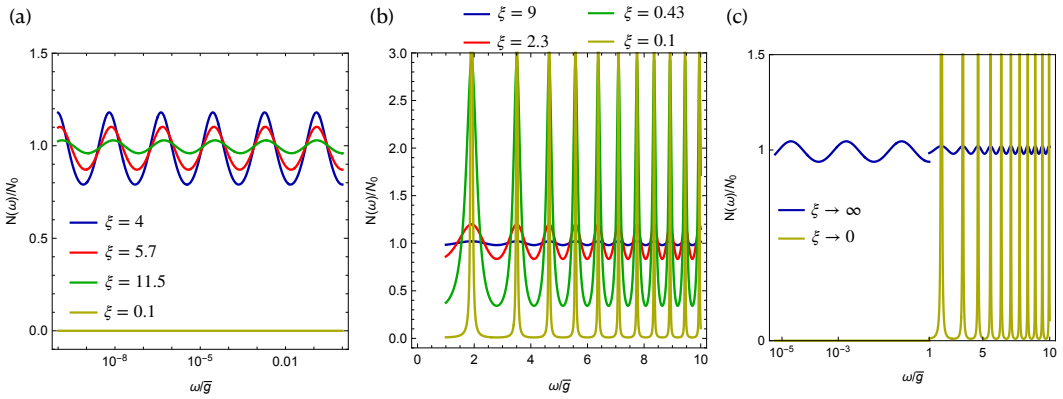

Figure 4.24: DoS $N_\xi(\omega)$ for (a) $\omega < \bar{g}$ and (b) $\omega > \bar{g}$ and for different ξ. For all $\xi > 0$, $N_\xi(\omega)$ remains finite down to $\omega = 0$ (a gapless superconductivity). For $\xi = 0$, the DoS $N_0(\omega)$ vanishes at small ω and has a set of $\delta-$functional peaks at $\omega > \bar{g}$. In panel (c) we present the schematic plot of the DoS at all frequencies.

and the corresponding $N_0(\omega)$ vanishes, like in BCS superconductor. We show this in Figure 5.8(a).

At $\omega > \bar{g}$, $\Delta_\xi(\omega)$ is given by (4.80), and $N_\xi(\omega) = N_0 \,\mathrm{Im}\tan[\phi_0(\omega) + i\log(1+\xi)]$. For $\xi > 0$, $N_\xi(\omega)$ oscillates around N_0 up to $\omega = \infty$. The amplitude of the oscillations increases with decreasing ξ. For $\xi = 0$, $N_0(\omega) = N_0\delta/(\cos^2\phi_0(\omega) + \delta^2)$, where $\delta = 0+$. This DoS consists of a set of $\delta-$functions at the points ω_k, for which $\phi_0(\omega_k) = \pi/2 + k\pi$ (k is an integer) (Refs [58, 99, 100]). We show this in Figure 5.8(b). In Figure 5.8(c) we show $N_\xi(\omega)$ in the whole range of frequencies.

At last, we discuss an interesting consequence of the continuous set of solutions, namely the phase fluctuations. We will formally discuss phase fluctuations in Chapter 6, where we only calculate the fluctuation effect from the largest solution with $n = 0$. But here since the solution becomes continuous the condensation energy spectrum becomes flat around $\xi = 0$, see Figure 4.23, and this fact opens up a channel where the superconducting phase change fluctuates without costing extra energy. To see how this happens, we calculate the phase stiffness.

Without introducing the continuous set of solutions, the bare phase stiffness at $T = 0$ is

$$\rho_s(T=0) \sim E_F \frac{\omega_D \Delta(0)}{\bar{g}^2} \sim \frac{T_p}{\lambda_E} \tag{4.81}$$

where $T_p \sim \Delta(0)$ is the onset temperature of the pairing. As long as $\lambda_E \leq 1$, $\rho_s(T = 0) > T_p$. With the renormalization from the continuous set of solutions, the fully dressed stiffness becomes

$$\rho_s(T) = \frac{T_p}{\lambda_E}\left(1 - \frac{T}{4\omega_D\lambda_E}\right) \tag{4.82}$$

We see from that the value of $\rho_s(T)$ at $T \to 0$ and $\omega_D \to 0$ depends on the order of limits. At $T = 0$, $\rho_s(0) = T_p/\lambda_E$ is finite and exceeds T_p. At $\omega_D \to 0$ the corrections to stiffness rapidly increase with T, and $\rho_s(T)$ becomes comparable to T at $T \sim \omega_D\lambda_E$. For the largest $\lambda_E \sim 1$, at which our theory is valid, this holds at $T \sim \omega_D$. It is tempting to associate this temperature with the actual T_c above which the system looses long-range phase coherence. And in the limit ω_D vanishes, the true transition temperature T_c vanishes.

Chapter 5

Odd frequency superconductivity at a quantum critical point.

So far our discussion on the solutions of (2.26) are restricted to the solutions with $\Delta(-\omega_m) = \Delta(\omega_m)$, i.e. the even frequency solutions. There are, however, solutions with odd frequency symmetry, namely $\Delta(-\omega_m) = -\Delta(\omega_m)$. In this Chapter we will see, these solutions are physically allowed according to Berezinskii rule, and have different symmetry properties from even frequency pairing.

Unlike even-ω pairing state which can be found in many conventional superconducting materials, odd-ω pairing state is rare yet there have been many efforts proposing its realization in condensed matter systems, by using either heterostructures or external driven fields[101, 102, 103]. For example, one can make a conventional BCS superconductor in contact with a ferromagnet, and odd-ω pairing arises near the interface as a result of proximity effect[104, 105]. Later it is found that spin rotation symmetry breaking by an external exchange field is not necessarily a key ingredient and one can simply make a p-wave superconductor in contact with a normal metal to realize odd-ω pairing[106, 107, 108, 109, 110]. In multiband systems where there is an additional index which enters the Pauli principle and has to be treated on equal footing as spin index, hybridization between different bands or orbitals also leads to possible realization of odd-ω pairing[111, 112, 113].

In addition to these theoretical scenarios, we study the odd frequency pairing in a

different system without heterostructure, external field and hybridization, which is the pairing system at a quantum critical point(QCP). Close to a QCP, the fermion-fermion interaction is mediated by order parameter fluctuations, and therefore becomes dynamic. If this interaction leads to superconductivity, the superconducting order parameter in principle has to incorporate the dependence on frequency, which is sometimes nontrivial. And like in many previous studies on odd frequency pairing, we will use Matsubara formalism in which the Berezinskii rule also applies. So from now on when we say a pairing state is even or odd in frequency, we implicitly means Matsubara frequency ω_m.

We first study the case $0 < \gamma < 1$ and find that there also exists an infinite number of odd-ω solutions $\Delta_n(\omega_m)$ to the gap equations, where the index n labels different solution and $n = 0, 1, 2, ...$ Then we focus on $n = 0$ solution which has the largest onset temperature($T_{p,0}$ is the largest), and solve the nonlinear gap equation on both Mastubara frequency axis and real frequency axis. We also apply the same analysis to look for possible odd frequency pairing state when $\gamma > 1$. Unlike the $\gamma < 1$ case, we don't have a solution to the nonlinear gap equation at finite T. At $T = 0$ however, we argue that multiple solutions to the linearized gap equation exists, but they do not develop to ordered states at finite T. Interestingly, we obtain a new linearized gap equation at $T = 0$, the solutions of which form a continuum in its parameter space. The solutions of the original equation, appear as critical curves in this continuum.

5.1 Berezinskii rule

The gap function that we keep seeking above, is also expressed as[2, 114]

$$\Delta_{ab,\alpha\beta}(\boldsymbol{r}, t) \propto \langle \mathcal{T} c_{a,\alpha}(\boldsymbol{r}, t) c_{b,\beta}(0, 0) \rangle \tag{5.1}$$

. Here $\mathcal{T}$ is time ordering operator, a, b are the orbital indexes and α, β are spin indexes. The space time coordinates $(\boldsymbol{r}, t)$ are in relative sense so the coordinates of the second fermion can be set to origin without loss of generality. A totally equivalent function $\Delta_{ab,\alpha\beta}(\boldsymbol{k}, \omega)$ is the Fourier transform of the above correlation function, which introduces momentum and frequency instead of space time coordinates. Properties of the superconductivity can be found by studying its gap function.

Fermion statistics puts constraint on the gap function, which can be seen by considering the following symmetry operations[115, 116, 117]: An orbital permutation operation O which permutes the orbital a and b, a spin permutation operation S which exchanges spin α and β, a coordinate permutation P^* which exchanges the spatial coordinates of the two fermions and thus change $\boldsymbol{r}$ into $-\boldsymbol{r}$ (by virtue of Fourier transform this operation turns $\boldsymbol{k}$ into $-\boldsymbol{k}$), and lastly a time permutation T^* which turns t into $-t$ (and thus ω into $-\omega$). The outcomes of P^* and T^* operation are similar to those of the parity and time-reversal operators but they are different essentially, since the permutation of two sets of space time coordinates does not necessarily involve reversing them and more importantly the time reversal operator is anti unitary which will turn the correlation function into its complex conjugate. According to fermion statistics, permutation of two fermions at equal time (hence $t = 0$) leads to an overall sign change of the two fermion state, namely $\Delta_{ab,\alpha\beta}(\boldsymbol{r}, 0) = -\Delta_{ba,\beta\alpha}(-\boldsymbol{r}, 0)$ or by Fourier transform $\int d\omega \Delta_{ab,\alpha\beta}(\boldsymbol{k}, \omega) = -\int d\omega \Delta_{ba,\beta\alpha}(-\boldsymbol{k}, \omega)$. The subtlety comes from the fact that this integration is formally from $-\infty$ to ∞, and it allows for two possibilities for the integrand:

$$\Delta_{ab,\alpha\beta}(\boldsymbol{k}, \omega) = -\Delta_{ba,\beta\alpha}(-\boldsymbol{k}, \omega) \tag{5.2}$$

or

$$\Delta_{ab,\alpha\beta}(\boldsymbol{k}, \omega) = -\Delta_{ba,\beta\alpha}(-\boldsymbol{k}, -\omega) \tag{5.3}$$

Apparently the first equation can be treated as a special case of the second equation, provided the gap function is even in ω. The second equation is more general and can be equivalently expressed as an operation constraint $OSP^*T^* = -1$ and it is first noticed by Berezinskii[116]. This rule for symmetry constraint opens up a broad class pairing states with $T^* = -1$ and is not only limited to the topic of superconductivity which we address in this paper.

Although the involvement of orbital degrees of freedom is important in multiband materials, we shall in this paper neglect the orbital dependence for simplicity and from now on focus on the one band case with $O = 1$. In an even-ω pairing state where $T^* = 1$, S and P^* must have opposite sign. Specifically, spin singlet pairing ($S = -1$) must be s-wave, p-wave, etc., in order to fulfill the condition $P^* = 1$. While for spin triplet pairing ($S = 1$), it must be p-wave, f-wave, etc. because $P = -1$ in this situation. These

even-ω paring states are so far the most acknowledged superconducting state studied intensively in literatures. In contrast, if we take the other possibility with $T^* = -1$ in the Berezinskii rule, we end up with a new pairing state where the gap function is odd in frequency. And according to the rule, S and P^* must have the same sign. Consequently a spin singlet pairing must be in p-wave, f-wave, etc., while a spin triplet pairing must be in s-wave, d-wave, etc.

5.2 Solutions on Matsubara axis

We shall search for an odd frequency pairing solution $\Phi(-\omega_m) = -\Phi(\omega_m)$ of the Eliashberg equations on Matsubara axis based on extension to $N \neq 1$. We focus on the case when $\gamma < 1$ in this section, and we will discuss the case $\gamma > 1$ in Sec.5.4.

5.2.1 linearized equation at $T = 0$: N_{cr} and exact solution

We first analize the linearized equaitons at zero temperature. The existence of solutions at $T = 0$ is a direct indication of existence of multiple solutions to the gap function, because otherwise we only have a solution to the non-linear gap equation. It can also help to identify the critical value N_{cr} which separate a non-Fermi liquid normal state and a superconducting state. The equation for self energy gives $\Sigma(\omega_m) = \bar{g}^\gamma \omega^{1-\gamma}/(1-\gamma)$. The gap equation is obtained by combining these equations in (2.29) and is expressed as

$$\Delta(\omega_m) = \frac{1}{2}\int_{-\infty}^{\infty} d\omega_n \left(\frac{1}{N}\frac{\Delta(\omega_n)}{\omega_n} - \frac{\Delta(\omega_m)}{\omega_m}\right)\frac{\mathrm{sgn}(\omega_n)}{|\omega_n - \omega_m|^\gamma} \tag{5.4}$$

Here we continue using ω_m to denote frequency even though it is a continuous variable. For the even frequency pairing, the exact solution of this integral equation has been found for $\gamma < 1$. Following almost completely parallel route, the exact solution of (5.4) can also be found. But before we embarking on presenting the exact solution, we first show that one can use series expansion to solve this equation at small frequencies. From this the value of N_{cr} can be determined.

We focus on odd frequency pairing by requiring $\Delta(-\omega_m) = -\Delta(\omega_m)$. Using this condition one can convert the integral interval into from 0 to ∞ and expand $\Delta(\omega_m)$ using series such that $\Delta(\omega_m)/\omega_m = \omega_m^\rho \sum_{n=0}^{\infty} C_n(\omega_m^\gamma)^n$ and we choose $|C_0| = 1$. Substitute

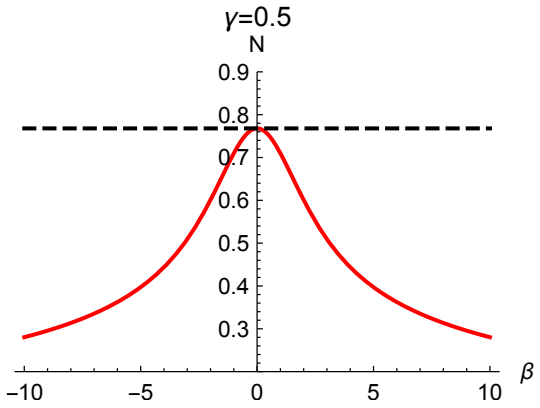

Figure 5.1: Solution of (5.5) for a particular $\gamma = 0.5$. The red curve is ϵ_β and is the r.h.s. of (5.5), while the black dashed line marks the location of N_{cr}. Apparently, this equation has solution only when $N < N_{cr}$.

this into (5.4) and regularize the integral using Gamma functions, we obtain an index equation that determines ρ. It is then found $\rho = \frac{\gamma}{2} - 1 + b$ and $b = i\gamma\beta_N$ is pure imaginary. The outcome of this fact is that, at lowest frequencies $\omega_m \ll 1$, the gap function behaves as $\Delta(\omega_m) = \mathrm{sgn}(\omega_m)|\omega_m|^{\gamma/2}\cos(\beta_N \log(|\omega_m|^\gamma) + \phi)$. The oscillations are logarithmic the same as the case for even frequency solution. The equation for β_N is

$$N = \epsilon_{\beta_N} = \frac{1-\gamma}{2\Gamma(\gamma)}|\Gamma(\frac{\gamma}{2} + i\gamma\beta_N)|^2 \left(\frac{\cosh \pi\gamma\beta_N}{\cos \pi\gamma/2} - 1\right) \tag{5.5}$$

This equation is pretty similar to that of even frequency pairing, there we have $+1$ for the last term inside the parenthesis. For a given $\gamma < 1$, ϵ_β as a function of β, has a maximum at $\beta = 0$ ans is symmetric. We show this in Fig5.1 for a particular case when $\gamma = 0.5$. This equation has solution only when $N \leq \epsilon_{\beta=0}$ and therefore, the critical value for N is $N_{cr} = \epsilon_{\beta=0}$. In Fig.5.2 we plot N_{cr} as a function of γ. For $\gamma < 1$, this curve increases monotonically with increasing γ, hits $N_{cr} = 1$ at $\gamma = 1$. In the opposite limit $\gamma \to 0$, $N_{cr} \to 0$.

The coefficients C_n is determined by a recursion relation $C_n = C_{n+1}I_\gamma(n+1)$ and

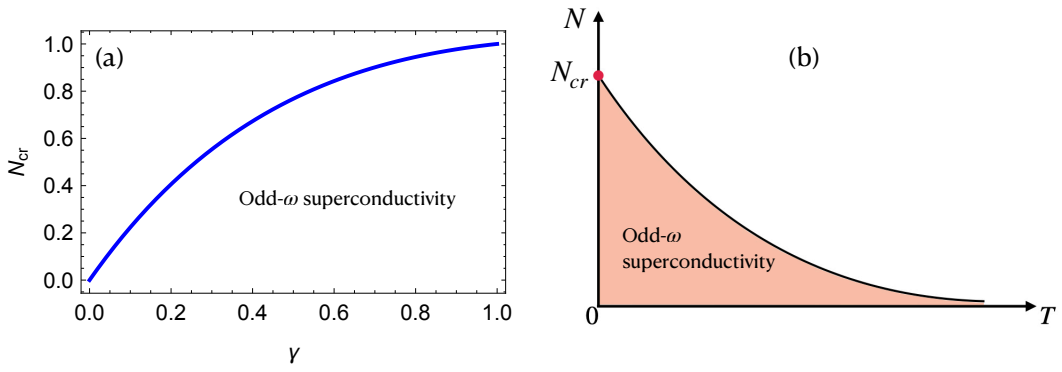

Figure 5.2: (a)N_{cr} as a function of γ for odd frequency pairing. For a given γ, linearized gap equation (5.4) has a solution only when $N < N_{cr}$. (b) The odd-ω superconductivity phase diagram for a particular γ.

is thus given by $C_n = C_0 \prod_{m=1}^{n} \frac{1}{I_\gamma(n)}$, where $I_\gamma(n)$ is given by

$$\begin{aligned} I_\gamma(n) = \frac{1}{2}\Big[\frac{1}{N}\Big(&B(1-\gamma, \frac{\gamma}{2}+\gamma n + i\gamma\beta_N) \\ &+B(1-\gamma, \frac{\gamma}{2}-\gamma n - i\gamma\beta_N) \\ &- B(\frac{\gamma}{2}+\gamma n + i\gamma\beta_N, \frac{\gamma}{2}-\gamma n - i\gamma\beta_N)\Big) - \frac{2}{1-\gamma}\Big] \end{aligned} \tag{5.6}$$

where $B(p,q)$ is Beta function. Note that $I_\gamma(0) = 0$ is exactly the index equation (5.5).

The method of local series expansion works only at $\omega_m < 1$. For large frequencies, it is apparent from the gap equation that $\Delta(\omega_m) \propto \mathrm{sgn}(\omega_m)/|\omega_m|^{\gamma+1}$. To see this, we note at $\omega_m \gg 1$, the $\Delta(\omega_m)/\omega_m$ term in (5.4) can be neglected. Using $\Delta(-\omega_m) = -\Delta(\omega_m)$ to convert the integral interval to $(0,\infty)$ then the interaction term is $\frac{1}{|\omega_m-\omega_n|^\gamma} - \frac{1}{|\omega_m+\omega_n|^\gamma} \approx 2\gamma\omega_n/|\omega_m|^{\gamma+1}$. Therefore, at large $\omega_m > 0$, $\Delta(\omega_m) \approx \gamma/(N|\omega_m|^{\gamma+1}) \int_1^\infty d\omega_n \Delta(\omega_n) \propto 1/|\omega_m|^{\gamma+1}$. The large frequency behavior of odd frequency $\Delta(\omega_m)$ is different from that of even frequency, there the contribution of interaction term from positive and negative frequency is additive, and as a result $\Delta(\omega_m) \sim 1/|\omega_m|^\gamma$.

An exact solution which connects the low frequency logarithmic oscillation and the high frequency power law decay exists. Here we only report the solution. Detailed derivation of this solution can be found in Ref. To obtain the solution, one needs to

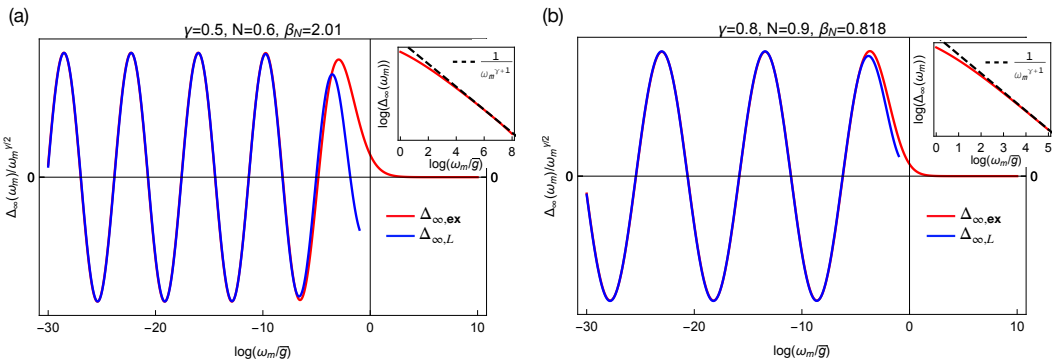

Figure 5.3: Solutions of the zero temperature linearized gap equation (5.4) for a two particular cases: (a)$\gamma = 0.5$, $N = 0.6$ (in this case $N_{cr} = 0.768$) and (b)$\gamma = 0.8$, $N = 0.9$ (in this case $N_{cr} = 0.945$). In both plots, the red curves correspond to the exact solution obtained using (5.7) and (5.8). The insets show that at large frequency $\Delta(\omega_m) \propto 1/\omega_m^{\gamma+1}$. The blue curves are obtained using small frequency series expansion, which we call local contribution $\Delta_{\infty,L}(\omega_m)$. At $\omega_m \ll 1$, $\Delta_{\infty,L}$ coincides with $\Delta_{\infty,\text{ex}}$ as expected, both showing logarithmic oscillations. In these plots we only show data for $\omega_m > 0$, and gap functions at negative frequencies are obtained using $\Delta(-\omega_m) = -\Delta(\omega_m)$.

first compute the integral,

$$I(\beta) = \frac{1}{2}\int_{-\infty}^{\infty} d\beta' \log|1 - \frac{1}{N}\epsilon_{\beta'}| \tanh(\pi(\beta' - \beta)) \tag{5.7}$$

where ϵ_β is the one given in (5.5). After obtaining this function, the gap function for $\omega_m > 0$ is given by

$$\Delta_{\text{ex}}(\omega_m) = \int_{-\infty}^{\infty} d\beta \frac{\cos[\beta \log(\omega_m^\gamma|1-\gamma|) + I(\beta)]}{\sqrt{\cosh[\pi(\beta - \beta_N)]\cosh[\pi(\beta + \beta_N)]}} \tag{5.8}$$

Here β_N is the solution of (5.5). To shed some light on these sophisticated integrals, we evaluate them numerically and show $\Delta_{\infty,\text{ex}}(\omega_m)$ in Fig.5.3 together with the local low frequency series expansion $\Delta_{\infty,L}(\omega_m)$ obtained from (5.6). Clearly the exact solution shows $1/|\omega|^{\gamma+1}$ decaying behavior at large frequencies. While at $\omega_m \ll 1$, $\Delta_{\infty,L}$ coincides with $\Delta_{\infty,\text{ex}}(\omega_m)$ as expected, and both show logarithmic oscillations.

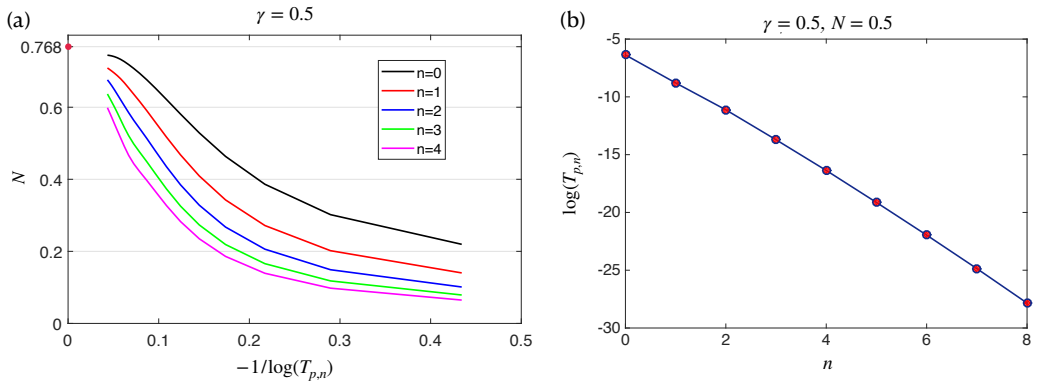

Figure 5.4: (a)The first five solutions to the linearized gap equation for $\gamma = 0.5$ and at various temperatures. For better illustration we plot N versus $-1/\log(T_{p,n})$. As $T \to 0$ (and hence $-1/\log(T) \to 0$), all curves will terminate at $N_{cr} = 0.768$, consistent with $T = 0$ analysis. (b) Linear dependence of $\log(T_{p,n})$ on n for a particular $\gamma = 0.5$ and $N = 0.5$, which indicates $T_{p,n}$ decays with n exponentially.

5.2.2 Linearized gap equation at finite temperature: The existence of multiple solutions

We now turn to finite temperature analysis of the linearized gap equation. We find that for a given $N < N_{cr}$ for a particular $\gamma < 1$, there is an infinite number of solutions to the gap equation, which we use an index $n = 0, 1, 2, ...$ to distinguish. In Fig.5.4(a) we show the first five solutions to the linearized gap equation for a particular $\gamma = 0.5$, by plotting the corresponding N v.s. T curve. All these curves stem from N_{cr} at $T = 0$ and decays monotonically with increasing T. Thus for any $N < N_{cr}$ the infinite set of solutions exists. Each of these solutions has its unique onset temperature for pairing $T_{p,n}$ and $\Delta_n(\omega_m)$ changes sign n times for $\omega_m > 0$. The sign preserving solution $\Delta_0(\omega_m)$ has the largest $T_{p,0}$, while other $T_{p,n}$ decays with n exponentially. We show this in Fig.5.4(b). This exponential decay is directly related to the logarithmic oscillation of $\Delta_\infty(\omega_m)$ found above. As $\Delta_\infty(\omega_m)$ corresponds to the case when $n \to \infty$, from $n-1$ to n there is half of oscillation period gained in $\Delta_n(\omega_m)$ which means $T_{p,n}$ must decay exponentially to reproduce the logarithmic oscillation.

These features are very similar those of the even frequency pairing solution reported in.However there is one major difference for the sign preserving solution with $n = 0$. In

both even and odd frequency pairing solutions, the self energy of the linearized equation vanishes at the first two Matsubara frequencies, namely $\Sigma(\pm\pi T) = 0$. This fact has non trivial impact on the even frequency pairing solution, which renders a prominent pairing vertex at these two frequencies. Indeed, if we consider the equation for $\Phi(\omega_m)$ only at $\pm\pi T$, the equation is simply $N\Phi(\pi T) = \Phi(-\pi T)/(2\pi T)^\gamma$. If the solution is even in ω_m, we immediately obtain $N = 1/(2\pi T)^\gamma$. This scaling holds even as $T \to 0$ and indicates N should be infinite in zero temperature limit, in contrast to $T = 0$ analysis in which a finite N_{cr} is present. Therefore there is a discontinuity between zero temperature and finite temperature results. $\Phi(\omega_m)$ at other frequencies can be viewed as induced by $\Phi(\pm\pi T)$ as they are all parametrically smaller. This first Matsubara physics only occur in the $n = 0$ sign preserving solution. For other solutions with $n > 0$ there is not such a discontinuity between $T = 0$ and $T \to 0$ analysis, and all $T_{p,n}$ curves terminates at N_{cr} in zero temperature limit. However, for the odd frequency solution, even in the sign preserving case ($n = 0$) $\Phi(\pi T)$ is vanishingly small and one cannot just only consider fermions at $\pm\pi T$ in the gap equation. In other words, the first Matsubara physics which arises in even frequency pairing does not hold for odd frequency pairing. As a result, finite temperature results extrapolate to zero temperature results continuously.

5.2.3 Nonlinear gap equation

The full equations can be solved by numerical iteration at finite temperatures. However this method is stable only for the solution with the largest onset temperature, i.e. $n = 0$ solution. Here we only focus on this solution. In Fig.5.5 we plot the numerical result for a particular case.

In the limit $T \to 0$, the summations in Eq.(**??**) reduce to integrations because $2\pi T \sum_m \to \int d\omega_m$ in zero temperature limit. To understand the behavior of the gap function at large frequencies, we can approximate the equations by two contributions

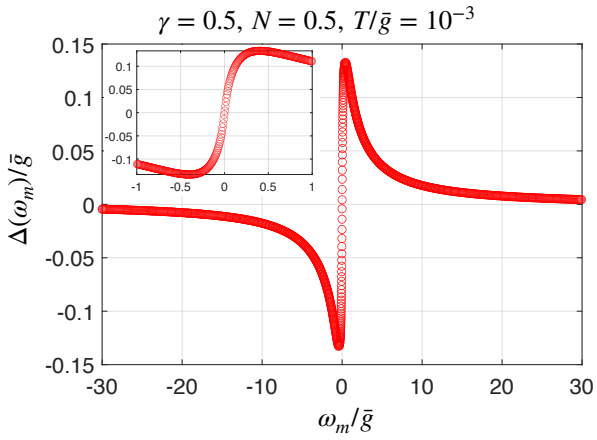

Figure 5.5: $\Delta(\omega_n)$ obtained from the nonlinear gap equation for $\gamma = 0.5$, $N = 0.5$ and $T/\bar{g} = 10^{-3}$. For a clear presentation of $\Delta(\omega_n)$ at small frequencies, we plot in the inset the same $\Delta(\omega_n)$ but in a much smaller frequency range.

from $|\omega_m| > |\omega_n|$ and $|\omega_m| < |\omega_n|$. For the pairing vertex, we have for $\omega_n \gg \bar{g}$,

$$\Phi(\omega_n) \approx \frac{\gamma \bar{g}^\gamma}{N\omega_n^{\gamma+1}} \int_0^{\omega_n} d\omega_m \frac{\Phi(\omega_m)\omega_m}{\sqrt{\tilde{\Sigma}^2(\omega_m) + \Phi^2(\omega_m)}} + \frac{\gamma \bar{g}^\gamma \omega_n}{N} \int_{\omega_n}^{\infty} \frac{d\omega_m}{\omega_m^{\gamma+1}} \frac{\Phi(\omega_m)}{\sqrt{\tilde{\Sigma}^2(\omega_m) + \Phi^2(\omega_m)}}$$
$$\tilde{\Sigma}(\omega_n) \approx \omega_n + \frac{\gamma \bar{g}^\gamma}{\omega_n^{\gamma+1}} \int_0^{\omega_n} d\omega_m \frac{\tilde{\Sigma}(\omega_m)\omega_m}{\sqrt{\tilde{\Sigma}^2(\omega_m) + \Phi^2(\omega_m)}} + \gamma \bar{g}^\gamma \omega_n \int_{\omega_n}^{\infty} \frac{d\omega_m}{\omega_m^{\gamma+1}} \frac{\tilde{\Sigma}(\omega_m)}{\sqrt{\tilde{\Sigma}^2(\omega_m) + \Phi^2(\omega_m)}} \tag{5.9}$$

In the limit $\omega_n \to \infty$, the first term of $\Phi(\omega_n)$ in (5.9) is the dominant term and the second one is negligible. For $\tilde{\Sigma}$ it will reduce to its bare ω_n term. Hence at large ω_n, $\Phi(\omega_n) \sim 1/\omega_n^{\gamma+1}$ while $\tilde{\Sigma}(\omega_n) \sim \omega_n$, and consequently $\Delta(\omega_n) \sim 1/\omega_n^{\gamma+1}$.

In the opposite limit when $\omega_n \to 0$, $\Phi(\omega_n)$ should be vanishingly small because we have $\Phi(\omega_n = 0) = 0$ for odd frequency pairing. This is different from even frequency pairing where $\Phi(\omega_n)$ saturates to some constant as $\omega_n \to 0$. For the same reason the self energy $\tilde{\Sigma}(\omega_n)$ also vanishes at $\omega_n \to 0$. To solve the nonlinear equation for small frequencies, we make the ansatz that $\Phi(\omega_n) \gg \tilde{\Sigma}(\omega_n)$ at $\omega_n \ll \bar{g}$. We will prove in the following that it's indeed the case. Using this ansatz, the two equations become

linearized, namely,(for $\omega_n > 0$)

$$\begin{aligned}\Phi(\omega_n) &= \frac{\bar{g}^\gamma}{2N}\int_0^\infty d\omega_m \left(\frac{1}{|\omega_n-\omega_m|^\gamma} - \frac{1}{(\omega_n+\omega_m)^\gamma}\right) \\ \tilde{\Sigma}(\omega_n) &= \omega_n + \frac{\bar{g}^\gamma}{2}\int_0^{\omega_n} d\omega_m \frac{\tilde{\Sigma}(\omega_m)}{\Phi(\omega_m)}\left(\frac{1}{|\omega_n-\omega_m|^\gamma} - \frac{1}{(\omega_n+\omega_m)^\gamma}\right)\end{aligned} \tag{5.10}$$

where we have approximately taken the upper limit of the integrations as ∞. The integrations in the equation of $\Phi(\omega_n)$ in Eq.(5.10) can be carried out explicitly, which gives out the result: $\Phi(\omega_n) = \frac{\bar{g}^\gamma}{N(1-\gamma)}\omega_n^{1-\gamma}$. At first glance, $\tilde{\Sigma}(\omega_n)$ scales as bare ω_n. But substituting this into Eq.(5.10) and the integration gives an additional $\omega_n \log \omega_n$ term, which at $\omega \to 0$ is larger than ω_n. For convenience we assume that the gap function scales as $\Delta(\omega_n) \sim \omega_n^a$ where a is to be determined. Then we have $\tilde{\Sigma}(\omega_n) = C\omega_n^{2-\gamma-a}$. The equation for self energy becomes,

$$C\left(1 - \frac{N(1-\gamma)}{2}Q_\gamma(a)\right) = \omega_n^{\gamma+a-1} \tag{5.11}$$

where

$$\begin{aligned}Q_\gamma(a) &= \int_0^\infty dx x^{1-a}\left(\frac{1}{|x-1|^\gamma} - \frac{1}{(x+1)^\gamma}\right) \\ &= B(2-a,1-\gamma) + B(1-\gamma, a+\gamma-2) - B(2-a,a+\gamma-2)\end{aligned} \tag{5.12}$$

To ensure the convergence of the integration in $Q_\gamma(a)$, we must have $\gamma + a > 1$ to avoid the UV divergence. Using this condition we see the rhs of Eq.(5.11) $\omega_n^{\gamma+a-1}$ tends to 0 as $\omega_n \to 0$ and the equation is reduced to

$$\frac{(1-\gamma)}{2}Q_\gamma(a) = \frac{1}{N} \tag{5.13}$$

From this equation, one can determine the index a for a given γ and N, and hence the scaling behavior of $\Delta(\omega_n)$ at small frequencies. We find for any $0 < \gamma < 1$, as long as $N < N_{cr}$ which is the condition for the onset of odd-ω pairing, a is always smaller than 1. To see this, we notice that the function $F(a) = (1-\gamma)Q_\gamma(a)/2$ diverges at $a = 1-\gamma$, and decays monotonically as a increases from $1-\gamma$ to 1. We show $F(a)$ for different γ in Fig.5.13(a) At $a = 1$, $F(1) = 1$ for any γ. The dashed lines in Fig.5.13(a) shows the

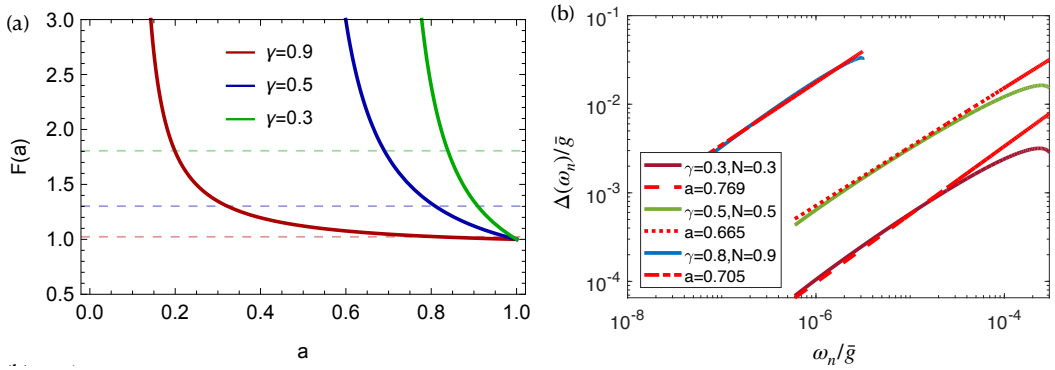

Figure 5.6: (a) The function $F(a) = (1-\gamma)Q_\gamma(a)/2$ for different γ. $F(a)$ diverges at $1-\gamma$ and decays monotonically before reaching 1 at $a = 1$. The dashed line shows the position of $1/N_{cr}$ for each γ. In order to have solution to Eq.(5.13) for $N < N_{cr}$, we always have $a < 1$. (b) Comparison between numerical results from the full nonlinear gap equation and the scaling form $\Delta(\omega_n) \sim \omega_n^a$ at small frequencies in zero temperature limit, where a is obtained from Eq(5.13) for a given γ and N. From clear presentation, the plot is in log-log scaling.

position of $1/N_{cr}$ for each γ. Notice from our above analysis on N_{cr} that $N_{cr} < 1$ for any $0 < \gamma < 1$, which means if $N < N_{cr}$ is satisfied, the equation $F(a) = 1/N$ always has a solution for $1-\gamma < a < 1$. This subtle fact reveals that at small frequencies, the gap function $\Delta(\omega_n) \sim \omega_n^a$ is much larger than the bare ω_n, because we always have $a < 1$. Similarly, from the ratio $\tilde{\Sigma}(\omega_n)/\Phi(\omega_n) \sim \omega_n^{1-a}$ we know as long as $a < 1$, $\tilde{\Sigma}(\omega_n) \ll \Phi(\omega_n)$ at small frequencies and therefore, the ansatz was guaranteed.

In order to confirm our analysis, we solve the full nonlinear equation using numerical iteration. In Fig.5.13(b) we show the numerical results, obtained for different γ, N at very low temperatures. As a comparison, we also show the scaling behavior $\Delta(\omega_n) \sim \omega_n^a$. From the figure it is clear that our analysis agree well with numerical results.

5.3 Solutions on real axis

We now turn to our analysis on the real axis. The two coupled equations can be analytically continued to real frequency axis by means of spectral representation of both fermion and boson Green's function. We follow similar procedure to even-ω solution in Ref.[118, 119, 120] and derive the two equation on real axis. The difference is that

for odd-ω pairing problem, the pairing vertex on Matsubara axis $\Phi(i\omega_m) = i\Phi(\omega_m)$ is purely imaginary(and so is the gap function $\Delta(i\omega_m) = i\Delta(\omega_m)$), in order to satisfy the property of Green's function that $G(-i\omega_m, \boldsymbol{k}) = G^*(i\omega_m, \boldsymbol{k})$. This implies on the real axis, the real part $\Phi'(\omega)$ is an odd function in ω while the imaginary part $\Phi''(\omega)$ is even in ω, so that we have $\Phi(-\omega) = -\Phi^*(\omega)$(and similarly $\Delta(-\omega) = -\Delta^*(\omega)$). Taking this into account and after some lengthy but straightforward derivation, we obtain the two equations below(for $\omega > 0$),

$$\begin{aligned}
\Phi(\omega) &= A(\omega) + \frac{i}{2N}\int_{-\infty}^{\infty} d\Omega V''(\Omega)\left[S_\Phi(\omega-\Omega)\left(\tanh\frac{\omega-\Omega}{2T} + \coth\frac{\Omega}{2T}\right) - S_\Phi(\omega)\frac{2T}{\Omega}\right] \\
\tilde{\Sigma}(\omega) &= B(\omega) + \frac{i}{2}\int_{-\infty}^{\infty} d\Omega V''(\Omega)\left[S_\Sigma(\omega-\Omega)\left(\tanh\frac{\omega-\Omega}{2T} + \coth\frac{\Omega}{2T}\right) - S_\Sigma(\omega)\frac{2T}{\Omega}\right]
\end{aligned} \tag{5.14}$$

where

$$\begin{aligned}
A(\omega) &= \frac{i\pi T}{N}\sum_{m\geq 0}\frac{\Phi(\omega_m)}{\sqrt{\tilde{\Sigma}^2(\omega_m) + \Phi^2(\omega_m)}}\left[V(\omega - i\omega_m) - V(\omega + i\omega_m)\right] \\
B(\omega) &= \omega + i\pi T\sum_{m\geq 0}\frac{\tilde{\Sigma}(\omega_m)}{\sqrt{\tilde{\Sigma}^2(\omega_m) + \Phi^2(\omega_m)}}\left[V(\omega - i\omega_m) - V(\omega + i\omega_m)\right]
\end{aligned} \tag{5.15}$$

and

$$\begin{aligned}
S_\Phi(\omega) = \frac{\Phi(\omega)}{\sqrt{\tilde{\Sigma}^2(\omega) - |\Phi|^2(\omega)}},\ S_\Sigma(\omega) &= \frac{\tilde{\Sigma}(\omega)}{\sqrt{\tilde{\Sigma}^2(\omega) - |\Phi|^2(\omega)}} \\
V''(\Omega) &= \left(\frac{\bar{g}}{|\Omega|}\right)^\gamma \sin\frac{\pi\gamma}{2}\,\mathrm{sgn}(\Omega)
\end{aligned} \tag{5.16}$$

It is worth noticing that the square root in the denominators in S_Φ and S_Σ should take the branch with positive imaginary part. The interaction terms in $A(\omega)$ and $B(\omega)$ with complex frequencies are obtained by spectral representation, namely,

$$V(\omega \pm i\omega_m) = \frac{1}{\pi}\int_{-\infty}^{\infty} d\Omega \frac{V''(\Omega)}{\Omega - (\omega \pm i\omega_m)} = \frac{\bar{g}^\gamma}{(\omega_m \mp i\omega)^\gamma} \tag{5.17}$$

Eq.(5.14) can be easily verified by taking $\omega \to i\omega_n = i(2n+1)\pi T$, i.e. by going back to Matsubara axis, and the equations should reduce to those in Eq.(**??**) if the analytic continuation has been done correctly. Indeed, with the replacement $\omega \to i\omega_n$ the thermal

factor $(\tanh\frac{i\omega_n-\Omega}{2T}+\coth\frac{\Omega}{2T})$ in Eq.(5.14) vanishes and the integral $\int d\Omega V''(\Omega)/\Omega = \pi V(i\Omega=0)$ accounts for the elimination of zero frequency transfer term in Eq.(**??**) ($\omega_m=\omega_n$ term). Taking into account the contributions from $A(i\omega_n)$ and $B(i\omega_n)$ and using the odd frequency property of both $\Phi(\omega_m)$ and $\tilde{\Sigma}(\omega_m)$, Eq.(**??**) is reproduced.

Although difficult to proceed analytically, the real axis $\Phi(\omega)$ and $\tilde{\Sigma}(\omega)$ can be obtained using numerical iteration method. First of all, since the evaluation of $A(\omega)$ and $B(\omega)$ terms requires the information on Matsubara axis, for practical purpose one should first solve (**??**) and use them as input. After obtaining $A(\omega)$ and $B(\omega)$ we can use them as initial inputs to run iteration. In this method, we will inevitably need some artificial parameters. For example, the frequency range has to be finite and discrete, in order to perform integration. For our evaluation, we take around 10^3 linear sampling points such that the discrete frequency takes the form $\Omega_j = j\times d\Omega$, where $j=1,2,...$ and $d\Omega$ is a small frequency width. In order to avoid the divergence in the integrand when $\Omega=0$, we shift the first frequency point slightly away from zero by setting $\Omega_{j=0}=d\Omega/s$ where s is some large number so that $\Omega_{j=0}\ll d\Omega$. In practice the concrete value of s does not affect the final result, as long as it leads to a convergent solution. In Fig.5.7 we show the numerical results for the real ω solution $\Delta(\omega)=\omega\Phi(\omega)/\tilde{\Sigma}(\omega)$ for two different (γ,N) obtained by solving Eq.(5.14) this way. For $\gamma=0.5, N=0.5$(Fig.5.7(a)), we take $d\Omega=0.01$ and $\Omega_{j=0}=d\Omega/30$, while for $\gamma=0.9, N=0.5$ (Fig.5.7(b)) we take $d\Omega=0.03$ and $\Omega_{j=0}=d\Omega/10$. By solving the linearized gap equation, we find that the onset temperatures are $T_{p,0}/\bar{g}\approx 1.71\times10^{-3}$ for $\gamma=0.5, N=0.5$ and $T_{p,0}=0.029$ for $\gamma=0.9, N=0.5$. We then study how the gap function $\Delta(\omega)$ evolves with T. We see in both cases, the gap function is dominantly real at small frequencies, and then at some finite frequency $\Delta''(\omega)$ quickly develops and at even larger frequency, both $\Delta'(\omega)$ and $\Delta''(\omega)$ decays. This behavior maintains even as T gets close to $T_{p,0}$ (see the curve of $T=1.5\times10^{-3}$ in Fig.5.7(a)), which is similar to that of even-ω pairing case in a conventional BCS superconductor, where the imaginary part of the gap function$\Delta''(\omega)$ is also almost zero up to some finite frequency at all temperatures below T_p. One striking difference from the even frequency pairing is that for odd frequency pairing, the real part of the gap function $\Delta'(\omega)$ must tend to zero at zero frequency, as shown in Fig.5.7. This is a direct consequence of $\Delta(-\omega)=-\Delta^*(\omega)$ for odd-ω pairing solution. While for even-ω pairing, $\Delta'(\omega)$ saturates to some finite value at $\omega\to0$.

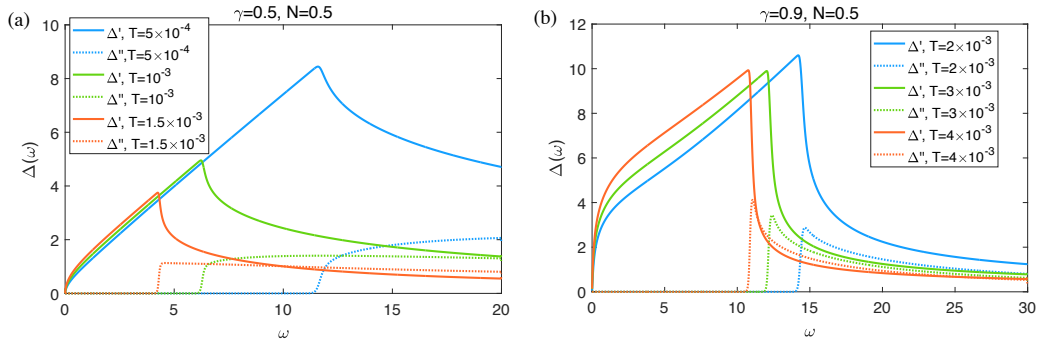

Figure 5.7: Gap function $\Delta(\omega) = \Delta'(\omega) + i\Delta''(\omega)$ along real ω axis obtained from Eq.(5.14), for $\gamma = 0.5$, $N = 0.5$ and $\gamma = 0.9$, $N = 0.5$. The $\omega < 0$ part is readily obtained using the relation $\Delta(-\omega) = -\Delta^*(\omega)$ for odd-ω pairing. Both $\Delta(\omega)$ and ω are in units of $\bar{g}$.

By solving Eq.(5.14) numerically, one can also obtained the quasiparticle density of states $N(\omega)$ from the solutions. $N(\omega)$ is obtained by integrating the spectral function over the momentum space, and in our model we have,

$$N(\omega) = \mathrm{Im}\left(i\frac{\tilde{\Sigma}(\omega)}{\sqrt{\tilde{\Sigma}^2(\omega) - |\Phi|^2(\omega)}}\right) \tag{5.18}$$

In Fig.5.8 we show $N(\omega)$ for the two different cases studied in Fig.5.7. We see from the figure that at any finite temperature, $N(\omega)$ at around $\omega = 0$ remains vanishingly small, as it actually vanishes in $T \to 0$. As the temperature increases, the gap width, defined as the distance of the two maximum positions in $N(\omega)$, narrows gradually, before it full closes as the temperature reaches $T_{p,0}$. This 'gap closing' behavior persists at any $T < T_{p,0}$, and is similar to that observed in conventional BCS superconductors, but is in distinct with what has been observed in the even-ω pairing state obtained within the same γ model. For the even-ω pairing, as we explained above, the 'gap closing' occurs only at a smaller temperature range $0 < T < T^*$ with $T^* < T_{p,0}$. At higher temperatures when $T^* < T < T_{p,0}$, related quantities at the first two Matsubara frequencies $\pm\pi T$ plays an important rule at temperature close to the onset temperature. Pairing vertex $\Phi(\omega_m)$ has a significant contribution from $\omega_m = \pm\pi T$ and as a result,

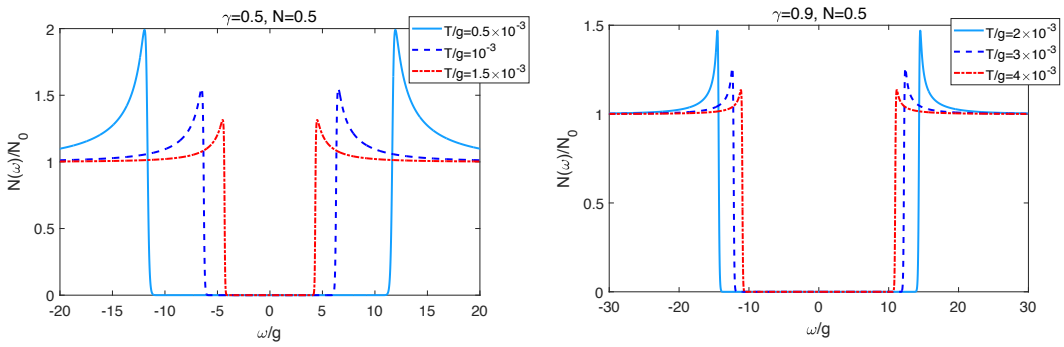

Figure 5.8: Density of states $N(\omega)$(measured from the normal state DoS N_0) for $\gamma = 0.5$ $N = 0.5$ and $\gamma = 0.9$ $N = 0.5$ at various temperatures. As temperature increases the gap in $N(\omega)$ gradually closes, but at around $\omega = 0$, $N(\omega)$ remains vanishingly small.

on real ω axis both $\Phi(\omega)$ and $\tilde{\Sigma}(\omega)$ shows ω/T scaling behavior, which means the characteristic frequencies in $N(\omega)$ increases with increasing T. Besides, it is found that $N(\omega = 0)$ acquires a finite weight which also increases with increasing T. Therefore, the gap in $N(\omega)$ gets gradually filled in the middle as T increases. This behavior is called 'gap filling'. However, for odd-ω pairing state, there is no such first Matsubara rule because $\Delta(\pm\pi T)$ has to vanish in $T \to 0$ limit and remains the smallest compared to $\Delta(\omega_m)$ at other frequencies(considering the frequencies smaller than the one beyond which $\Delta(\omega_m)$ decays). And there does not exist a crossover temperature scale T^*. Therefore, the 'gap filling' behavior which is a direct consequence of the first Matsubara rule, is reasonably absent in the odd-ω pairing state.

We note that the quasi particle DoS that we obtain here is different from those in previous studies on odd-ω pairing, in a sense that we don't observe a zero energy peak in $N(\omega)$ from our model. However the DoS of odd-ω superconducting phase obtained from, e.g. s-wave superconductor/ferromagnet or p-wave superconductor/normal metal heterostructures, does exhibit such zero energy peak. Given this, we argue that the existence of zero energy peak in $N(\omega)$ can't be used as a fingerprint of odd-ω pairing, at least in systems where the superconducting phase is built on an underlying QCP.

5.4 The case $\gamma > 1$

Up till now our study was limited to $\gamma < 1$. In Sec.5.2.1 we show the critical value N_{cr} increases monotonically with γ and reaches $N_{cr} = 1$ at $\gamma = 1$. At first glance one could continue the analysis for $\gamma > 1$ to see whether such a critical value for N still exists or not. However it is easy to notice that for $\gamma > 1$, both the pairing vertex $\Phi(\omega_m)$ and self energy $\Sigma(\omega_m)$ contain divergence at $T = 0$. This is a IR divergence in the sense that it comes from the limit $\omega_m \to \omega_n$ in the integrand, and becomes regular at finite T. In the original model where $N = 1$, this singular behavior can be removed once we reformulate the problem in terms of $\Delta(\omega_m) = \omega_m \Phi(\omega_m)/\tilde{\Sigma}(\omega_m)$. To see this, one can return to Eq.(2.26) with a general N. For $N = 1$, the cancellation between $\Delta(\omega_m)$ and $\Delta(\omega_n)\omega_m/\omega_n$ in the numerator of the integrand as $\omega_m \to \omega_n$ guarantees the convergence of the integral. But for $N \neq 1$, this integral is divergent, which gives rise to a divergent $\Delta(\omega_m)$ for $N < 1$ and a vanishing $\Delta(\omega_m)$ for $N > 1$.

A logical way to overcome this troublesome divergence at $N \neq 1$ is to move the system away from a QCP. This can be realized by adding a finite mass M_b in the interaction term. After doing so, Eq.(2.26) gets modified into

$$\Delta(\omega_n) = \pi T \sum_{\omega_m} \frac{\frac{1}{N}\Delta(\omega_m) - \Delta(\omega_n)\frac{\omega_m}{\omega_n}}{\sqrt{\omega_m^2 + \Delta^2(\omega_m)}} \frac{1}{|(\omega_m - \omega_n)^2 + M_b^2|^{\gamma/2}} \tag{5.19}$$

In $T = 0$ limit, the integral becomes regular as long as M_b remains finite. We are particularly interested in the case of $N = 1$, where the gap equation is regular even if we take $M_b = 0$. To test the existence of such solutions at $N = 1$, we first focus on the linearized equation, which can be deduced directly from the above nonlinear equation and is written as

$$\omega_n D(\omega_n) = \pi T \sum_{\omega_m} \frac{\frac{1}{N}D(\omega_m) - D(\omega_n)}{((\omega_m - \omega_n)^2 + M_b^2)^{\gamma/2}} \operatorname{sgn}\omega_m \tag{5.20}$$

Where $D(\omega_n) = \Delta(\omega_n)/\omega_n$ is an even function of ω_n for odd-frequency pairing. Below we depart from this equation and seek for odd-frequency solutions at $\gamma > 1$.

$M_b = 0$, $T = 0$ **and** $N = 1$

For $M_b = 0$ the linearized equation is exactly Eq.(5.4). Therefore, we can look for solutions at $N = 1$ by the same approach as we show in Sec.5.2.1. At $\omega_m < 1$, we again expand the solution as $D(\omega_m) = \omega_m^\rho \sum_{n=0}^{\infty} C_n \omega_m^{\gamma n}$. Substituting this solution back into the equation gives the following equation that determines the value of ρ,

$$B(1-\gamma, \rho+1) + B(1-\gamma, \gamma-\rho-1) - B(\rho+1, \gamma-\rho-1) = \frac{2}{1-\gamma} \tag{5.21}$$

There are two solutions of ρ to this equation: $\rho_1 = 0$ and $\rho_2 = \gamma - 2$. Both of them are real numbers for all $\gamma > 1$. This is in contrast to the case of $\gamma < 1$ and $N < N_{cr}$ discussed in Sec.5.2.1, where we also have two solutions for ρ which, however, are complex and their imaginary parts lead to logarithmic oscillation of $\Delta(\omega_m)$ at $\omega_m \ll 1$. Real solutions of ρ implies that at $\omega \ll 1$, the solution must behaves like $\Delta(\omega_m)/\omega_m = C_1 + C_2 \omega_m^{\gamma-2}$. We can only determines one of the two factors C_1 and C_2 by matching the solution to it's boundary condition at large ω_m, i.e. we must have $\Delta(\omega_m) \sim 1/\omega_m^{\gamma+1}$ at $\omega_m \gg 1$. The other factor is free since the overall magnitude of a solution to the linearized equation is not fixed.

The solution at $\gamma = 2$ is critical for obvious reason: at $\gamma \to 2$, the power law scaling of $\Delta(\omega_m)/\omega_m = C_1 + C_2 \omega_m^{\gamma-2}$ reduces to logarithmic scaling. In fact, by following the same route as stated in Sec.5.2.1, we find an exact solution to the linearized equation at $\gamma = 2$ and $N = 1$, and from this the logarithmic scaling at small ω_m is readily confirmed. To this end, we first compute (5.5) at $\gamma = 2$ and $N = 1$. In this special case it takes a simple form

$$\epsilon_\beta = \frac{\pi\beta}{\tanh \pi\beta} \tag{5.22}$$

Then using this we can evaluate the integral in Eq.(5.7). The exact solution is given by an integration similar to Eq.(5.8), but with $\beta_N = 0$, since β_N is the solution of the equation $\epsilon_{\beta_N} = N$ and from (5.22) we must have $\beta_{N=1} = 0$. Namely we have an expression for the solution which is

$$\Delta_{\rm ex}(\omega_m) = \int_{-\infty}^{\infty} d\beta \frac{\cos[\beta \log \omega_m^2 + I(\beta)]}{\cosh \pi\beta} \tag{5.23}$$

In Fig.5.9 we plot this exact solution. At $\omega_m \ll 1$, $\Delta_{ex}(\omega_m)/\omega_m$ scales linear in $\log \omega_m$,

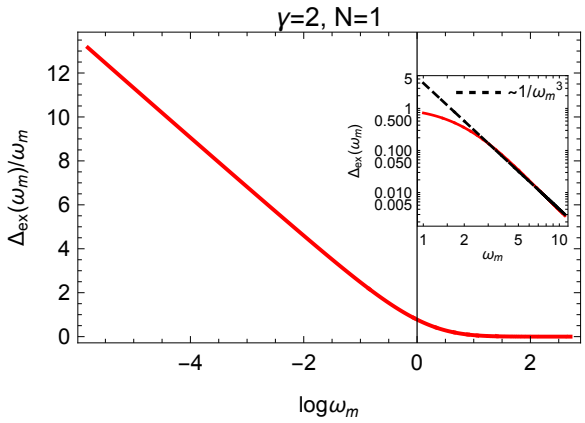

Figure 5.9: Exact solution to the linearized gap equation of odd-frequency pairing for $\gamma = 2$ and $N = 1$. At small ω_m, $\Delta_{ex}(\omega_m)/\omega_m$ scales linear in $\log \omega_m$. While at large ω_m, Δ_{ex} decays as $1/\omega_m^3$. In all range of $\omega_m > 0$, this solution remains sign-preserving. This is different from the exact solution at $\gamma < 1$ and $N < N_{cr}$ which changes sign infinite number of times.

while at $\omega_m \gg 1$ we clearly see $\Delta(\omega_m) \sim 1/\omega_m^3$. The large frequency behavior is consistent with $\gamma < 1$ case where we find the large ω_m for odd-frequency pairing is $1/\omega_m^{\gamma+1}$. This solution is a sign preserving solution, in contrast to the case when $\gamma < 1$ and $N < N_{cr}$ where we find the solution change sign an infinite number of times.

Applying this method to seek for an exact solution at other $\gamma > 1$ is rather challenging, and we did not find such an solution by doing so. However the case of $\gamma = 2$ clearly provides strong evidence that our small ω_m the power-law scaling $\Delta(\omega_m)/\omega_m = C_1 + C_2\omega_m^{\gamma-2}$ obtained from series expansion is logical. This small ω_m behavior is different from the logarithmic scale oscillation presented in Fig.5.3 for $\gamma < 1$ and $N < N_{cr}$. However, it is worth noticing that the oscillation is replaced by power-law once $N \to N_{cr}$. From Fig.5.2(b) we know that the system terminates at $N = N_{cr}$ at zero temperature so even the largest $T_{p,0}$ vanishes. Therefore, it is equivalent to say that for $\gamma < 1$ once the gap function displays a power-law scaling at $\omega_m \ll 1$, the system is in its critical point and all $T_{p,n}$ vanish. By analogy, in our preset case when $\gamma > 1$ and $N = 1$, we argue that the all the onset temperatures $T_{p,n}$ also vanish, and as a result we don't have solution to the linearized equation at any finite T. We confirm this argument by analyzing the linearized gap equation with $M_b = 0$ at finite T in the following.

$M_b = 0$ **and** $T > 0$

At arbitrary finite temperature, the divergence of the gap equation, Eq. (2.26), at $N \neq 1$ is regularized. To rationalize its effect, one can single it out from the integral and move it to the l.h.s. of the gap equation, which gives rise to

$$D(\omega_n)\left(\omega_n - (\frac{1}{N} - 1)\Sigma(\omega_n)\right) = \frac{\pi T}{N}\sum_{\omega_m}\left(D(\omega_m) - D(\omega_n)\right)\frac{\mathrm{sgn}(\omega_m)}{|\omega_m - \omega_n|^\gamma}, \tag{5.24}$$

where $\Sigma(\omega_n)$ is the self-energy introduced in Eq.(2.29) and given explicitly by

$$\Sigma(\omega_n) = \frac{H_\gamma(n)}{(2\pi T)^{\gamma-1}}, \tag{5.25}$$

and $H_\gamma(n) = \sum_k^n 1/k^\gamma$ is the Harmonic number. In the zero-temperature limit, the r.h.s. of Eq.(5.24) is given by a convergent integral, while the coefficients of $D(\omega_n)$ on the l.h.s. depends on the dimensionless ratio $a_\gamma = (1/N - 1)/T^{\gamma-1}$, indicating the singular behavior of the gap function in the double limit $N \to 1$ and $T \to 0$. For any finite frequency, the Matsubara number $n \to \infty$ at zero temperature and thus $H_\gamma(n \to \infty) = \zeta(\gamma)$ which is finite for $\gamma > 1$. The limiting form of the gap equation reads

$$D(\omega_n)\left(\omega_n - a_\gamma\zeta(\gamma)/(2\pi)^{\gamma-1}\right) = \frac{1}{2N}\int d\omega_m \left(D(\omega_m) - D(\omega_n)\right)\frac{\mathrm{sgn}(\omega_m)}{|\omega_m - \omega_n|^\gamma}. \tag{5.26}$$

The case with $a_\gamma = 0$ corresponds to original problem with $N = 1$ and has been just discussed. Below we show that it has also solutions at finite a_γ. This gives rise to a critical phase boundary

$$\frac{1}{N} - 1 = a_\gamma T^{\gamma-1}. \tag{5.27}$$

We note that the same equation is obtained at zero temperature but in the presence of a finite M_b (see next section), which explicitly indicates the same role played by a finite temperature or mass in cutting-off the I.R. divergence. While more analysis of this equation is provided in the next section, we provide numerical evidence about the relation in Eq.(5.27).

For that purpose, we solved the linearized gap equation with $M_b = 0$ at finite temperature is given by Eq.(2.29) for a generic γ, which is equivalent to an eigen problem

with N playing the role of eigenvalue and $\Phi(\omega_m)$ the eigenfunction. From this perspective, N is an output parameter. The size of the kernel matrix to be diagonalized is infinite, thus for a given $T > 0$ there is an infinite number of eigenvalues corresponding to different solution $\Delta_n(\omega_m)$. Since we are interested in a possible solution at $N = 1$, we solve the eigenvalues at different T and look for possible $T_{p,n}$ at which the $n-$th eigenvalue crosses $N = 1$.

In the upper panel of Fig.5.10 we show our numerical results of the first five solutions for several $\gamma > 1$. Instead of plotting N, we plot $\log(1/N - 1)$ as a function of $\log T$. In all cases, even the largest eigenvalue ($n = 0$, corresponds to sign-preserving solution) is smaller than $N = 1$ at the lowest temperature that we can set(In practice we take 10^4 Matsubara points for numerics), hence $1 - N$ is always positive. More interestingly, at small T there is a linear relation between $\log(1/N - 1)$ and $\log T$ which indicates that $1 - N$ is unlikely to vanish at any finite T. In fact, the slope can be perfectly fitted using $a_{\gamma,n}T^{\gamma-1}$ scaling. With this, we have confirmed the scaling relation in Eq.(5.27) and $a_\gamma = a_{\gamma,n}$ (from the numerics we have $a_{\gamma,0} < a_{\gamma,1} < a_{\gamma,2} < ...$). This relation is a direct evidence that there is no solution to the linearized gap equation with $N = 1$ at any finite temperature, for any given $\gamma > 1$. We therefore argue that the odd-frequency pairing order is not possible at finite temperature in the original model.

$M_b \to 0$, $T = 0$ and $N \to 1$

We see from above that there is no solution to the linearized gap equation at $T > 0$. Here we return to $T = 0$ case but with a finite boson mass. In the above zero temperature analysis for the case of $M_b = 0$ and $N = 1$, we find a power-law solution at $\omega_m \ll 1$ for $\gamma > 1$ and an exact solution at $\gamma = 2$. Once the boson mass M_b is finite, the eigenvalue N in the linearized equation is reduced. The two quantities M_b and N are not independent as they are connected by Eq.(5.20). One would expect $N \to 1$ as $M_b \to 0$. In order to find their exact relation at small M_b, we solved (5.20) numerically. In the lower panel of Fig.5.10, we plot $\log(1/N - 1)$ as a function of $\log(M_b)$ for several γ and at a rather low temperature $T = 5 \times 10^{-5}$ (which we believe is small enough to give indistinguishable results as $T = 0$ case). It is clear that the relation between these

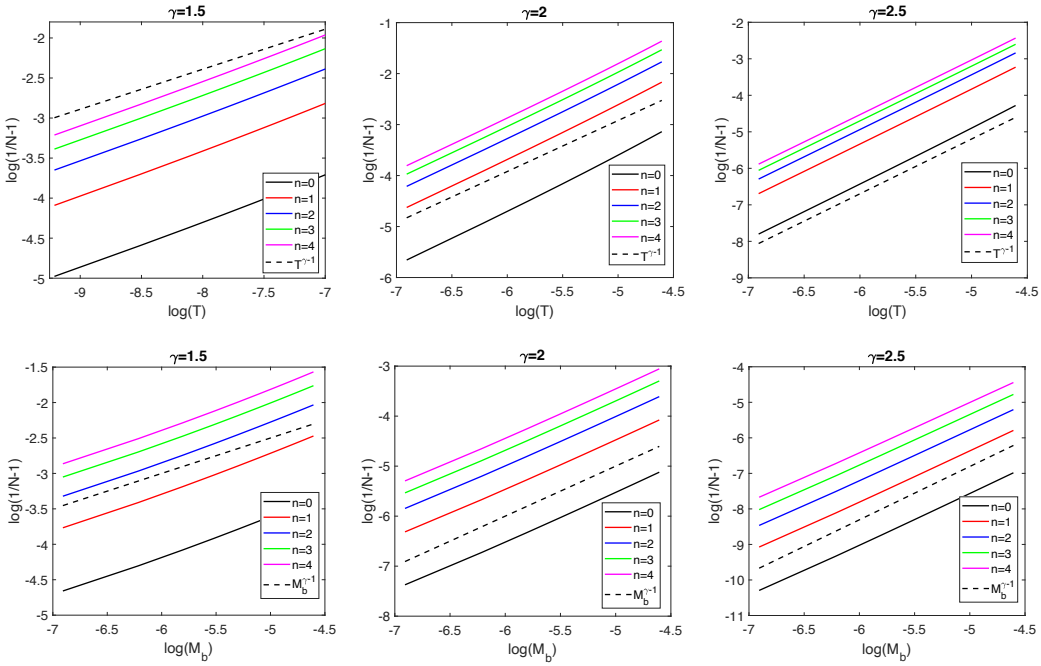

Figure 5.10: Upper panel: The first five solutions to the linearized gap equation at finite temperature and zero boson mass for $\gamma > 1$. These plots shows how the eigenvalues N for different solution evolves with temperature. For convenience of illustration, we plot $\log(1/N-1)$ in the vertical axis and $\log(T)$ on the horizontal axis. For comparison we also show $T^{\gamma-1}$ as the dashed line. It is then clear that (5.27) is verified. This scaling relation is a direct evidence that as long as $T > 0$, $1 - N$ remains positive thus N is always smaller than 1. Namely, there is no solution to the linearized gap equation with $N = 1$ at $T > 0$. Lower panel: Numerical evidence of the relation between N and M_b at small M_b obtained by solving Eq.(5.20) at a very small $T = 5 \times 10^{-5}$. It is clear that $\log(1/N-1)$ depends on $\log(M_b)$ linearly, and the slope perfectly matches $\gamma - 1$ which is indicated by the fitting lines. Consequently we have verified the scaling relation in (5.28).

two is linear, regardless of γ. In fact, by fitting the data, we find

$$\frac{1}{N} - 1 = b_\gamma M_b^{\gamma-1} \tag{5.28}$$

where $b_\gamma = b_{\gamma,n}$ is some γ-dependent constant which also depends on n (from the numerics we have $b_{\gamma,0} < b_{\gamma,1} < b_{\gamma,2} < ...$).

To understand how the solution behaves at $M_b = 0$, we investigate the equation with $M_b > 0$ and in the end take the limit $M_b \to 0$. At $T = 0$, Eq.(5.20) can be rewritten as

$$\omega_n D(\omega_n) = \frac{1}{2}\left(\frac{1}{N} - 1\right) D(\omega_n) \int \frac{d\omega_m \operatorname{sgn}\omega_m}{((\omega_m-\omega_n)^2 + M_b^2)^{\gamma/2}} + \frac{1}{2N}\int \frac{d\omega_m [D(\omega_m) - D(\omega_n)] \operatorname{sgn}\omega_m}{((\omega_m-\omega_n)^2 + M_b^2)^{\gamma/2}} \tag{5.29}$$

The first integral in the l.h.s. is finite and can be carried out explicitly. In the region where $M_b \ll \omega_n$, it gives $1/M_b^{\gamma-1}$ scaling. Combining this fact with (5.28) and noticing that the second integral in the l.h.s. is regular at small M_b, we arrive at a new gap equation in the limit of $M_b \to 0$(and therefore $N \to 1$),

$$D(\omega_n)\left(\omega_n - b_\gamma \frac{\sqrt{\pi}\Gamma[(\gamma-1)/2]}{2\Gamma(\gamma/2)}\right) = \frac{1}{2}\int \frac{d\omega_m [D(\omega_m) - D(\omega_n)] \operatorname{sgn}\omega_m}{|\omega_m - \omega_n|^\gamma} \tag{5.30}$$

This new equation enlarges the solution space of Eq.(5.4) by introducing the b_γ term. Indeed by taking $b_\gamma = 0$ one reproduces Eq.(5.4) with $N = 1$. We know from above that at $b_\gamma = 0$ the solution behaves like $D(\omega_m) = C_1 + C_2\omega_m^{\gamma-2}$ at $\omega_m \ll 1$, which is confirmed by the exact solution we find for $\gamma = 2$. It is then natural to question the existence of a solution for $b_\gamma > 0$, and if it exists how it behaves with ω_m. It's worth noting that we will be seeking for solutions $\Delta(\omega_m)$ which are continuous for all ω_m. In the case of $\gamma < 1$, although we can find a $\Delta(\omega_m) \sim \omega_m^{\gamma-1}$ (at $\omega_m \ll 1$) which satisfies (5.4) with $N = 1$, this solution is non-physical since it's discontinuous at $\omega_m = 0$.

Eq.(5.30) with a generic b_γ is difficult to solve so that one has to rely on numerics. But before that we notice some informative results can already be obtained by approximating Eq.(5.30) with a differential equation, and the latter is more friendly to solve. To this end, one needs to first substitute $\int d\omega_m \operatorname{sgn}\omega_m/|\omega_m - \omega_m|^\gamma \approx 2\gamma(\int_0^{\omega_n} d\omega_m \omega_m/\omega_n^{\gamma+1} + \int_{\omega_n}^{\infty} d\omega_m \omega_n/\omega_m^{\gamma+1})$ into Eq.(5.30) and then differentiate both side with respective to ω_n.

The differential equation obtained this way is

$$\begin{aligned}&\bar{D}''(x)x^2(x+1+\gamma/2-\tilde{b}_\gamma x^{1-1/\gamma})\\&+\bar{D}'(x)\frac{2x}{\gamma}\left((\gamma-1)x-1-\gamma/2-\tilde{b}_\gamma(\gamma-2)x^{1-1/\gamma}\right)\\&-\bar{D}(x)\frac{2}{\gamma}\left(x-1-\gamma/2-\frac{3(\gamma-1)}{2\gamma}\tilde{b}_\gamma x^{1-1/\gamma}\right)=0\end{aligned}\tag{5.31}$$

where $x=\omega_n^\gamma$, $\bar{D}(x)=D(x)x^{2/\gamma}$ and $\tilde{b}_\gamma=b_\gamma\frac{\sqrt{\pi}\Gamma[(\gamma-1)/2]}{2\Gamma(\gamma/2)}$. Normally two boundary conditions are needed for this second order equation. In our current situation, the overall magnitude of $D(\omega_n)$ is not fixed, and we only demand that the solution behaves like $D(\omega_n)\sim 1/\omega_n^{\gamma+2}$[or equivalently $\bar{D}(x)\sim 1/x$] at large frequency.

Eq.(5.31) has solution for any $\gamma>1$ and $b_\gamma\geq 0$. In the special case $b_\gamma=0$, it can be expressed analytically,

$$\bar{D}(x)=C_1x^{2/\gamma}+C_2x\frac{{}_2F_1\left(2,\frac{\gamma-2}{\gamma},2-\frac{2}{\gamma},-\frac{2x}{2+\gamma}\right)}{(2+\gamma)^2(2-\gamma)}\tag{5.32}$$

At $x\ll 1$ the function ${}_2F_1\left(2,\frac{\gamma-2}{\gamma},2-\frac{2}{\gamma},-\frac{2x}{2+\gamma}\right)$ becomes a constant, and therefore $\bar{D}(x)$ scales as $C_1x^{2/\gamma}+C_2x$[namely $D(\omega_n)=C_1+C_2\omega_n^{\gamma-2}$] which is fully consistent with our previous analysis using local series expansion. One of the coefficients C_1 and C_2 is determined by the boundary conditions at large frequency. To see this we notice that in the limit of $x\to\infty$, ${}_2F_1\left(2,\frac{\gamma-2}{\gamma},2-\frac{2}{\gamma},-\frac{2x}{2+\gamma}\right)x=\alpha_1x^{2/\gamma}+\alpha_2/x$. By properly choosing C_2, we can eliminate the $x^{2/\gamma}$ term in $\bar{D}(x)$ and therefore $\bar{D}(x)\sim 1/x$ at large x. In the general case with a nonzero b_γ in Eq.(5.31), it is more involved to write down an analytical expression of the solution, but still one can numerically solve this equation with proper boundary condition. In Fig.5.11 we show typical solutions for $\gamma=1.8$ and $\gamma=2.5$ with several different b_γ. We clearly see that at $\omega_m\ll 1$ the solution still maintains the form $D(\omega_m)=C_1+C_2\omega_m^{\gamma-2}$ regardless of b_γ, but the relative value between C_1 and C_2 indeed changes with b_γ. At some critical values $b^*_{\gamma,n}$ where $n=0,1,2,...$, C_2 vanishes and thus $D(\omega_m)$ saturates to constant value as $\omega_m\to 0$. Moreover, C_2 changes sign once b_γ crosses these critical values. For $\gamma<2$ the sign changing behavior of the coefficient C_2 also means the sign changing in $D(\omega_n)$ since $\omega_n^{\gamma-2}$ is the largest term at $\omega_n\ll 1$.

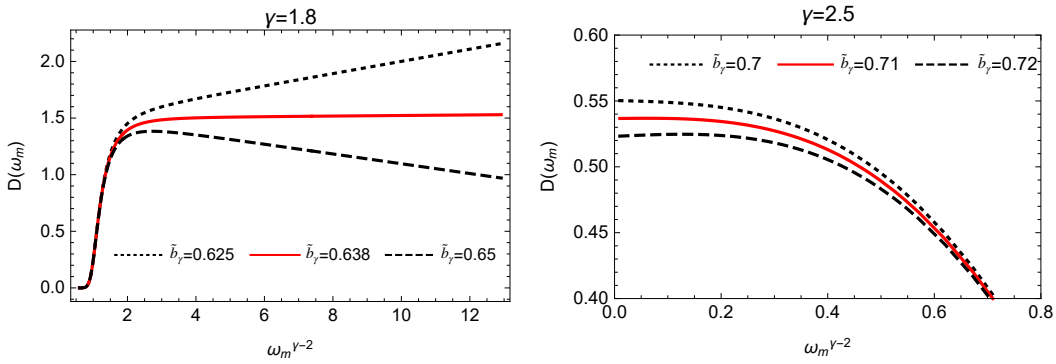

Figure 5.11: Solutions to Eq.(5.31) with $\tilde{b}_\gamma > 0$ for $\gamma < 2$ and $\gamma > 2$. At $\omega_m \ll 1$ we clearly see $D(\omega_m) = C_1 + C_2\omega_m^{\gamma-2}$. The relative value of C_1 and C_2 is determined by the boundary condition that $D(\omega_m) \sim 1/\omega_m^{\gamma+2}$ at $\omega_m \gg 1$ and is therefore dependent on $\tilde{b}_\gamma$. At some critical values $\tilde{b}^*_{\gamma,n}$, the $\omega_m^{\gamma-2}$ term in $D(\omega_m)$ vanishes and $D(\omega_m \to 0)$ saturates to constant. From the plots we can extract the first critical value($\tilde{b}^*_{\gamma,0} = 0.638$ for $\gamma = 1.8$ and $\tilde{b}^*_{\gamma,0} = 0.71$ for $\gamma = 2.5$), around which C_2 changes sign.

The same behavior of the solution $D(\omega_m)$ (at small and large ω_m) and the existence of critical values for the parameter b_γ, can be seen from solving Eq.(5.30) directly. To be precise, we apply numerical iteration to solve (5.30) and find there exists a set of critical values $b_{\gamma,n}$ at which $D(\omega_m)$ saturates to a constant at $\omega_m \ll 1$. This is completely parallel with the features observed using differential equation, except that the values $b_{\gamma,n}$ are slightly different from $b^*_{\gamma,n}$ introduced previously. In fact, the solutions with $b_\gamma = b_{\gamma,n}$ are exactly the same ones obtained by solving Eq.(5.20) with a vanishingly small M_b. This is because Eq.(5.30) generalizes Eq.(5.20) and enlarges its solution space. In Fig.5.12(a) we show a comparison between two solutions obtained from these two equations at a particular $\gamma = 2$. The red dashed curve is obtained from solving (5.30) using iteration at it's first critical value $b_{\gamma,n=0} = 0.56$, while the green curve is the first eigenfunction from diagonalizing (5.20). We clearly see there is a good agreement. The critical values $b_{\gamma,n}$ from both equations should also be consistent. Indeed by using the data in Fig.**??** to fit (5.28) we obtain $b_\gamma \approx 0.6$, which is very close $b_{\gamma,n=0} = 0.56$. When inputting a smaller T in (5.20), these two values will be even closer.

For b_γ other than those critical values, it's hard to provide a rigorous proof whether the solutions of Eq.(5.30) exist, but we attempt to draw a positive conclusion based on

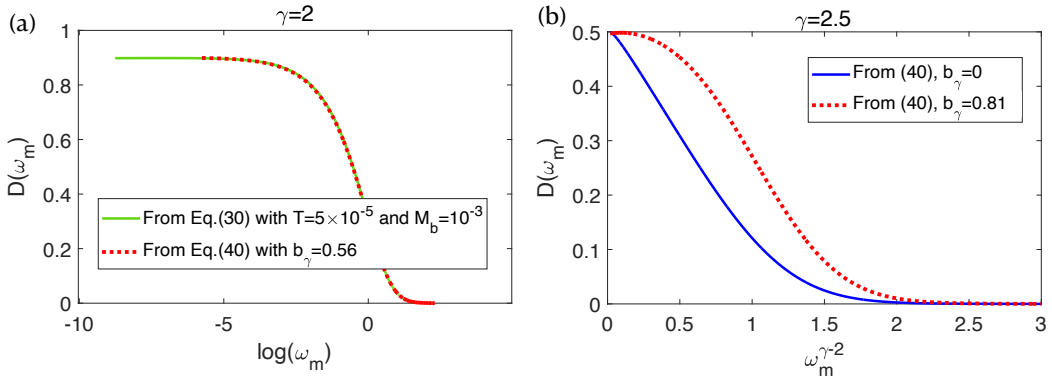

Figure 5.12: (a) Comparison between the solution from the generalized integral equation (5.30) with b_γ at its first critical value $b_{\gamma,n=0} = 0.56$, and the original linearized equation (5.20) with a small M_b. These two solutions coinciding with each other confirms the consistency between (5.20) and (5.30) with $b_\gamma = b_{\gamma,n}$. It is also clear that $D(\omega_m)$ saturates to some constant at small ω_m. (b) Solutions of Eq.(5.30) for $\gamma = 2.5$. For a generic b_γ, $D(\omega_m) = C_1 + C_2\omega_m^{\gamma-2}$ at small ω_m. This is confirmed from the blue curve which shows linear dependence on $\omega_m^{\gamma-2}$ at small ω_m. While at the critical values $b_{\gamma,n}$ (we show $n = 0$ case here and $b_{\gamma,n=0} = 0.81$), the $\omega_m^{\gamma-2}$ scaling disappears and $D(\omega_m)$ saturates to some constant, as can be seen from the red dashed curve.

numerical evidence. First we notice for all $\gamma > 1$ the solution is stable against iteration at $b_\gamma = b_{\gamma,n}$ when $D(\omega_m)$ is finite at small ω_m. Then for $\gamma > 2$ we use the same method to study the equation with arbitrary $b_\gamma \geq 0$ and also find stable, convergent solution which behaves as $D(\omega_m) = C_1 + C_2\omega_m^{\gamma-2}$ at small ω_m (See Fig.5.12(b) where we plot the solution against $\omega_m^{\gamma-2}$ for $b_\gamma = 0$ and $b_\gamma = 0.81$, its first critical value). Note this form is also finite at small ω_m and it is consistent with the results from analyzing (5.31), the differential equation. As for the case when $\gamma < 2$, iteration is not stable for arbitrary $b_\gamma \neq b_{\gamma,n}$, but becomes increasingly stable when b_γ approaches the critical values $b_{\gamma,n}$. We argue that for $\gamma < 2$ the solution also exists and still behaves like $D(\omega_m) = C_1 + C_2\omega_m^{\gamma-2}$, which diverges at $\omega_m = 0$. It is this zero point divergence that destabilizes numerical iteration. Therefore, like the case of the differential equation (5.31), there also exists a solution to the full, generalized equation (5.30) for any $b_\gamma \geq 0$.

In Fig.5.13 we come up with a phase diagram at $T = 0$ and $N = 1$ based on the above arguments. The solution of the generalized gap equation (5.30) exists for $b_\gamma \geq 0$, $\gamma > 1$, which forms a continuum in the b_γ-γ plane. For a given γ, the solution behaves

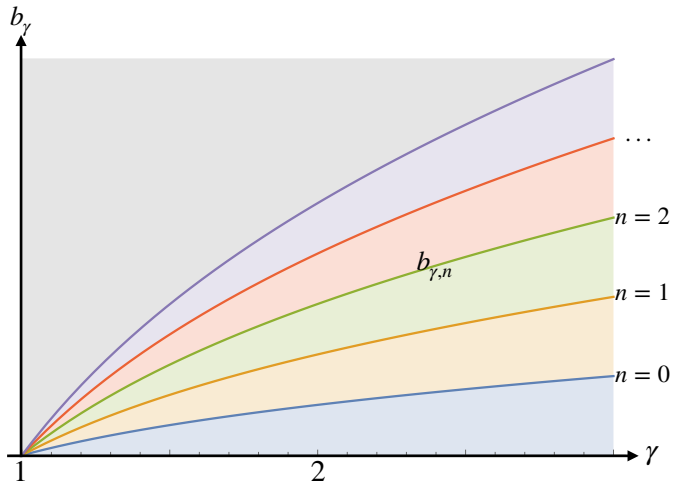

Figure 5.13: Phase diagram of odd-frequency pairing in the b_γ-γ plane for $N = 1$, $\gamma > 1$ and $T = 0$. Although we don't have solutions to the nonlinear gap equation at $N = 1$ and $T > 0$, we do have solutions to the linearized equation (5.30) at $T = 0$. The solutions form a continuum in the plane. At an infinite set of critical curves, the solutions coincide with the eigenfunctions obtained from (5.20), in $T \to 0$ and $M_b \to 0$ limit. The continuum of these solutions will collapse to the critical curves once we keep a finite mass term in the l.h.s. of (5.30).

like $D(\omega_m) = C_1 + C_2\omega_m^{\gamma-2}$ (for $\gamma = 2$ it reduces to $D(\omega_m) = C_1 + C_2\log(\omega_m)$) at small ω_m, and the relative value between C_1 and C_2 changes with b_γ. At a set of critical values $b_{\gamma,n}$ where $n = 0, 1, 2, ...$(shown as the critical curves in Fig.5.13), the factor C_2 vanishes and $D(\omega_m)$ becomes a constant at $\omega_m \ll 1$. Another interesting feature is C_2 changes sign once b_γ crosses its critical value. Therefore, in the case of $1 < \gamma \leq 2$ where $\omega_m^{\gamma-2}$ diverges at $\omega_m = 0$, $D(\omega_m)$ acquires one sign changes when b_γ crosses $b_{\gamma,n}$, and for $b_{\gamma,n} < b_\gamma \leq b_{\gamma,n+1}$, it has n sign changes for $\omega_m > 0$. The critical value $b_{\gamma,n}$ coincides with the one obtained using the n-th solution of (5.20) to fit the relation $1/N - 1 = b_{\gamma,n}M_b^{\gamma-1}$, in the limit of $T \to 0$ and $M_b \to 0$. In fact, at these critical values the solution obtain from (5.30) are the same with the n-th eigenfunction from (5.20), if we take the limit $T \to 0$ and $M_b \to 0$ in the latter equation. From this perspective, (5.30) generalizes (5.20) by enlarging the solution space. One should also note that this property is unique only when we take $M_b \to 0$ when deriving (5.30). For example, if we keep a finite mass term in the l.h.s. of (5.30), the continuum in the phase diagram will collapse to the critical curves.

Chapter 6

Fluctuations in superconductivity near a quantum critical point

The γ-model that we have been studying unveils the interplay between superconducting order and the non-Fermi liquid tendency in an itinerant system close to a QCP. In deriving the two coupled Eliashberg equations in Chapter 2, we explicitly see these two equations are essentially the mean field equations which fails to include fluctuation effects. As depicted in Figure 6.1, the SC order parameter $\Delta = |\Delta|e^{\theta}$ can fluctuate through its modulus $|\Delta|$ as well as its phase θ. The former often involves large energy exchange with external field and is dubbed as Higgs mode. In this paper we are more concerned about the low energy phase fluctuation mode, which will eventually restore the $U(1)$ symmetry and destroy SC.

To understand stability of SC state at finite temperature, one may need to go beyond the Eliashberg type theory and study the effect of fluctuation inside SC order for quantum critical systems. The SC can be understood in the context of Anderson-Higgs mechanism [121] which describing spontaneous breaking of $U(1)$ symmetry. Before symmetry breaking, a complex fermion with double degrees of freedom is coupled to the $U(1)$ gauge field. Upon symmetry breaking, the mass of one fermionic degree of freedom is eaten by the gauge field that gives rise to a massive gauge field with a finite mass ρ_s and a massless Goldstone mode. The remaining massive fermionic degree of freedom is the amplitude fluctuation while the Goldstone mode is called phase fluctuation.

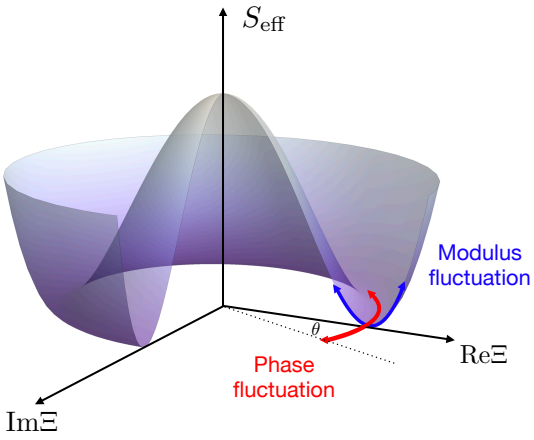

Figure 6.1: Fluctuations of superconductivity ground state. The complex order parameter Ξ acquires a fixed phase θ in SC state and breaks $U(1)$ symmetry. However if low energy phase fluctuation is strong, the $U(1)$ symmetry can be restored and superconductivity is destroyed.

The mass term ρ_s serves as a benchmark of a SC phase in at least two ways. First, because the gauge field acquires a finite mass upon symmetry breaking, the magnetic field $\boldsymbol{B}$ decays rapidly in space and vanishes after a finite distance $\lambda \propto 1/\sqrt{\rho_s}$ which is the Meissner effect in SC phase. The mass term also appears in the London equation for current response, $\boldsymbol{J} = \rho_s \boldsymbol{A}^{\perp}$ where $\boldsymbol{A}^{\perp}$ is the transverse component of the vector field which is gauge invariant. This explains the dissipationless current of a SC phase. However, strong enough fluctuations reduce the ρ_s and can eventually restore $U(1)$ symmetry. For low energy excitations, the massless phase fluctuations dominate over amplitude fluctuations. In static and long wavelength limit, the phase part of action is also related to ρ_s via $S_\theta \propto \int dr \rho_s (\nabla\theta)^2$. So this ρ_s is also referred as phase stiffness of a superconductor. Evaluations of the phase fluctuations are mostly based on BCS model in previous studies and how ρ_s changes with temperature in SC near a QCP is still not fully understood. Below we will first obtain an expression for ρ_s from gauge transformation method, and we will use that to examine phase fluctuations in γ-model.

6.1 Phase stiffness: derivation

In Sec.2.2.1 it is shown that the Eliashberg equations are essentially the saddle point equations for the action (2.13) which fails to include fluctuation effects. Put it explicitly, we defined $\Phi(k)$ as the special version of a generalized pairing vertex $\Xi(q,k)$ when assuming no fluctuation at $q=0$. In order to include fluctuations, we allow for a small deviation from the saddle point, and in this case q could become finite. The fluctuation of superconductivity can be examined by looking into the pairing vertex $\Xi(q,k)$, and the corresponding action is given in (2.15). It includes both the modulus fluctuation and the phase fluctuation. The former is Higgs mode and to observe it one needs to apply Terra Hz technique to shake the whole ground state, therefore it is not of our interest here. The latter tends to restore $U(1)$ symmetry and induces a Goldstone mode which dominates for low energy fluctuations. The phase fluctuation encoded in (2.15) can be extracted by means of local gauge transformation of fermionic fields. To this end we write the off-diagonal term in (2.13) in real space $\sum_{k,q}\Xi(q,k)\bar{\psi}_\uparrow(k+\frac{q}{2})\bar{\psi}_\downarrow(-k+\frac{q}{2}) = \int dr|\tilde{\Xi}(r,0)|e^{i\theta(r)}\bar{\psi}_\uparrow(r)\bar{\psi}_\downarrow(r)$, where we have present the phase factor $\theta(r)$ explicitly and $r=(\boldsymbol{r},\tau)$. $\tilde{\Xi}$ is the Fourier transform of $\Xi(q,k)$. For s-wave superconductivity that we consider here, the gap function is isotropic on Fermi surface and does not depend on angle so we can safely ignore the $\boldsymbol{k}$ dependence of Ξ. The gap function does depend on Matsubara frequency ik_n, however at lowest frequencies we can approximate it as a constant. Consequently the Fourier transform of this component results in a delta function and this off-diagonal term becomes local in real space. This locality eases the way of a local gauge transformation of the fermion fields $\bar{\psi}_\uparrow(r)\to\bar{\psi}_\uparrow(r)e^{-i\theta(r)/2}$ and $\bar{\psi}_\downarrow(r)\to\bar{\psi}_\downarrow(r)e^{-i\theta(r)/2}$ that can cancel out the phase factor from $\tilde{\Xi}(r,0)$. Under this specific choice of gauge the off-diagonal terms do not contain phase $\theta(r)$ anymore, and one can directly read the phase part action from diagonal terms in (2.13).

Explicitly, the local gauge transformation

$$\sum_{k,q}\Xi(q,k)\bar{\psi}_\uparrow(k+\frac{q}{2})\bar{\psi}_\downarrow(-k+\frac{q}{2}) = \int dr|\tilde{\Xi}(r,0)|e^{i\theta(r)}\bar{\psi}_\uparrow(r)\bar{\psi}_\downarrow(r) \tag{6.1}$$

that eliminates the phase in off-diagonal term in (2.13) also induces a change in the diagonal term, $S\to S+S'$(In principle the action for the fermion field is gauge invariant,

and this change in diagonal term is compensated by the corresponding change in the $U(1)$ gauge field $\boldsymbol{A}$ and ϕ. We don't introduce gauge field here because we are interested in separating out the phase part in the action). The additional action S' acquired in the diagonal term of (2.13) is easily obtained by first Fourier transforming to real space and then returning back to momentum-frequency space.

$$\begin{aligned} S' = \sum_{\sigma} \int dr \bar{\psi}_{\sigma}(r) \left(\frac{i}{2} \partial_{\tau} \theta(r) + \frac{(\nabla \theta(r))^2}{8m} + \frac{i}{4m} \nabla \theta(r) \cdot \overleftrightarrow{\nabla} \right) \psi_{\sigma}(r) = \\ \sum_{k,k',\sigma} \bar{\psi}_{\sigma}(k) \left(\frac{\omega_n - \omega_m}{2} \theta(k-k') - \frac{1}{\beta V} \sum_{q} \frac{\boldsymbol{q} \cdot (\boldsymbol{k} - \boldsymbol{k'} - \boldsymbol{q})}{8m} \theta(q) \theta(k-k'-q) \right. \\ \left. + \frac{i(|\boldsymbol{k}|^2 - |\boldsymbol{k'}|^2)}{4m} \theta(k-k') \right) \psi_{\sigma}(k') \end{aligned} \tag{6.2}$$

where $\overleftrightarrow{\nabla} = \overrightarrow{\nabla} - \overleftarrow{\nabla}$ and m is electron mass. In S' we neglect the contribution arising from the self energy term, because of two reasons. First we consider small fluctuations near saddle point, therefore, self energy $\Sigma(k)$ is almost a constant with respect to momentum $\boldsymbol{k}$. Second indeed the frequency dependence of Σ also gives rise to frequency component of the action for the phase $\theta(r)$, however this frequency component is irrelevant to phase stiffness. Now including the phase fluctuation part the total action in (2.13) can be rewritten as

$$S_{tot} = \sum_{k,k'} \bar{\Sigma}(k) \chi^{-1}(k-k') \Sigma(k) + \sum_{k,k',q} \bar{\Xi}(q,k) \chi^{-1}(k-k') \Xi(q,k') + \sum_{k,k'} \bar{\Psi}(k) (G^{-1}_{k,k'} - \Theta_{k,k'}) \Psi(k') \tag{6.3}$$

where the matrix $\Theta_{k,k'}$ is

$$\begin{aligned} \Theta_{k,k'} = & \left(-\frac{\omega_n - \omega_m}{2} \theta(k-k') + \frac{1}{\beta V} \sum_{q} \frac{\boldsymbol{q} \cdot (\boldsymbol{k} - \boldsymbol{k'} - \boldsymbol{q})}{8m} \theta(q) \theta(k-k'-q) \right) \sigma_3 \\ & - \left(\frac{i(|\boldsymbol{k}|^2 - |\boldsymbol{k'}|^2)}{4m} \theta(k-k') \right) \sigma_0 \end{aligned} \tag{6.4}$$

The integration over fermion field can be carried out explicitly, and we arrive at

$$\begin{aligned} S_{tot} = &\sum_{k,k'} \bar{\Sigma}(k)\chi^{-1}(k-k')\Sigma(k) + \sum_{k,k',q} \bar{\Xi}(q,k)\chi^{-1}(k-k')\Xi(q,k') \\ &- \mathrm{Tr}\ln\left(\hat{G}^{-1}\right) + \sum_n \frac{1}{n}\mathrm{Tr}\left(\hat{G}\hat{\Theta}\right)^n \end{aligned} \tag{6.5}$$

where the last term contains information of phase fluctuations and vanishes when taking $q = 0$. When no fluctuations are present, this action is reduced to the one in (2.16). For small fluctuations around saddle point which we consider here, both the self energy Σ and the pairing vertex Ξ (in mean field level, Φ) take their saddle point value, which can be obtained from Eliashberg equations. Under this approximation the matrix $\hat{G}$ takes its mean field form

$$\hat{G}^0 = \frac{1}{(\omega_n + \Sigma(\omega_n))^2 + \xi_{\boldsymbol{k}}^2 + \Phi(\omega_n)^2} \times \begin{pmatrix} i\omega_n + \xi_{\boldsymbol{k}} + i\Sigma(\omega_n) & \Phi(\omega_n) \\ \Phi(\omega_n) & i\omega_n - \xi_{\boldsymbol{k}} + i\Sigma(\omega_n) \end{pmatrix} \tag{6.6}$$

where $\Sigma(k_n)$ and $\Phi(k_n)$ are the solutions of Eq.(2.25)[1]. In this way the phase part can be separated out straightforwardly. Up to Gaussian level, we only need $\mathrm{Tr}(\hat{G}^0\hat{\Theta}) + \frac{1}{2}\mathrm{Tr}(\hat{G}^0\hat{\Theta}\hat{G}^0\hat{\Theta})$, and the resulting action is

$$S_{\text{eff}}[\theta] = \frac{1}{8}\sum_q \left(A_q(i\Omega_m)^2 - 2B_q^a(i\Omega_m)q^a + C_q^{ab}q^aq^b\right)\theta(q)\theta(-q) \tag{6.7}$$

where the coefficients are

$$\begin{aligned} A_q &= \mathrm{Tr}\left(\hat{G}^0(k+q)\sigma_3\hat{G}^0(k)\sigma_3\right) \\ B_q^a &= \mathrm{Tr}\left(\frac{k^a}{m}\hat{G}^0(\boldsymbol{k}+\frac{\boldsymbol{q}}{2}, i\omega_n + i\Omega_m)\sigma_3\hat{G}^0(\boldsymbol{k}-\frac{\boldsymbol{q}}{2}, i\omega_n)\sigma_0\right) \\ C_q^{ab} &= -\frac{1}{m}\mathrm{Tr}\left(\hat{G}^0(k)\sigma_3\right)\delta_{ab} + \mathrm{Tr}\left(\frac{k^ak^b}{m^2}\hat{G}^0(\boldsymbol{k}+\frac{\boldsymbol{q}}{2}, i\omega_n + i\Omega_m)\sigma_0\hat{G}^0(\boldsymbol{k}-\frac{\boldsymbol{q}}{2}, i\omega_n)\sigma_0\right) \end{aligned} \tag{6.8}$$

and the index a and b are for spacial dimension. This expression has been obtained in Ref.[122] The difference between our results and the previous ones is encoded in $\hat{G}^0$

[1] We need to be careful here, because the mean field solutions we are seeking here should be the full solutions, i.e. the ones including thermal fluctuations. In (2.25) the thermal piece $m = n$ term has been excluded.

through $\Sigma(\omega_n)$ and $\Phi(\omega_n)$ which differ from their counterparts in conventional BCS model. Note that in the first term of C_q^{ab} the trace result is nothing but fermion density n (including spin) of the system. By taking the static, long wavelength limit, and assuming the system is isotropic in all directions so that k_x^2, k_y^2 and $\boldsymbol{k}^2/2$ are all equivalent inside the trace operator, (6.7) is directly reduced to

$$S_{\text{eff}}[\theta] = \frac{1}{2}\sum_{\boldsymbol{q}} \rho_s \boldsymbol{q}^2 \theta(\boldsymbol{q})\theta(-\boldsymbol{q}), \tag{6.9}$$

which defines phase stiffness of the system,

$$\rho_s(T) = \frac{n}{4m} + \frac{1}{4}\,\text{Tr}\left(\frac{\boldsymbol{k}^2}{2m^2}\hat{G}^0(\boldsymbol{k}+\frac{\boldsymbol{q}}{2}, i\omega_n)\hat{G}^0(\boldsymbol{k}-\frac{\boldsymbol{q}}{2}, i\omega_n)\right), \tag{6.10}$$

where the n is electron density including spin degeneracy and m is electron mass. In 2D system one can also express n/m using Fermi energy: $n/m = E_F/\pi$. The trace operator includes integration over frequency and momentum, and also the matrix trace in spin space. The matrix Green's function $\hat{G}^0$ has saddle point solutions as its entries,

$$\begin{aligned}\hat{G}^0(\boldsymbol{k}, i\omega_n) = &\frac{1}{\tilde{\Sigma}(\omega_n)^2 + \xi_{\boldsymbol{k}}^2 + \Phi(\omega_n)^2}\times \\ &\begin{pmatrix} i\tilde{\Sigma}(\omega_n) + \xi_{\boldsymbol{k}} & \Phi(\omega_n) \\ \Phi(\omega_n) & i\tilde{\Sigma}(\omega_n) - \xi_{\boldsymbol{k}}\end{pmatrix}\end{aligned} \tag{6.11}$$

Therefore, one has to solve the mean field equation (2.25) first before calculating ρ_s.

Although we obtain the the phase stiffness from writing the phase only action explicitly, it can also be obtained from electromagnetic response theory, and the two terms in Eq. (6.10) corresponds to diamagnetic and paramagnetic components of electric current. The paramagnetic contribution is nothing but a current-current correlation bubble $\Pi_{JJ}(i\Omega_m, \boldsymbol{q})$ shown in Figure 6.2 This bubble is non analytic at $q = 0$. Its value depends on specific ways to approach $q = 0$, either by taking $\Omega_m = 0$ first and then take $\boldsymbol{q} \to 0$ or by taking $\boldsymbol{q} = 0$ first and then take $\Omega_m \to 0$. This non-analyticity arises from the fact that the integrand at $q = 0$, namely $\frac{\boldsymbol{k}^2}{2m^2}\hat{G}^0(\boldsymbol{k}, i\omega_n)\hat{G}^0(\boldsymbol{k}, i\omega_n)$ becomes a non integrable function due to its lack of absolute convergence. The integral of its absolute value, $\text{Tr}\left(\frac{\boldsymbol{k}^2}{2m^2}|\hat{G}^0(\boldsymbol{k}, i\omega_n)\hat{G}^0(\boldsymbol{k}, i\omega_n)|\right)$ is logarithmically divergent in large frequency or

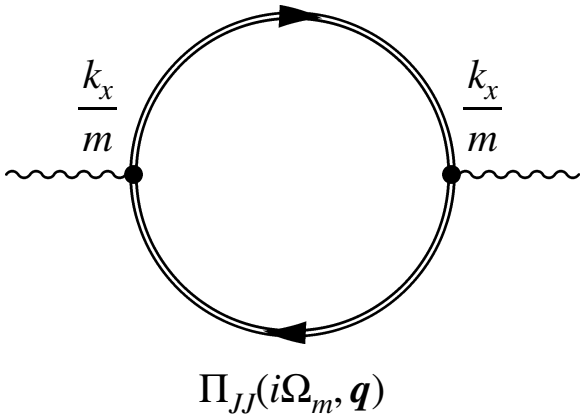

Figure 6.2: Paramagnetic contribution to $\rho_s(T)$, which is a current-current correlation bubble evaluated in SC state. The double line represents a matrix form of Green's function written in Nambu basis, see Eq. (6.6), while the black dots represent current vertices.

momentum limit. As a result $\Pi_{JJ}(0,0)$ takes different value when we change the order of integration for frequency and momentum. Thus a conventional safe way is to keep $\boldsymbol{q}$ finite and do frequency summation first, after this we take $\boldsymbol{q} \to 0$ limit and integrate over momentum. We show this procedure explicitly in the following BCS case where frequency summation is feasible. For cases other than BCS model, when self energy and pairing vertex are all frequency dependent, it's not possible to obtain frequency summation analytically. However, one can prove that this non analyticity can be resolved by incorporating the diamagnetic contribution via longitudinal sum rule, which expresses the electron density via a current-current response function:

$$\frac{n}{m} = -\operatorname{Tr}\left(\frac{\boldsymbol{k}^2}{2m^2}\hat{G}^0_{\Phi=0}(\boldsymbol{k}+\frac{\boldsymbol{q}}{2}, i\omega_n)\hat{G}^0_{\Phi=0}(\boldsymbol{k}-\frac{\boldsymbol{q}}{2}, i\omega_n)\right). \tag{6.12}$$

The subscript $\Phi = 0$ means that there is no pairing vertex in the Green's function and $\hat{G}^0_{\Phi=0}$ reduces to normal Green's function. This directly indicates that at $T = T_p$ diamagnetic and paramagnetic components cancel each other and as we must have $\rho_s(T_p) = 0$ as expected. Substituting Eq. (6.12) into Eq. (6.10) we end up with two terms in the integral. It is easy to see the integral over the sum of these two terms becomes

absolutely convergent and hence regular, since the logarithmic divergence has been removed by certain cancellation between the two terms at large frequency or momentum. Now we can take $\boldsymbol{q} = 0$ in the integrand, and integrate over momentum first. The result is

$$\rho_s(T) = \frac{E_F}{4\pi}\pi T \sum_{\omega_n} \frac{\Phi(\omega_n)^2}{[\tilde{\Sigma}(\omega_n)^2 + \Phi(\omega_n)^2]^{3/2}}. \tag{6.13}$$

where $\tilde{\Sigma}(\omega_n) = \omega_n + \Sigma(\omega_n)$ and $\Phi(\omega_n)$ are solutions to the mean field Eliashberg equations (2.25), but with $m = n$ term included.

6.2 Results and analysis

In this section we show the numerical results for the temperature evolution of ρ_s. Before considering pairing in quantum critical systems, we first apply our analysis to the conventional BCS model and calculate ρ_s based on formulas derived in previous section. The purpose has two fold. On one hand, we can verify the consistency between Eq. (6.10) and Eq. (6.13). On the other hand, the conventional BCS result for ρ_s can serve as a contrast to the unconventional behavior of ρ_s in quantum critical systems.

6.2.1 BCS limit

In this subsection we show our calculation of $\rho_s(T)$ based on BCS model, in which $\Phi(\omega_n) = \Delta$ and $\tilde{\Sigma}(\omega_n) = \omega_n$, i.e. without the effect of non-Fermi liquid correction. Although the phase stiffness for BCS model is well documented [114], we provide the calculation here as a contrast to the case in quantum critical systems, and by doing this we also show the consistency between Eq. (6.10) and Eq. (6.13). Starting from Eq. (6.10), the Matsubara summation can then be performed, and when the $\boldsymbol{q} \to 0$ limit is taken, we have Method I for obtained the stiffness

$$\text{Method I:}\quad \rho_s(T) = \frac{E_F}{4\pi}\left(1 - \int_{-\omega_D}^{\omega_D} d\xi_{\boldsymbol{k}} \frac{\beta}{e^{\beta E_{\boldsymbol{k}}} + e^{-\beta E_{\boldsymbol{k}}} + 2}\right), \tag{6.14}$$

where $E_{\boldsymbol{k}}^2 = \xi_{\boldsymbol{k}}^2 + \Delta^2$ and ω_D is energy cutoff which we approximately take to infinity for practical purpose. In $T \to 0$ limit, $\beta \to \infty$ and the integral becomes $\int_{\omega_D}^{\omega_D} d\xi_{\boldsymbol{k}} \beta e^{-\beta E_{\boldsymbol{k}}} \to 0$. Then there is only diamagnetic contribution and $\rho_s(T \to 0) = n/(4m) = E_F/(4\pi)$.

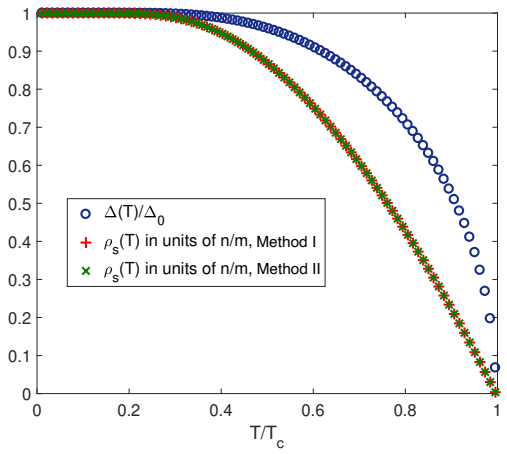

Figure 6.3: Superconducting gap $\Delta(T)$ and phase stiffness $\rho_s(T)$ as a function of T, obtained from BCS model. The red and green crosses are obtained from (6.14) and (6.15) respectively, and they coincide as expected. In zero temperature limit, ρ_s saturates to $E_F/(4\pi)$.

In order to make a better sense of Eq. (6.14), we first solve the non-linear BCS gap equation $\frac{1}{g\nu} = \int_0^{\omega_D} d\xi_{\boldsymbol{k}} \frac{\tanh(\beta E_{\boldsymbol{k}}/2)}{E_{\boldsymbol{k}}}$ to obtain $\Delta(T)$ as a function of temperature T, from which $\Delta_0 = \Delta(T=0)$ and the transition temperature T_c can be obtained. In practice we fix the value of $g\nu$, the product of the coupling constant g and the density of states around Fermi surface ν, while searching for Δ at a given T that satisfies the equation. After obtaining $\Delta(T)$ the stiffness is calculated using Eq. (6.14). As a comparison we also start from Eq. (6.13) to do calculation. In BCS model, Eq. (6.13) gets modified into

$$\text{Method II:}\quad \rho_s(T) = \frac{E_F}{4\pi}\pi T \sum_{\omega_n} \frac{\Delta^2}{(\omega_n^2+\Delta^2)^{3/2}}. \tag{6.15}$$

Again once we solve $\Delta(T)$ from the nonlinear equation $\rho_s(T)$ can be obtained. In zero temperature limit, the summation reduces to integration and one can easily find that $\pi T \sum_{\omega_n} \frac{\Delta^2}{(\omega_n^2+\Delta^2)^{3/2}} = \int_0^\infty d\omega_m \frac{\Delta^2}{(\omega_n^2+\Delta^2)^{3/2}} = 1$ as expected. In Figure 6.3 we show the numerical results obtained both way. Clearly the two approaches to evaluating stiffness yield exactly the same results. At low temperatures, $\rho_s(T)$ saturates to n/m. As temperature increases, $\rho_s(T)$ decreases monotonically and vanishes at $T = T_c$ as expected.

6.2.2 Quantum critical systems

For superconductivity in quantum critical systems the dynamic structure of the self energy and the pairing vertex has to be retained, and this very fact impedes the possibility of carrying out the Matsubara summation analytically. We therefore implement the frequency summation numerically, based on Eq. (6.13). Before doing this, we obtain the mean field values for the pairing vertex $\Phi(\omega_n)$ and self energy $\tilde{\Sigma}(\omega_n)$, by solving the saddle point equation Eq. (2.25). As is mentioned in the previous section, in γ model, both $\Phi(\omega_n)$ and $\tilde{\Sigma}(\omega_n)$ contain contribution from $V(0)$ which is divergent at a QCP but becomes finite when the system is moved away from a QCP. This piece can be treated as thermal fluctuation and thus can be extracted by introducing a new set of quantities $\Phi^*(\omega_n)$ and $\tilde{\Sigma}^*(\omega_n)$. The equation for $\Phi^*(\omega_n)$ and $\tilde{\Sigma}^*(\omega_n)$ are similar with (2.25) but without $\omega_n = \omega_m$ term in the summation. The transformation $\{\tilde{\Sigma}, \Phi\} \to \{\tilde{\Sigma}^*, \Phi^*\}$ leaves the ratio $\Phi/\tilde{\Sigma}$ invariant. As a result the gap function $\Delta(\omega_n) = \omega_n \Phi(\omega_n)/\tilde{\Sigma}(\omega_n)$ is immune to $V(0)$. Using this fact and introducing the inverse quasiparticle residue $Z(\omega_n)$ via $\Phi(\omega_n) = Z(\omega_n)\Delta(\omega_n)$ and $\tilde{\Sigma}(\omega_n) = Z(\omega_n)\omega_n$, we can rewrite (6.10) as

$$\rho_s(T) = \frac{E_F}{4\pi} \pi T \sum_{\omega_n} \frac{1}{Z(\omega_n)} \frac{\Delta(\omega_n)^2}{[\omega_n^2 + \Delta(\omega_n)^2]^{3/2}}, \tag{6.16}$$

This expression differs from (6.15) in two aspects. First, the gap function $\Delta(\omega_n)$ now depends on frequencies. Second, the appearance of $Z(\omega_n)$ which incorporates strong thermal fluctuations renders a drastic deviation from the conventional BCS results. This can be seen by expressing $Z(\omega_n)$ through $V(0)$,

$$Z(\omega_n) = \frac{\tilde{\Sigma}^*(\omega_n)}{\omega_n} \left(1 + \frac{\pi T V(0)}{\sqrt{\tilde{\Sigma}^*(\omega_n)^2 + \Phi^*(\omega_n)^2}} \right) \tag{6.17}$$

A knowledge on the temperature dependence on $V(0)$ is also important for understanding the temperature evolution of physical quantities that depend on $V(0)$. To this end, we use the 2D Ising nematic quantum criticality as an example. It is found that in this case the finite T nematic order fluctuation mediated interaction takes the form[40]

$$\tilde{\chi}_{\rm nem}(i\Omega_m = 0, \boldsymbol{q}) = \frac{C}{T + \kappa \boldsymbol{q}^2} \tag{6.18}$$

where C and κ are dimensionful constants. From this one can immediately check by integration over momentum that $V(0) \propto 1/T^{1/2}$. Indeed taking this form $V(0)$ diverges in zero temperature limit, signaling the closeness to a QCP. To generalize, we model the temperature dependence as

$$V(0) = \lambda \frac{\bar{g}^{\alpha}}{T^{\alpha}} \tag{6.19}$$

We introduce dimensionless λ to describe its strength and α which falls into the range $0 < \alpha < 1$ in order to satisfies (i) $V(0)$ diverges upon approaching a QCP from finite temperature, and (ii) $\pi T V(0)$ is still small compared to E_F. As is true for γ, we anticipate different pairing systems correspond to different α, for instance $\alpha = 1/2$ in the Ising nematic case. However how the correspondence is set up requires more involved work on particular thermodynamic susceptibilities and is beyond the scope of this paper. The Eliashberg small parameter now scales with temperature as $T^{1-\alpha}$, and it's small at smallest temperatures. Under the scaling assumption (6.19), the combined factor $\pi T V(0) = \lambda \pi \bar{g}^{\alpha} T^{1-\alpha}$ serves as a source of thermal fluctuation and takes its largest value at the largest temperature of our interest – T_p, and becomes vanishingly small at zero temperature limit. The strength of the thermal fluctuation is determined by the λ defined in (6.19).

At finite temperature, SC stiffness becomes dependent on the strength $\pi T V(0)$ with $V(0)$ given in (6.19), where we introduced two dimensionless parameters λ and α. λ describes how strong the thermal fluctuation is, and α controls the scaling behavior which is different for different pairing system. And in order to validate the Eliashberg theory at lowest temperature, we require that $0 < \alpha < 1$. As a first example, we show our results in Figure 6.4 for the case of a 2D Ising nematic QCP, which corresponds to $\gamma = 1/3$ and $\alpha = 1/2$.

In the case of weak thermal fluctuations($\lambda = 1$), $\rho_s(T)$ shows a non monotonic dependence on T: It first increases with T, reaches a maximum and then decays and vanishes at T_p. The reason why $\rho_s(T)$ first increases in this case is because quantum fluctuation which peaks at $T = 0$ becomes weaker as T increases. Although thermal fluctuations increases with T, it's still small in this temperature range. As a result the combination of quantum and thermal fluctuations decreases with T hence $\rho_s(T)$

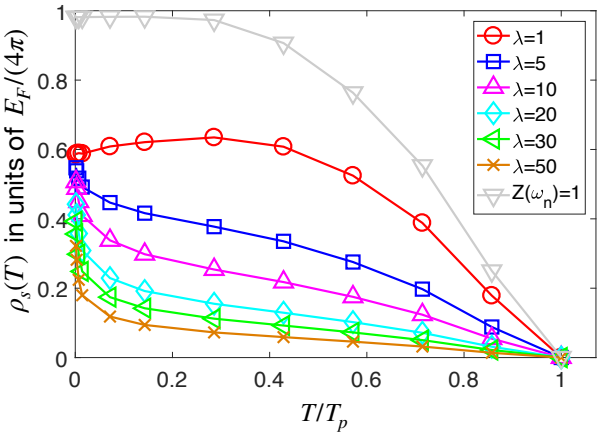

Figure 6.4: Temperature evolution of SC stiffness $\rho_s(T)$ near a 2D Ising nematic QCP ($\gamma = 1/3$ and $\alpha = 1/2$) for different thermal strength λ. $\rho_s(T)$ non monotonic on T at small λ but becomes monotonically decaying at larger T. Despite of different λ, ρ_s vanishes at around $T = T_p \approx 7\bar{g}$. For comparison we also plot the results by intentionally taking $Z(\omega_n) = 1$ in our calculation, which is almost identical to the BCS result in Figure 6.3.

increases. The decaying of $\rho_s(T)$ at larger T is simply due to the strong thermal fluctuations. For comparison, we also obtain $\rho_s(T)$ with NFL effects intentionally taken out, by taking $Z(\omega_n) = 1$ in our calculation, see the gray triangles in Figure 6.4. It almost coincides with the conventional BCS result we shown in Figure 6.3.

In Figure 6.5 we show more results for various γ, α and λ. For $\gamma < 2$, $\rho_s(T)$ all shows non monotonic dependence on T in weak thermal strength (small λ), and this behavior changes into monotonic decreasing at larger λ. In the special case when $\gamma = 2$, the non monotonic behavior exists for all λ and α, as a consequence of the fact that ρ_s vanishes at both $T = 0$ and $T = T_p$. At a given temperature, ρ_s decreases with increasing λ and α, which is totally expected since larger λ means larger thermal fluctuation, and larger α means the thermal fluctuation piece $\pi TV(0) = \lambda\pi\bar{g}T^{1-\alpha}$ is larger for $T < \bar{g}$. In the case when $\pi TV(0) \gg \bar{g}$, we can approximate $Z(\omega_n)$ by $\pi TV(0)/\sqrt{\omega_n^2 + \Delta(\omega_n)^2}$ and from (6.16) we have $\rho_s(T) \approx \frac{E_F}{4\pi}\frac{1}{V(0)}\sum_n \frac{\Delta(\omega_n)^2}{\omega_n^2+\Delta(\omega_n)^2}$. Close the T_p, the gap function

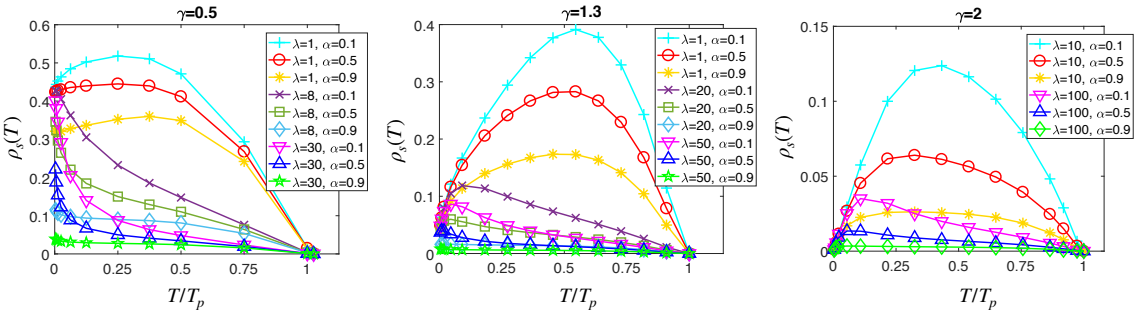

Figure 6.5: Temperature evolution of SC phase stiffness $\rho_s(T)$ (in units of $E_F/(4\pi)$) for $\gamma = 0.5$, 1.3 and 2 and for various α and λ. In zero temperature limit $\rho_s(T = 0)$ is vanishingly small measured in E_F. At finite temperatures, ρ_s decreases with increasing λ and α. For $\gamma < 2$ the non monotonic behavior of $\rho_s(T)$ is seen for weak thermal strength (small λ) and its transition to monotonically decaying at larger λ is also clear. At the special case $\gamma = 2$, because ρ_s vanishes at $T = 0$, the curve $\rho_s(T)$ always remains non monotonic.

$\Delta(\omega_n) \sim \Delta(T)$ is small compared to ω_n, we then have

$$\rho_s(T) \approx \frac{1}{4V(0)} \frac{\Delta(T)^2}{T^2} \frac{E_F}{4\pi} \tag{6.20}$$

To reveal the full picture of how an underlying QCP affects the SC above it, we introduce a new tuning parameter in $V(0)$ to model the distance away from a QCP at $T = 0$, and modify (6.19) as

$$V(0) = \frac{\lambda \bar{g}^\alpha}{(\delta|h - h_c| + T)^\alpha} \tag{6.21}$$

where $h = h_c$ is the location of a QCP and δ is small parameter. We take $|h - h_c|$ to be small, and assume with this condition the nonzero frequency transfer effective interaction $V(\Omega_m \neq 0)$ still takes its form $\bar{g}^\gamma/|\Omega_m|^\gamma$. In Figure 6.6 we present the results of ρ_s close to a QCP for the cases of $\gamma = 0.3$ and $\gamma = 5$, which correspond to 2D Ising nematic QCP and 2D antiferromagnetic QCP respectively. To control the difference, we take $\lambda = 20$ and $\alpha = 0.5$ in both cases. It is clear that for both situation $\rho_s(T)$ is monotonic decreasing with T for any given h. As for a given T close to zero, ρ_s is smallest at $h = h_c$, this indicates that a closeness to a QCP tends to reduce ρ_s.

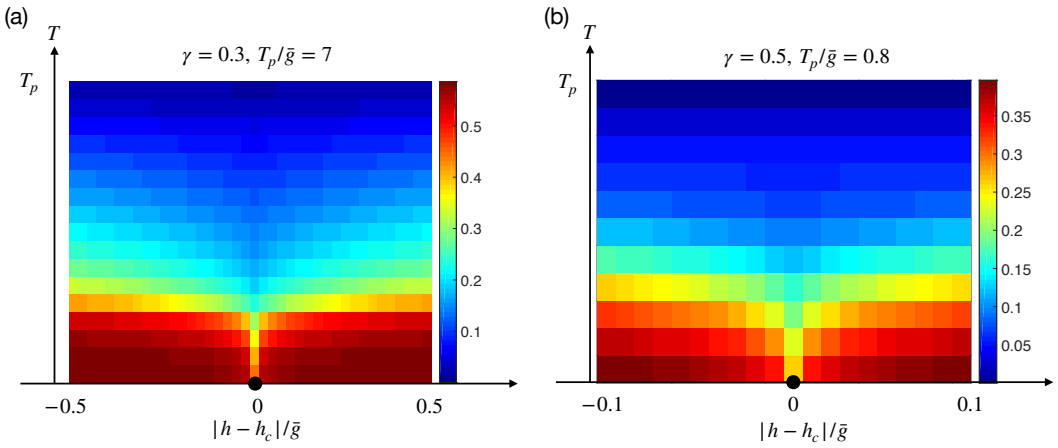

Figure 6.6: SC phase stiffness ρ_s (in units of $\frac{E_F}{4\pi}$) as a function of T and the tuning parameter h near a (a) Ising nematic QCP and (b) Antiferromagnetic QCP. The black dots denote the position of a QCP where $h = h_c$. Here we take $\lambda = 20$ and $\alpha = 0.5$ in both cases.

This reduction would not exist if we take $Z(\omega_n) = 1$ in calculation. The large region of small $\rho_s(T)$ shows in Figure 6.6 implies the possibility of pseudogap physics in γ model. Once there is strong phase fluctuations and the $U(1)$ symmetry is restored, SC is destroyed even though the modulus $|\Delta|$ is still finite. This finite gap is still present in spectral function and thus is observable. Our results show that this pseudogap physics is a direct result of the NFL impact on SC. It would not arise if we intentionally exclude the NFL correction to the fermion energy, and in that case the system behaves like a conventional BCS superconductor. This special interplay between SC state and NFL tendency is thus a unique feature of the presence of QCP in an itinerant fermion system.

Chapter 7

Conclusion and outlook

We studied the pairing problem in a system where fermions interact with each other by exchanging a collective bosonic fluctuation mode, which occurs when a Fermi liquid ground state is close to some QCP. The same interaction that gives rise to superconductivity, also leads to non-Fermi liquid behavior, if there is no superconductivity setting in. But in reality, the two tendencies, or the two fates for fermions, are competitive with each other. Superconductivity is about physics on Fermi surface, and it needs fermions, which are quasiparticles in the system, to form Cooper pairs in order to condensate, but non-Fermi liquid tendency diminish fermion coherence and thus is detrimental to the developing of superconducting long range order.

To address the interplay between superconductivity and non-Fermi liquid, we introduce a general pairing model, in which the pairing interaction on Fermi surface, after momentum average, takes a simpling form: $V(\Omega_m) = \bar{g}^\gamma/|\Omega_m|^\gamma$, where $\bar{g}$ is an effective coupling constant, and $\gamma > 0$ is a dynamical exponent. We have seen in Chapter 2 that a lot of pairing models near a QCP can be mapped into this model, thus a thorough study on this model may reveal the unusual and complex phases that has been observed in correlated electronic materials such as heavy fermion compounds, Copper based and iron based high T_c superconductors etc. Given this particular fermion interaction, a natural questions arises: in the competition between superconductivity and non-Fermi liquid, which one is the winner? We adopt an approximated methods that Eliashberg first used in his study on phonon-mediated superconductivity. In this approximation, one neglects the vertex correction when evaluating fermion self energy. In phonon-mediated

systems, the approximation is validated via a small parameter $\lambda = \omega_D/E_F \approx \sqrt{m/M}$ where m is electron mass and M is ion mass. However for γ model, one should be careful because the justification of Eliashberg theory is case by case. For strong coupling limit of phonon-mediated interaction, $\lambda = \bar{g}^2/(\omega_D E_F)$, and we are in the limit of $\omega_D \to 0$ but $\omega_D E_F$ is still large. For pairing at a nematic QCP, $\lambda = \bar{g}/E_F$. And for pairing in spin-fermion model, $\lambda = 1/$ where N is the number of hot spots. In most cases, as long as the Fermi energy E_F is the largest, we can make use of Eliashberg approximation. Bases on this, we derived two coupling Eliashberg equations for the pairing vertex $\Phi(\omega_m)$ and fermion self energy $\Sigma(\omega_m)$. Properties of this pairing model can be seen by solving these equations and as a conclusion, we plot the phase diagram of γ-model in Figure 7.1

We solve the gap equation on Matsubara axis Chapter 2, and obtain the pairing temperature T_p, the gap amplitude Δ_0 and their ratio. In the limit of $\gamma \to 0$, the interaction becomes a constant, just like that in a BCS model. But because the interaction extends to infinite frequency in γ-model, we find both T_p and Δ_0 diverges in the limit $\gamma \to 0$. Thus the T_p curve in Figure 7.1 goes to infinity as $\gamma \to 0$. However, we they diverges in exactly the same manner, such that their ratio $2\Delta_0/T_p$ remains the BCS value. For larger γ, we find T_p gradually decrease with increasing γ, and saturates to $\bar{g}/(2\pi)$ when $\gamma \to \infty$. This is different from BCS theory, in which the pairing temperature is $T_p \sim e^{1/\bar{g}}$. At $\gamma \to 3$, we find Δ_0 diverges. As a result, the ratio $2\Delta_0/T_p$ is a monotonically increasing function of γ.

In Chapter 3, we present an interesting point about pairing at a QCP. We find, by using an extended model with a large N factor, that when the pairing equation on Matsubara axis is dominated by the first two frequencies $\pm\pi T$, the spectral properties along real frequency axis is a function of ω/T. This ω/T scaling means the characteristic frequency in density of states $N(\omega)$, increases linearly in T. This is the very reason behind the 'gap filling' behavior observed in many cuprates. The 'gap filling' behavior is the phenomenon that when T increases, the peak position in $N(\omega)$ also increase, and so does the weight at $N(\omega = 0)$. Namely, when T increases, we observe the weight in $N(\omega)$ fills in the middle. This is in contrast to the conventional BCS materials, where what we observe is the opposite: as T increase the peak position in $N(\omega)$ moves towards smaller value, whine $N(\omega = 0)$ still remains vanishingly small even if $T \geq T_p$. This is

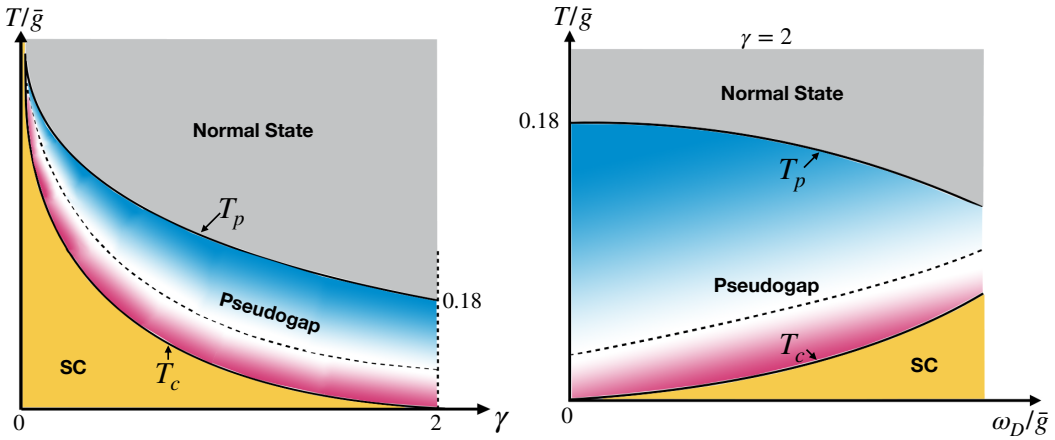

Figure 7.1: Right panel: The phase diagram of the γ model for a generic $\gamma < 2$ at a finite T and vanishing ω_D. For any $\gamma < 2$, the true SC transition temperature T_c is finite, but is smaller than the onset temperature for the paring, T_p. In between T_c and T_p, the system displays a pseudogap behavior. There are two distinct behaviors in the pseudogap regime: close to T_p, the spectral function and the DoS display gap filling behavior, while close to T_c, the behavior becomes more conventional and the gap frequency shifts to a smaller value as T increases. Left panel: The phase diagram of the γ model for $\gamma = 2$ in variables $(T/\bar{g}, \omega_D/\bar{g})$, where ω_D is the mass of a pairing boson. T_p is the onset temperature of the pairing, and T_c is the actual superconducting transition temperature, below which the system establishes phase coherence. In between the system displays pseudogap behavior, in which fermionic pairs are formed, but there is no macroscopic phase coherence. The dashed line separates the two regimes within the pseudogap phase – the one at higher T, where the system behavior is chiefly determined by fermions with the two lowest Matsubara frequencies $\pm\pi T$, and the one at lower T, when fermions with all Matsubara frequencies contribute to the pairing. In these two regimes the system displays gap filling and gap closing behavior, respectively.

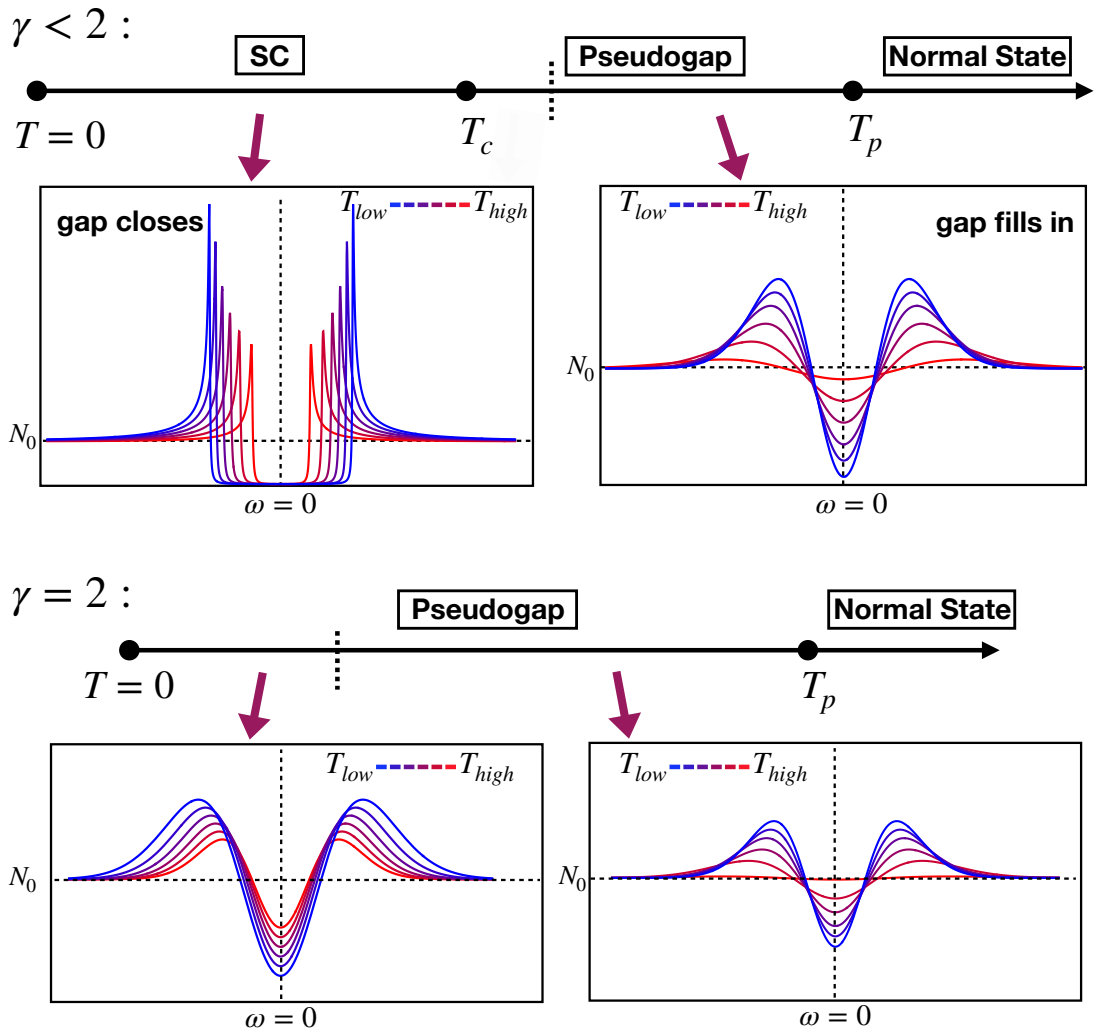

Figure 7.2: The temperature evolution of the DoS $N(\omega)$. For $\gamma < 2$ (upper panel) there is a SC order at $T < T_c$. In this regime and in the pseudogap state at $T \geq T_c$, the temperature variation of $N(\omega)$ resembles that in a conventional BCS superconductor, i.e. when T increases, the position of the maximum in $N(\omega)$ moves to a smaller frequency. At larger T within the pseudogap phase, $N(\omega)$ displays gap filling behavior when the peak position increases with increasing T and $N(\omega = 0)$ increases towards its normal state value. For $\gamma = 2$ (lower panel), $T_c = 0$, but the two different regimes of pseudogap behavior are present.

called 'gap closing' because as T increases the gap in $N(\omega)$ gradually closes. Back in the original case when $N = 1$, we do observe two distinct behaviors in the temperature evolution of $N(\omega)$, and a crossover between these two, see the Dashed line in Figure 7.1. At higher T, where the first two frequencies $\pi \pm T$ are still in dominant in gap equations, we have 'gap filling' behavior; while at lower T when all frequencies contribute to the gap equation equally, the system behaves like a conventional BCS superconductor with 'gap closing'. For details on the distinction between these two behaviors, see Figure 7.2.

In Chapter 4 we come to a more interesting aspect of the gap equations of pairing at a QCP. We find unlike conventional BCS gap equation, there exists an infinite number of solutions $\Delta_n(\omega_m)$ to our gap equations in γ-model. These multiple solutions correspond to different local minima of the total free energy, and has their unique pairing temperature $T_{p,n}$. We find the gap amplitudes and $T_{p,n}$ decays with n in an exponential way. Moreover, the gap structure $\Delta_n(\omega_m)$ are also different. By analyzing the linearized gap equations at $T = 0$ and finite T, we find $\Delta_n(\omega_m)$ changes sign n times for $\omega_m \in (0, \infty)$. The sign preserving $n = 0$ solution is the one with the largest pairing temperature $T_{p,0}$. If we move the system away from a QCP, we will see the solutions disappear one by one, and at some point, there is only one solution left, like in BCS theory. For $\gamma > 1$, we analytically continue the solution from the Matsubara axis to the whole upper half frequency plane. The position where $\Delta(z) = 0$ is a nodal point for the gap function, or a vortex point for the gap phase $\eta(z)$, defined as $\Delta(z) = |\Delta(z)|e^{i\eta(z)}$. We find, for a solution Δ_n, in addition to n vortices on Matsubara axis, there are other vortices in the upper half plane. The number of these additional vortices, are likely to be independent to n, but increases as γ increases, and become infinite in the limit $\gamma \to 2$. The presence of these vortices means if we go along real frequency axis, the phase $\eta(\omega)$ with accumulates multiples times of 2π, and both the real and imaginary part of the gap function $\Delta'(\omega)$ and $\Delta''(\omega)$ oscillates. The case $\gamma = 2$ is of particular interest. Physically it corresponds to the strong coupling limit of phonon-mediated pairing system. We find in this situation, the discrete set of solutions become continuous, described be a factor $\xi \geq 0$. All the solutions with finite n now collapse into $\xi = 0$, which means Δ_n with finite n now become the same. The density of states $N(\omega)$ in this case is just a collection of delta functions. The existence of a continuous solutions opens up a phase fluctuation channel. Near the solution bottom when $\xi \to 0$, superconducting phase can fluctuates

around different solutions without costing extra energy. As a result, the phase stiffness scales as ω_D and vanishes if $\omega_D \to 0$. A system with a finite mean field solution Δ but vanishing phase stiffness is in the pseudogap regime.

In Chapter 5 we discussed the odd frequency solutions ($\Delta(-\omega_m) = -\Delta(\omega_m)$) to the gap equation in γ-model. Previous studies on odd frequency pairing focused on building heterostructure using superconductor and ferromagnet, or similar setup, and they find in the interface there could be odd frequency pairing. We find, for pairing at a QCP, the odd frequency pairing can also exist. We find such solutions for $\gamma < 1$ and $N < 1$. The gap function at small frequencies, scales as $\Delta(\omega_m) \sim \omega_m^a$ with $a < 1$, and is larger than ω_m. The implication out of this is there is no zero bias peak in the measured density of states. This is different from previous findings using S/F heterostructure, where people using zero bias peak to identify odd frequency pairing. In the last Chapter 6, we study the phase fluctuation in γ-model. We derived the expression for calculating phase stiffness $\rho_s(T)$, and use it to evaluate its temperature evolution.

The study of superconductivity in correlated systems has been a hot area in condensed matter community for years, yet still there are many interesting things to be discovered. γ-model provides a simplified way to explain unusual behaviors of superconductivity in systems where there is a quantum critical point. It also offers an alternative way to realize phases such as pseudogap and odd frequency pairing. We believe in future works, one can even use γ model to study non-Fermi liquid, or include fermion feedback to the boson propagator to have a more accurate pairing interaction, or adding repulsive interaction and so on.

References

[1] Shina Tan. Energetics of a strongly correlated fermi gas. *Annals of Physics*, 323(12):2952–2970, 2008.

[2] A. A. Abrikosov, L. P. Gorkov, and I. E. Dzyaloshinski, *Methods of Quantum Feld Theory in Statistical Physics*, 2nd edition, (Pergamon Oxford, 1965).

[3] J. M. Luttinger and J. C. Ward. Ground-state energy of a many-fermion system. ii. *Phys. Rev.*, 118:1417–1427, Jun 1960.

[4] C.J Pethick and D.G Ravenhall. Growth of instabilities in a normal fermi liquid. *Annals of Physics*, 183(1):131–165, 1988.

[5] T. Moriya. *Spin fluctuations in itinerant electron magnetism*. Springer series in solid-state sciences. Springer-Verlag, 1985.

[6] Vadim Oganesyan, Steven A. Kivelson, and Eduardo Fradkin. Quantum theory of a nematic fermi fluid. *Phys. Rev. B*, 64:195109, Oct 2001.

[7] Dmitrii L. Maslov and Andrey V. Chubukov. Fermi liquid near pomeranchuk quantum criticality. *Phys. Rev. B*, 81:045110, Jan 2010.

[8] Christoph J. Halboth and Walter Metzner. d. *Phys. Rev. Lett.*, 85:5162–5165, Dec 2000.

[9] J. Quintanilla and A. J. Schofield. Pomeranchuk and topological fermi surface instabilities from central interactions. *Phys. Rev. B*, 74:115126, Sep 2006.

[10] T. Senthil. Critical fermi surfaces and non-fermi liquid metals. *Phys. Rev. B*, 78:035103, Jul 2008.

[11] J. E. Hirsch. Spin-split states in metals. *Phys. Rev. B*, 41:6820–6827, Apr 1990.

[12] Andrey V. Chubukov and Dmitrii L. Maslov. Spin conservation and fermi liquid near a ferromagnetic quantum critical point. *Phys. Rev. Lett.*, 103:216401, Nov 2009.

[13] A. J. Leggett. Theory of a superfluid fermi liquid. i. general formalism and static properties. *Phys. Rev.*, 140:A1869–A1888, Dec 1965.

[14] Egor I. Kiselev, Mathias S. Scheurer, Peter Wölfle, and Jörg Schmalian. Limits on dynamically generated spin-orbit coupling: Absence of $l = 1$ pomeranchuk instabilities in metals. *Phys. Rev. B*, 95:125122, Mar 2017.

[15] Yi-Ming Wu, Avraham Klein, and Andrey V. Chubukov. Conditions for $l = 1$ pomeranchuk instability in a fermi liquid. *Phys. Rev. B*, 97:165101, Apr 2018.

[16] Ar. Abanov, A. V. Chubukov, and A. M. Finkel'stein. Coherent vs . incoherent pairing in 2d systems near magnetic instability. *EPL (Europhysics Letters)*, 54(4):488, 2001.

[17] Ar. Abanov, Andrey V. Chubukov, and J. Schmalian. Quantum-critical theory of the spin-fermion model and its application to cuprates: Normal state analysis. *Advances in Physics*, 52(3):119–218, 2003.

[18] Ar. Abanov and Andrey V. Chubukov. A relation between the resonance neutron peak and arpes data in cuprates. *Phys. Rev. Lett.*, 83:1652–1655, Aug 1999.

[19] Sung-Sik Lee. Low-energy effective theory of fermi surface coupled with u(1) gauge field in $2 + 1$ dimensions. *Phys. Rev. B*, 80:165102, Oct 2009.

[20] Denis Dalidovich and Sung-Sik Lee. Perturbative non-fermi liquids from dimensional regularization. *Phys. Rev. B*, 88:245106, Dec 2013.

[21] Subir Sachdev, Max A. Metlitski, Yang Qi, and Cenke Xu. Fluctuating spin density waves in metals. *Phys. Rev. B*, 80:155129, Oct 2009.

[22] Eun Gook Moon and Subir Sachdev. Competition between spin density wave order and superconductivity in the underdoped cuprates. *Phys. Rev. B*, 80:035117, Jul 2009.

[23] Eun-Gook Moon and Andrey Chubukov. Quantum-critical pairing with varying exponents. *Journal of Low Temperature Physics*, 161(1):263–281, Oct 2010.

[24] Max A. Metlitski and Subir Sachdev. Quantum phase transitions of metals in two spatial dimensions. i. ising-nematic order. *Phys. Rev. B*, 82:075127, Aug 2010.

[25] Max A. Metlitski and Subir Sachdev. Quantum phase transitions of metals in two spatial dimensions. ii. spin density wave order. *Phys. Rev. B*, 82:075128, Aug 2010.

[26] R. Mahajan, D. M. Ramirez, S. Kachru, and S. Raghu. Quantum critical metals in $d = 3 + 1$ dimensions. *Phys. Rev. B*, 88:115116, Sep 2013.

[27] A. Liam Fitzpatrick, Shamit Kachru, Jared Kaplan, and S. Raghu. Non-fermi-liquid fixed point in a wilsonian theory of quantum critical metals. *Phys. Rev. B*, 88:125116, Sep 2013.

[28] A. Liam Fitzpatrick, Shamit Kachru, Jared Kaplan, and S. Raghu. Non-fermi-liquid behavior of large-N_B quantum critical metals. *Phys. Rev. B*, 89:165114, Apr 2014.

[29] Gonzalo Torroba and Huajia Wang. Quantum critical metals in $4 - \epsilon$ dimensions. *Phys. Rev. B*, 90:165144, Oct 2014.

[30] A. Liam Fitzpatrick, Gonzalo Torroba, and Huajia Wang. Aspects of renormalization in finite-density field theory. *Phys. Rev. B*, 91:195135, May 2015. and references therein.

[31] D. J. Scalapino. A common thread: The pairing interaction for unconventional superconductors. *Rev. Mod. Phys.*, 84:1383–1417, Oct 2012.

[32] Samuel Lederer, Yoni Schattner, Erez Berg, and Steven A. Kivelson. Superconductivity and non-fermi liquid behavior near a nematic quantum critical point. *Proceedings of the National Academy of Sciences*, 114(19):4905–4910, 2017.

[33] L. Fratino, P. Sémon, G. Sordi, and A.-M. S. Tremblay. An organizing principle for two-dimensional strongly correlated superconductivity. *Scientific Reports*, 6:22715, 03 2016.

[34] S. Maiti and A. V. Chubukov in "Novel Superfluids", Bennemann and Ketterson eds., Oxford University Press (2014), and references therein.

[35] Max A. Metlitski, David F. Mross, Subir Sachdev, and T. Senthil. Cooper pairing in non-fermi liquids. *Phys. Rev. B*, 91:115111, Mar 2015.

[36] Yuxuan Wang and Andrey V. Chubukov. Superconductivity at the onset of spin-density-wave order in a metal. *Phys. Rev. Lett.*, 110:127001, Mar 2013.

[37] Andrey V. Chubukov and Peter Wölfle. Quasiparticle interaction function in a two-dimensional fermi liquid near an antiferromagnetic critical point. *Phys. Rev. B*, 89:045108, Jan 2014.

[38] Eduardo Fradkin, Steven A. Kivelson, Michael J. Lawler, James P. Eisenstein, and Andrew P. Mackenzie. Nematic fermi fluids in condensed matter physics. *Annual Review of Condensed Matter Physics*, 1(1):153–178, 2010.

[39] S. Lederer, Y. Schattner, E. Berg, and S. A. Kivelson. Enhancement of superconductivity near a nematic quantum critical point. *Phys. Rev. Lett.*, 114:097001, Mar 2015.

[40] Max H. Gerlach, Yoni Schattner, Erez Berg, and Simon Trebst. Quantum critical properties of a metallic spin-density-wave transition. *Phys. Rev. B*, 95:035124, Jan 2017.

[41] Yoni Schattner, Samuel Lederer, Steven A. Kivelson, and Erez Berg. Ising nematic quantum critical point in a metal: A monte carlo study. *Phys. Rev. X*, 6:031028, Aug 2016.

[42] Xiaoyu Wang, Yoni Schattner, Erez Berg, and Rafael M. Fernandes. Superconductivity mediated by quantum critical antiferromagnetic fluctuations: The rise and fall of hot spots. *Phys. Rev. B*, 95:174520, May 2017.

[43] Kristjan Haule and Gabriel Kotliar. Strongly correlated superconductivity: A plaquette dynamical mean-field theory study. *Phys. Rev. B*, 76:104509, Sep 2007.

[44] Wenhu Xu, Gabriel Kotliar, and Alexei M. Tsvelik. Quantum critical point revisited by dynamical mean-field theory. *Phys. Rev. B*, 95:121113, Mar 2017.

[45] Sung-Sik Lee. Recent developments in non-fermi liquid theory. *Annual Review of Condensed Matter Physics*, 9(1):227–244, 2018.

[46] D. T. Son. Superconductivity by long-range color magnetic interaction in high-density quark matter. *Phys. Rev. D*, 59:094019, Apr 1999.

[47] N. E. Bonesteel, I. A. McDonald, and C. Nayak. Gauge fields and pairing in double-layer composite fermion metals. *Phys. Rev. Lett.*, 77:3009–3012, Sep 1996.

[48] Ziqiang Wang, Wenjin Mao, and Kevin Bedell. Superconductivity near itinerant ferromagnetic quantum criticality. *Phys. Rev. Lett.*, 87:257001, Nov 2001.

[49] R. Roussev and A. J. Millis. Quantum critical effects on transition temperature of magnetically mediated p-wave superconductivity. *Phys. Rev. B*, 63:140504, Mar 2001.

[50] Andrey V. Chubukov, Alexander M. Finkel'stein, Robert Haslinger, and Dirk K. Morr. First-order superconducting transition near a ferromagnetic quantum critical point. *Phys. Rev. Lett.*, 90:077002, Feb 2003.

[51] A. J. Millis. Nearly antiferromagnetic fermi liquids: An analytic eliashberg approach. *Phys. Rev. B*, 45:13047–13054, Jun 1992.

[52] C. Castellani, C. Di Castro, and M. Grilli. Singular quasiparticle scattering in the proximity of charge instabilities. *Phys. Rev. Lett.*, 75:4650–4653, Dec 1995.

[53] A. Perali, C. Castellani, C. Di Castro, and M. Grilli. d-wave superconductivity near charge instabilities. *Phys. Rev. B*, 54:16216–16225, Dec 1996.

[54] S. Andergassen, S. Caprara, C. Di Castro, and M. Grilli. Anomalous isotopic effect near the charge-ordering quantum criticality. *Phys. Rev. Lett.*, 87:056401, Jul 2001.

[55] Debanjan Chowdhury and Subir Sachdev. Feedback of superconducting fluctuations on charge order in the underdoped cuprates. *Phys. Rev. B*, 90:134516, Oct 2014.

[56] Debanjan Chowdhury and Subir Sachdev. Density-wave instabilities of fractionalized fermi liquids. *Phys. Rev. B*, 90:245136, Dec 2014.

[57] Yuxuan Wang and Andrey V. Chubukov. Enhancement of superconductivity at the onset of charge-density-wave order in a metal. *Phys. Rev. B*, 92:125108, Sep 2015.

[58] R. Combescot. Strong-coupling limit of eliashberg theory. *Phys. Rev. B*, 51:11625–11634, May 1995.

[59] Bergmann, G. and Rainer, D. Z. Physik (1973) 263: 59.

[60] Philip B. Allen and Dierk Rainer. Phonon suppression of coherence peak in nuclear spin relaxation rate of superconductors. *Nature*, 349:396 EP –, Jan 1991.

[61] P. B. Allen and R. C. Dynes. Transition temperature of strong-coupled superconductors reanalyzed. *Phys. Rev. B*, 12:905–922, Aug 1975.

[62] F. Marsiglio, M. Schossmann, and J. P. Carbotte. Iterative analytic continuation of the electron self-energy to the real axis. *Phys. Rev. B*, 37:4965–4969, Apr 1988.

[63] F. Marsiglio and J. P. Carbotte. Gap function and density of states in the strong-coupling limit for an electron-boson system. *Phys. Rev. B*, 43:5355–5363, Mar 1991.

[64] F. Marsiglio and J. P. Carbotte. *Electron-Phonon Superconductivity*, pages 73–162. Springer Berlin Heidelberg, Berlin, Heidelberg, 2008.

[65] A.E. Karakozov, E.G. Maksimov, and A.A. Mikhailovsky. The investigation of eliashberg equations for superconductors with strong electron-phonon interaction. *Solid State Communications*, 79(4):329 – 335, 1991.

[66] D.J. Scalapino. CRC Press, 1969.

[67] J. P. Carbotte. Properties of boson-exchange superconductors. *Rev. Mod. Phys.*, 62:1027–1157, Oct 1990.

[68] F. Marsiglio and J. P. Carbotte. Gap function and density of states in the strong-coupling limit for an electron-boson system. *Phys. Rev. B*, 43:5355–5363, Mar 1991.

[69] R. Combescot. Strong-coupling limit of eliashberg theory. *Phys. Rev. B*, 51:11625–11634, May 1995.

[70] Yuxuan Wang, Artem Abanov, Boris L. Altshuler, Emil A. Yuzbashyan, and Andrey V. Chubukov. Superconductivity near a quantum-critical point: The special role of the first matsubara frequency. *Phys. Rev. Lett.*, 117:157001, Oct 2016.

[71] Øystein Fischer, Martin Kugler, Ivan Maggio-Aprile, Christophe Berthod, and Christoph Renner. Scanning tunneling spectroscopy of high-temperature superconductors. *Rev. Mod. Phys.*, 79:353–419, Mar 2007.

[72] T. J. Reber, N. C. Plumb, Z. Sun, Y. Cao, Q. Wang, K. McElroy, H. Iwasawa, M. Arita, J. S. Wen, Z. J. Xu, G. Gu, Y. Yoshida, H. Eisaki, Y. Aiura, and D. S. Dessau. The origin and non-quasiparticle nature of fermi arcs in bi2sr2cacu2o8+d. *Nature Physics*, 8:606 EP –, Jul 2012.

[73] T. J. Reber, N. C. Plumb, Y. Cao, Z. Sun, Q. Wang, K. McElroy, H. Iwasawa, M. Arita, J. S. Wen, Z. J. Xu, G. Gu, Y. Yoshida, H. Eisaki, Y. Aiura, and D. S. Dessau. Prepairing and the "filling" gap in the cuprates from the tomographic density of states. *Phys. Rev. B*, 87:060506, Feb 2013.

[74] Haoxiang Li, Xiaoqing Zhou, Stephen Parham, Theodore J. Reber, Helmuth Berger, Gerald B. Arnold, and Daniel S. Dessau, Nature Communications, vol. 9, 26 (2018).

[75] Haoxiang Li, Xiaoqing Zhou, Stephen Parham, Kyle N. Gordon, R. D. Zhong, J. Schneeloch, G. D. Gu, Y. Huang, H. Berger, G. B. Arnold, D. S. Dessau, arXiv:1809.02194.

[76] Takeshi Kondo, Ari D. Palczewski, Yoichiro Hamaya, Tsunehiro Takeuchi, J. S. Wen, Z. J. Xu, Genda Gu, and Adam Kaminski. Formation of gapless fermi arcs

and fingerprints of order in the pseudogap state of cuprate superconductors. *Phys. Rev. Lett.*, 111:157003, Oct 2013.

[77] Takeshi Kondo, A. F. Santander-Syro, O. Copie, Chang Liu, M. E. Tillman, E. D. Mun, J. Schmalian, S. L. Bud'ko, M. A. Tanatar, P. C. Canfield, and A. Kaminski. Momentum dependence of the superconducting gap in ndfeaso$_{0.9}$f$_{0.1}$ single crystals measured by angle resolved photoemission spectroscopy. *Phys. Rev. Lett.*, 101:147003, Oct 2008.

[78] A. Kanigel, M. R. Norman, M. Randeria, U. Chatterjee, S. Souma, A. Kaminski, H. M. Fretwell, S. Rosenkranz, M. Shi, T. Sato, T. Takahashi, Z. Z. Li, H. Raffy, K. Kadowaki, D. Hinks, L. Ozyuzer, and J. C. Campuzano. Evolution of the pseudogap from fermi arcs to the nodal liquid. *Nature Physics*, 2:447 EP –, Jun 2006.

[79] A. Kanigel, U. Chatterjee, M. Randeria, M. R. Norman, S. Souma, M. Shi, Z. Z. Li, H. Raffy, and J. C. Campuzano. Protected nodes and the collapse of fermi arcs in high-T_c cuprate superconductors. *Phys. Rev. Lett.*, 99:157001, Oct 2007.

[80] H. Ding, J. C. Campuzano, A. F. Bellman, T. Yokoya, M. R. Norman, M. Randeria, T. Takahashi, H. Katayama-Yoshida, T. Mochiku, K. Kadowaki, and G. Jennings. Momentum dependence of the superconducting gap in bi$_2$sr$_2$cacu$_2O_8$. *Phys. Rev. Lett.*, 74:2784–2787, Apr 1995.

[81] J.C. Campuzano, M.R. Norman, and M. Randeria "Photoemission in the high-T_c superconductors", in "Superconductivity: Novel Superconductors", v.2, K.H. Bennemann and J.B. Ketterson eds, Springer 2008.

[82] Andrea Damascelli, Zahid Hussain, and Zhi-Xun Shen. Angle-resolved photoemission studies of the cuprate superconductors. *Rev. Mod. Phys.*, 75:473–541, Apr 2003.

[83] Makoto Hashimoto, Inna M. Vishik, Rui-Hua He, Thomas P. Devereaux, and Zhi-Xun Shen. Energy gaps in high-transition-temperature cuprate superconductors. *Nature Physics*, 10:483 EP –, Jun 2014. Review Article.

[84] P. D. Johnson, T. Valla, A. V. Fedorov, Z. Yusof, B. O. Wells, Q. Li, A. R. Moodenbaugh, G. D. Gu, N. Koshizuka, C. Kendziora, Sha Jian, and D. G. Hinks. Doping and temperature dependence of the mass enhancement observed in the cuprate $bi_2sr_2cacu_2O_{8+\delta}$. *Phys. Rev. Lett.*, 87:177007, Oct 2001.

[85] A. A. Kordyuk and S. V. Borisenko. Arpes on high-temperature superconductors: Simplicity vs. complexity (review article). *Low Temperature Physics*, 32(4):298–304, 2006.

[86] A. A. Kordyuk. Pseudogap from arpes experiment: Three gaps in cuprates and topological superconductivity (review article). *Low Temperature Physics*, 41(5):319–341, 2015.

[87] Yang He, Yi Yin, M. Zech, Anjan Soumyanarayanan, Michael M. Yee, Tess Williams, M. C. Boyer, Kamalesh Chatterjee, W. D. Wise, I. Zeljkovic, Takeshi Kondo, T. Takeuchi, H. Ikuta, Peter Mistark, Robert S. Markiewicz, Arun Bansil, Subir Sachdev, E. W. Hudson, and J. E. Hoffman. Fermi surface and pseudogap evolution in a cuprate superconductor. *Science*, 344(6184):608–611, 2014.

[88] Yingying Peng, Jianqiao Meng, Daixiang Mou, Junfeng He, Lin Zhao, Yue Wu, Guodong Liu, Xiaoli Dong, Shaolong He, Jun Zhang, Xiaoyang Wang, Qinjun Peng, Zhimin Wang, Shenjin Zhang, Feng Yang, Chuangtian Chen, Zuyan Xu, T. K. Lee, and X. J. Zhou. Disappearance of nodal gap across the insulator-superconductor transition in a copper-oxide superconductor. *Nature Communications*, 4:2459 EP –, Sep 2013. Article.

[89] P. Monthoux, D. Pines, and G. G. Lonzarich. Superconductivity without phonons. *Nature*, 450:1177, 2007.

[90] Ar. Abanov, A. V. Chubukov, and Schmalian J. Fingerprints of spin mediated pairing in cuprates. *Journal of Electron spectroscopy and related phenomena*, 117:129, 2001.

[91] Artem Abanov and Andrey V. Chubukov. Interplay between superconductivity and non-fermi liquid at a quantum critical point in a metal. i. the γ model and

its phase diagram at $T = 0$: The case $0 < \gamma < 1$. *Phys. Rev. B*, 102:024524, Jul 2020.

[92] Yuxuan Wang, Artem Abanov, Boris L. Altshuler, Emil A. Yuzbashyan, and Andrey V. Chubukov. Superconductivity near a quantum-critical point: The special role of the first matsubara frequency. *Phys. Rev. Lett.*, 117:157001, Oct 2016.

[93] S. Raghu, Gonzalo Torroba, and Huajia Wang. Metallic quantum critical points with finite bcs couplings. *Phys. Rev. B*, 92:205104, Nov 2015.

[94] Huajia Wang, Yuxuan Wang, and Gonzalo Torroba. Superconductivity versus quantum criticality: Effects of thermal fluctuations. *Phys. Rev. B*, 97:054502, Feb 2018.

[95] Yi-Ming Wu, Shang-Shun Zhang, Artem Abanov, and Andrey V. Chubukov. Interplay between superconductivity and non-fermi liquid at a quantum critical point in a metal. iv. the γ model and its phase diagram at $1 < \gamma < 2$. *Phys. Rev. B*, 103:024522, Jan 2021.

[96] Y. Wada. The effect of quasiparticle damping on the ratio between the energy gap and the transition temperature of lead. *Rev. Mod. Phys.*, 36:253–257, Jan 1964.

[97] John Bardeen and Michael Stephen. Free-energy difference between normal and superconducting states. *Phys. Rev.*, 136:A1485–A1487, Dec 1964.

[98] Robert Haslinger and Andrey V. Chubukov. Condensation energy in strongly coupled superconductors. *Phys. Rev. B*, 68:214508, Dec 2003.

[99] Ilya Esterlis and Jörg Schmalian. Cooper pairing of incoherent electrons: An electron-phonon version of the sachdev-ye-kitaev model. *Phys. Rev. B*, 100:115132, Sep 2019.

[100] Daniel Hauck, Markus J. Klug, Ilya Esterlis, and Jörg Schmalian. Eliashberg equations for an electron-phonon version of the sachdev-ye-kitaev model: Pair breaking in non-fermi liquid superconductors. *Annals of Physics*, 417:168120, 2020.

[101] Jacob Linder, Takehito Yokoyama, Asle Sudbø, and Matthias Eschrig. Pairing symmetry conversion by spin-active interfaces in magnetic normal-metal–superconductor junctions. *Phys. Rev. Lett.*, 102:107008, Mar 2009.

[102] M. Houzet and A. I. Buzdin. Long range triplet josephson effect through a ferromagnetic trilayer. *Phys. Rev. B*, 76:060504, Aug 2007.

[103] Jacob Linder and Jason W. A. Robinson. Superconducting spintronics. *Nature Physics*, 11(4):307–315, Apr 2015.

[104] F. S. Bergeret, A. F. Volkov, and K. B. Efetov. Long-range proximity effects in superconductor-ferromagnet structures. *Phys. Rev. Lett.*, 86:4096–4099, Apr 2001.

[105] A. F. Volkov, F. S. Bergeret, and K. B. Efetov. Odd triplet superconductivity in superconductor-ferromagnet multilayered structures. *Phys. Rev. Lett.*, 90:117006, Mar 2003.

[106] Y. Tanaka, Y. Asano, A. A. Golubov, and S. Kashiwaya. Anomalous features of the proximity effect in triplet superconductors. *Phys. Rev. B*, 72:140503, Oct 2005.

[107] Y. Tanaka, S. Kashiwaya, and T. Yokoyama. Theory of enhanced proximity effect by midgap andreev resonant state in diffusive normal-metal/triplet superconductor junctions. *Phys. Rev. B*, 71:094513, Mar 2005.

[108] Y. Tanaka and A. A. Golubov. Theory of the proximity effect in junctions with unconventional superconductors. *Phys. Rev. Lett.*, 98:037003, Jan 2007.

[109] Y. Tanaka, Y. Tanuma, and A. A. Golubov. Odd-frequency pairing in normal-metal/superconductor junctions. *Phys. Rev. B*, 76:054522, Aug 2007.

[110] M. Eschrig, T. Löfwander, T. Champel, J. C. Cuevas, J. Kopu, and Gerd Schön. Symmetries of pairing correlations in superconductor–ferromagnet nanostructures. *Journal of Low Temperature Physics*, 147(3):457–476, May 2007.

[111] Annica M. Black-Schaffer and Alexander V. Balatsky. Odd-frequency superconducting pairing in multiband superconductors. *Phys. Rev. B*, 88:104514, Sep 2013.

[112] Alex Aperis, Pablo Maldonado, and Peter M. Oppeneer. Ab initio theory of magnetic-field-induced odd-frequency two-band superconductivity in mgb_2. *Phys. Rev. B*, 92:054516, Aug 2015.

[113] Yasuhiro Asano and Akihiro Sasaki. Odd-frequency cooper pairs in two-band superconductors and their magnetic response. *Phys. Rev. B*, 92:224508, Dec 2015.

[114] J.R. Schrieffer. Benjamin, New York, 1964.

[115] Alexander Balatsky and Elihu Abrahams. New class of singlet superconductors which break the time reversal and parity. *Phys. Rev. B*, 45:13125–13128, Jun 1992.

[116] V. L. Berezinskii. New model of the anisotropic phase of superfluid he ^{3}. *JETP Letters*, 20:287, Nov 1974.

[117] Jacob Linder and Alexander V. Balatsky. Odd-frequency superconductivity. *Rev. Mod. Phys.*, 91:045005, Dec 2019.

[118] Yi-Ming Wu, Artem Abanov, Yuxuan Wang, and Andrey V. Chubukov. Special role of the first matsubara frequency for superconductivity near a quantum critical point: Nonlinear gap equation below T_c and spectral properties in real frequencies. *Phys. Rev. B*, 99:144512, Apr 2019.

[119] F. Marsiglio, M. Schossmann, and J. P. Carbotte. Iterative analytic continuation of the electron self-energy to the real axis. *Phys. Rev. B*, 37:4965–4969, Apr 1988.

[120] F. Marsiglio and J. P. Carbotte. Gap function and density of states in the strong-coupling limit for an electron-boson system. *Phys. Rev. B*, 43:5355–5363, Mar 1991.

[121] P. W. Anderson. Plasmons, gauge invariance, and mass. *Phys. Rev.*, 130:439–442, Apr 1963.

[122] L. Benfatto, A. Toschi, and S. Caprara. Low-energy phase-only action in a superconductor: A comparison with the XY model. *Phys. Rev. B*, 69:184510, May 2004.